

NO-A104 923

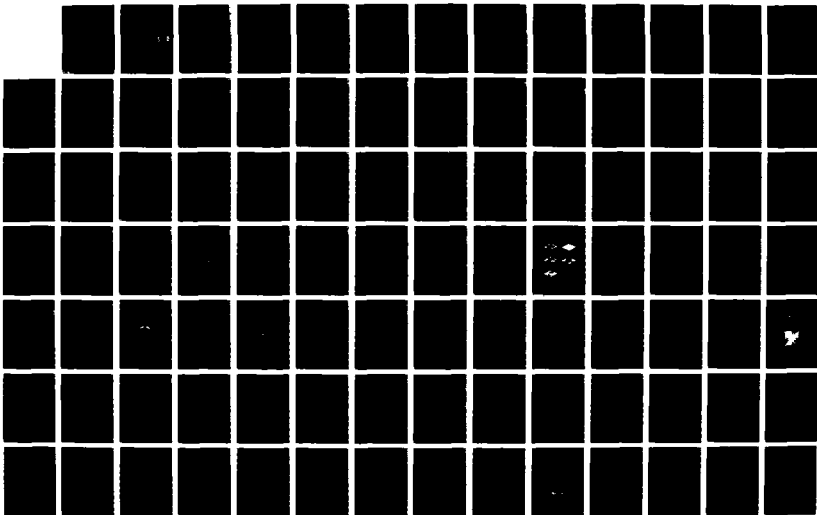
METHODS FOR CORRECTION OF REFRACTIVE ERRORS(U) PURDUE
UNIV LAFAYETTE IN SCHOOL OF ELECTRICAL ENGINEERING
A C KAK 31 DEC 85 DAND17-82-C-2019

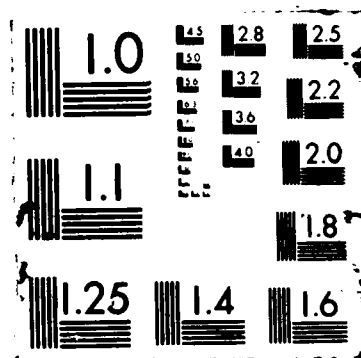
1/3

UNCLASSIFIED

F/G 20/6

NL





AD-A184 923

DTIC ACCESSION NUMBER

LEVEL

PHOTOGRAPH THIS SHEET

INVENTORY

METHODS FOR CORRECTION OF REFRACTIVE ERRORS

DOCUMENT IDENTIFICATION

31 Dec 1985

This document has been approved
for public release and sale; its
distribution is unlimited.

DISTRIBUTION STATEMENT

ACCESSION FOR

NTIS GRA&I ☒

DTIC TAB ☐

UNANNOUNCED ☐

JUSTIFICATION

BY

DISTRIBUTION /

AVAILABILITY CODES

DIST

AVAIL AND/OR SPECIAL

A-1

DISTRIBUTION STAMP



DTIC
ELECTE
OCT 14 1987
S E D

DATE ACCESSIONED

DATE RETURNED

87 10 6 120

DATE RECEIVED IN DTIC

REGISTERED OR CERTIFIED NO.

PHOTOGRAPH THIS SHEET AND RETURN TO DTIC-FDAC

AD-A184 923

AD_____

METHODS FOR CORRECTION OF REFRACTIVE ERRORS

A. C. Kak

Final Report

December 31, 1985

Supported by

**U. S. Army Medical Research and Development Command
Fort Detrick, Frederick, Maryland 21701**

Contract Number DAMD17-82-C-2019

**School of Electrical Engineering
Purdue University
West Lafayette, IN 47907**

**Approved for public release;
Distribution Unlimited**

**The findings of this report are not to be construed as an
official Department of the Army position unless so designated
by other authorized documents.**

REPORT DOCUMENTATION PAGE				Form Approved OMB No. 0704-0188	
1a. REPORT SECURITY CLASSIFICATION Unclassified			1b. RESTRICTIVE MARKINGS		
2a. SECURITY CLASSIFICATION AUTHORITY			3. DISTRIBUTION / AVAILABILITY OF REPORT Approved for public release; Distribution unlimited		
2b. DECLASSIFICATION / DOWNGRADING SCHEDULE					
4. PERFORMING ORGANIZATION REPORT NUMBER(S)			5. MONITORING ORGANIZATION REPORT NUMBER(S)		
6a. NAME OF PERFORMING ORGANIZATION Purdue University School of Electrical Engineering		6b. OFFICE SYMBOL (if applicable)	7a. NAME OF MONITORING ORGANIZATION		
6c. ADDRESS (City, State, and ZIP Code) West Lafayette, IN 47907			7b. ADDRESS (City, State, and ZIP Code)		
8a. NAME OF FUNDING / SPONSORING ORGANIZATION U.S. Army Medical Research & Development Command		8b. OFFICE SYMBOL (if applicable)	9. PROCUREMENT INSTRUMENT IDENTIFICATION NUMBER DAMD17-82-C-2019		
8c. ADDRESS (City, State, and ZIP Code) Fort Detrick Frederick, Maryland 21701-5012			10. SOURCE OF FUNDING NUMBERS		
			PROGRAM ELEMENT NO. 62777A	PROJECT NO. 3E1- 62777A878	TASK NO. BB
11. TITLE (Include Security Classification) Methods for Correction of Refractive Errors					
12. PERSONAL AUTHOR(S) A. C. Kak					
13a. TYPE OF REPORT Final		13b. TIME COVERED FROM 1/1/82 TO 12/31/84		14. DATE OF REPORT (Year, Month, Day) 1985 December 31	
15. PAGE COUNT 225					
16. SUPPLEMENTARY NOTATION					
17. COSATI CODES			18. SUBJECT TERMS (Continue on reverse if necessary and identify by block number)		
FIELD	GROUP	SUB-GROUP			
06	18				
06	16				
19. ABSTRACT (Continue on reverse if necessary and identify by block number)					
20. DISTRIBUTION / AVAILABILITY OF ABSTRACT <input type="checkbox"/> UNCLASSIFIED/UNLIMITED <input type="checkbox"/> SAME AS RPT <input type="checkbox"/> DTIC USERS					
21. ABSTRACT SECURITY CLASSIFICATION					
22a. NAME OF RESPONSIBLE INDIVIDUAL Mrs. Virginia M. Miller			22b. TELEPHONE (Include Area Code) 301/663-7325		22c. OFFICE SYMBOL SGRD-RMI-S

TABLE OF CONTENTS

	Page
LIST OF TABLES.....	vi
LIST OF FIGURES.....	vii
ABSTRACT.....	xv
CHAPTER 1 - INTRODUCTION.....	1
References	6
CHAPTER 2 - DIFFRACTED PROJECTIONS.....	9
2.1 Introduction	9
2.2 Homogeneous Wave Equation	10
2.3 Inhomogeneous Wave Equation.....	14
2.4 Approximations to the Wave Equation.....	18
2.4.1 The First Born Approximation.....	18
2.4.2 The First Rytov Approximation.....	19
References	25
CHAPTER 3 - THE FOURIER DIFFRACTION THEOREM	27
3.1 Introduction.....	27
3.2 Decomposing the Green's Function	29
3.2.1 Plane Wave Approach	29
3.2.2 Fourier Transform Approach.....	33
3.3 Limit of the Fourier Diffraction Theorem	39
3.4 The Data Collection Process	42
3.4.1 Plane Wave Illumination	42
3.4.2 Synthetic Aperture.....	44
3.4.3 Broadband Illumination	50
References	53

CHAPTER 4 - RECONSTRUCTION PROCEDURES	55
4.1 Introduction.....	55
4.2 Frequency Domain Interpolation	56
4.3 Backpropagation Algorithms	63
4.4 Signal Processing Concerns	69
References	78
CHAPTER 5 - LIMITATIONS.....	79
5.1 Introduction.....	79
5.2 Mathematical Limitations	80
5.2.1 Evaluation of the Born Approximation	80
5.2.2 Evaluation of the Rytov Approximation	81
5.2.3 Comparison of the Born and Rytov Approximation.....	88
5.3 Evaluation of Reconstruction Algorithms	90
5.4 Experimental Limitations.....	97
5.4.1 Evanescent Waves	98
5.4.2 Sampling the Received Wave	98
5.4.3 The Effects of a Finite Receiver Length.....	99
5.4.4 Evaluation of the Experimental Effects	102
5.4.5 Optimization	102
5.4.6 Limited Views	106
References.....	109
CHAPTER 6 - HIGHER ORDER APPROXIMATIONS TO THE SCATTERED FIELD.....	110
6.1 Introduction	110
6.2 The Singularity of the Green's Function	111
6.3 Fixed Point Methods	112
6.3.1 The Born Series.....	117
6.3.2 Born Series with Attenuation.....	136
6.3.3 Rytov Series.....	143
6.4 Matrix Formulation.....	148
References.....	179

CHAPTER 7 - HIGHER ORDER RECONSTRUCTION ALGORITHMS	182
7.1 Introduction	182
7.2 Non Linear Approach	183
7.3 Perturbation Algorithms	184
7.4 Fixed Point Algorithms	191
References	196
CHAPTER 8 - CONCLUSIONS	198
BIBLIOGRAPHY	205
VITA	212

LIST OF TABLES

Table	Page
4.1 Mean Squared Error in a reconstruction of a cylinder using three interpolation schemes.....	77
5.1 Summary of parameters for diffraction tomography simulations	92
5.2 Comparison of Algorithms	97
6.1 Average value of the Green's function of a $1/4\lambda$ region sampled on an NxN grid	114
6.2 The average and maximum cosine of the angle between hyperplanes is shown as a function of the refractive index and number of equations skipped.....	168
7.1 The number of partial field terms and integrals needed to calculate each iteration of the inverse higher order Born series.....	190

LIST OF FIGURES

Figure	Page
1.1 The Fourier transform of a projection is equal to the two dimensional Fourier transform of the object along a radial line.....	3
2.1 A plane wave with direction cosines ($\sqrt{k_0^2 - k_y^2}, k_y$) is shown propagating between the lines $x=l_0$ and $x=l_1$	13
3.1 The Fourier Diffraction Theorem.....	28
3.2 A typical diffraction tomography experiment	30
3.3 Two dimensional Fourier representation of the Helmholtz equation. (a) The object, (b) the incident field, (c) the Green's function, (d) the (space domain) product of the object and the incident field and (e) the two dimensional Fourier transform of the scattered field.....	34
3.4 Integration path in the complex plane for inverting the two dimensional Fourier transform of the scattered field.	37
3.5 Estimate of the two dimensional Fourier transform of the object are available along the solid arc for transmission tomography and the dashed arc for reflection tomography.....	40
3.6 As the illuminating frequency is increased the Fourier Diffraction Theorem becomes equivalent to the Fourier Slice Theorem.....	41

Figure	Page
3.7 Estimates of the object's two dimensional Fourier transform are available along the circular arcs for plane wave illumination.	43
3.8 A typical synthetic aperture tomography experiment.....	45
3.9 By adding a phase to the field transmitted from each transmitter any desired plane wave can be synthesized.....	46
3.10 Estimates of the Fourier transform of an object in a synthetic aperture experiment are available in the shaded region.....	48
3.11 A typical Vertical Seismic Profiling (VSP) experiment.....	49
3.12 Estimate of the Fourier transform of an object are available in the shaded region for a VSP experiment (a). If, in addition, the object is real valued then the symmetry of the Fourier transform can be used to get the coverage shown in (b).	51
3.13 One view of a broadband diffraction tomography experiment will generate estimates of the object along the arcs in (a). With four views of the object complete coverage can be obtained as shown in (b).	52
4.1 Each projection is measured using the phi-omega coordinate system shown here.	57
4.2 A second change of variables is used to relate the projection data to the object's Fourier transform.....	58
4.3 Uniformly sampling the projection in the space domain leads to uneven spacing of the samples of the Fourier transform of the object along the semi-circular arc.	60
4.4 The $k_0 \vec{s}_0$ and $k \vec{s}_0$ used in the backpropagation algorithm are shown here.	64

4.5	In backpropagation the project is backprojected with a depth dependent filter function. At each depth, η , the filter corresponds to propagating the field at a distance of $\Delta\eta$.	67
4.6	The signal processing steps in a typical diffraction tomography algorithm are shown here. The steps that are needed are shown with a solid box while the optional steps are shown with dashed lines.	70
4.7	The center line of reconstructions are shown here with the size of the projection doubled and the Hamming window added. All reconstruction shown here are without low pass filtering.	71
4.8	The center line of reconstructions are shown here with the size of the projection doubled and the Hamming window added. All reconstruction shown here are with low pass filtering.	72
4.9	The spectrum of the field before (top graph) and after (bottom graph) multiplying by a Hamming window in the space domain are shown here.	74
4.10	Reconstructions of a cylinder are shown comparing nearest neighbor and bilinear interpolation for frequency domain and space domain reconstruction algorithms.	76
5.1	Simulated reconstructions using the Born approximation for 16 objects with four refractive indices between 1.001 and 1.20 and four radii between 1 and 10λ .	82
5.2	The center line for the reconstructions shown in Figure 5.1.	83
5.3	Simulated reconstructions using the Born approximation for 16 objects with four refractive indices between 1.001 and 1.10 and four radii between 1 and 100λ .	87
5.4	The relative mean squared error for reconstructions using the Born (solid line) and Rytov (dashed line) approximations. The error for a total of 60 objects with a radius of 1, 2 and 3 wavelengths are shown.	89

5.5	The relative mean squared error for reconstructions using the Born (solid line) and Rytov (dashed line) approximations. The error for a total of 120 objects with a refractive index of 1.01, 1.02 and 1.03 are shown.	91
5.6	A modified version of the Shepp and Logan head phantom is used to test reconstruction algorithms. The numbers represent the relative change in refractive index from the background value of 1.0.	93
5.7	Assuming the Fourier Slice Theorem is valid the scattered field can easily be computed as the values of the Fourier transform of the rotated and translated ellipse.	95
5.8	The above images show the results of using the (a) interpolation, (b) backpropagation and (c) modified backpropagation algorithms on reconstruction quality. The solid lines in the graphs represent the reconstructed value along a line through the center of the three ellipses at the bottom of the phantom.	96
5.9	The field scattered by an object is measured along a receiver line with finite length.	100
5.10	Reconstructions of an object using a detector spacing of (a) $.5\lambda$, (b) 1.0λ , (c) 1.5λ and (d) 2.0λ are shown here.	103
5.11	These figures show the coverage in the frequency domain for six different receiver limitations (from [Dev84]).	107
5.12	Images due to the limited field of views as shown in Figure 5.11 from [Dev84].	108
6.1	The real part of the function $g(rv-rvp)$ is shown here sampled on a 4×4 grid (top) and a 16×16 grid (bottom).	113
6.2	An initial estimate for the solution of the equation $f(x)=x$ is refined using the iteration $x_i=f(x_{i-1})$	115

6.3	The incident field is scattered against each cylinder and the resulting fields are propagated to other cylinder for additional scattering.....	119
6.4	An experiment used to illustrate the higher order Born series.....	123
6.5	Exact scattered field for the object shown in Figure 6.4. The real component of the field is shown as a solid line while the imaginary component is dashed.	124
6.6	The scattered field as calculated from the Born series using terms numbered from 1 to 100.....	125
6.7	Total energy in the higher order scattered field versus iteration number.	129
6.8	Region of convergence for the Born series using sampling intervals of $.125\lambda$, $.25\lambda$ and $.5\lambda$	130
6.9	Born series region of convergence for two cylinders of radius r separated by 1λ . The solid lines show the convergence for two orientations. The dashed line shows the convergence for a single cylinder of radius r	131
6.10	Born series region of convergence for an ellipse. The solid lines show the convergence for the ellipse as a function of its major axis (upper line) and minor axis (lower line). The dashed line shows the convergence for a single cylinder.	133
6.11	Born series region of convergence for the object shown in Figure 6.10 but rotated 90 degrees.	134
6.12	The region of convergence for two orientations of an ellipse are compared. The upper curve represents the convergence for the ellipse shown in Figure 6.11 while the lower curve represents the convergence shown in Figure 6.10.....	135

6.13 The region of convergence for the Born series as a function of cylinder radius and attenuation. The attenuation is plotted in units of nepers (1 neper represents an attenuation of the fields amplitude by 63% per wavelength.).....	137
6.14 The Fourier transform of several steps in the derivation of the scattered field in an attenuating media.....	140
6.15 The region of convergence for the Born series as a function of cylinder radius and average attenuation of the media.	142
6.16 The exact scattered field from a 2λ cylinder with a refractive index of 1.13 is shown here. The real part of the field is shown as a solid line while the imaginary component is represented as a dashed line.	145
6.17 Twenty iterations of the Rytov series are shown demonstrating the convergence of the Rytov series to the field shown in Figure 6.16.....	146
6.18 The convergence of the Born and the Rytov series are compared. The upper line represents the Rytov series.	149
6.19 The region of convergence of the Rytov series for two cylinders. The experiment here is identical to that shown in Figure 6.9 but the results are independent of orientation.	151
6.20 The region of convergence of the Rytov series for an ellipse. The upper solid line is plotted as a function of the major axis while the lower solid line is a function of the minor axis. The solid line represents the convergence for a single cylinder.	151
6.21 The convergence of the Rytov series is shown as a function of the cylinders radius and attenuation. The attenuation of the object is shown in nepers.	152

6.22 The convergence of the Rytov series is shown as a function of the cylinder radius and the average attenuation of the media. The attenuation is shown in nepers.....	153
6.23 An initial estimate for the solution, x^j , is refined by finding the closest point on the line, x^{j+1}	158
6.24 The point x^2 is a better estimate of the solution point than any other point on the line DC.	159
6.25 The orthogonality of the hyperplanes determines the rate of convergence. If the hyperplanes are perpendicular then the solution will be reached in only one iteration (a) while it will take much longer if the hyperplanes are nearly parallel (b).	161
6.26 The real parts of the scattered field are compared as computed by the Kaczmarz approach (solid line) and the exact solution to the boundary conditions (dashed line).	163
6.27 Three iterations of the Kaczmarz algorithm are shown to demonstrate the convergence of the approach to a single answer.....	165
6.28 The order equations are considered can affect the rate of convergence. If the two sets of parallel lines are considered separately (a) then the convergence is twice as slow as it would be if they are interleaved (b).	167
6.29 The residue remaining after the first 16 iterations of the Kaczmarz algorithm are shown as a function of the number of equations skipped (δ_E).	170
6.30 The field after one iteration is shown as a function of the number of equations skipped.	171
6.31 The exact scattered field and the result of 32 iterations of the Kaczmarz algorithm are compared here. In each case the real component of the field is shown as a solid line while the imaginary component is shown as a dashed line.	174

- 7.1 First order reconstructions of four objects at the limit of the Born series are shown here. Objects with a reconstruction worse than these can not be improved by an inversion procedure based on the Born series because the Born series will not converge.....192

ABSTRACT

This work reviews the theory and limits of first order diffraction tomography and studies iterative techniques that can be used to improve the quality of tomographic imaging with diffracting sources. Conventional (straight-ray) tomographic algorithms are not valid when used with acoustic or microwave energy. Thus more sophisticated algorithms are needed.

First order diffraction tomography uses a linearized version of the wave equation and gives an especially simple reconstruction algorithm. This work reviews first order approximations to the scattered field and studies the quality of the reconstructions when the assumptions behind these approximations are violated. It will be shown that the Born approximation is valid when the phase change across the object is less than π and the Rytov approximation is valid when the refractive index changes by less than two or three percent.

Better reconstructions will be based on higher order approximations to the scattered field. This work describes two fixed point algorithms (the Born and the Rytov approximations) and an algebraic approach to more accurately calculate the scattered fields. The limits of each of these approaches is discussed and simulated results are shown.

Finally a review of higher order inversion techniques is presented. Each of these techniques is reviewed and some of their limitations are discussed.

h

CHAPTER 1

INTRODUCTION

The word tomography comes from the Greek words tomo, meaning sectional, and graphy, meaning representation. Thus a tomographic image is a cross sectional image of an object. As the term is used today tomography refers to a procedure to collect data about the internal structure of an object and then mathematically generate an image of some otherwise hidden property of the object.

Diffraction, on the other hand, describes the spreading of acoustic and electromagnetic waves as they propagate through space and around objects. While conventional tomography uses x-rays to generate an image of the object's x-ray attenuation other sources of energy can also be used. Thus diffraction tomography uses diffracting energy sources to illuminate the object and then generates a cross sectional image of the object. Since ultrasound and microwaves diffract and refract as they pass through most objects they require more sophisticated algorithms than the ones used for x-ray tomography. These new algorithms for diffraction tomography are the subject of this work.

Tomography first became practical only a few years ago with the invention of the CAT (Computer Assisted Tomography) scanner [Hou72]. Hounsfield implemented a machine that illuminated an object with x-rays and measured the proportion of energy that passed through the object. Then by inverting a large system of equations he was able to generate an accurate estimate of the spatial variation of x-ray attenuation in the object.

The ability to generate a tomographic image of an object has revolutionized the medical field. For the first time it was possible to get a clear image of the internal morphology of a patient without the use of surgery. Now, x-ray CAT scanners are routinely built with resolutions of less than a millimeter and images with more than 512x512 pixels [Kak85, Her80, Mac83, Bar81].

While medical CAT scanners often generate an image of an object's x-ray attenuation there are limitations to this procedure. Foremost is the fact that

not all types of soft tissue are differentiated by their x-ray attenuation. Thus x-ray CAT scans have wide use for orthopedic medicine but are of limited use, for example, in diagnosing malignant vs. benign tumors. In addition x-rays are an ionizing radiation and thus there is a small chance of cancer with each use. This prevents, for example, the use of x-ray CAT scanners for mass screening of female patients for breast cancer.

X-ray tomography is based on the Fourier Slice Theorem. Consider the experiment shown on the left side of Figure 1.1. Here a projection is shown that represents the attenuation of the object along each of the indicated lines. The Fourier Slice Theorem states that the Fourier transform of the projection is equal to the values of the two dimensional Fourier transform of the object along a radial line. An estimate of the object can then be formed by measuring projections at a number of angles and then simply inverting the Fourier data.

Conventional tomography is based on the idea that x-rays travel in straight lines through the object and a projection measures the total x-ray attenuation of the object along straight lines. When the object is relatively large and has a small refractive index it is possible to use other types of energy, for example microwaves, seismic and ultrasound, to image the object. With a small refractive index the energy doesn't bend as it goes through the object and thus it is possible to measure the attenuation of the object along straight lines. This is the only requirement needed to use the Fourier Slice Theorem and form an image of the object's acoustic or microwave attenuation [Gre74, Gre75, Car76, Jak76, Glo77 and Cra82].

Since microwaves and acoustic waves are easier to generate and measure than x-rays it is also possible to generate images of the object's refractive index. As was mentioned earlier it is necessary to assume that the refractive index change is small so that the energy doesn't bend as it travels through the object. If a projection is measured representing the delay encountered by the energy as it travels through different parts of the object then an image is formed of the object's acoustic or electromagnetic refractive index. This extra information can often make it easier to characterize the object.

Two methods have been used to form images when the energy no longer travels through the object in a straight line. Perhaps the most straightforward approach is to simply model the flow of energy through the object as a ray and calculate its location based on the refractive index of the object [And82, Her76, Her73]. Unfortunately these algorithms can only be used when the refractive index change is less than 10 or 20 percent and most of the energy is refracted instead of diffracted. Thus this approach is only valid when the wavelength of

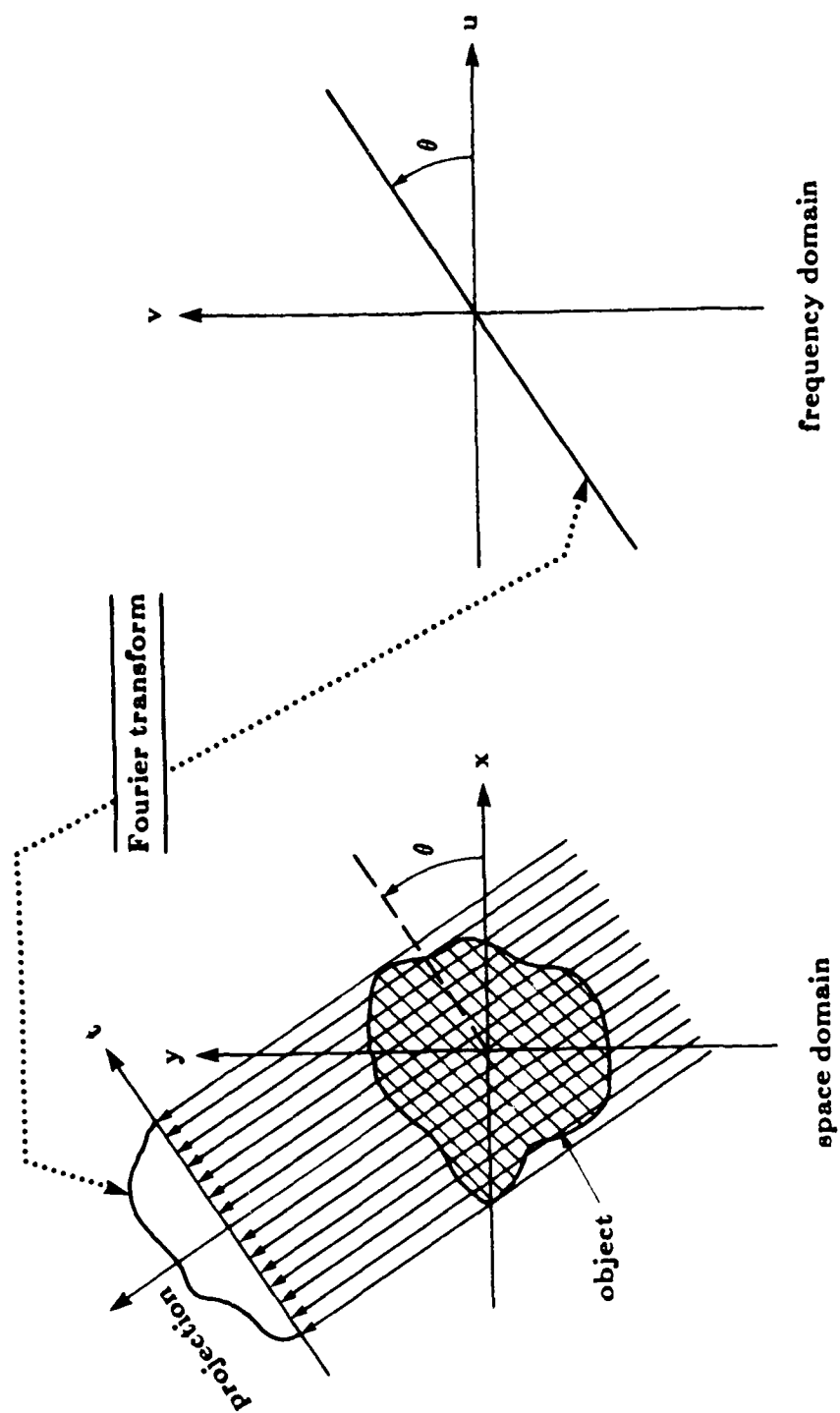


Figure 1.1 The Fourier transform of a projection is equal to the two dimensional Fourier transform of the object along a radial line.

the energy is much smaller than any details of the object [And84].

A second approach is to model the flow of energy through the object with the wave equation. While this approach is more accurate than other approaches it is not always possible to invert the resulting system of equations and find a closed form solution. This is the core of the problem for successful diffraction tomographic images.

A simple approach to solve the wave equation is to linearize it [Ish78, Che60, Sla84, Mue79, Wol69]. This is usually done by assuming that the object represents a very small perturbation to the field. Only the linear terms are retained and all higher order terms are simply ignored. Unfortunately this approach is also limited to those object that satisfy the constraints of the approximations. As will be shown later in this work linearizing the wave equation greatly limits the objects that can be imaged.

Finally in the past years work has been done on iterative techniques to solve the wave equation. Most of the work was originally applied to the inverse scattering problem of high energy physics [Bal78, New66, Tay83] and only recently applied to the diffraction tomography problem.

This work is in three parts: the derivation of the wave equation and first order reconstruction algorithms, limitations of first order algorithms and finally a summary of iterative techniques that can be applied to the diffraction tomography problem.

First in Chapter 2 the wave equation is defined for both acoustic and electromagnetic experiments. This scalar equation is valid for both types of energy and forms the basis of all work to be described here. In addition the Born and Rytov approximations are introduced and a linearized model for the scattered field as a function of the object is derived.

In Chapter 3 the linearized wave equation is inverted to find an expression for the object given the scattered field. This leads to the Fourier Diffraction Theorem which is fundamental to diffraction tomography. Finally several experimental procedures are described that generate enough data to uniquely determine the object.

Chapter 4 is a discussion of the numerical algorithms to invert the scattered data. Both of these algorithms are computationally very expensive and the algorithm used will depend on the architecture of the available computer resources. In addition some of the signal processing issues will be discussed and simulation results presented.

The limitations of the first order algorithms are presented in Chapter 5. Both the mathematical approximations and the experimental limitations contribute to the error in the final image but in different ways. The mathematical approximations are only valid for a small range of object and if these limits are exceeded then no amount of data will improve the reconstruction. The experimental limitations, on the other hand, are entirely caused by the ability to only collect a finite amount of data. The experimental errors can always be reduced by using more data or more accurate signal processing algorithms.

The severe limitations of first order diffraction algorithms is addressed in Chapters 6 and 7. The major problem in diffraction tomography is to find a method to invert the wave equation. In Chapters 2, 3 and 4 of this work this is done by linearizing the wave equation but as seen this severely limits the objects that can be imaged.

Chapter 6, therefore, discusses two approaches to model the scattered field given the (complex) refractive index of the object. This is the forward problem and both approaches are iterative. The simpler of the two approaches includes more than just the linear terms in the perturbation approach described in Chapter 2. This gives a series solution for the scattered field and simulations studying the type of objects for which these series converge will be presented. The second approach to solve the forward problem exploits the simple structure of the problem to compute a brute force solution. Objects with large refractive indices eventually cause this algorithm to converge too slowly for the method to be practical.

Finally Chapter 7 presents a survey of several approaches that have been proposed as better solutions for the inverse problem. Each of these algorithms has limitations and some of these limitations and computational aspects will be discussed.

References

- [And82] A. H. Andersen and A. C. Kak, "Digital ray tracing in two-dimensional refractive fields," *The Journal of the Acoustical Society of America*, Vol. 72, November 1982, pp. 1593-1606.
- [And84] A. H. Anderson and A. C. Kak, *The application of ray tracing towards a correction for refracting effects in computed tomography with diffracting sources*, TR-EE 84-14, School of Electrical Engineering, Purdue University, 1984.
- [Bal78] H. P. Baltes (editor), *Inverse Source Problems in Optics*, Springer-Verlag, 1978.
- [Bar81] H. H. Barrett and W. Swindell, *Radiological Imaging: The Theory of Image Formation, Detection and Processing*, Academic Press, New York, 1981.
- [Car76] P. L. Carson, T. V. Oughton, and W. R. Hendee, "Ultrasound transaxial tomography by reconstruction," in *Ultrasound in Medicine II*, D. N. White and R. W. Barnes, eds., Plenum Press, 1976, pp. 391-400.
- [Che60] L. A. Chernov, *Wave Propagation in a Random Medium*, McGraw Hill Book Company, New York, 1960.
- [Glo77] G. H. Glover and J. L. Sharp, "Reconstruction of ultrasound propagation speed distribution in soft tissue: Time-of-flight tomography," *IEEE Trans. Sonics and Ultrasonics*, Vol. SU-24, July 1977, pp. 229-234.
- [Gre74] J. F. Greenleaf, S. A. Johnson, S. L. Lee, G. T. Herman, and E. H. Wood, "Algebraic reconstruction of spatial distributions of acoustic absorption within tissue from their two dimensional acoustic projections," in *Acoustical Holography*, Plenum Press, 1974, pp. 591-603.
- [Gre75] J. F. Greenleaf, S. A. Johnson, W. F. Wamoya, and F. A. Duck, "Algebraic reconstruction of spatial distributions of acoustic velocities in tissue from their time-of-flight profiles," in *Acoustical Holography*, Plenum Press, 1975, pp. 71-90.

- [Her73] G. T. Herman, A. Lent, and S. Rowland, "ART: Mathematics and applications: A report on the mathematical foundations and on applicability to real data of the algebraic reconstruction techniques," *J. Theor. Biol.*, Vol. 43, 1973, pp. 1-32.
- [Her76] G. T. Herman, A. V. Lakshminarayanan, A. Naparstek, E. L. Ritman, R. A. Robb, and E. H. Wood, "Rapid computerized tomography," *Med. Data Process.*, 1976, pp. 582-598.
- [Her80] G. T. Herman, *Image Reconstructions from Projections*, Academic Press, New York, 1980.
- [Hou72] G. N. Hounsfield, *A method of apparatus for examination of a body by radiation such as x-ray or gamma radiation*, Patent Specification 1283915, The Patent Office, 1972.
- [Ish78] A. Ishimaru, *Wave Propagation and Scattering in Random Media*, Academic Press, New York, 1978.
- [Jak76] C. V. Jakowatz Jr. and A. C. Kak, *Computerized tomography using x-rays and ultrasound*, Research Report TR-EE 76-26, School of Electrical Engineering, Purdue University, 1976.
- [Kak85] A. C. Kak and B. Roberts, "Image reconstruction from projections," in *Handbook of Image Processing*, T. Y. Young and K. S. Fu, eds., Academic Press, 1985.
- [Mac83] Albert Macovski, *Medical Imaging Systems*, Prentice Hall, Englewood Cliffs, NJ, 1983.
- [Mue79] R. K. Mueller, M. Kaveh, and G. Wade, "Reconstructive tomography and applications to ultrasonics," *Proceedings of the IEEE*, Vol. 67, 1979, pp. 567-587.
- [New66] R. G. Newton, *Scattering Theory of Waves and Particles*, McGraw-Hill Book Company, New York, 1966.
- [Sla84] Malcolm Slaney, A. C. Kak, and L. E. Larsen, "Limitations of imaging with first order diffraction tomography," *IEEE Transactions on Microwave Theory and Techniques*, August 1984, pp. 860-873.
- [Tay83] J. R. Taylor, *Scattering Theory: The Quantum Theory of Nonrelativistic Collisions*, Robert E. Krieger Publishing Company, Malabar, FL, 1983.

- [Wol69] E. Wolf, "Three-dimensional structure determination of semi-transparent objects from holographic data," *Optics Communications*, Vol. 1, 1969, pp. 153-156.

CHAPTER 2

DIFFRACTED PROJECTIONS

2.1 Introduction

Tomography with diffracting energy can not be modeled with the same equations used to model projections in conventional, straight ray, tomography. Acoustic and electromagnetic waves do not travel along straight rays and the projections are not line integrals. Instead the flow of energy will be described with the wave equation and in the limit of very short wavelengths or objects where the effects of refraction are small it will be shown that the diffracted projections can be approximated by a non diffracting projection

First consider the propagation of waves in homogeneous media. The wave equation is a second order linear differential equation and under certain conditions it can be shown that an expression for the field at every other point in space can be written.

The problem is not to image a homogeneous media but one that is inhomogeneous. To solve the inhomogeneous wave equation, one of two approximations, the Born or the Rytov, must be used. With these two approximations expressions for the field scattered by the inhomogeneities of the media can be written.

The theory to be discussed will be applicable to both two and three dimensional structures. Even in a three dimensional world a two dimensional model can often be used if the object varies slowly in one direction. This assumption, for example, is often made in conventional computerized tomography where images are made of a single slice of the object. The theory of diffraction tomography will be presented almost entirely in two dimensions for two reasons. More importantly, the ideas behind the theory are often easier to visualize (and certainly to draw) in two dimensions. In addition technology has yet to make it practical to implement large three dimensional transforms and then to display the results. This limitation will certainly be eliminated in the near future and where the differences are significant both the two and three dimensional solutions will be indicated.

2.2 Homogeneous Wave Equation

In a constant or homogeneous media the propagation of acoustic or electromagnetic waves can be modeled with the scalar Helmholtz equation. For a temporal frequency of ω radians per second (rps) a field, $u(\vec{r})$, satisfies the equation

$$(\nabla^2 + k_0^2)u(\vec{r}) = 0. \quad (2.1)$$

For homogeneous media the wavenumber, k_0 , is a constant related to the wavelength, λ , of the wave by

$$k_0 = \frac{2\pi}{\lambda}. \quad (2.2)$$

The wavelength, λ , is related to the temporal frequency of the wave by the propagation speed in the media, c , or

$$\lambda = \frac{2\pi}{\omega}c \quad (2.3)$$

Since the theory of diffraction tomography is normally derived based on coherent fields the time dependence of most fields will be suppressed in this work. Thus all fields should be multiplied by $e^{-j\omega t}$ to find the measured field as a function of time. The extension of this theory to broadband fields is discussed in Section 3.4.3

For acoustic (or ultrasonic) tomography, $u(\vec{r})$ can be the pressure field at position \vec{r} . For the electromagnetic case, assuming the applicability of a scalar propagation equation, $u(\vec{r})$ may be set equal to the complex amplitude of the electric field along its polarization. In both cases the time dependence of the fields are suppressed and $u(\vec{r})$ represents the complex amplitude of the field. As a function of time and space the field is given by

$$u(\vec{r}, t) = \text{Real Part} \left\{ u(\vec{r})e^{-j\omega t} \right\}. \quad (2.4)$$

The vector gradient operator, ∇ , can be expanded into its two dimensional representation and the wave equation becomes

$$\frac{\partial^2 u(\vec{r})}{\partial x^2} + \frac{\partial^2 u(\vec{r})}{\partial y^2} + k_0^2 u(\vec{r}) = 0. \quad (2.5)$$

As a trial solution let

$$u(\vec{r}) = e^{j\vec{k} \cdot \vec{r}} \quad (2.6)$$

where the vector $\vec{k} = (k_x, k_y)$ is the two dimensional propagation vector and

$u(\vec{r})$ represents a two dimensional plane wave of spatial frequency $|\vec{k}|$. This form of $u(\vec{r})$ represents the basis function for the two dimensional Fourier transform; using it, any two dimensional function can be represented as a weighted sum of plane waves. Calculating the derivatives as indicated in equation (2.5) it can be seen that all plane waves that satisfy the condition

$$|\vec{k}|^2 = k_x^2 + k_y^2 = k_0^2 \quad (2.7)$$

are valid solutions to the wave equation. This condition is consistent with an intuitive picture of a wave and description of the wave equation above, since for any frequency wave only a single wavelength can exist no matter which direction it propagates.

The homogeneous wave equation is a linear differential equation so the general solution can be written as a weighted sum of each possible plane wave solution. In two dimensions, at a temporal frequency of ω , the field, $u(\vec{r})$ is given by

$$u(\vec{r}) = \frac{1}{2\pi} \int_{-\infty}^{\infty} \alpha(k_y) e^{j(k_x x + k_y y)} dk_y + \frac{1}{2\pi} \int_{-\infty}^{\infty} \beta(k_y) e^{j(-k_x x + k_y y)} dk_y \quad (2.8)$$

and by equation (2.7)

$$k_x = \sqrt{k_0^2 - k_y^2}. \quad (2.9)$$

The form of this equation might be surprising to the reader for two reasons. First, the integral has been split into two parts. The coefficients of waves traveling to the right are represented by $\alpha(k_y)$ and those traveling to the left by $\beta(k_y)$. In addition the limits of the integrals have been set to go from $-\infty$ to ∞ . For k_y^2 greater than k_0^2 the radical in equation (2.9) becomes imaginary and the plane wave becomes an evanescent wave. These are valid solutions to the wave equation but because k_y is imaginary the exponential has a real or attenuating component. This real component causes the amplitude of the wave to either grow or decay exponentially. In practice, these evanescent waves only occur to satisfy boundary conditions, always decay rapidly far from the boundary, and can often be ignored at distance greater than 10λ from the inhomogeneity.

The limited range of valid solutions to the wave equation allows (under certain condition) an expression to be written for the field in all of two-space given the amplitude of the field along a line. The three dimensional version of this idea gives the field in three-space if the field is known at all points on a plane.

Consider a source of plane waves to the left of a vertical line as shown in Figure 2.1. By calculating the one-dimensional Fourier transform of the field along the line the field can be decomposed into a number of one-dimensional components. Each of these one dimensional components can then be attributed to one of the valid plane wave solutions to the homogeneous wave equation because for any one frequency component, k_y , there can exist only two plane waves that satisfy the wave equation. Since the incident field has already been constrained to propagate toward the right (all sources are to the left of the measurement line) then a one-dimensional Fourier component at a frequency of k_y can be attributed to a two dimensional wave with a propagation vector of $(\sqrt{k_0^2 - k_y^2}, k_y)$.

This can be put on a more mathematical basis if the one-dimensional Fourier transform of the field is compared to the general form of the wave equation. If waves that are traveling to the left are ignored then the general solution to the wave equation becomes

$$u(\vec{r}) = \frac{1}{2\pi} \int_{-\infty}^{\infty} \alpha(k_y) e^{j(k_x x + k_y y)} dk_y \quad (2.10)$$

Now if the coordinate system is moved so that the measurement line is at $x = 0$ then the expression for the field becomes equal to the one-dimensional Fourier transform of the field or

$$u(\vec{r}) = \frac{1}{2\pi} \int_{-\infty}^{\infty} \alpha(k_y) e^{jk_y y} dk_y. \quad (2.11)$$

This equation establishes the link between the one-dimensional Fourier transform of the field along the line to the two-dimensional field. The coefficients $\alpha(k_y)$ are given from the one dimensional Fourier transform of the field by

$$\alpha(k_y) = \text{Fourier Transform} \left\{ u(0, y) \right\} \quad (2.12)$$

The simple form of a plane wave allows an expression to be written relating the field on two parallel lines. If *a priori* it is known that all the sources for the field are positioned, for example, left of the line at $x=l_0$ then the field $u(x=l_0, y)$ can be decomposed into its plane wave components. Given a plane wave $u_{\text{plane wave}}(x=l_0, y) = \alpha e^{j(k_x l_0 + k_y y)}$ the field undergoes a phase shift as it propagates to the line $x=l_1$, and the field can be written

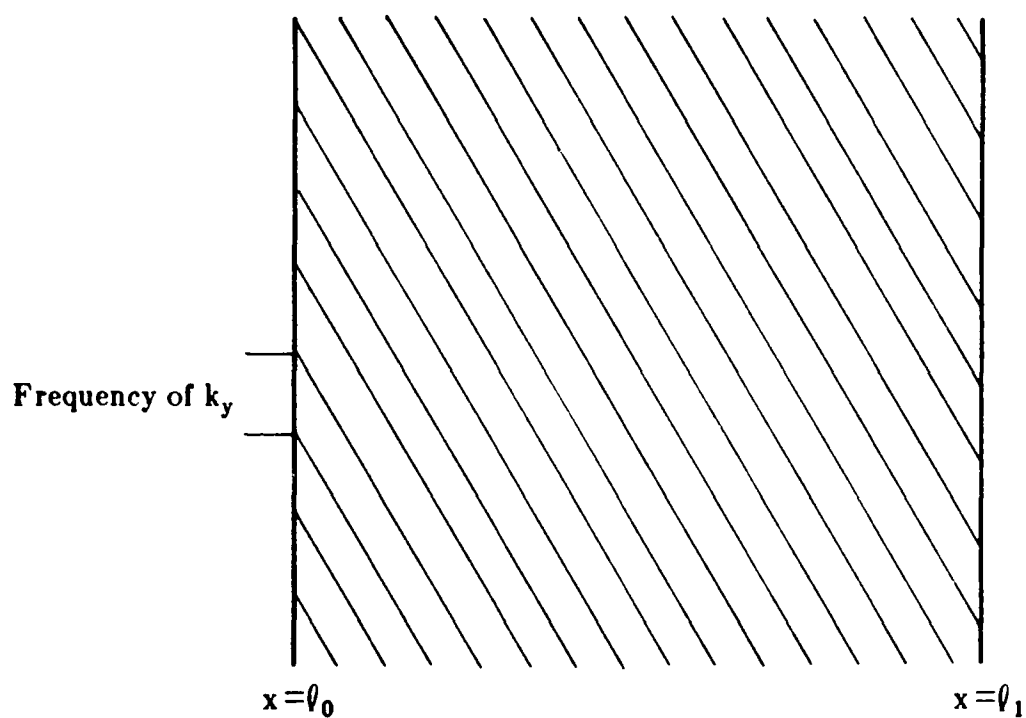


Figure 2.1

A plane wave with direction cosines $(\sqrt{k_0^2 - k_y^2}, k_y)$ is shown propagating between the lines $x=l_0$ and $x=l_1$.

$$u_{\text{plane wave}}(x=l_1, y) = \alpha e^{j(k_x l_0 + k_y y)} e^{jk_x(l_1 - l_0)} = u_{\text{plane wave}}(x=l_0, y) e^{jk_x(l_1 - l_0)} \quad (2.13)$$

Thus the complex amplitude of the plane wave at $x=l_1$ is related to its complex amplitude at $x=l_0$ by a factor of $e^{jk_x(l_1 - l_0)}$.

The complete process of finding the field at a line $x=l_1$ follows in three steps.

- 1) Take the Fourier transform of $u(x=l_0, y)$ to find the Fourier decomposition of u as a function of k_y .
- 2) Propagate each plane wave to the line $x=l_1$ by multiplying its complex amplitude by the phase factor $e^{jk_x(l_1 - l_0)}$, where as before $k_x = \sqrt{k_0^2 - k_y^2}$.
- 3) Find the inverse Fourier transform of the plane wave decomposition to find the field at $u(x=l_1, y)$.

2.3 Inhomogeneous Wave Equation

For imaging in an inhomogeneous media a more general form of the wave equation is written as

$$\left[\nabla^2 + k(\vec{r})^2 \right] u(\vec{r}) = 0. \quad (2.14)$$

For the electromagnetic case it is necessary to ignore the effects of polarization so that $k(\vec{r})$ is a scalar function representing the refractive index of the medium. Now write

$$k(\vec{r}) = k_0 n(\vec{r}) = k_0 [1 + n_\delta(\vec{r})] \quad (2.15)$$

where k_0 represents the average wavenumber of the media and $n_\delta(\vec{r})$ represents the refractive index deviations. In general it will be assumed that the object has a finite size and therefore $n_\delta(\vec{r})$ is zero outside the object. Rewriting the wave equation

$$(\nabla^2 + k_0^2) u(\vec{r}) = -k_0^2 [n(\vec{r})^2 - 1] u(\vec{r}) \quad (2.16)$$

where $n(\vec{r})$ is the electromagnetic refractive index of the media and is given by

$$n(\vec{r}) = \sqrt{\frac{\mu(\vec{r})\epsilon(\vec{r})}{\mu_0\epsilon_0}}. \quad (2.17)$$

Here μ and ϵ have been used to represent the magnetic permeability and dielectric constant and the subscript zero to indicate their average values. This new term, on the right hand side of equation (2.16), is known as a forcing function for the differential equation $(\nabla^2 + k_0^2)u(\vec{r})$.

Note that equation (2.16) is a *scalar* wave propagation equation. Its use implies that there is no depolarization as the electromagnetic wave propagates through the medium. It is known [Ish78] that the depolarization effects can be ignored only if the wavelength is much smaller than the correlation size of the inhomogeneities in the object. If this condition is not satisfied, then strictly speaking the following vector wave propagation equation must be used

$$\nabla^2 \vec{E}(\vec{r}) + k_0^2 n^2 \vec{E}(\vec{r}) - 2 \nabla \left[\frac{\nabla n}{n} \cdot \vec{E} \right] = 0 \quad (2.18)$$

where \vec{E} is the electric field vector. A vector theory for diffraction tomography based on this equation has yet to be developed.

For the acoustic case, first order approximations give the following wave equation [Kak84]

$$(\nabla^2 + k_0^2)u(\vec{r}) = -k_0^2 [n^2(\vec{r}) - 1]u(\vec{r}) \quad (2.19)$$

where n is the *complex refractive index* at position \vec{r} , and is equal to

$$n(\vec{r}) = \frac{c_0}{c(\vec{r})}, \quad (2.20)$$

where c_0 is the propagation velocity in the medium in which the object is immersed, and $c(\vec{r})$ is the propagation velocity at location \vec{r} in the object. For the acoustic case where only the compressional waves in a viscous compressible fluid are involved, the speed of sound is given by

$$c(\vec{r}) = \frac{1}{\sqrt{\rho\kappa}} \quad (2.21)$$

where ρ and κ are the *local density* and the *complex compressibility* at location \vec{r} .

The forcing function in equation (2.19) is only valid provided the first and higher order derivatives of the medium parameters can be ignored. If the inhomogeneity can be modeled as a viscous compressible fluid, an exact form for the wave equation is given by

$$(\nabla^2 + k_0^2)u(\vec{r}) = k_0^2 \gamma_\kappa u - \nabla \cdot (\gamma_\rho \nabla u) \quad (2.22)$$

where

$$\gamma_\kappa = \frac{\kappa - \kappa_0}{\kappa_0} \quad (2.23)$$

$$\gamma_\rho = \frac{\rho - \rho_0}{\rho}. \quad (2.24)$$

κ_0 and ρ_0 are either the compressibility and density of the medium in which the object is immersed, or the average compressibility and the density of the object, depending upon how the process of imaging is modeled. On the other hand, if the object is a solid and can be modeled as a linear isotropic viscoelastic medium, the forcing function possesses another more complicated form. Since this form involves tensor notation, it will not be presented here and the interested reader is referred to [Iwa75].

Due to the similarities of the electromagnetic and acoustic wave equations a general form of the wave equation can be written as

$$(\nabla^2 + k_0^2)u(\vec{r}) = -o(\vec{r})u(\vec{r}) \quad (2.25)$$

where

$$o(\vec{r}) = k_0^2[n^2(\vec{r}) - 1] \quad (2.26)$$

To hide some of the mathematical details the term $o(\vec{r})$ will be used to represent all inhomogeneities of the object. Later the object will be reconstructed in terms of the object function, $o(\vec{r})$, and the reader is referred to equation (2.26) to put the reconstruction in terms of the refractive index.

Consider the field, $u(\vec{r})$, to be the sum of two components. The incident field, $u_0(\vec{r})$, is the field present without any inhomogeneities or a solution to the equation

$$(\nabla^2 + k_0^2)u_0(\vec{r}) = 0. \quad (2.27)$$

That leaves the scattered field, $u_s(\vec{r})$, as that part of the field due to the object inhomogeneities or

$$u_s(\vec{r}) = u(\vec{r}) - u_0(\vec{r}). \quad (2.28)$$

The wave equation becomes

$$(\nabla^2 + k_0^2)u_s(\vec{r}) = -u(\vec{r})o(\vec{r}). \quad (2.29)$$

The scalar Helmholtz equation (2.29) cannot be solved for $u_s(\vec{r})$ directly but a solution can be written in terms of the Green's function [Mor53]. The Green's function, which is a solution of the differential equation

$$(\nabla^2 + k_0^2)g(\vec{r}|\vec{r}') = -\delta(\vec{r} - \vec{r}'), \quad (2.30)$$

is written in three-space as

$$g(\vec{r}|\vec{r}') = \frac{e^{jk_0R}}{4\pi R} \quad (2.31)$$

with

$$R = |\vec{r} - \vec{r}'|. \quad (2.32)$$

In two dimensions the solution of (2.30) is written in terms of a zero-order Hankel function of the first kind, and can be expressed as

$$g(\vec{r}|\vec{r}') = \frac{j}{4} H_0^{(1)}(k_0 R). \quad (2.33)$$

In both cases, the Green's function, $g(\vec{r}|\vec{r}')$, is only a function of the difference $\vec{r} - \vec{r}'$ so the function will often be represented as simply $g(\vec{r} - \vec{r}')$. Because the object function in equation (2.30) represents a point inhomogeneity, the Green's function can be considered to represent the field resulting from a single point scatterer.

It is possible to represent the forcing function of the wave equation as an array of impulses or

$$o(\vec{r})u(\vec{r}) = \int o(\vec{r}')u(\vec{r}')\delta(\vec{r} - \vec{r}')d\vec{r}'. \quad (2.34)$$

In this equation the forcing function of the inhomogeneous wave equation is represented as a summation of impulses weighted by $o(\vec{r})u(\vec{r})$ and shifted by \vec{r} . The Green's function represents the solution of the wave equation for a single delta function; because the left hand side of the wave equation is linear, a solution can be written by summing the scattered field due to each individual point scatterer.

Using this idea, the total field due to the impulse $o(\vec{r}')u(\vec{r}')\delta(\vec{r} - \vec{r}')$ is written as a summation of scaled and shifted versions of the impulse response, $g(\vec{r})$. This is a simple convolution and the total radiation from all sources on the right hand side of (2.29) must be given by the following superposition:

$$u_s(\vec{r}) = \int g(\vec{r} - \vec{r}')o(\vec{r}')u(\vec{r}')d\vec{r}'. \quad (2.35)$$

At first glance it might appear that this is the solution needed for the scattered field, but it is not that simple. An integral equation for the scattered field, u_s , has been written in terms of the total field, $u = u_0 + u_s$. This equation needs to be solved for the scattered field and two approximations that allow this to be done will now be discussed.

2.4 Approximations to the Wave Equation

In the last section an inhomogeneous integral equation was derived to represent the scattered field, $u_s(\vec{r})$, as a function of the object, $o(\vec{r})$. This equation cannot be solved directly, but a solution can be written using either of the two approximations described here. These approximations, the Born and the Rytov, are valid under different conditions but the form of the resulting solutions are quite similar. These approximations are the basis of the Fourier Diffraction Theorem.

Mathematically speaking equation (2.35) is a Fredholm equation of the second kind. A number of mathematicians have presented works describing the solution of scattering integrals [Hoc73, Col83] and they should be consulted for the theory behind the approximations to be presented here.

2.4.1 The First Born Approximation

The first Born approximation is the simpler of the two approaches. Recall that the total field, $u(\vec{r})$, is expressed as the sum of the incident field, $u_0(\vec{r})$, and a small perturbation, $u_s(\vec{r})$, or

$$u(\vec{r}) = u_0(\vec{r}) + u_s(\vec{r}). \quad (2.36)$$

The integral of equation (2.35) is now written as

$$u_s(\vec{r}) = \int g(\vec{r}-\vec{r}') o(\vec{r}') u_0(\vec{r}') d\vec{r}' + \int g(\vec{r}-\vec{r}') o(\vec{r}') u_s(\vec{r}') d\vec{r}' \quad (2.37)$$

but if the scattered field, $u_s(\vec{r})$, is small compared to $u_0(\vec{r})$ the effects of the second integral can be ignored to arrive at the approximation

$$u_s(\vec{r}) \simeq u_B(\vec{r}) = \int g(\vec{r}-\vec{r}') o(\vec{r}') u_0(\vec{r}') d\vec{r}'. \quad (2.38)$$

The first Born approximation is valid only when the magnitude of the scattered field,

$$u_s(\vec{r}) = u(\vec{r}) - u_0(\vec{r}), \quad (2.39)$$

is smaller than the magnitude of the incident field, u_0 . If the object is a homogeneous cylinder it is possible to express this condition as a function of the size of the object and the refractive index. Let the incident wave, $u_0(\vec{r})$, be a plane wave propagating in the direction of the vector, \vec{k}_0 . For a large object, the field inside the object will not be well approximated by the incident field

$$u(\vec{r}) = u_{\text{object}}(\vec{r}) \neq Ae^{j\vec{k}_0 \cdot \vec{r}} \quad (2.40)$$

but instead will be a function of the change in refractive index, n_δ . Along a ray

through the center of the cylinder and parallel to the direction of propagation of the incident plane wave the field inside the object becomes a slow (or fast) version of the incident wave or

$$u_{\text{object}}(\vec{r}) = Ae^{j(1+n_\delta)\vec{k}_0\vec{r}}. \quad (2.41)$$

Since the wave is propagating through the object the phase difference between the incident field and the field inside the object is approximately equal to the integral through the object of the change in refractive index. For a homogeneous cylinder of radius 'a' wavelengths the total phase shift through the object becomes

$$\text{Phase Change} = 4\pi n_\delta \frac{a}{\lambda} \quad (2.42)$$

where λ is the wavelength of the incident wave. For the Born approximation to be valid, a necessary condition is that the change in phase between the incident field and the wave propagating through the object be less than π . This condition can be expressed mathematically as [New66]

$$an_\delta < \frac{\lambda}{4}. \quad (2.43)$$

2.4.2 The First Rytov Approximation

The Rytov approximation is another approximation to the scattered field and is valid under slightly different restrictions. It is derived by considering the total field to be represented as a complex phase or [Ish78]

$$u(\vec{r}) = e^{\phi(\vec{r})} \quad (2.44)$$

and rewriting the wave equation (2.14)

$$(\nabla^2 + k^2)u = 0 \quad (2.45)$$

as

$$\nabla^2 e^{\phi} + k^2 e^{\phi} = 0 \quad (2.46)$$

$$\nabla[\nabla\phi e^{\phi}] + k^2 e^{\phi} = 0 \quad (2.47)$$

$$\nabla^2\phi e^{\phi} + (\nabla\phi)^2 e^{\phi} + k^2 e^{\phi} = 0 \quad (2.48)$$

and finally

$$(\nabla\phi)^2 + \nabla^2\phi + k_0^2 = -o(\vec{r}). \quad (2.49)$$

(Although all the fields (ψ and ϕ) are a function of \vec{r} , to simplify the notation

the argument of these functions will be dropped.) Expressing the total complex phase, ϕ , can be expressed as the sum of the incident phase function, ϕ_0 , and the scattered complex phase, ϕ_s , or

$$\phi(\vec{r}) = \phi_0(\vec{r}) + \phi_s(\vec{r}) \quad (2.49)$$

where

$$u_0(\vec{r}) = e^{i\phi_0(\vec{r})} \quad (2.50)$$

to find that

$$(\nabla\phi_0)^2 + 2\nabla\phi_0 \cdot \nabla\phi_s + (\nabla\phi_s)^2 + \nabla^2\phi_0 + \nabla^2\phi_s + k_0^2 + o(\vec{r}) = 0. \quad (2.51)$$

As in the Born approximation it is possible to set the zero perturbation equation equal to zero. Doing this, the homogeneous wave equation can be written

$$k_0^2 + (\nabla\phi_0)^2 + \nabla^2\phi_0 = 0. \quad (2.52)$$

Substituting this into equation (2.51) the wave equation becomes

$$2\nabla\phi_0 \cdot \nabla\phi_s + \nabla^2\phi_s = -(\nabla\phi_s)^2 - o(\vec{r}). \quad (2.53)$$

This equation is still inhomogeneous but can be linearized by considering the following relation:

$$\nabla^2(u_0\phi_s) = \nabla(\nabla u_0 \cdot \phi_s + u_0 \nabla\phi_s) \quad (2.54)$$

or by expanding the first derivative on the right hand side of this equation

$$\nabla^2(u_0\phi_s) = \nabla^2 u_0 \cdot \phi_s + 2\nabla u_0 \cdot \nabla\phi_s + u_0 \nabla^2\phi_s \quad (2.55)$$

Using a plane wave for the incident field,

$$u_0 = A e^{i\vec{k}_0 \cdot \vec{r}}, \quad (2.56)$$

the second gradient of the incident field is

$$\nabla^2 u_0 = -k_0^2 u_0 \quad (2.57)$$

so that equation (2.55) may be rewritten as

$$2u_0 \nabla\phi_0 \cdot \nabla\phi_s + u_0 \nabla^2\phi_s = \nabla^2(u_0\phi_s) + k_0^2 u_0\phi_s. \quad (2.58)$$

This result can be substituted into equation (2.53) to find

$$(\nabla^2 + k_0^2)u_0\phi_s = -u_0 \left[(\nabla\phi_s)^2 + o(\vec{r}) \right] \quad (2.59)$$

The solution to this differential equation can again be expressed as an integral equation. This becomes

$$u_0\phi_s = \int_{V'} g(\vec{r}-\vec{r}') u_0 \left[(\nabla\phi_s)^2 + o(\vec{r}) \right] d\vec{r}'. \quad (2.60)$$

Using the Rytov Approximation it is necessary to assume that the term in brackets in the above equation can be approximated by

$$(\nabla\phi_s)^2 - o(\vec{r}) \simeq -o(\vec{r}). \quad (2.61)$$

When this is done, the first order Rytov approximation to the function $u_0\phi_s$ becomes

$$u_0\phi_s = \int_{V'} g(\vec{r}-\vec{r}') u_0(\vec{r}') o(\vec{r}') d\vec{r}'. \quad (2.62)$$

Thus ϕ_s , the complex phase of the scattered field, is given by

$$\phi_s(\vec{r}) = \frac{1}{u_0(\vec{r})} \int_{V'} g(\vec{r}-\vec{r}') u_0(\vec{r}') o(\vec{r}') d\vec{r}'. \quad (2.63)$$

Substituting the expression for u_B given in equation (2.38) the first Rytov approximation can be written

$$\phi_s(\vec{r}) = \frac{u_B(\vec{r})}{u_0(\vec{r})}. \quad (2.64)$$

The Rytov approximation is valid under a less restrictive set of conditions than the Born approximation [Che60, Kel69]. In deriving the Rytov approximation it was necessary to assume that

$$\int_{V'} g(\vec{r}-\vec{r}') u_0(\vec{r}') o(\vec{r}') d\vec{r}' \gg \int_{V'} g(\vec{r}-\vec{r}') u_0(\vec{r}') (\nabla\phi_s)^2 d\vec{r}'. \quad (2.65)$$

If the object is smaller than a wavelength then both the field and the object can be assumed to be constant compared to the object function and the above relation can be written

$$g(\vec{r}-0) u_0(0) \int_{V'} o(\vec{r}') d\vec{r}' \gg g(\vec{r}-0) u_0(0) \int_{V'} (\nabla\phi_s)^2 d\vec{r}'. \quad (2.66)$$

When the term $(\nabla\phi_s)^2$ is small outside the object this relation can be further simplified to find

$$o(\vec{r}) \gg (\nabla\phi_s)^2. \quad (2.67)$$

If $o(\vec{r})$ is written in terms of the change in refractive index

$$o(\vec{r}) = k_0^2 [n^2(\vec{r}) - 1] = k_0^2 [(1 + n_\delta(\vec{r}))^2 - 1] \quad (2.26)$$

and the square of the refractive index is expanded to find

$$o(\vec{r}) = k_0^2 [(1 + 2n_\delta(\vec{r}) + n_\delta^2(\vec{r})) - 1] \quad (2.68)$$

$$o(\vec{r}) = k_0^2 [2n_\delta(\vec{r}) + n_\delta^2(\vec{r})]. \quad (2.69)$$

To a first approximation the object function is linearly related to the refractive index or

$$o(\vec{r}) \simeq 2k_0^2 n_\delta(\vec{r}). \quad (2.70)$$

The condition needed for the Rytov approximation (see equation (2.67) can be rewritten as

$$n_\delta \gg \frac{(\nabla \phi_s)^2}{k_0^2}. \quad (2.71)$$

This can be justified by observing that to a first approximation the scattered phase, ϕ_s , is linearly dependent on the refractive index change, n_δ , and therefore the first term in equation (2.65) above can be safely ignored for small n_δ .

The term $\nabla \phi_s$ is the change in the complex scattered phase per unit distance and by dividing by the wavenumber

$$k_0 = \frac{2\pi}{\lambda} \quad (2.72)$$

a necessary condition for the validity of the Rytov approximation is

$$n_\delta \gg \left[\frac{\nabla \phi_s \lambda}{2\pi} \right]^2. \quad (2.73)$$

Unlike the Born approximation, it is the change in scattered phase, ϕ_s , over one wavelength that is important and not the total phase. Thus, because of the ∇ operator, the Rytov approximation is valid when the phase change over a single wavelength is small.

Estimating $u_B(\vec{r})$ for the Rytov case is slightly more difficult. In an experiment the total field, $u(\vec{r})$, is measured. An expression for $u_B(\vec{r})$ is found by recalling the expression for the Rytov solution to the total wave

$$u(\vec{r}) = u_0 + u_s(\vec{r}) = e^{\phi_0 + \phi_s}. \quad (2.74)$$

and then rearranging the exponentials to find

$$u_s = e^{\phi_0 + \phi_s} e^{\phi_0} \quad (2.75)$$

$$u_s = e^{\phi_0} \left(e^{\phi_s} - 1 \right) \quad (2.76)$$

$$u_s = u_0 \left(e^{\phi_s} - 1 \right). \quad (2.77)$$

Inverting this to find an estimate for the scattered phase, ϕ_s , the scattered phase is

$$\phi_s(\vec{r}) = \ln \left[\frac{u_s}{u_0} + 1 \right]. \quad (2.78)$$

Then expand ϕ_s in terms of equation (2.64) to obtain the following estimate for the Rytov estimate of $u_B(\vec{r})$

$$u_B(\vec{r}) = u_0(\vec{r}) \ln \left[\frac{u_s}{u_0} + 1 \right]. \quad (2.79)$$

Since the natural logarithm is a multiple valued function, one must be careful at each position to choose the correct value. For continuous functions this is not difficult because only one value will satisfy the continuity requirement. On the other hand for discrete (or sampled) signals the choice is not nearly as simple and one must resort to a phase wrapping algorithm to choose the proper phase. Phase unwrapping has been described in a number of works [Tri77, OCo78, Kav84, McG82, Kav84]. Due to the "+1" factor inside the logarithmic term, this is only a problem if u_s is on the order of or larger than u_0 . Thus both the Born and the Rytov techniques can be used to estimate $u_B(\vec{r})$.

While the Rytov approximation is valid over a larger class of objects, it is possible to show that the Born and the Rytov approximations produce the same result for objects that are small and deviate only slightly from the average refractive index of the medium. Consider first the Rytov expression to the total field. This is given by

$$u(\vec{r}) = e^{\phi_0 + \phi_s}. \quad (2.80)$$

Substituting an expression for the scattered phase, (2.64) and the incident field, (2.56) into this expression

$$u(\vec{r}) = e^{-jk_0 \vec{z} \cdot \vec{r} + \exp(-jk_0 \vec{z} \cdot \vec{r}) u_I(\vec{r})} \quad (2.81)$$

or

$$u(\vec{r}) = u_0(\vec{r})e^{\exp(jk_0\vec{s}\cdot\vec{r})u_B(\vec{r})}. \quad (2.82)$$

For small u_B , the first exponential can be expanded in terms of its power series. Throwing out all but the first two terms the total field is approximately equal to

$$u(\vec{r}) = u_0(\vec{r}) \left[1 + e^{-jk_0\vec{s}\cdot\vec{r}} u_B(\vec{r}) \right] \quad (2.83)$$

or

$$u(\vec{r}) = u_0(\vec{r}) + u_B(\vec{r}). \quad (2.84)$$

Thus when the magnitude of the scattered field is small the Rytov solution is approximately equal to the Born solution given in equation (2.38).

The similarity between the expressions for the first order Born and Rytov solutions will form the basis of the reconstruction algorithms to be derived here. In the Born approximation the complex amplitude of the scattered field is measured and this is used as an estimate of the function u_B while in the Rytov case u_B is estimated from the complex phase of the scattered field. Since the Rytov approximation is considered more accurate than the Born approximation it should provide a better estimate of u_B . In Chapter 5 of this work, after deriving reconstruction algorithms based on the Fourier Diffraction Theorem, simulations comparing the Born and the Rytov approximations will be discussed.

References

- [Che60] L. A. Chernov, *Wave Propagation in a Random Medium*, McGraw Hill Book Company, New York, 1960.
- [Col83] David Colton and Rainer Kress, *Integral Equation Methods in Scattering Theory*, John Wiley and Sons, New York, NY, 1983.
- [Hoc73] Harry Hochstadt, *Integral Equations*, John Wiley and Sons, New York, NY, 1973.
- [Ish78] A. Ishimaru, *Wave Propagation and Scattering in Random Media*, Academic Press, New York, 1978.
- [Iwa75] K. Iwata and R. Nagata, "Calculation of refractive index distribution from interferograms using the Born and Rytov's approximations," *Jap. J. Appl. Phys.*, Vol. 14, 1975, pp. 1921-1927.
- [Kak84] A. C. Kak, "Tomographic imaging with diffracting and non-diffracting sources," in *Array Signal Processing*, Simon Haykin, ed., Prentice Hall, 1984.
- [Kav84] M. Kaveh, M. Soumekh, and J. F. Greenleaf, "Signal processing for diffraction tomography," *IEEE Transactions on Sonics and Ultrasonics*, Vol. SU-31, July 1984, pp. 230-239.
- [McG82] R. McGowan and R. Kuc, "A direct relation between a signal time series and its unwrapped phase," *IEEE Transactions on Acoustics, Speech and Signal Processing*, Vol. ASSP-30, October 1982, pp. 719-726.
- [Mor53] Philip M. Morse and Herman Feshbach, *Methods of Theoretical Physics*, McGraw Hill Book Company, New York, 1953.
- [New66] R. G. Newton, *Scattering Theory of Waves and Particles*, McGraw-Hill Book Company, New York, 1966.
- [OCo78] B. T. O'Connor and T. S. Huang, *Techniques for determining the stability of two-dimensional recursive filters and their application to image restoration*, TR-EE 78-18, School of Electrical Engineering, Purdue University, pp 6-24.

- [Tri77] J. M. Tribolet, "A new phase unwrapping algorithm," *IEEE Transactions on Acoustics, Speech and Signal Processing*, Vol. ASSP-25, April 1977, pp. 170-177.

CHAPTER 3

THE FOURIER DIFFRACTION THEOREM

3.1 Introduction

Fundamental to diffraction tomography is the *Fourier Diffraction Projection Theorem*, which relates the Fourier transform of the measured forward scattered data with the Fourier transform of the object. *The theorem is valid when the inhomogeneities in the object are only weakly scattering and can be stated as [Kak84]:*

When an object, $f(x,y)$, is illuminated with a plane wave as shown in Figure 3.1, the Fourier transform of the forward scattered fields measured on line TT' gives the values of the 2-D transform, $F(\omega_1, \omega_2)$, of the object along a circular arc in the frequency domain, as shown in the right half of the figure.

The importance of the theorem is made obvious by noting that if an object is illuminated by plane waves from many directions over 360° , the resulting circular arcs in the (ω_1, ω_2) -plane will fill the frequency domain. The function $f(x,y)$ may then be recovered by Fourier inversion.

Before giving a short proof of the theorem, first a few words about the dimensionality of the object compared to that of the scattered fields. Although the theorem talks about a two-dimensional object, what is actually meant is an object that does not vary in the z direction. In other words, the theorem is about any cylindrical object whose cross-sectional distribution is given by the function $f(x,y)$. The forward scattered fields are measured on a line of detectors along TT' in Figure 3.1.

If a truly three-dimensional object is illuminated by a plane wave, the forward scattered fields would now have to be measured by a planar array of detectors. The Fourier transform of the fields measured by such an array would give the values of the 3-D transform of the object over a spherical surface. This was first shown by Wolf [Wol69]. A more recent exposition is in [Nah84 and Dev84], where the authors have also presented a new synthetic

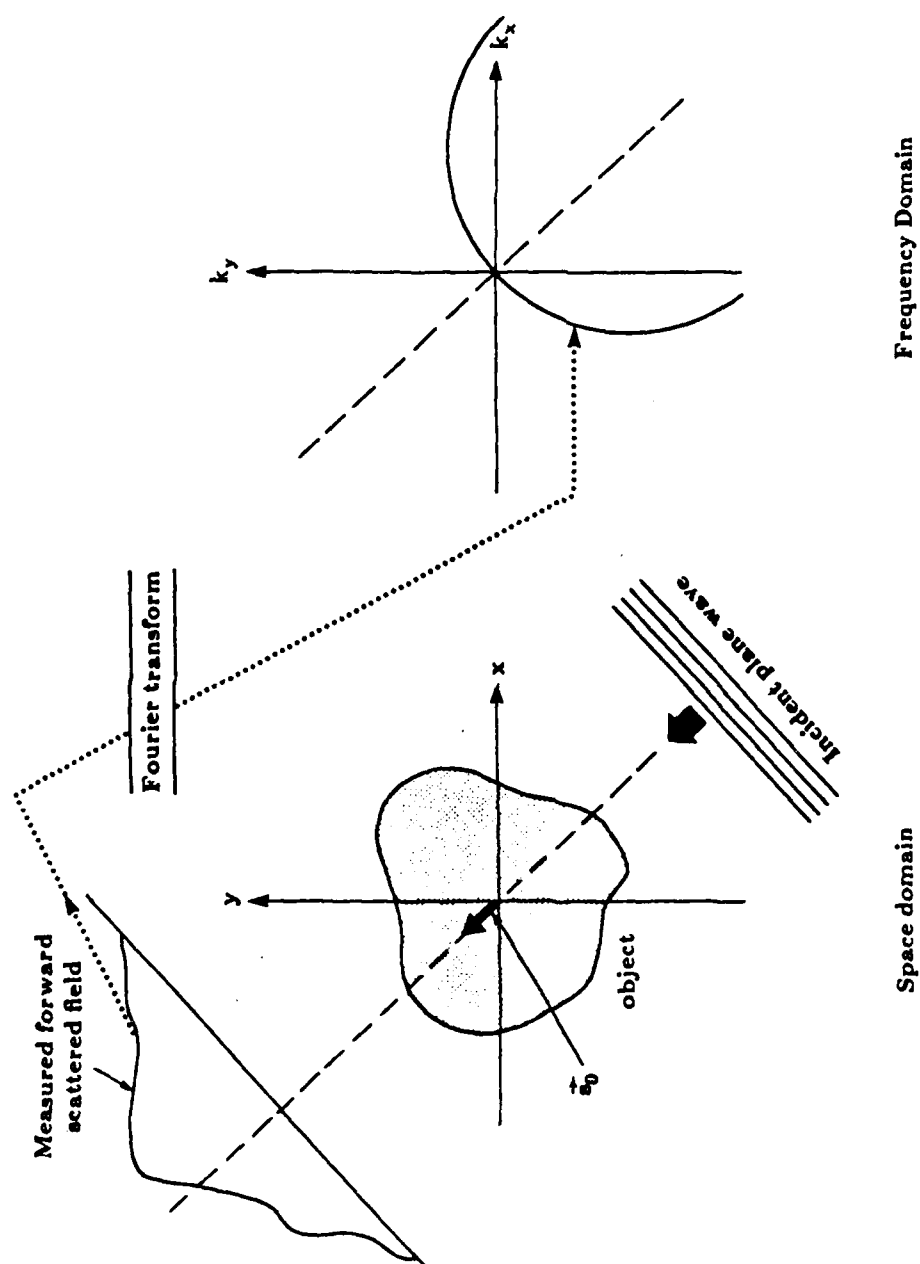


Figure 3.1 The Fourier Diffraction Theorem.

aperture procedure for a full three dimensional reconstruction using only two rotational positions of the object. This chapter, however, will continue to work with two dimensional objects in the sense described here. A recent work describing some of the errors in this approach is [LuZ84].

3.2 Decomposing the Green's Function

Earlier in this work, the scattered field due to a weakly scattering object was expressed as the convolution

$$u_B(\vec{r}) = \int o(\vec{r}') u_0(\vec{r}') g(\vec{r} - \vec{r}') d\vec{r}' \quad (3.1)$$

where $u_B(\vec{r})$ represents the complex amplitude of the field as in the Born approximation or the incident field, $u_0(\vec{r})$, times the complex scattered phase, $\phi_s(\vec{r})$, in the Rytov approximation. From this integral there are two approaches to the derivation of the Fourier Diffraction Theorem. Many researchers [Mue79, Gre78, Dev82] have expanded the Green's function into its plane wave decomposition and then noticed the similarity of the resulting expression and the Fourier transform of the object. Alternatively, if the Fourier transform of each component of this equation (3.1) is taken then the Fourier Diffraction Theorem can be derived in a manner that can be easily visualized and points towards efficient computer implementations. This work will present both approaches to the derivation of the Fourier Diffraction Theorem: the first because the math is more straightforward, the second because it provides more insight into the difference between transmission and reflection tomography.

First the Green's function will be decomposed into its plane wave components.

3.2.1 Plane Wave Approach

The integral equation for the scattered field (3.1) can be considered as a convolution of the Green's Function, $g(\vec{r} - \vec{r}')$, and the product of the object function, $o(\vec{r}')$, and the incident field, $u_0(\vec{r}')$. Consider the effect of a single plane wave illuminating an object. The forward scattered field will be measured at the receiver line as is shown in Figure 3.2.

A single plane wave in two dimensions can be represented as

$$u_0(\vec{r}) = e^{j\vec{K} \cdot \vec{r}} \quad (3.2)$$

where $\vec{K} = (k_x, k_y)$ satisfies the following relationship

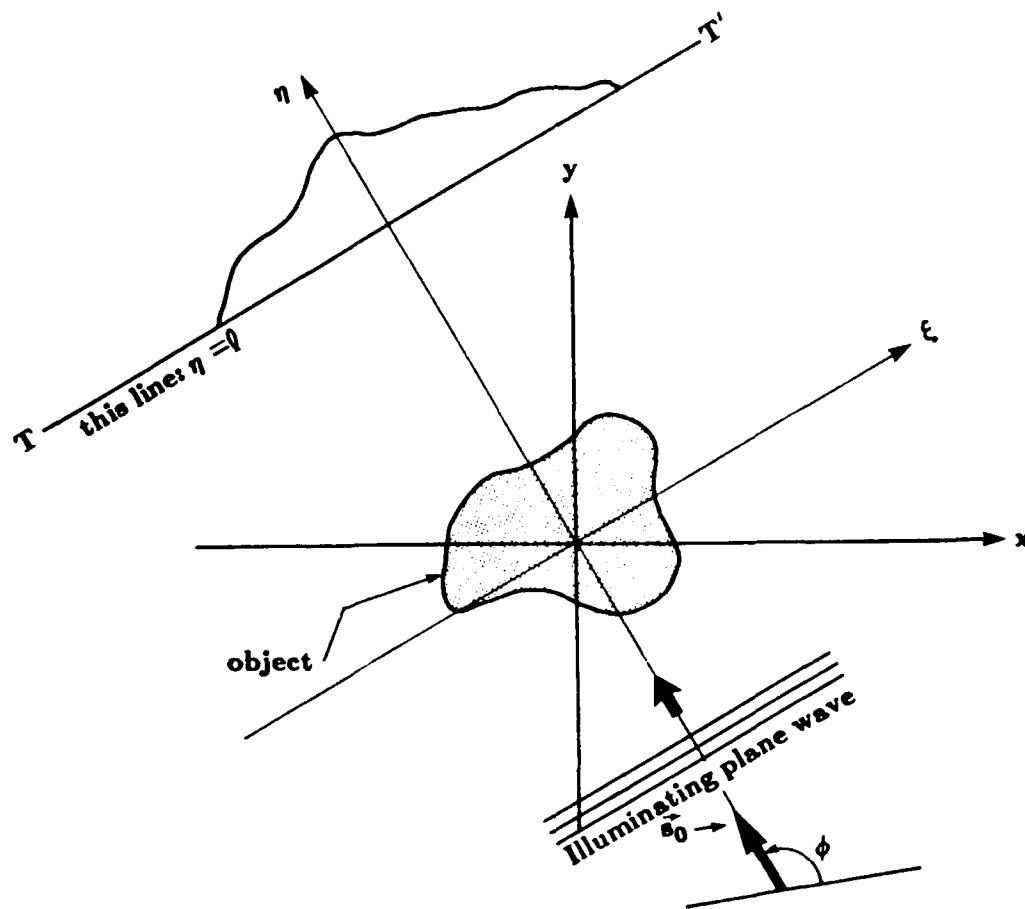


Figure 3.2

A typical diffraction tomography experiment

$$k_0^2 = k_x^2 + k_y^2. \quad (3.3)$$

From earlier in this work, the two dimensional Green's function is given by

$$g(\vec{r}|\vec{r}') = \frac{j}{4} H_0(k_0|\vec{r}-\vec{r}'|) \quad (3.4)$$

and H_0 is the zero-order Hankel function of the first kind. The function H_0 has the plane wave decomposition [Mor53]

$$H_0(k|\vec{r}-\vec{r}'|) = \frac{1}{\pi} \int_{-\infty}^{\infty} \frac{1}{\beta} e^{j[\alpha(x-x') + \beta|y-y'|]} d\alpha \quad (3.5)$$

where $\vec{r} = (x, y)$, $\vec{r}' = (x', y')$ and

$$\beta = \sqrt{k_0^2 - \alpha^2}. \quad (3.6)$$

Basically, equation (3.5) expresses a cylindrical wave, H_0 , as a superposition of plane waves. At all points, the wave centered at \vec{r}' is traveling outward; for points such that $y > y'$ the plane waves propagate upward while for $y < y'$ the plane waves propagate downward. In addition, for $|\alpha| \leq k_0$, the plane waves are of the ordinary type, propagating along the direction given by $\tan^{-1}(\beta/\alpha)$. However, for $|\alpha| > k_0$, β becomes imaginary, the waves decay exponentially and they are called *evanescent waves*. Evanescent waves are usually of no significance beyond about 10 wavelengths from the source.

Substituting this expression, (3.5), into the expression for the scattered field, (3.1), the scattered field can now be written

$$u_B(\vec{r}) = \frac{j}{4\pi} \int o(\vec{r}') u_0(\vec{r}') \int_{-\infty}^{\infty} \frac{1}{\beta} e^{j[\alpha(x-x') + \beta|y-y'|]} d\alpha d\vec{r}' \quad (3.7)$$

In order to show the first steps in the proof of this theorem, assume for notational convenience that the direction of the incident plane wave is along the positive y-axis. Thus the incident field is given by

$$u_0(\vec{r}) = e^{j\vec{s}_0 \cdot \vec{r}} \quad (3.8)$$

where $\vec{s}_0 = (0, k_0)$. Since in transmission imaging the scattered fields are measured by a linear array located at $y = l_0$, where l_0 is greater than any y-coordinate within the object (see Figure 3.2), the term $|y-y'|$ in the above expression may simply be replaced by $l_0 - y'$ and the resulting form may be rewritten

$$u_B(x, y=l_0) = \frac{j}{4\pi} \int_{-\infty}^{\infty} d\alpha \int \frac{O(\vec{r}')}{\beta} e^{j[\alpha(x-x') + \beta(l_0-y')] } e^{jk_0 y'} d\vec{r}' \quad (3.9)$$

Recognizing part of the inner integral as the two-dimensional Fourier transform of the object function evaluated at a frequency of $(\alpha, \beta-k_0)$ the scattered field can be written

$$u_B(x, y=l_0) = \frac{j}{4\pi} \int_{-\infty}^{\infty} \frac{1}{\beta} e^{j(\alpha x + \beta l_0)} O(\alpha, \beta-k_0) d\alpha \quad (3.10)$$

where O has been used to designate the two dimensional Fourier transform of the object function.

Let $U_B(\omega, l_0)$ denote the Fourier transform of the one dimensional scattered field, $u_B(x, l_0)$, with respect to x , that is

$$U_B(\omega, l_0) = \int_{-\infty}^{\infty} u_B(x, l_0) e^{j\omega x} dx \quad (3.11)$$

As mentioned before, the physics of wave propagation dictate that the highest angular spatial frequency in the measured scattered field on the line $y=l_0$ is unlikely to exceed k_0 . Therefore, in almost all practical situations, $U_s(\omega, l_0) = 0$ for $|\omega| > k_0$. This is consistent with neglecting the evanescent modes as described earlier.

If the Fourier transform of the scattered field is found by substituting equation (3.10) into equation (3.11) then using the following property of Fourier integrals

$$\int_{-\infty}^{\infty} e^{j(\omega - \alpha)x} dx = 2\pi \delta(\omega - \alpha) \quad (3.12)$$

where $\delta(\cdot)$ is the Dirac delta function discussed in Chapter 2 the scattered field can be written

$$U_B(\alpha, l_0) = \frac{j}{2\sqrt{k_0^2 - \alpha^2}} e^{j\sqrt{k_0^2 - \alpha^2} l_0} O(\alpha, \sqrt{k_0^2 - \alpha^2} - k_0) \quad (3.13)$$

$$\text{for } |\alpha| < k_0.$$

This expression relates the two dimensional Fourier transform of the object to the one dimensional Fourier transform of the field at the receiver line. The factor

$$\frac{j}{2\sqrt{k_0^2 - \alpha^2}} e^{j\sqrt{k_0^2 - \alpha^2} l_0} \quad (3.14)$$

is a simple constant for a fixed receiver line. As α varies from $-k_0$ to k_0 , the coordinates $(\alpha, \sqrt{k_0^2 - \alpha^2} - k_0)$ in the Fourier transform of the object function trace out a semicircular arc in the (u, v) -plane as shown in Figure 3.1. This proves the Fourier Diffraction Theorem.

To summarize, if the Fourier transform of the forward scattered data is found when the incident illumination is propagating along the positive y -axis, the resulting transform will be zero for angular spatial frequencies $|\alpha| > k_0$. For $|\alpha| < k_0$, the transform of the data gives values of the Fourier transform of the object on the semicircular arc are shown in Figure 3.1 in the (u, v) -plane. The endpoints A and B of the semicircular arc are at a distance of $\sqrt{2}k_0$ from the origin in the frequency domain.

3.2.2 Fourier Transform Approach

Another approach to the derivation of the Fourier Diffraction Theorem is possible if the scattered field

$$u_B(\vec{r}) = \int o(\vec{r}') u_0(\vec{r}') g(\vec{r} - \vec{r}') d\vec{r}' \quad (3.15)$$

is considered entirely in the Fourier domain. The plots of Figure 3.3 will be used to illustrate the various transformations that take place.

Again consider the effect of a single plane wave illuminating an object. The forward scattered field will be measured at the receiver line as is shown in Figure 3.2.

The integral equation for the scattered field can be considered as a convolution of the Green's Function, $g(\vec{r} - \vec{r}')$, and the product of the object function, $o(\vec{r}')$, and the incident field, $u_0(\vec{r}')$. First define the following Fourier transform pairs.

$$o(\vec{r}) \leftrightarrow O(\vec{K})$$

$$g(\vec{r} - \vec{r}') \leftrightarrow G(\vec{K}) \quad (3.16)$$

$$u(\vec{r}) \leftrightarrow U(\vec{K})$$

The integral solution to the wave equation can now be written in terms of these Fourier transforms or

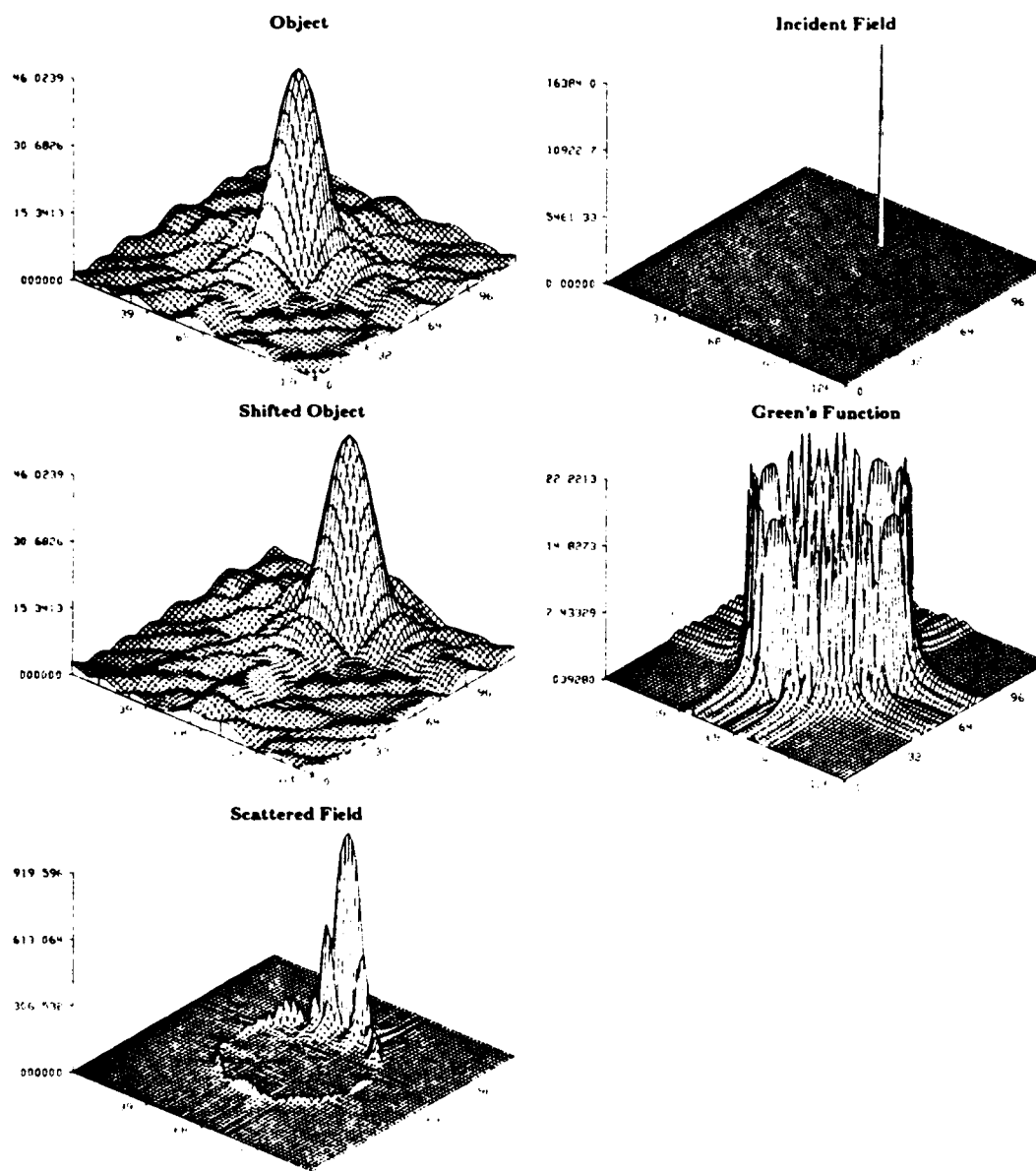


Figure 3.3

Two dimensional Fourier representation of the Helmholtz equation. (a) The object, (b) the incident field, (c) the Green's function, (d) the (space domain) product of the object and the incident field and (e) the two dimensional Fourier transform of the scattered field.

$$U_s(\vec{\Lambda}) = G(\vec{\Lambda}) \left\{ O(\vec{\Lambda}) * U_0(\vec{\Lambda}) \right\} \quad (3.17)$$

where '*' has been used to represent convolution and $\vec{\Lambda} = (\alpha, \gamma)$. In equation (3.2) an expression for u_0 was presented. Its Fourier transform is given by

$$U_0(\vec{\Lambda}) = 2\pi\delta(\vec{\Lambda} - \vec{K}) \quad (3.18)$$

and thus the convolution of equation (3.17) becomes a shift in the frequency domain or

$$O(\vec{\Lambda}) * U_0(\vec{\Gamma}) = 2\pi O(\vec{\Lambda} - \vec{K}). \quad (3.19)$$

This convolution is illustrated in Figures 3.3a-c for a plane wave propagating with direction vector, $\vec{K} = (0, k_0)$. Figure 3.3a shows the Fourier transform of a single cylinder of radius 1λ and Figure 3.3b is the Fourier transform of the incident field. The resulting multiplication in the space domain or convolution in the frequency domain is shown in Figure 3.3c.

To find the Fourier transform of the Green's function the Fourier transform of the equation for a point scatterer

$$(\nabla^2 + k_0^2)g(\vec{r}|\vec{r}') = -\delta(\vec{r} - \vec{r}'), \quad (3.20)$$

is taken to find

$$(-\Lambda^2 + k_0^2)G(\vec{\Lambda}|\vec{r}') = -e^{-j\vec{\Lambda} \cdot \vec{r}'}. \quad (3.21)$$

Rearranging terms the following expression for the Fourier transform of the Green's function is found

$$G(\vec{\Lambda}|\vec{r}') = \frac{e^{-j\vec{\Lambda} \cdot \vec{r}'}}{\Lambda^2 - k_0^2}. \quad (3.22)$$

This has a singularity for all $\vec{\Lambda}$ such that

$$|\Lambda|^2 = \alpha^2 + \gamma^2 = k_0^2. \quad (3.23)$$

An approximation to $G(\vec{\Lambda})$ is shown in Figure 3.3d.

The Fourier transform representation is misleading because it represents a point scatterer as both a sink and a source of waves. A single plane wave propagating from left to right can be considered in two different ways depending on the point of view. From the left side of the scatter, the point scatterer represents a sink to the wave while to the right of the scatterer the

wave is spreading from a source point. Clearly, it is not possible for a scatterer to be both a point source and sink, and later when our expression for the scattered field is inverted, it will be necessary to choose a solution that leads to outgoing waves only.

The effect of the convolution shown in equation (3.15) is a multiplication in the frequency domain of the shifted object function, (3.19), and the Green's function, (3.22), evaluated at $\vec{r}' = 0$. The scattered field is written as

$$U_s(\vec{\Lambda}) = 2\pi \frac{O(\vec{\Lambda}-\vec{K})}{\Lambda^2 - k^2}. \quad (3.24)$$

This result is shown in Figure 3.3e for a plane wave propagating along the y-axis. Since the largest frequency domain components of the Green's function satisfy equation (3.23), the Fourier transform of the scattered field is dominated by a shifted and sampled version of the object's Fourier transform.

An expression for the field at the receiver line will now be derived. For simplicity it will continue to be assumed that the incident field is propagating along the positive y axis or $\vec{K} = (0, k_0)$. The scattered field along the receiver line ($x, y=l_0$) is simply the inverse Fourier transform of the field in equation (3.24). This is written as

$$u(x, y=l_0) = \frac{1}{4\pi^2} \int_{-\infty}^{\infty} \int_{-\infty}^{\infty} U_s(\vec{\Lambda}) e^{j\vec{\Lambda} \cdot \vec{r}} d\alpha d\gamma \quad (3.25)$$

which, using (3.24), can be expressed as

$$u_s(x, y=l_0) = \frac{1}{4\pi^2} \int_{-\infty}^{\infty} \int_{-\infty}^{\infty} \frac{O(\alpha, \gamma - k_0)}{\alpha^2 + \gamma^2 - k_0^2} e^{j(\alpha x + \gamma l_0)} d\alpha d\gamma. \quad (3.26)$$

First find the integral with respect to γ . For a given α , the integral has a singularity for

$$\gamma_{1,2} = \pm \sqrt{k_0^2 - \alpha^2} \quad (3.27)$$

Using contour integration the integral can be evaluated with respect to γ along the path shown in Figure 3.4. By adding $\frac{1}{2\pi}$ of the residue at each pole the scattered field is expressed

$$u_s(x, y) = \frac{1}{2\pi} \int \Gamma_1(\alpha; y) e^{j\alpha x} d\alpha + \frac{1}{2\pi} \int \Gamma_2(\alpha; y) e^{j\alpha x} d\alpha \quad (3.28)$$

where

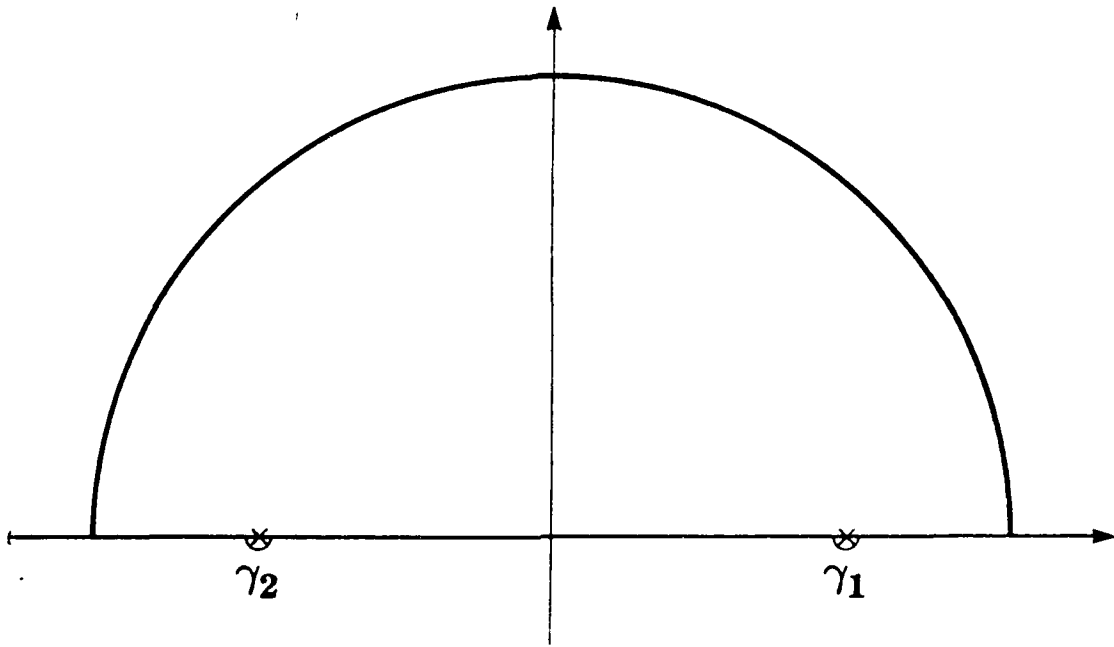


Figure 3.4

Integration path in the complex plane for inverting the two dimensional Fourier transform of the scattered field.

$$\Gamma_1 = \frac{jO(\alpha, \sqrt{k_0^2 - \alpha^2} - k_0)}{2\sqrt{k_0^2 - \alpha^2}} e^{j\sqrt{k_0^2 - \alpha^2}l_0} \quad (3.29)$$

and

$$\Gamma_2 = \frac{-jO(\alpha, -\sqrt{k_0^2 - \alpha^2} - k_0)}{2\sqrt{k_0^2 - \alpha^2}} e^{-j\sqrt{k_0^2 - \alpha^2}l_0} \quad (3.30)$$

Examining the above pair of equations it can be seen that Γ_1 represents the solution in terms of plane waves traveling along the positive y axis while Γ_2 represents plane waves traveling in the -y direction.

As was discussed earlier, the Fourier transform of the Green's function (3.22) represents the field due to both a point source and a point sink but the two solutions are distinct for receiver lines that are outside the extent of the object. First consider the scattered field along the line $y = l_0$ where l_0 is greater than the y-coordinate of all points in the object. Since all scattered fields originate in the object, plane waves propagating along the positive y axis represent outgoing waves while waves propagating along the negative y axis represent waves due to a point sink. Thus for $y > \text{object}$ (i.e. the receiver line is above the object) the outgoing scattered waves are represented by Γ_1 or

$$u_s(x, y) = \frac{1}{2\pi} \int \Gamma_1(\alpha; y) e^{j\alpha x} d\alpha \quad y > \text{object} \quad (3.31)$$

Conversely for a receiver along a line $y = l_0$ where l_0 is less than the y-coordinate of any point in the object the scattered field is represented by Γ_2 or

$$u_s(x, y) = \frac{1}{2\pi} \int \Gamma_2(\alpha; y) e^{j\alpha x} d\alpha \quad y < \text{object} \quad (3.32)$$

In general the scattered field will be written as as

$$u_s(x, y) = \frac{1}{2\pi} \int \Gamma(\alpha; y) e^{j\alpha x} d\alpha \quad (3.33)$$

and it will be understood that values of the square root in the expression for Γ should be chosen that lead only to outgoing waves.

Taking the Fourier transform of both sides of equation (3.33) the Fourier transform of the scattered field at the receiver line is written

$$\int u(x, y=l_0) e^{-j\alpha x} dx = \Gamma(\alpha, l_0). \quad (3.34)$$

But since by equations (3.29) and (3.30), $\Gamma(\alpha, l_0)$ is equal to a phase shifted version of the object function then the Fourier transform of the scattered field

along the line $y=l_0$ is related to the Fourier transform of the object along a circular arc. The use of the contour integration is further justified by noting that only those waves that satisfy the relationship

$$\alpha^2 + \gamma^2 = k_0^2 \quad (3.35)$$

will be propagated and thus it is safe to ignore all waves not on the k_0 -circle.

This result is diagrammed in Figure 3.5. The circular arc represents the locus of all points (α, γ) such that $\gamma = \pm \sqrt{k_0^2 - \alpha^2}$. The solid line shows the outgoing waves for a receiver line at $y=l_0$ above the object. This can be considered transmission tomography. Conversely the dashed line indicates the locus of solutions for the reflection tomography case, or $y=l_0$ is below the object.

3.3 Limit of the Fourier Diffraction Theorem

While at first the derivations of the Fourier Slice Theorem and the Fourier Diffraction Theorem seem quite different, it is interesting to note that in the limit of very high energy waves or, equivalently, very short wavelengths the Fourier Diffraction Theorem is closely approximated by the Fourier Slice Theorem. Recall that the Fourier transform of a diffracted projection corresponds to samples of the two dimensional Fourier transform of an object along a circular arc. As shown in Figure 3.1 the radius of the arc is equal to k_0 which is given by

$$k_0 = \frac{2\pi}{\lambda} \quad (3.36)$$

and λ is the wavelength of the energy. As the wavelength is decreased, the wavenumber, k_0 , and the radius of the arc in the object's Fourier domain grows. This process is illustrated in Figure 3.6 where the semicircular arc resulting from a diffraction experiment is shown at six different frequencies.

An example might make this idea clearer. Compare an ultrasonic diffraction apparatus and a typical x-ray scanner. The ultrasonic experiment might be carried out at a frequency of 5 MHz and a wavelength in water of .3 mm. This corresponds to a k_0 of 333 radians/meter. On the other hand, an x-ray source with a 100 keV beam has a wavelength of .012 μ M. The result is that a diffraction experiment gives samples along an arc of radius 5×10^8 radians/meter. Certainly for all physiological features (i.e. resolutions of < 1000 radians/meter) the arc can be considered a straight line and the Fourier Slice Theorem is an excellent model of the propagation of x-rays.

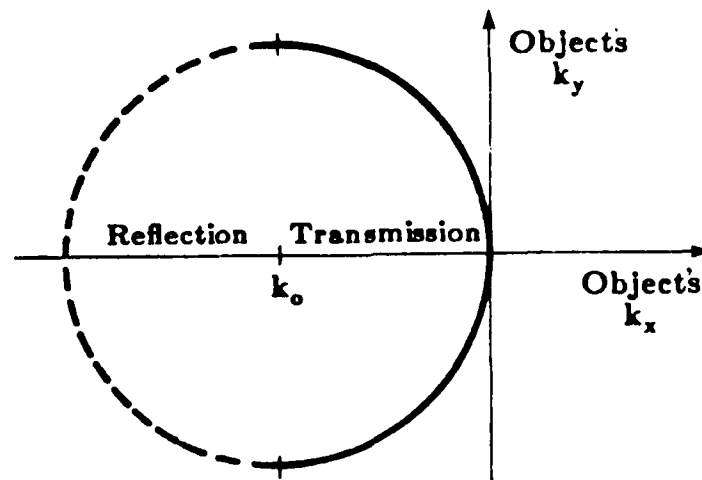


Figure 3.5

Estimate of the two dimensional Fourier transform of the object are available along the solid arc for transmission tomography and the dashed arc for reflection tomography.

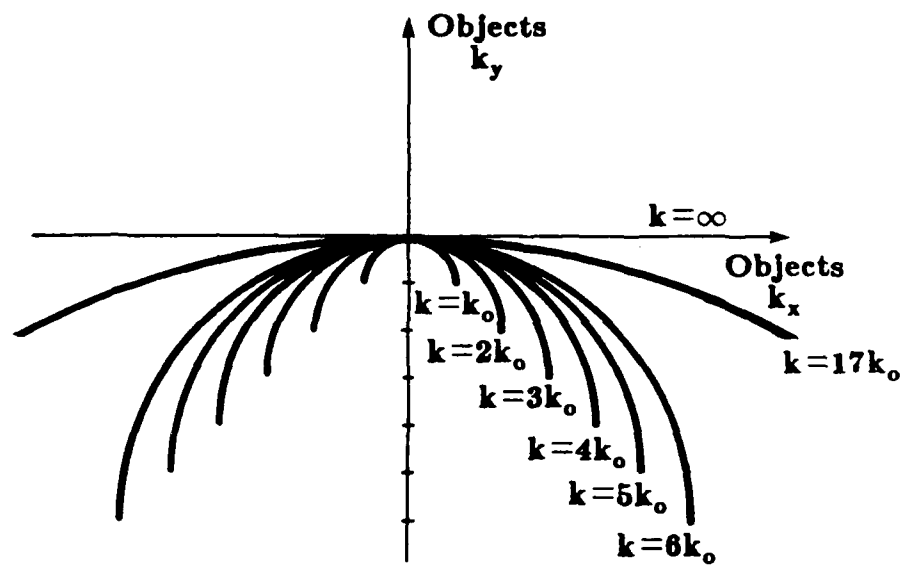


Figure 3.6

As the illuminating frequency is increased the Fourier Diffraction Theorem becomes equivalent to the Fourier Slice Theorem.

3.4 The Data Collection Process

The best that can be hoped for in any tomographic experiment is to estimate the Fourier transform of the object for all frequencies within a disk centered at the origin. For objects that do not have any frequency content outside the disk then the reconstruction procedure is perfect.

There are several different procedures that can be used to estimate the object function from the scattered field. A single plane wave provides exact information (up to a frequency of $\sqrt{2}k_0$) about the Fourier transform of the object along a circular arc. Two of the simplest procedures involve changing the orientation and frequency of the incident plane waves to move the frequency domain arcs to a new position. By appropriately choosing an orientation and a frequency it is possible to estimate the Fourier transform of the object at any given frequency. In, addition it is possible to change the radius of the semicircular arc by varying the frequency of the incident field and thus generating an estimate of the entire Fourier transform of the object.

3.4.1 Plane Wave Illumination

The most straightforward data collection procedure consists of rotating the object and measuring the scattered field for different orientations. Each orientation will produce an estimate of the object's Fourier transform along a circular arc and these arcs will rotate as the object is rotated. When the object is rotated through a full 360 degrees an estimate of the object will be available for the entire Fourier disk.

The coverage for this method is shown in Figure 3.7 for a simple experiment with 8 projections of 9 samples each. Notice that there are two arcs that pass through each point of Fourier space. Generally it will be necessary to choose one estimate as better.

On the other hand if the reflected data is collected by measuring the field on the same side of the object as the source then estimates of the object are available for frequencies greater than $\sqrt{2}k_0$. This follows from Figure 3.5.

The first experimental results for diffraction tomography were presented by Carter and Ho [Car70, Car74, Car76 and Ho76]. They used an optical plane wave to illuminate a small glass object and were able to measure the scattered fields using a hologram. Later a group of researchers at the University of Minnesota carried out the same experiments using ultrasound and gelatine phantoms. Their results are discussed in [Kav82].

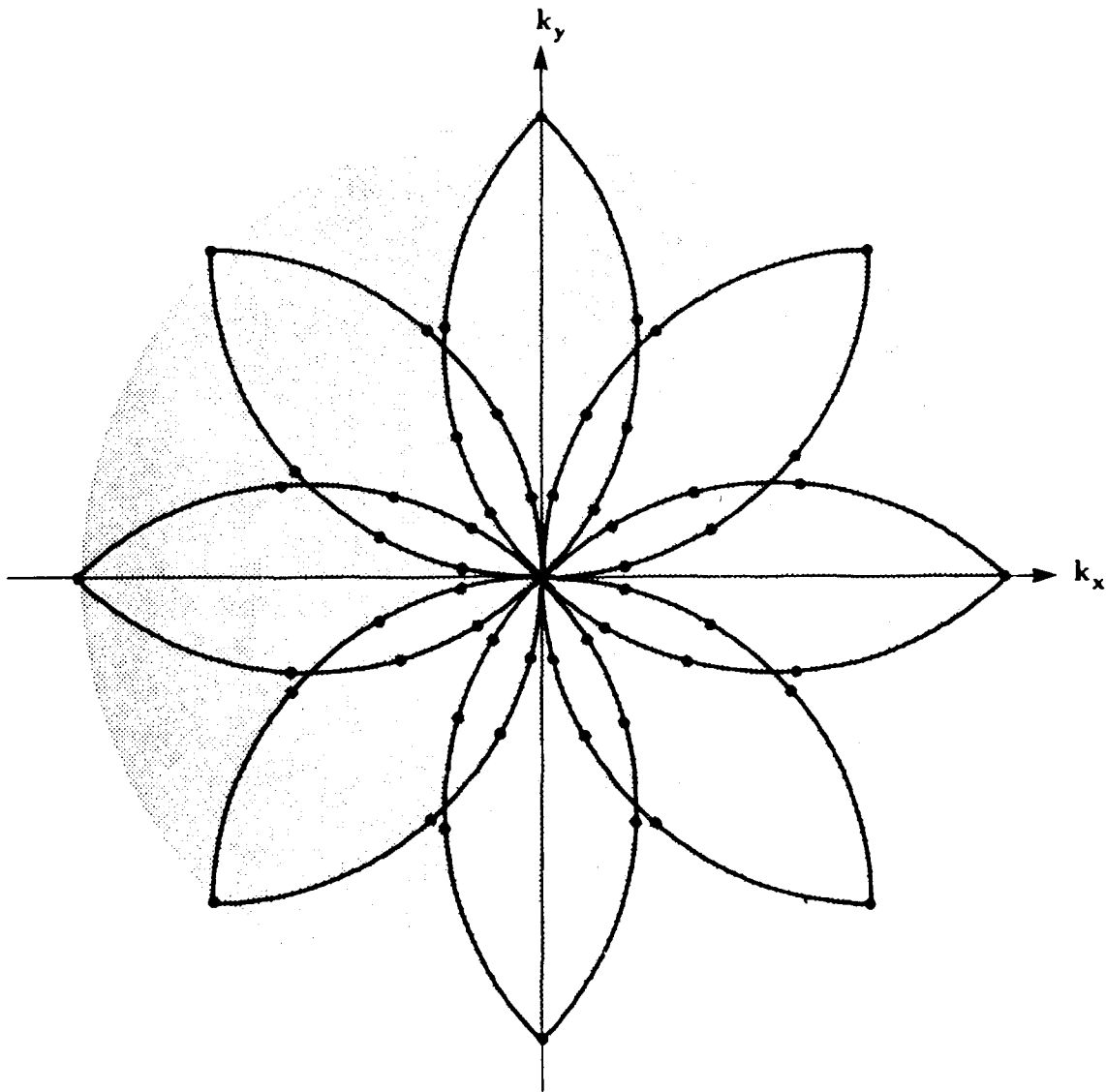


Figure 3.7

Estimates of the object's two dimensional Fourier transform are available along the circular arcs for plane wave illumination.

3.4.2 Synthetic Aperture

Nahamoo and Kak [Nah82, Nah84] and Devaney [Dev84] have proposed a method that requires only two rotational views of an object. Consider an arbitrary source of waves in the transmitter plane as shown in Figure 3.8. The transmitted field, u_t , can be represented as a weighted set of plane waves by taking the Fourier transform of the transmitter aperture function [Goo68]. Doing this the transmitted field can be expressed as

$$u_t(x) = \frac{1}{4\pi^2} \int_{-\infty}^{\infty} A_t(k_x) e^{jk_x x} dk_x. \quad (3.37)$$

Moving the source to a new position, η , the plane wave decomposition of the transmitted field becomes

$$u_t(x; \eta) = \frac{1}{4\pi^2} \int_{-\infty}^{\infty} \left[A_t(k_x) e^{jk_x \eta} \right] e^{jk_x x} dk_x. \quad (3.38)$$

Given the plane wave decomposition, the incident field in the plane follows simply as

$$u_i(\eta; x, y) = \int_{-\infty}^{\infty} \left[\frac{1}{4\pi^2} A_t(k_x) e^{jk_x \eta} \right] e^{j(k_x x + k_y y)} dk_x. \quad (3.39)$$

In equation (3.34) an equation for the scattered field from a single plane wave was presented. Because of the linearity of the Fourier transform, the effect of each plane wave, $e^{j(k_x x + k_y y)}$, can be weighted by the expression in brackets above and superimposed to find the Fourier transform of the total scattered field due to the incident field $u_i(x; \eta)$ as [Nah82]

$$U_s(\eta; \alpha) = \int_{-\infty}^{\infty} \left[A_t(k_x) e^{jk_x \eta} \right] \frac{O(\alpha - k_x, \gamma - k_y)}{j2\gamma} dk_x. \quad (3.40)$$

Taking the Fourier transform of both sides with respect to the transmitter position, η , the Fourier transform of the scattered field with respect to both the transmitter and the receiver position is given by

$$U_s(k_x; \alpha) = A_t(k_x) \frac{O(\alpha - k_x, \gamma - k_y)}{j2\gamma} k_x. \quad (3.41)$$

This approach gets the name synthetic aperture because a phase is added to the field measured for each transmitter position to synthesize a transmitted plane wave. Thus this method has a lot in common with the theory of phased arrays. Figure 3.9 shows that by properly phasing the wave transmitted at each transmitter location a plane wave can be generated that travels in an

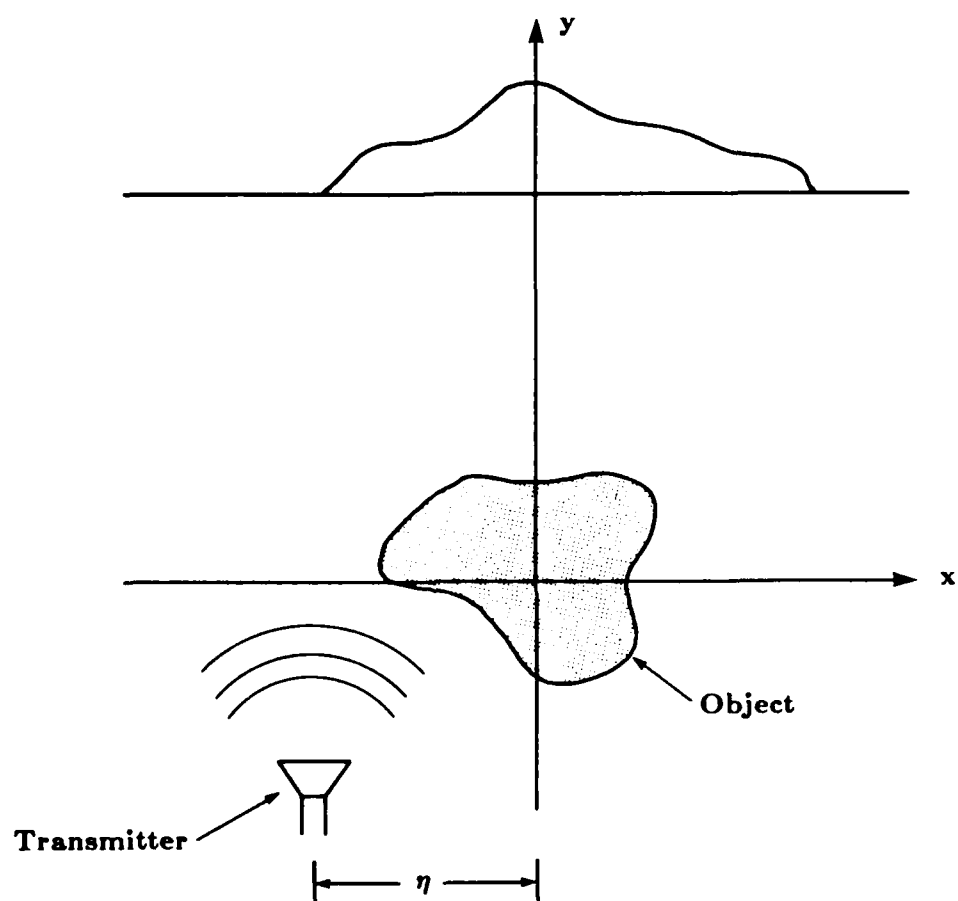


Figure 3.8 A typical synthetic aperture tomography experiment.

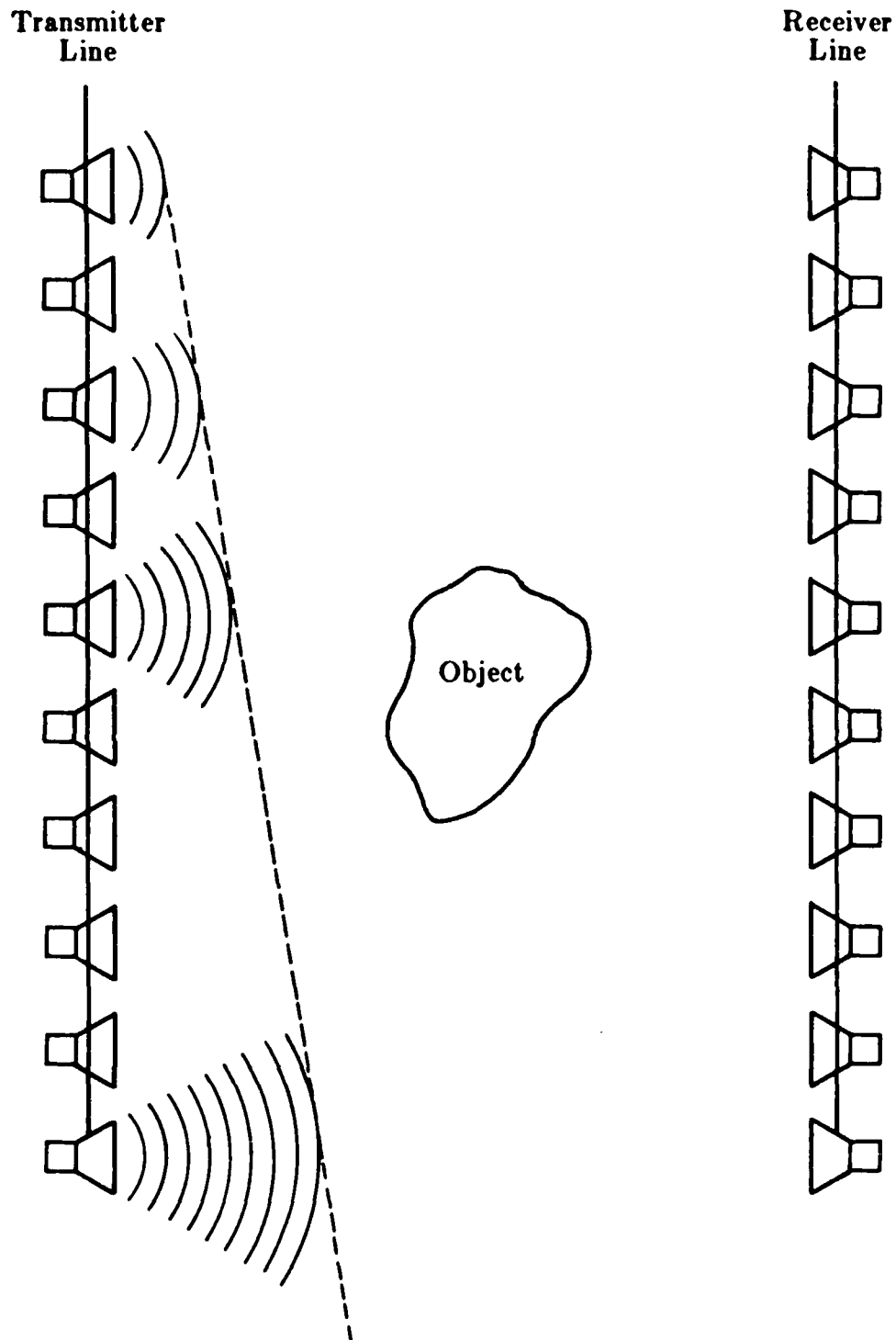


Figure 3.9

By adding a phase to the field transmitted from each transmitter any desired plane wave can be synthesized.

arbitrary direction. Since the system is linear it doesn't matter whether the phase is added to the transmitted signal or as part of the reconstruction procedure. Thus multiplying the received field for each transmitter position by the pure phase term $e^{jk_x\eta}$, where η represents the location of the transmitter, is equivalent to an experiment with an incident plane wave with the direction vector $(k_x, \sqrt{k_0^2 - k_x^2})$.

By collecting the scattered field along the receiver line as a function of transmitter position, η , an expression can be written for the scattered field. Like the simpler case with plane wave incidence, the scattered field is related to the Fourier transform of the object along an arc. Unlike the previous case, though, the coverage due to a single view of the object is a pair of circular disks as shown in Figure 3.10. Here a single view consists of transmitting from all positions in a line and measuring the scattered field at all positions along the receiver line. By rotating the object by 90 degrees it is possible to generate the complimentary disk and to fill the Fourier domain.

The coverage shown in Figure 3.10 is constructed by calculating $(\vec{K} - \vec{\Lambda})$ for all vectors (\vec{K}) and $(\vec{\Lambda})$ that satisfy the experimental constraints. Not only must each vector satisfy the wave equation but it is also necessary that only forward traveling plane waves be used. The dashed line in Figure 3.10 shows the valid propagation vectors $(-\vec{\Lambda})$ for the transmitted waves. To each possible vector $(-\vec{\Lambda})$ a semicircular set of vectors representing each possible received wave can be added. The locus of received plane waves is shown as a solid semi-circle centered at each of the transmitted waves indicated by an 'x'. The entire coverage for the synthetic aperture approach is shown as the shaded areas.

In addition to the diffraction tomography configurations proposed by Mueller and Nahamoo other approaches have been proposed. In Vertical Seismic Profiling (VSP) [Dev84] the scattering between the surface of the Earth and a borehole is measured. Alternately a broadband incident field can be used to illuminate the object. In both cases, the goal is to estimate the Fourier transform of the object.

In geophysical imaging it is not possible to generate or receive waves from all positions around the object. If it is possible to drill a borehole then it is possible to perform VSP and obtain information about most of the object. A typical experiment is shown in Figure 3.11. So as to not damage the borehole, acoustic waves are generated at the surface using acoustic detonators or other methods and the scattered field is measured in the borehole.

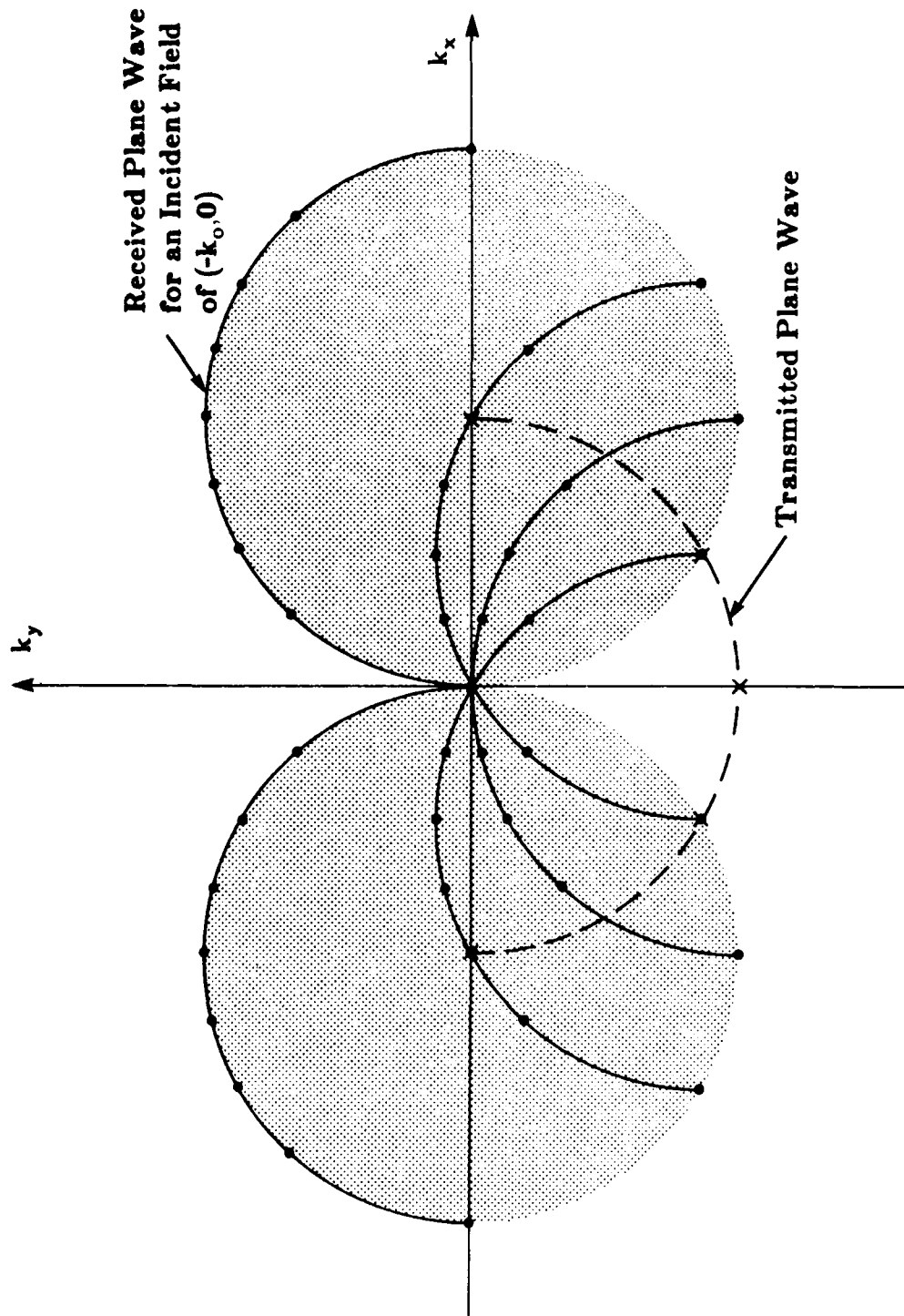


Figure 3.10 Estimates of the Fourier transform of an object in a synthetic aperture experiment are available in the shaded region.

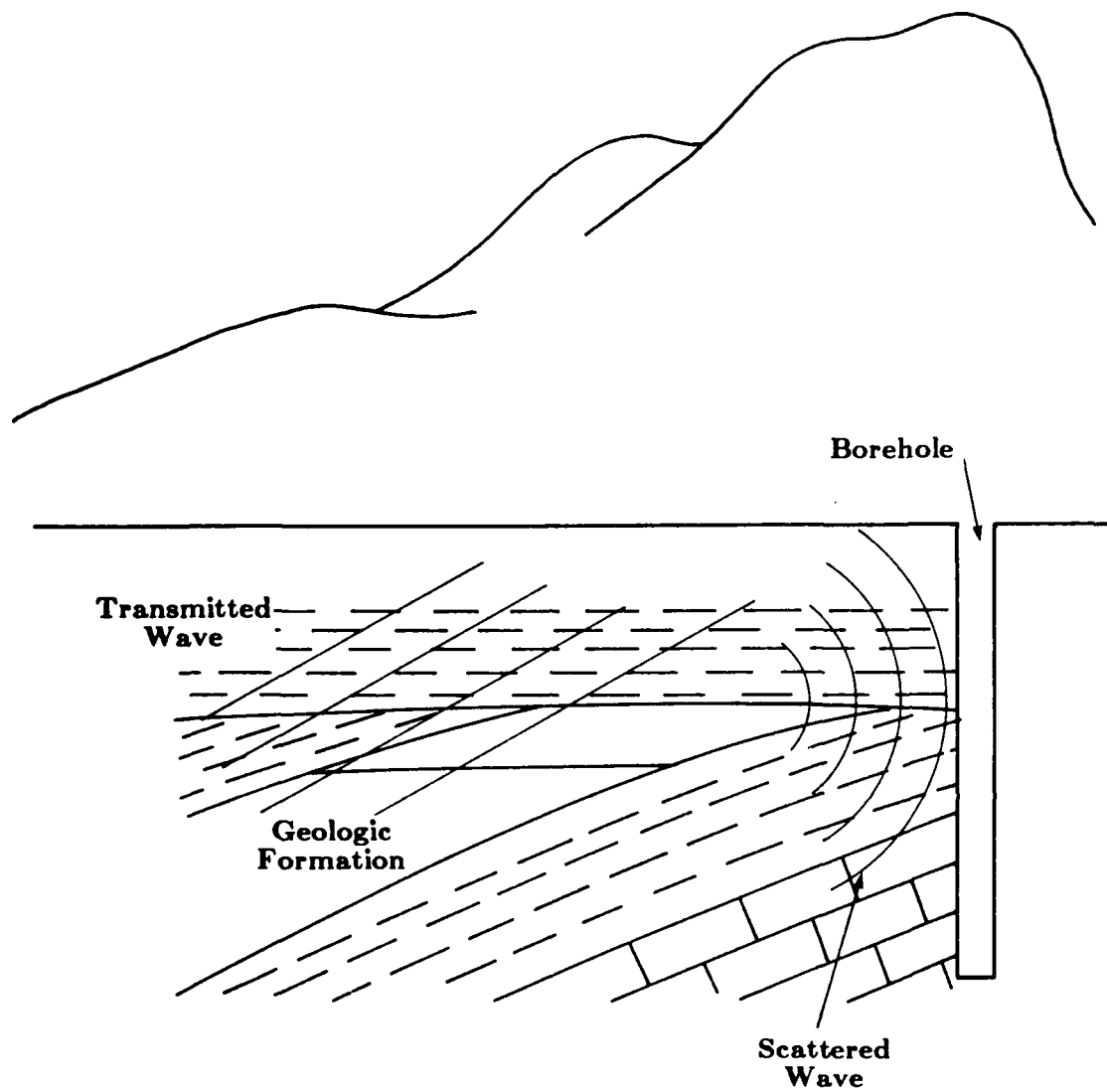


Figure 3.11 A typical Vertical Seismic Profiling (VSP) experiment.

The coverage in the frequency domain is similar to the synthetic aperture approach. Plane waves at an arbitrary downward direction are synthesized by appropriately phasing the transmitting transducers. The receivers will receive any waves traveling to the right. The resulting coverage for this method is shown in Figure 3.12a. If it can be assumed that the object function is real valued then the symmetry of Fourier transform for real valued functions can be used to obtain the coverage in Figure 3.12b.

3.4.3 Broadband Illumination

It is also possible to perform an experiment for broadband illumination [Ken82]. Up until this point only narrow band illumination has been considered; wherein the field at each point can be completely described by its complex amplitude.

Now consider a transducer that illuminates an object with a wave of the form $a_t(k_x, t)$. Taking the Fourier transform in the time domain this wave can be decomposed into a number of experiments. Let

$$A_t(k_x, \omega) = \int_{-\infty}^{\infty} a_t(k_x, t) e^{-j\omega t} dt \quad (3.42)$$

where ω is related to k_ω by

$$k_\omega = \frac{c}{\omega}, \quad (3.43)$$

c is the speed of propagation in the media and the wavevector (k_x, k_y) satisfies the wave equation

$$k_x^2 + k_y^2 = k_\omega^2. \quad (3.44)$$

If a plane wave illumination of spatial frequency k_x and a temporal frequency ω leads to the scattered field $u_s(k_x, \omega; y)$ then the total scattered field is given by a weighted superposition of the scattered fields or

$$u_s(k_x; y) = \int_{-\infty}^{\infty} A_t(k_x, \omega) u_s(k_x, \omega; y) d\omega. \quad (3.45)$$

For plane wave incidence the coverage for this method is shown in Figure 3.13a. Figure 3.13b shows that by doing four experiments at 0, 90, 180 and 270 degrees it is possible to gather information about the entire object.

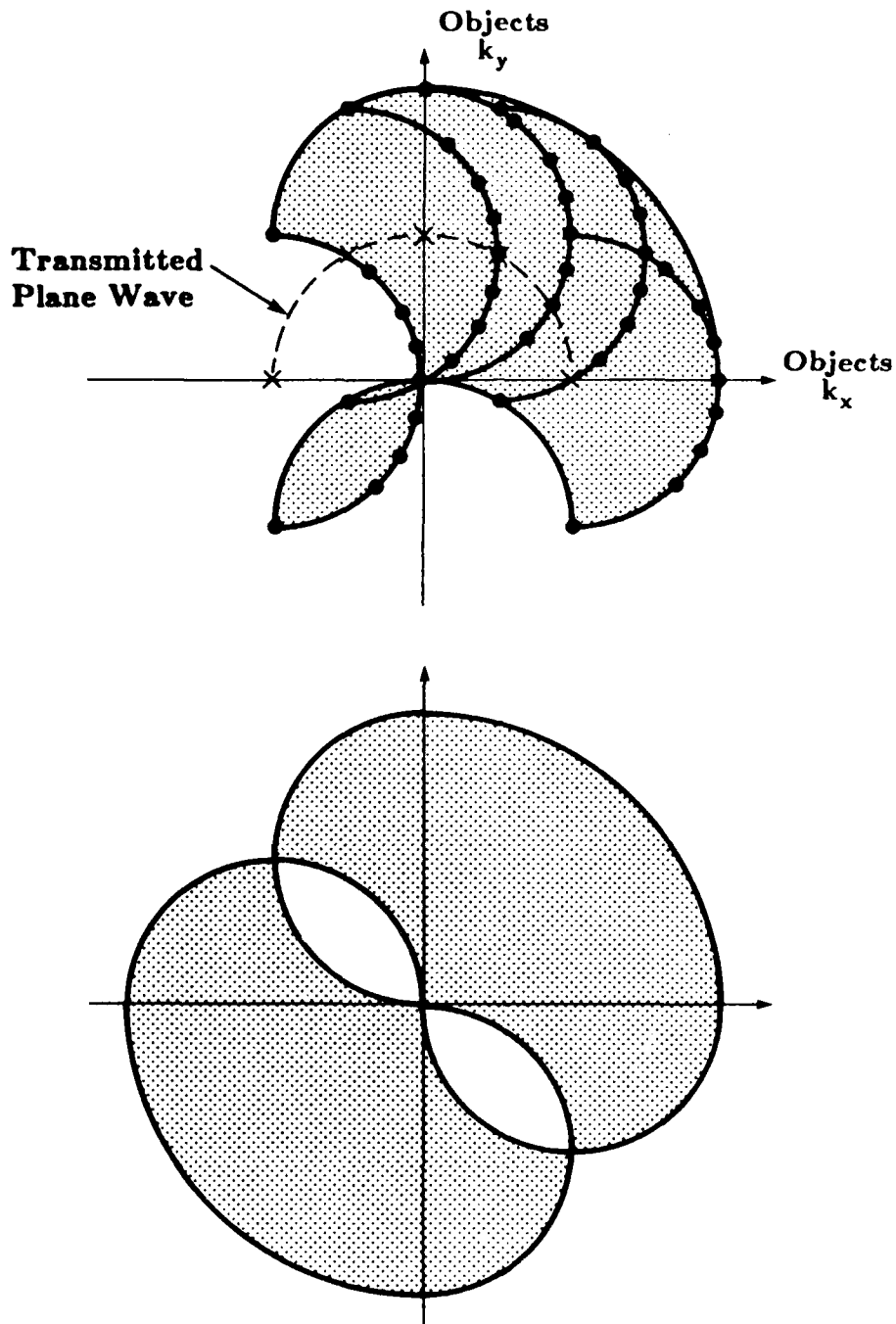


Figure 3.12

Estimate of the Fourier transform of an object are available in the shaded region for a VSP experiment (a). If, in addition, the object is real valued then the symmetry of the Fourier transform can be used to get the coverage shown in (b).

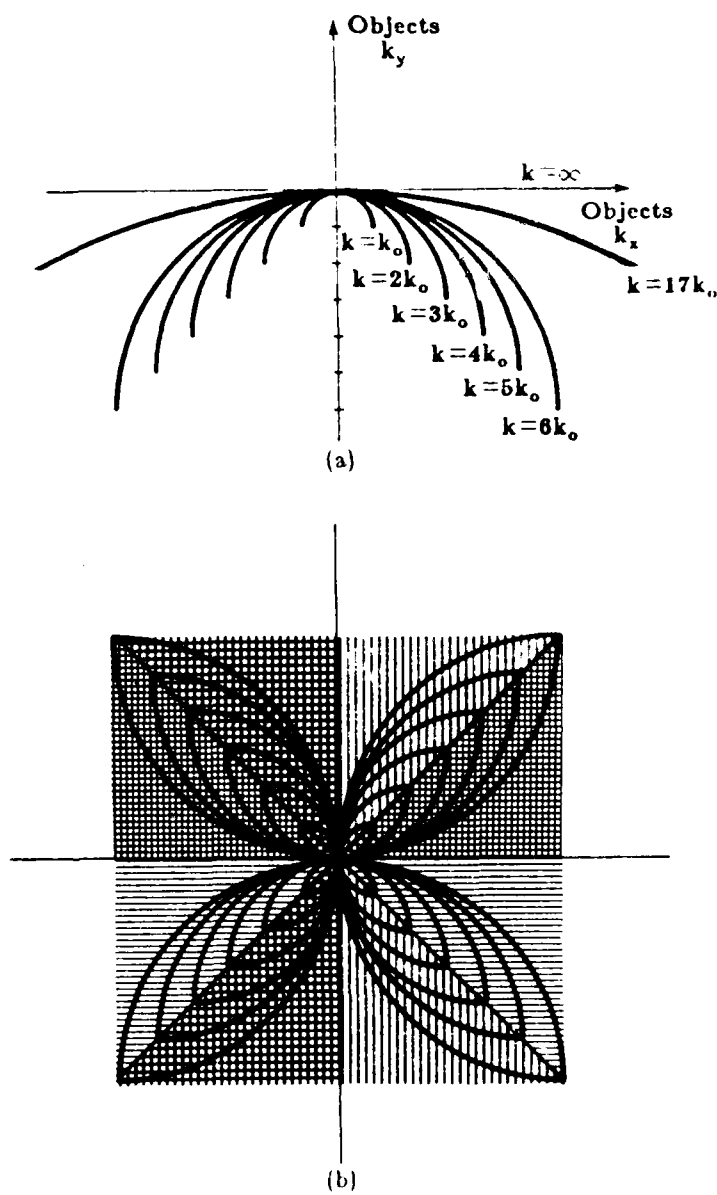


Figure 3.13

One view of a broadband diffraction tomography experiment will generate estimates of the object along the arcs in (a). With four views of the object complete coverage can be obtained as shown in (b).

References

- [Car70] William H. Carter, "Computational reconstruction of scattering objects from holograms," *Journal of the Optical Society of America*, Vol. 60, March 1970, pp. 306-314.
- [Car74] W. H. Carter and P. C. Ho, "Reconstruction of inhomogeneous scattering objects from holograms," *Applied Optics*, Vol. 13, January 1974, pp. 162-172.
- [Car76] P. L. Carson, T. V. Oughton, and W. R. Hendee, "Ultrasound transaxial tomography by reconstruction," in *Ultrasound in Medicine II*, D. N. White and R. W. Barnes, eds., Plenum Press, 1976, pp. 391-400.
- [Dev82] A. J. Devaney, "A filtered backpropagation algorithm for diffraction tomography," *Ultrasonic Imaging*, Vol. 4, 1982, pp. 336-350.
- [Dev84] A. J. Devaney, "Geophysical diffraction tomography," *IEEE Transaction Geological Science, Special Issue on Remote Sensing*, Vol. GE-22, January 1984, pp. 3-13.
- [Goo68] J. W. Goodman, *Introduction to Fourier Optics*, McGraw Hill Book Company, San Francisco, 1968.
- [Gre78] J. F. Greenleaf, S. K. Kenue, B. Rajagopalan, R. C. Bahn, and S. A. Johnson, "Breast imaging by ultrasonic computer-assisted tomography," in *Acoustical Imaging*, A. Metherell, ed., Plenum Press, 1978.
- [Kak84] A. C. Kak, "Tomographic imaging with diffracting and non-diffracting sources," in *Array Processing Systems*, Simon Haykin, ed., Prentice Hall, 1984.
- [Kav82] M. Kaveh, M. Soumekh, and R. K. Mueller, "Tomographic imaging via wave equation inversion," *ICASSP 82*, May 1982, pp. 1553-1556.
- [Ken82] S. K. Kenue and J. F. Greenleaf, "Limited angle multifrequency diffraction tomography," *IEEE Transactions on Sonics and Ultrasonics*, Vol. SU-29, July 1982, pp. 213-217.

- [LuZ84] Z. Q. Lu, M. Kaveh, and R. K. Mueller, "Diffraction tomography using beam waves: Z-average reconstruction," *Ultrasonic Imaging*, Vol. 6, January 1984, pp. 95-102.
- [Mor53] Philip M. Morse and Herman Feshbach, *Methods of Theoretical Physics*, McGraw Hill Book Company, New York, 1953.
- [Mue79] R. K. Mueller, M. Kaveh, and G. Wade, "Reconstructive tomography and applications to ultrasonics," *Proceedings of the IEEE*, Vol. 67, 1979, pp. 567-587.
- [Nah82] D. Nahamoo and A. C. Kak, *Ultrasonic diffraction imaging*, TR-EE 82-20, School of Electrical Engineering, Purdue University, 1982.
- [Nah84] D. Nahamoo, S. X. Pan, and A. C. Kak, "Synthetic aperture diffraction tomography and its interpolation-free computer implementation," *IEEE Transactions on Sonics and Ultrasonics*, Vol. SU-31, July 1984, pp. 218-229.
- [Wol69] E. Wolf, "Three-dimensional structure determination of semi-transparent objects from holographic data," *Optics Communications*, Vol. 1, 1969, pp. 153-156.

CHAPTER 4

RECONSTRUCTION PROCEDURES

4.1 Introduction

The Fourier Diffraction Theorem as derived in Chapter 3 shows that when an object is illuminated with a plane wave traveling in the positive y -direction, the Fourier transform of the forward scattered fields gives values of the object's Fourier transform on an arc. Therefore, if an object is illuminated from many different directions it is possible, in principle, to fill up a disc of diameter $\sqrt{2}k$ in the frequency domain with samples of the Fourier transform of the object and then reconstruct the object by direct Fourier inversion. Therefore, diffraction tomography, using forward scattered data only, determines the object up to a maximum angular spatial frequency of $\sqrt{2}k$. To this extent, the reconstructed object is a low pass version of the original. In practice, the loss of resolution caused by this bandlimiting is negligible, being more influenced by considerations such as the aperture sizes of the transmitting and receiving elements, etc.

The fact that the frequency domain samples are available over circular arcs, whereas for convenient display it is desired to have samples over a rectangular lattice, is a source of computational difficulty in reconstruction algorithms for diffracting tomography. It should also be clear that by illuminating the object over 360° , a *double* coverage of the frequency domain is generated; note, however, that this double coverage is uniform. If the illumination is restricted to a portion of 360° there still will be a complete coverage of the frequency domain, however in that case there would be patches in the (ω_1, ω_2) -plane where there would be a double coverage. In reconstructing from circular arc grids to rectangular grids, it is often easier to contend with a uniform double coverage, as opposed to a coverage that is single in most areas and double in patches.

However, for some applications not given to data collection from all possible directions, it is useful to bear in mind that it is not necessary to go completely around an object to get complete coverage of the frequency domain. In principle, it should be possible to get an equal quality reconstruction when

illumination angles are restricted to a 180° plus interval, the angles in excess of 180° being required to complete the coverage of the frequency domain.

There are two computational strategies for reconstructing the object given measurements of the scattered field. As pointed out by [Sou84a] the two algorithms can be considered as interpolation in the frequency domain and in the space domain and are analogous to the direct Fourier inversion and backprojection algorithms of conventional tomography. Unlike conventional tomography, where backprojection is the preferred approach, the computational expense of space domain interpolation of diffracted projections makes frequency domain interpolation the preferred approach.

The remainder of this section will consist of derivations of the frequency domain and space domain interpolation algorithms. In both cases plane wave illumination will be assumed and the reader is referred to [Dev82, Pan83] for reconstruction algorithms for the synthetic aperture approach and to [Sou84b] for the general case.

4.2 Frequency Domain Interpolation

In order to discuss the frequency domain interpolation between a circular grid on which the data is generated by diffraction tomography, and a rectangular grid suitable for image reconstruction, parameters for representing each grid must be selected and then the relationship between the two sets of parameters written.

In Chapter 3, $U_B(\omega)$ was used to denote the Fourier transform of the transmitted data when an object is illuminated with a plane wave traveling along the positive y direction. Now $U_{B,\phi}(\omega)$ is used to denote this Fourier transform, where the subscript ϕ indicates the angle of illumination. This angle is measured as shown in Figure 4.1. Similarly, $Q(\omega, \phi)$ will be used to indicate the values of $o(\omega_1, \omega_2)$ along a semi-circular arc oriented at an angle ϕ as shown in Figure 4.2 or

$$Q(\omega, \sqrt{k_0^2 - \omega^2} - k_0) \quad |\omega| < k_0. \quad (4.1)$$

Therefore, when an illuminating plane wave is incident at angle ϕ , the equality

$$U_B(\alpha, l_0) = \frac{j}{2\sqrt{k_0^2 - \alpha^2}} e^{j\sqrt{k_0^2 - \alpha^2} l_0} O(\alpha, \sqrt{k_0^2 - \alpha^2} - k_0) \quad (4.2)$$

can be rewritten as

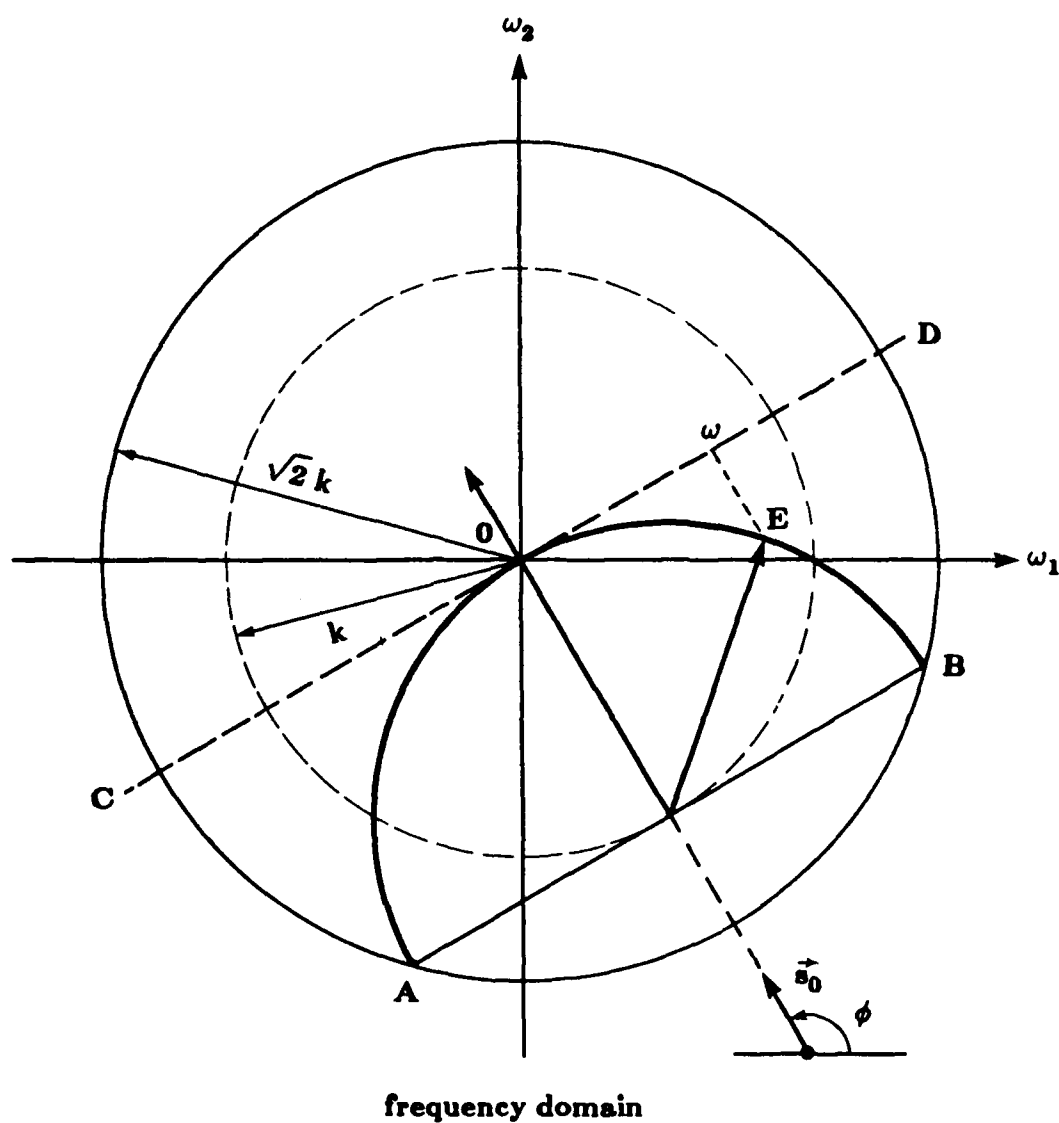


Figure 4.1

Each projection is measured using the phi-omega coordinate system shown here.

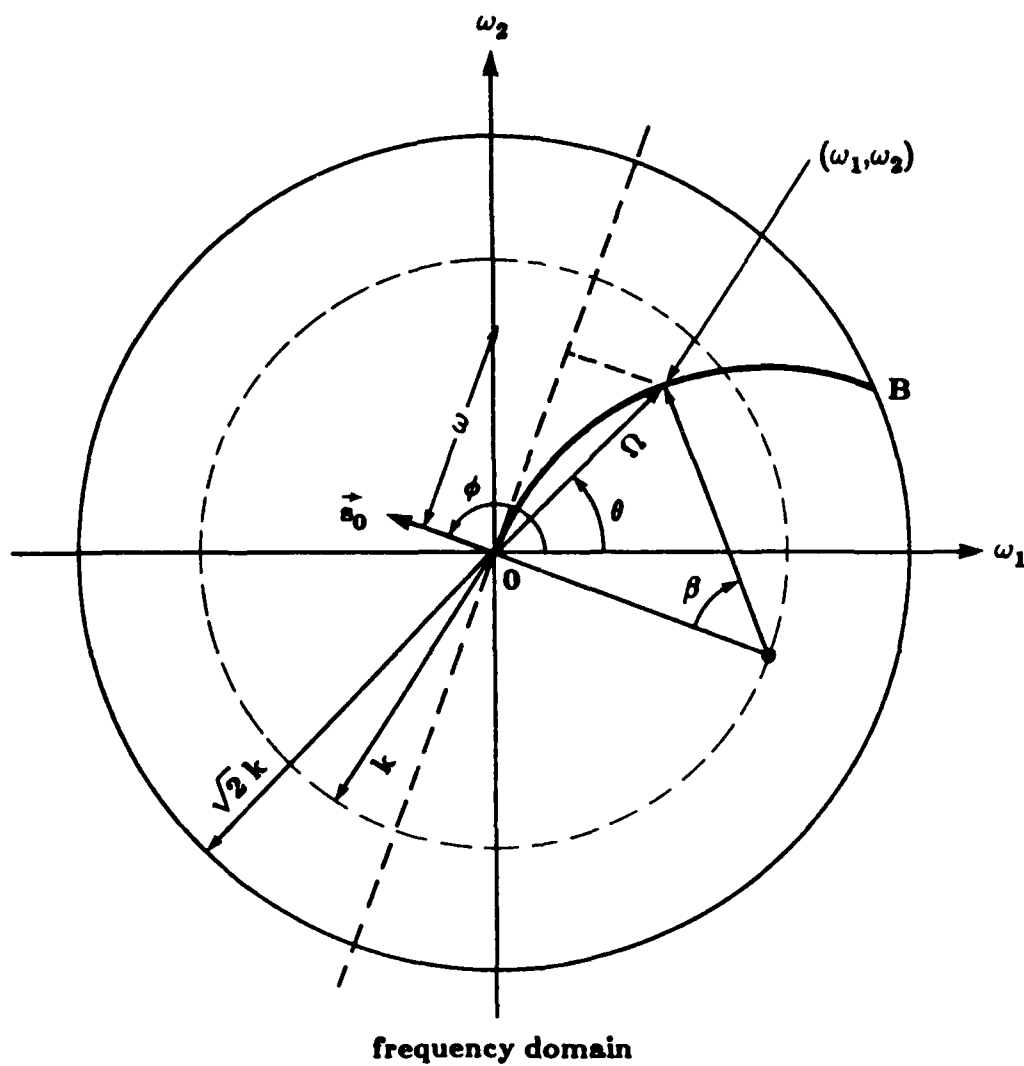


Figure 4.2

A second change of variables is used to relate the projection data to the object's Fourier transform.

$$u_{B,\phi}(\omega) = \frac{j}{2} \frac{1}{\sqrt{k^2 - \omega^2}} \exp \left[j\ell \sqrt{k^2 - \omega^2} \right] Q(\omega, \phi) \quad \text{for } |\omega| < k. \quad (4.3)$$

In most cases the transmitted data will be uniformly sampled in space, and a *discrete* Fourier transform of this data will generate uniformly spaced samples of $U_{B,\phi}(\omega)$ in the ω domain. Since $Q(\omega)$ is the Fourier transform of the object along the circular arc AOB in Figure 4.1 and since κ is the projection of a point on the circular arc on the tangent line CD, the uniform samples of Q in κ translate into non-uniform samples along the arc AOB as shown in Figure 4.3. For this reason designate each point on the arc AOB by its (ω, ϕ) parameters. [Note that (ω, ϕ) are *not* the polar coordinates of a point on arc AOB in Figure 4.2. Therefore, ω is *not* the radial distance in the (ω_1, ω_2) plane. For point E shown, the parameter ω is obtained by projecting E onto line CD.] The rectangular coordinates in the frequency domain will remain (ω_1, ω_2) .

Before the relationships between (ω, ϕ) and (ω_1, ω_2) , is presented it must be mentioned that the points generated by the AO and OB portions of the arc AOB must be considered separately as ϕ is varied from 0 to 2π . This is done because as mentioned before, the arc AOB generates a double coverage of the frequency domain, as ϕ is varied from 0 to 2π , which is undesirable for discussing a one-to-one transformation between the (ω, ϕ) parameters and the (ω_1, ω_2) coordinates.

Now reserve (ω, ϕ) parameters to denote the arc grid generated by one projection. It is important to note that for this arc grid, ω varies from 0 to k and ϕ from 0 to 2π .

The transformation equations between (ω, ϕ) and (ω_1, ω_2) will now be presented. This is accomplished in a slightly round-about manner by first defining polar coordinates (Ω, θ) in the (ω_1, ω_2) -plane as shown in Figure 4.2. In order to go from (ω_1, ω_2) to (ω, ϕ) , first transform from the former coordinates to (Ω, θ) and then from (Ω, θ) to (ω, ϕ) . The rectangular coordinates (ω_1, ω_2) are related to the polar coordinates (Ω, θ) by (Figure 4.2)

$$\Omega = \sqrt{\omega_1^2 + \omega_2^2} \quad (4.4)$$

$$\theta = \tan^{-1} \left(\frac{\omega_2}{\omega_1} \right) \quad (4.5)$$

In order to relate (Ω, θ) to (ω, ϕ) , a new angle β , which is the angular position of a point (ω_1, ω_2) on arc OB in Figure 4.2, is introduced. Note from the figure that the point characterized by angle β is also characterized by parameter ω .

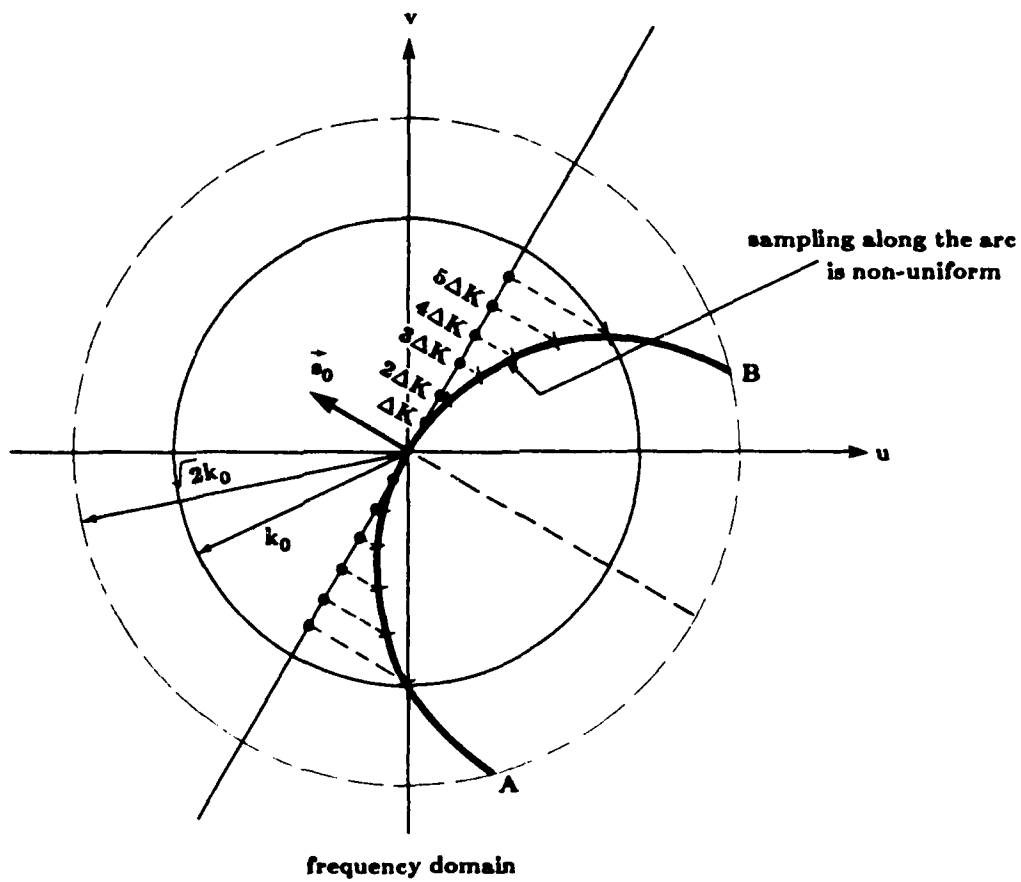


Figure 4.3

Uniformly sampling the projection in the space domain leads to uneven spacing of the samples of the Fourier transform of the object along the semi-circular arc.

The relationship between ω and β is given by

$$\omega = k \sin \beta. \quad (4.4)$$

The following relationship exists between the polar coordinates (Ω, θ) on the one hand and the parameters β and ϕ on the other:

$$\beta = 2 \sin^{-1} \frac{\Omega}{2k} \quad (4.6)$$

$$\phi = \theta + \frac{\pi}{2} + \frac{\beta}{2}. \quad (4.7)$$

By substituting Equation (4.6) in (4.4) and then using (4.4), ω can be expressed in terms of ω_1 and ω_2 . This result is shown below. Similarly, by substituting Equation (4.5) in (4.7), the following expression is obtained for ω and ϕ

$$\omega = \sin \left\{ 2 \sin^{-1} \left[\frac{\sqrt{\omega_1^2 + \omega_2^2}}{2k} \right] \right\} \quad (4.8)$$

$$\phi = \tan^{-1} \left[\frac{\omega_2}{\omega_1} \right] + \sin^{-1} \left[\frac{\sqrt{\omega_1^2 + \omega_2^2}}{2k} \right] + \frac{\pi}{2}. \quad (4.9)$$

These are the transformation equations for interpolating from the (ω, ϕ) parameters used for data representation to the (ω_1, ω_2) parameters needed for inverse transformation.

To convert a particular rectangular point into (ω, ϕ) domain, substitute its ω_1 and ω_2 values in Equations (4.8) and (4.9). The resulting values for ω and ϕ may not correspond to any for which $Q(\omega, \phi)$ is known. By virtue of equation (4.3), $Q(\omega, \phi)$ will only be known over a uniformly sampled set of values for ω and ϕ . In order to determine Q at the calculated ω and ϕ , the following procedure is used. Given $N_\omega \times N_\phi$ uniformly located samples, $Q(\omega_i, \phi_j)$, calculate a bilinearly interpolated value of this function at the desired ω and ϕ by using

$$Q(\omega, \phi) = \sum_{i=1}^{N_\omega} \sum_{j=1}^{N_\phi} Q(\omega_i, \phi_j) h_1(\omega - \omega_i) h_2(\phi - \phi_j), \quad (4.10)$$

where

$$h_1(\omega) = \begin{cases} 1 - \frac{|\omega|}{\Delta\omega} & 0 \\ |\omega| \leq \Delta\omega & \text{otherwise,} \end{cases} \quad (4.11)$$

$$h_2(\phi) = \begin{cases} 1 - \frac{|\phi|}{\Delta\phi} & 0 \\ |\phi| \leq \Delta\phi & \text{otherwise;} \end{cases} \quad (4.12)$$

$\Delta\phi$ and $\Delta\omega$ are the sampling intervals for ϕ and ω , respectively. When expressed in the manner shown above, bilinear interpolation may be interpreted as the output of a filter whose impulse response is $h_1 h_2$.

The results obtained with bilinear interpolation can be considerably improved if the sampling density in the (ω, ϕ) -plane is increased by using the computationally efficient method of zero-extending the inverse two-dimensional inverse *Fast Fourier Transform* (FFT) of the $Q(\omega_i, \phi_j)$ matrix. The technique consists of first taking a two-dimensional inverse FFT of the $N_\omega \times N_\phi$ matrix consisting of the $Q(\omega_i, \phi_j)$ values, zero-extending the resulting $N_\omega \times N_\phi$ array of numbers to, perhaps, $mN_\omega \times nN_\phi$ and then taking the FFT of this new array. The result is an mn -fold increase in the density of samples in the (ω, ϕ) -plane. After computing $Q(\omega, \phi)$ at each point of a rectangular grid by the procedure outlined above, the object $f(x, y)$ is obtained by a simple 2-D inverse FFT.

The use of bilinear interpolation and zero padding are both good techniques for resampling a function but they are used here in a non standard way. Typically interpolation algorithms are derived assuming that the sampled data can be described as nearly linear (when using bilinear interpolation) and frequency limited (when using Fourier domain zero padding) [Con80, Sto80, Act70]. In this application, when resampling the data from a circular grid to a rectangular grid, the function is assumed to be smooth in the Fourier domain. This assumption is reasonable since the data is assumed to be well behaved.

The interpolation described above, however, is carried out in a rectilinear version of the (ω, ϕ) coordinate system. Thus four points in the (ω, ϕ) space, where data is available, are first assumed to be at the four corners of a rectangle and then the interpolation is calculated for a point in the middle. This is an approximation because the four data points actually define a smooth function that is defined along four points on two of the circular arcs. As will be seen in the reconstructions the effect of this approximation is small but it should be remembered when comparing interpolation schemes.

4.3 Backpropagation Algorithms

It has recently been shown by Devaney [Dev82] and Kaveh [Kav82] that there is an alternative method for reconstructing images from the diffracted projection data. This procedure, called the *filtered-backpropagation method*, is similar in spirit to the filtered-backprojection techniques which (due to their superior numerical accuracy) have been one factor in the enormous success of x-ray tomography. Unfortunately, whereas the filtered-backprojection algorithms also possess efficient implementations, the same cannot be said for the filtered-backpropagation algorithms. The latter class of algorithms is computationally intensive, much more so than the interpolation procedure discussed above. With regard to accuracy, they do not seem to possess any advantage especially if interpolation is carried out after increasing the sampling density by appropriate zero-padding as discussed above.

The derivation of the backpropagation algorithm will follow as presented by Devaney [Dev82]. First consider the inverse Fourier transform of the object function,

$$o(rv) = \frac{1}{(2\pi)^2} \int_{-\infty}^{\infty} \int_{-\infty}^{\infty} O(\vec{K}) e^{i\vec{K} \cdot rv} d\vec{K}. \quad (4.13)$$

This integral represents the object function in terms of the Fourier transform of the object along a rectangular grid. As already discussed, a diffraction tomography experiment measures the Fourier transform of the object along circular arcs; thus it will be easier to perform the integration if it is modified to use the projection data more naturally. This will be done using two coordinate transformations: the first one will exchange the rectangular grid for a set of semicircular arcs and the second will map the arcs into their plane wave decomposition.

First exchange the rectangular grid for semi-circular arcs. To do this represent $\vec{K}=(k_x, k_y)$ in equation (4.13) by the vector sum

$$\vec{K} = k_0(\vec{s}-\vec{s}_0) \quad (4.14)$$

where $\vec{s}_0=(\cos\phi_0, \sin\phi_0)$ and $\vec{s}=(\cos\chi, \sin\chi)$ are unit vectors representing the direction of the wavevector for the transmitted and the received plane waves respectively. This coordinate transformation is illustrated in figure 4.4.

To find the Jacobian of this transformation write

$$k_x = k_0(\cos\chi - \cos\phi_0) \quad (4.15)$$

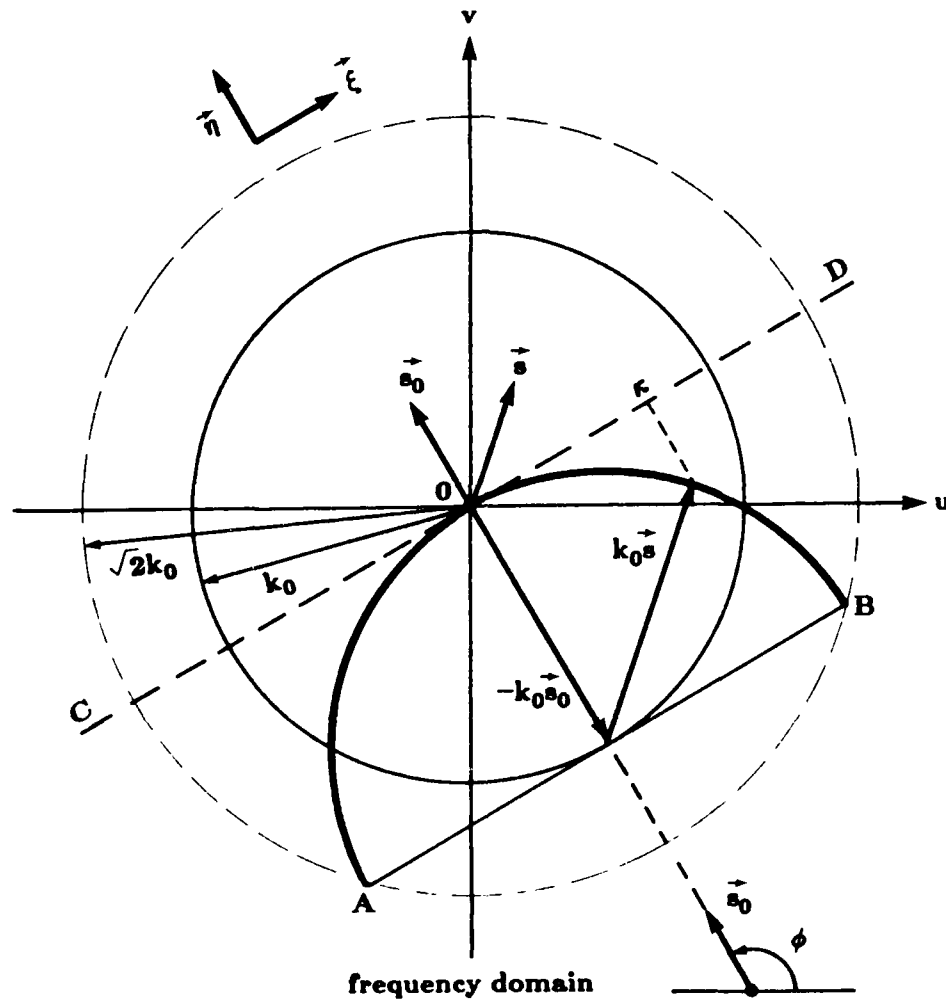


Figure 4.4

The $k_0 \vec{s}_0$ and $k \vec{s}_0$ used in the backpropagation algorithm are shown here.

$$k_y = k_0(\sin\chi - \sin\phi_0) \quad (4.16)$$

and

$$dk_x dk_y = |k_0^2 \sin(\chi - \phi_0)| d\chi d\phi_0 \quad (4.17)$$

$$= k_0 \sqrt{1 - \cos^2(\chi - \phi_0)} d\chi d\phi_0 \quad (4.18)$$

$$= k_0 \sqrt{1 - (\vec{s} \cdot \vec{s}_0)^2} d\chi d\phi_0 \quad (4.19)$$

and then equation (4.13) becomes

$$o(rv) = \frac{1}{(2\pi)^2} \left(\frac{1}{2}\right) k_0^2 \int_0^{2\pi} \int_0^{2\pi} \sqrt{1 - (\vec{s} \cdot \vec{s}_0)^2} O[k_0(\vec{s} - \vec{s}_0)] e^{jk_0(\vec{s} - \vec{s}_0) \cdot rv} d\chi d\phi_0. \quad (4.20)$$

The factor of $\frac{1}{2}$ is necessary because as discussed in section 4.2 the (χ, ϕ_0) coordinate system gives a double coverage of the (k_x, k_y) space.

This integral gives an expression for the scattered field as a function of the (χ, ϕ_0) coordinate system. While the data that is collected will actually be a function of ϕ_0 , the projection angle, and κ , the one dimensional frequency of the scattered field along the receiver line. To make the final coordinate transformation take the angle χ to be relative to the (κ, γ) coordinate system diagramed in Figure 4.4. This is a more natural representation since the data available in a diffraction tomography experiment lies on a semicircle and therefore the data is available only for $0 \leq \chi \leq \pi$. The χ integral in equation (4.20) above can be rewritten by noting

$$\cos\chi = \kappa/k_0 \quad (4.21)$$

$$\sin\chi = \gamma/k_0 \quad (4.22)$$

and therefore

$$d\chi = \frac{-1}{k_0\gamma} d\kappa. \quad (4.23)$$

The χ integral becomes

$$\frac{1}{k_0} \int_{-k_0}^{k_0} \frac{d\kappa}{\gamma} |\kappa| O[k_0(\vec{s} - \vec{s}_0)] e^{jk_0(\vec{s} - \vec{s}_0) \cdot rv} d\kappa. \quad (4.24)$$

Using the Fourier Diffraction Theorem as represented by equation (4.2) the Fourier transform of the object function, O , can be approximated by a simple function of the first order Born field, u_B , at the receiver line. Thus the object

function in equation (4.24) can be written

$$O\left[k_0(\vec{s}-\vec{s}_0)\right] = -2\gamma j U_B(\kappa, \gamma-k_0) e^{-j\gamma l_0}. \quad (4.25)$$

In addition if a rotated coordinate system is used for $r = (\xi, \eta)$ where

$$\xi = x \sin \phi - y \cos \phi \quad (4.26)$$

and

$$\eta = x \cos \phi + y \sin \phi \quad (4.27)$$

then the dot product $k_0(\vec{s}-\vec{s}_0)$ can be written

$$\kappa \xi + (\gamma - k_0) \eta. \quad (4.28)$$

The coordinates (ξ, η) are illustrated in Figure 4.5. Using the results above the χ integral is now written as

$$\frac{2j}{k_0} \int_{-k_0}^{k_0} d\kappa |\kappa| U_B(\kappa, \gamma - k_0) e^{-j\gamma l_0} e^{\kappa \xi + (\gamma - k_0) \eta} \quad (4.29)$$

and the equation for the object function in equation (4.20) becomes

$$o(rv) = \frac{jk_0}{(2\pi)^2} \int_0^{2\pi} d\phi_0 \int_{-k_0}^{k_0} d\kappa |\kappa| U_B(\kappa, \gamma - k_0) e^{-j\gamma l_0} e^{j\kappa \xi + j(\gamma - k_0) \eta}. \quad (4.30)$$

To bring out the filtered-backpropagation implementation, the inner integration is written here separately:

$$\Pi_\phi(\xi, \eta) = \frac{1}{2\pi} \int_{-\infty}^{\infty} \Gamma_\phi(\omega) H(\omega) G_\eta(\omega) \exp(j\omega \xi) d\omega \quad (4.31)$$

where

$$\begin{aligned} H(\omega) &= |\omega|, & |\omega| &\leq k_0 \\ &= 0, & |\omega| &> k_0 \\ G_\eta(\omega) &= \exp\left[j(\sqrt{k_0^2 - \omega^2} - k_0)\right], & |\omega| &\leq k_0 \\ &= 0, & |\omega| &> k_0 \end{aligned} \quad (4.32)$$

and

$$\Gamma_\phi(\omega) = U_B(\kappa, \gamma - k_0) e^{-j\gamma l_0}. \quad (4.33)$$

Without the extra filter function $G_\eta(\omega)$, the rest of Equation (4.31) would correspond to the filtering operation of the projection data in x-ray tomography. The filtering as called for by the transfer function $G_\eta(\omega)$ is depth

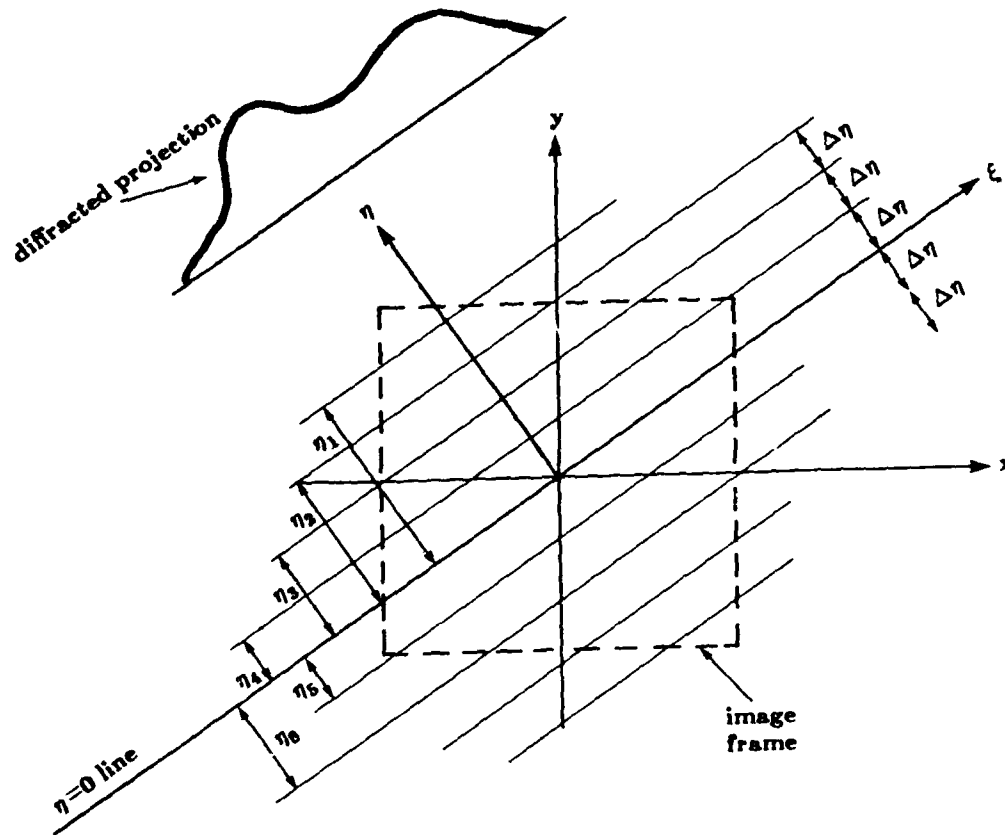


Figure 4.5

In backpropagation the project is backprojected with a depth dependent filter function. At each depth, η , the filter corresponds to propagating the field at a distance of $\Delta\eta$.

dependent due to the parameter η , which is equal to $x\cos\phi + y\sin\phi$.

In terms of the filtered projections $\Pi_\phi(\xi, \eta)$ in Equation (4.31), the reconstruction integral of Equation (4.30) may be expressed as

$$f(x, y) = \frac{1}{2\pi} \int_0^{2\pi} d\phi \Pi_\phi(x\sin\phi - y\cos\phi, x\cos\phi + y\sin\phi) \quad (4.34)$$

The computational procedure for reconstructing an image on the basis of Equations (4.31) and (4.34) may be presented in the form of the following steps:

- STEP 1: In accordance with Equation (4.31), filter each projection with a separate filter for each depth in the image frame. For example, if only 9 depths are used as shown in Figure 4.5, 9 different filters would need to be applied to the diffracted projection shown there. [In most cases for 128×128 reconstructive, the number of discrete depths chosen for filtering the projection will also be around 128. If there are much less than 128, spatial resolution will be lost.] [Cra79]
- STEP 2: To each pixel (x, y) in the image frame, in accordance with Equation (4.34) allocate a value of the filtered projection that corresponds to the nearest depth line.
- STEP 3: Repeat the preceding 2 steps for all projections. As a new projection is taken up, add its contribution to the current sum at pixel (x, y) .

The depth dependent filtering in Step 1 makes this algorithm computationally very demanding. For example, if N_η depth values are used, the processing of each projection will take $(N_\eta + 1)$ Fast Fourier Transforms (FFT's). If the total number of projections is N_ϕ , this translates into $(N_\eta + 1)N_\phi$ FFT's. For most $N \times N$ reconstructions, both N_η and N_ϕ will be approximately equal to N . Therefore, the filtered-backpropagation algorithm will require approximately N^2 FFT's compared to $4N$ FFT's for bilinear interpolation. [For precise comparisons, it must be mentioned that the FFT's for the case of bilinear interpolation are longer due to zero-padding.]

Devaney [Dev82] has also proposed a modified filtered-backpropagation algorithm, in which $G_\eta(\omega)$ is simply replaced by a single $G_{\eta_0}(\omega)$ where $\eta_0 = x_0\cos\phi + y_0\sin\phi$, (x_0, y_0) being the coordinates of the point where local accuracy in reconstruction is desired. [Elimination of depth dependent filtering reduces the number of FFT's to $2N_\phi$.]

4.4 Signal Processing Concerns

The reconstruction algorithms described above and in [Pan83] involve a number of signal processing steps. The following work describes the quality of the final reconstruction when small changes are made to the signal processing procedure. These changes are valid for reconstruction algorithms using either space (backpropagation) or frequency domain interpolation.

Assuming first order approximations are valid, the algorithm for reconstructing an object from diffracted projections is briefly as follows:

- 1) Collect the data
- 2) Fourier Transform each projection
- 3) Estimate the 2-dimensional Fourier transform of the object from the transformed projections
- 4) Perform a 2-dimensional inverse Fourier transform to get an estimate of the object.

At each step of this procedure signal processing theory suggests a number of procedures to improve the reconstruction. These include

- a) Zero padding the projection data to reduce the effects of interperiod interference. This also increases the resolution in the frequency domain and should make interpolation easier.
- b) Applying a Hamming window to the projection data to smooth out the data at the ends of the receiver.
- c) Multiplying the two dimensional Fourier Transform of the object by a Low Pass Filter (LPF) (a Hamming window in this case) to reduce the effects of high frequency noise.

These new steps are illustrated in Figure 4.6 where optional steps have been indicated with dashed boxes. we have indicated the optional steps with dashed boxes.

To evaluate the effects of each of these changes Figure 4.7 and Figure 4.8 shows the center line of reconstructions using all eight possible combinations of options. The data was generated for a cylinder of radius 1λ and a refractive index change of $.5\%$.

An important part of the reconstruction process is filtering the projection data. For efficiency reasons the filter is implemented with an FFT algorithm but these algorithms do not perform an aperiodic convolution like that used in linear systems theory. Instead a filter implemented with FFT's performs circular convolution.

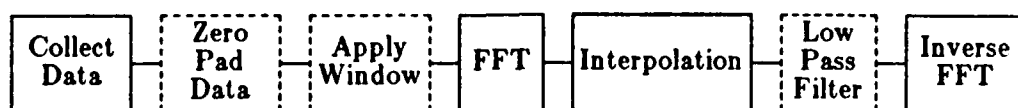


Figure 4.6

The signal processing steps in a typical diffraction tomography algorithm are shown here. The steps that are needed are shown with a solid box while the optional steps are shown with dashed lines.

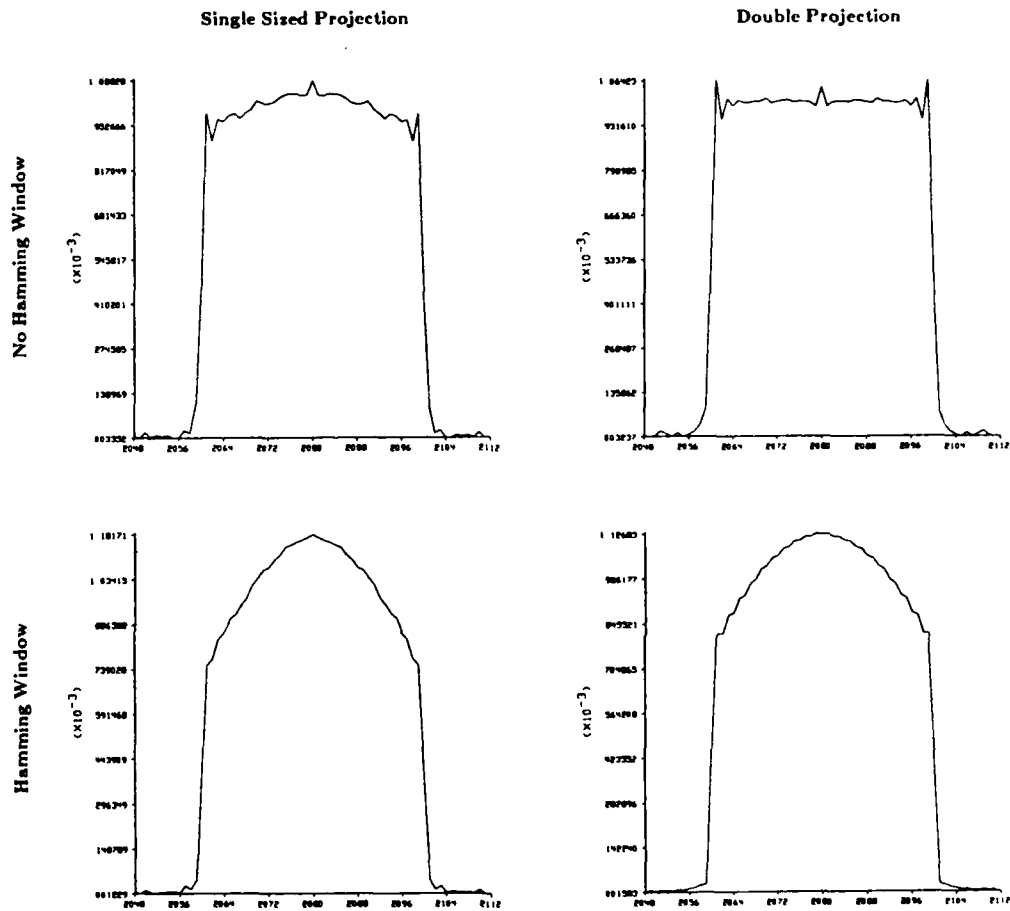


Figure 4.7

The center line of reconstructions are shown here with the size of the projection doubled and the Hamming window added. All reconstruction shown here are without low pass filtering.

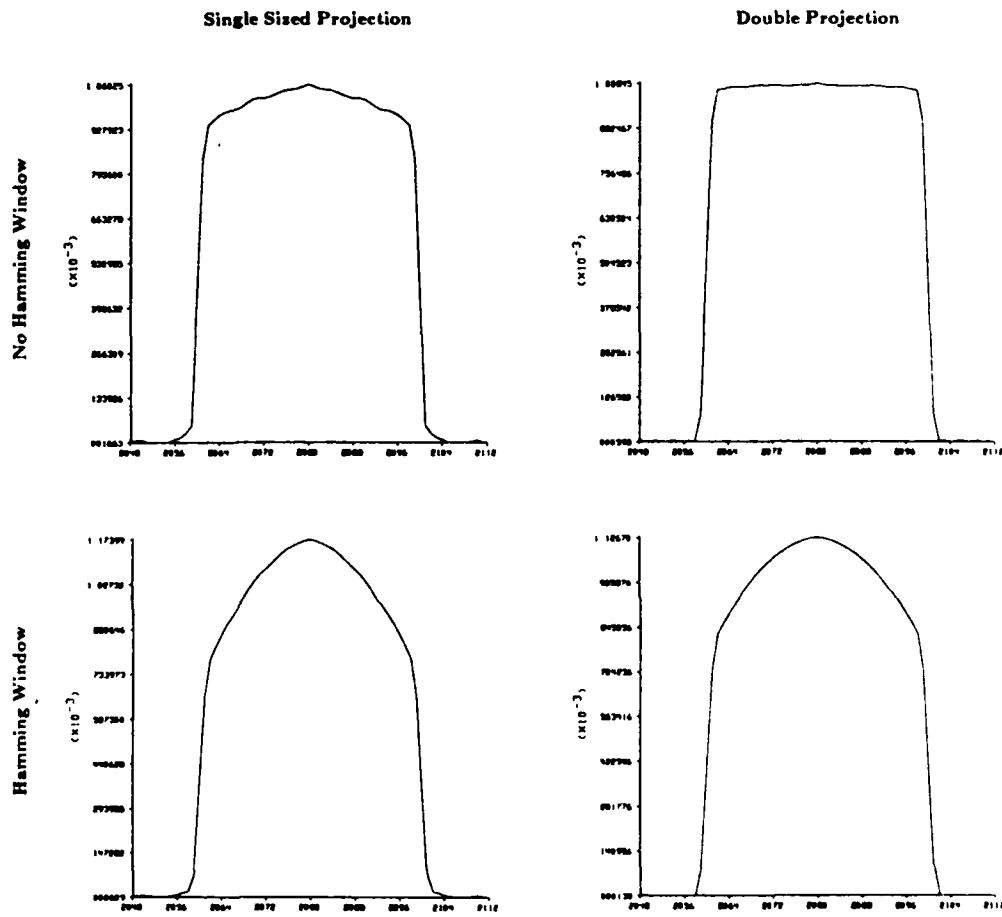


Figure 4.8

The center line of reconstructions are shown here with the size of the projection doubled and the Hamming window added. All reconstruction shown here are with low pass filtering.

If the data is first padded with zeros so that the new data sequence is twice as long as the original then the results produced by circular and aperiodic convolution are the same. In addition, zero padding the original projection increases the resolution of the data in the frequency domain and thus makes a simple interpolation scheme more accurate. Unfortunately the extra data more than doubles the computational time. (For example an FFT takes $N \log N$ operations so when N is doubled the computational expense goes up by a factor of

$$\frac{(2N) \log_2(2N)}{N \log_2 N} = 2 \left[1 + \frac{2}{\log_2 N} \right] \quad (4.35)$$

Based on the reconstructions shown in Figure 4.7 it is possible to conclude that doubling the size of the projection data only makes a small improvement in the quality of the reconstructions. Since the extra zeros more than double the computational expense involved in filtering the data it is probably best not to zero pad.

A second signal processing concern is due to data truncation. In a real world experiment it is only possible to collect and process a finite amount of data. Generally this isn't a problem since the data eventually goes to zero outside of some range and the data can be truncated without loss of information. This is certainly true, for example, in x-ray CT projections but is not true with diffracted projections. With fields the amplitude decays proportional to $\frac{1}{R}$ and consequently the projection data never goes to zero.

Mathematically the data truncation error can be modeled as a multiplication in the space domain by a rectangular window [Opp75]. In the frequency domain this is equivalent to convolving the data with a sinc function and thus smoothes the frequency domain signal. A number of windows like the Hamming window have been designed to reduce the effects of data truncation.

Figure 4.7 shows that a Hamming window does not have the same positive effect with diffracted projections. In this case most of the high frequency information is at either end of the projection and thus the window only serves to attenuate the high frequency components. This is shown in Figure 4.9 where the Fourier transform of the diffracted projection is shown before (top graph) and after (bottom graph) applying a Hamming window to the projection data. The loss of high frequency data caused by the Hamming window leads to the rounded edges shown in the reconstructions shown in Figure 4.7.

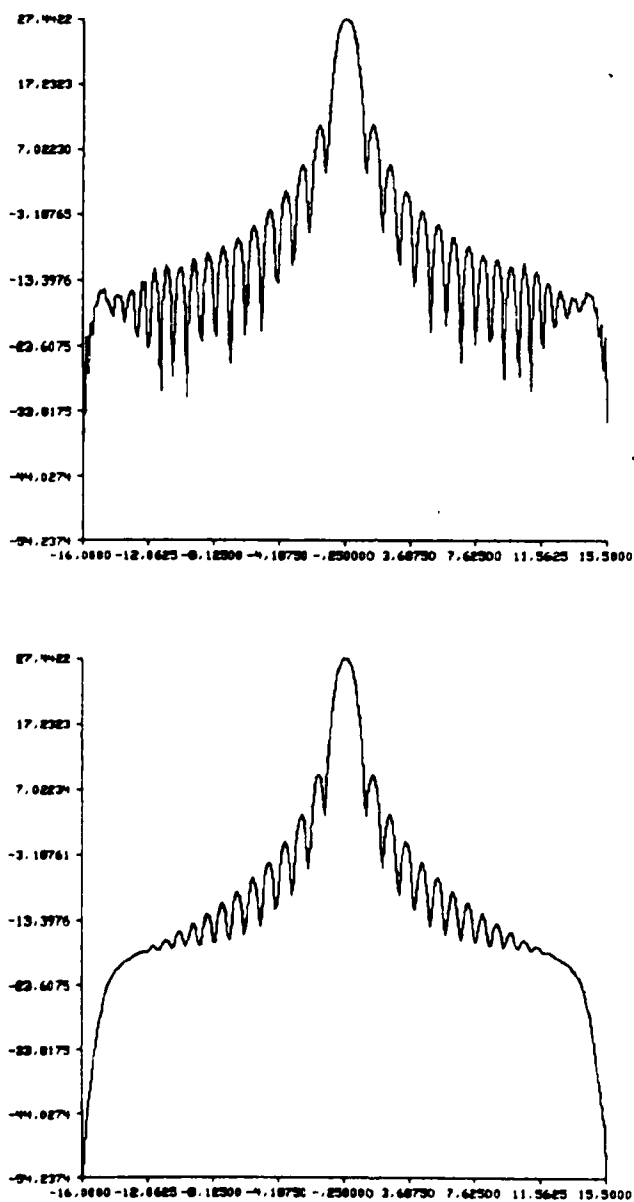


Figure 4.9

The spectrum of the field before (top graph) and after (bottom graph) multiplying by a Hamming window in the space domain are shown here.

Finally a very large improvement is observed by adding a Low Pass Filter before inverse Fourier transforming the data. The filtering done before interpolation includes a $1/k$ term which also serves to enhance the high frequency noise. By adding a LPF this effect is counteracted.

The best results would be obtained if it would be possible to characterize the spectral density of the signal and the noise and then design a Wiener filter. This is a difficult problem and adequate results were obtained by using a Low Pass Filter of the form

$$w(\omega) = 0.54 + 0.46\cos\left(\frac{\omega T}{2}\right) \quad (4.36)$$

Based on the results shown in Figure 4.7 and 4.8 the best reconstructions are obtained if a low pass filter is used to smooth the final reconstruction but that zero padding the projection data and applying a Hamming window to the projection data do not improve the results.

Finally a small improvement was made to the backpropagation algorithm by using bilinear interpolation instead of nearest neighbor. The backpropagation algorithm consists of both a depth dependent filter and then the addition to each pixel of a portion of the backpropagated field. In the original formulation each pixel is assigned the nearest neighbor in the field, but as shown in Figure 4.10 even better results are obtained if the valued added to each pixel is calculated using bilinear interpolation. Compared to the expense of doing the backpropagation filter the bilinear interpolation cost is inconsequential and thus worth the effort.

This is also shown when the Mean Squared Error in the reconstructions is computed. The table below compares the error for bilinear interpolation versus nearest neighbor and bilinear backpropagation. As can be seen from Table 4.1, bilinear interpolation significantly improves the reconstruction.

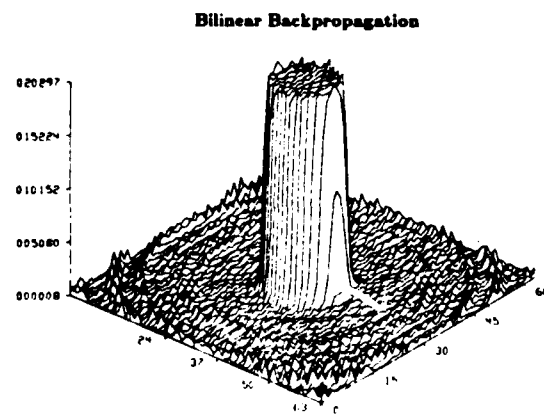
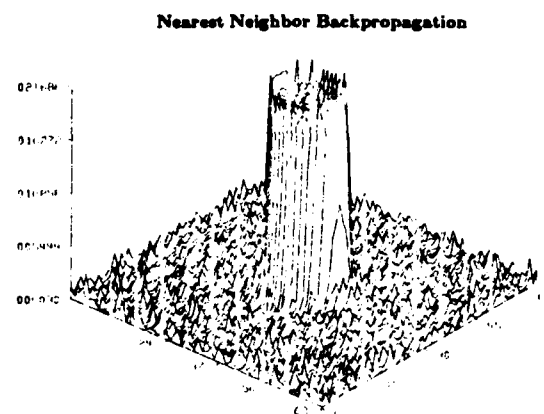
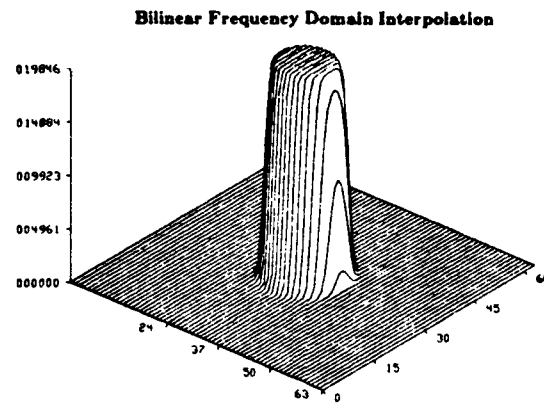


Figure 4.10

Reconstructions of a cylinder are shown comparing nearest neighbor and bilinear interpolation for frequency domain and space domain reconstruction algorithms.

Table 4.1. Mean Squared Error in a reconstruction of a cylinder using three interpolation schemes.

Mean Squared Error	
Bilinear Interpolation	4.8%
Nearest Neighbor Backpropagation	6.8%
Bilinear Backpropagation	4.8%

References

- [Act70] F. S. Acton, *Numerical Methods that Work*, Harper & Row, New York, 1970.
- [Con80] S. D. Conte and C. deBoor, *Elementary Numerical Analysis*, McGraw-Hill, New York, 1980.
- [Cra79] C. R. Crawford and A. C. Kak, "Aliasing artifacts in computerized tomography," *Appl. Opt.*, Vol. 18, 1979, pp. 3704-3711.
- [Dev82] A. J. Devaney, "A filtered backpropagation algorithm for diffraction tomography," *Ultrasonic Imaging*, Vol. 4, 1982, pp. 336-350.
- [Kav82] M. Kaveh, M. Soumekh, and R. K. Mueller, "Tomographic imaging via wave equation inversion," *ICASSP 82*, May 1982, pp. 1553-1556.
- [Opp75] A. V. Oppenheim and R. W. Schaffer, *Digital Signal Processing*, Prentice-Hall, Englewood Cliffs, NJ, 1975.
- [Pan83] S. X. Pan and A. C. Kak, "A computational study of reconstruction algorithms for diffraction tomography: Interpolation vs. filtered-backpropagation," *IEEE Transactions on Acoustics, Speech and Signal Processing*, October 1983, pp. 1262-1275.
- [Sou84a] M. Soumekh, M. Kaveh, and R. K. Mueller, "Fourier domain reconstruction methods with application to diffraction tomography," *Acoustical Imaging*, Vol. 13, 1984, pp. 17-30.
- [Sou84b] M. Soumekh and M. Kaveh, "Image reconstruction from frequency domain data on arbitrary contours," *International Conference on Acoustics, Speech and Signal Processing*, 1984, pp. 12A.2.1 - 12A.2.4.
- [Sto80] Josef Stoer and Roland Bulirsch, *Introduction to Numerical Analysis*, Springer-Verlag, New York, 1980.

CHAPTER 5 LIMITATIONS

5.1 Introduction

The quality of a first order diffraction tomographic reconstruction is limited by both mathematical approximations and experimental limitations. In the derivation of a model for the scattered fields either the Born or the Rytov approximation is used to solve the integral equations for the scattered field. These approximations are a source of error and limit the types of objects that can be imaged with diffraction tomography. The only way to reduce this type of error is to use a better model or a higher order approximation. Better models for the scattered field will be discussed in Chapter 6.

The experimental limitations, on the other hand, are caused by a shortage of data. It is only possible to collect a finite amount of data about the scattered field and the experimental errors can be attributed to interpolation errors, aliasing and the finite aperture. Up to the limit in resolution caused by evanescent waves and the limit in quality due to the Born and the Rytov approximations it is possible to improve a reconstruction by collecting additional data.

Computer simulations are presented in this chapter illustrating the errors in first order diffraction tomography. To study the effects of the Born and the Rytov approximations it is necessary to calculate (or even measure) the exact scattered fields and then use the most accurate reconstruction algorithms available. The experimental errors can be minimized by calculating a large number of data points and using a circularly symmetric object to reduce the errors due to angular sampling. If experimental errors are minimized then the only remaining source of errors are caused by the approximations made in the reconstruction algorithm. As already mentioned the mathematical limitations on the reconstructions are a function of the object's size and refractive index.

The experimental errors are highlighted by minimizing the algorithmic errors. This can be done in two ways. The more straightforward method is to choose a small object with a small change in refractive index. As the size of the object and its refractive index are reduced both the Born and the Rytov

approximations more accurately model the exact scattered field. A second approach is to assume the Born or Rytov approximations are valid then use the Fourier Diffraction Theorem to generate the scattered fields from the Fourier transform of the object. In both cases the amount of data calculated is varied to highlight the different experimental errors.

5.2 Mathematical Limitations

In diffraction tomography there are different approximations involved in the forward and inverse directions. In the forward process it is necessary to assume that the object is weakly scattering so that either the Born or the Rytov approximations can be used. Once an expression for the scattered field is derived it is necessary to not only to measure the scattered fields but then numerically implement the inversion process.

To study the limits of the mathematical approximations the exact field for the scattered field from a cylinder as shown by Weeks [Wee64] and by Morse and Ingard [Mor68] is calculated for cylinders of various sizes and refractive index. In the simulations that follow a single plane wave of unit wavelength is incident on the cylinder and the scattered field is measured along a line at a distance of 100 wavelengths from the origin. In addition all refractive index changes are modeled as monopole (omnidirectional) scatterers. By doing this the directional dependence of dipole scatterers does not have to be taken into account.

At the receiver line the received wave is measured at 512 points spaced at $1/2$ wavelength intervals. In all cases the rotational symmetry of a single cylinder at the origin is used to reduce the computation time of the simulations. Since all projections are identical this eliminates any angular interpolation error.

5.2.1 Evaluation of the Born Approximation

In using the Born approximation it is necessary to assume that the amplitude of the scattered field is small compared to the incident field. As already discussed the Born approximation is most sensitive to phase changes and this will be shown, first qualitatively and then quantitatively. From Chapter 2 the phase change is given by

$$\text{Phase Change} = 4\pi n_{\delta} \frac{a}{\lambda} \quad (5.1)$$

where the cylinder has a radius of 'a' and a refractive index of $1+n_{\delta}$.

AD-A184 923

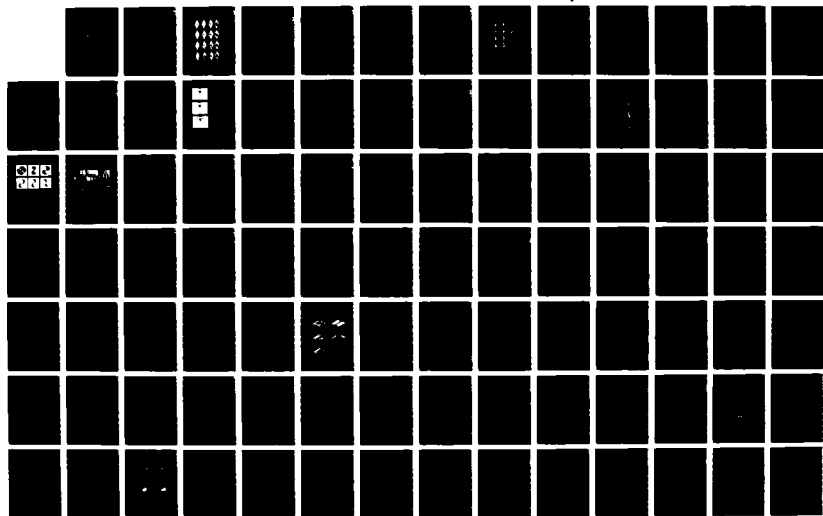
METHODS FOR CORRECTION OF REFRACTIVE ERRORS(U) PURDUE
UNIV LAFAYETTE IN SCHOOL OF ELECTRICAL ENGINEERING
A C KAK 31 DEC 85 DAND17-82-C-2019

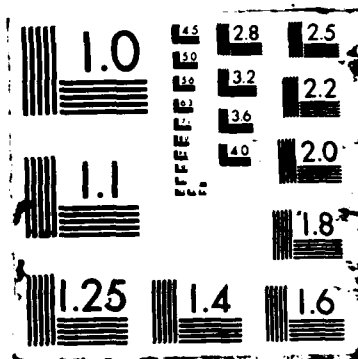
2/3

UNCLASSIFIED

F/G 28/6

NL





The results shown in Figure 5.1 are for cylinders of four different refractive indices. In addition Figure 5.2 shows plots of each reconstruction along a line through the center of the cylinder. Notice that the y coordinate (refractive index) of the center line is plotted in terms of change from unity.

Simulations are shown for refractive indices that range from .1% change (refractive index of 1.001) to a 40% change (refractive index of 1.4). For each refractive index, cylinders of size 1, 2, 4 and 10 wavelengths are shown. This gives a range of phase changes across the cylinder (see equation (5.1) above) from $.004\pi$ to 16π .

Clearly, all the cylinders of refractive index 1.001 in Figure 5.1 are perfectly reconstructed. As equation (5.1) predicts the results get worse as the product of refractive index and radius gets larger. The largest refractive index that is successfully reconstructed is for the cylinder in Figure 5.1 of radius 1 wavelength and a refractive index that differed by 20% from the surrounding medium.

While it is difficult to evaluate quantitatively the three dimensional plots it is certainly reasonable to conclude that only cylinders where the phase change across the object is less than or equal to $.8\pi$ are adequately reconstructed. In general the reconstruction for each cylinder where the phase change across the cylinder is greater than π shows severe artifacts near the center. This limitation in the phase change across the cylinder is consistent with the condition described in Chapter 2.

5.2.2 Evaluation of the Rytov Approximation

Figure 5.3 shows the simulated results for 16 reconstructions using the Rytov approximation. To emphasize the insensitivity of the Rytov approximation to large objects the largest object simulated has a diameter of 100λ .

It should be pointed out that the rounded edges of the 1λ reconstructions are not due to any limitation of the Rytov approximation but instead are the result of a two dimensional low pass filtering of the reconstructions. Recall that for a transmission experiment an estimate of the object's Fourier transform is only available up to frequencies less than $\sqrt{2}k_0$. Thus the reconstructions shown in Figure 5.3 show the limitations of both the Rytov approximation and the Fourier Diffraction Theorem.

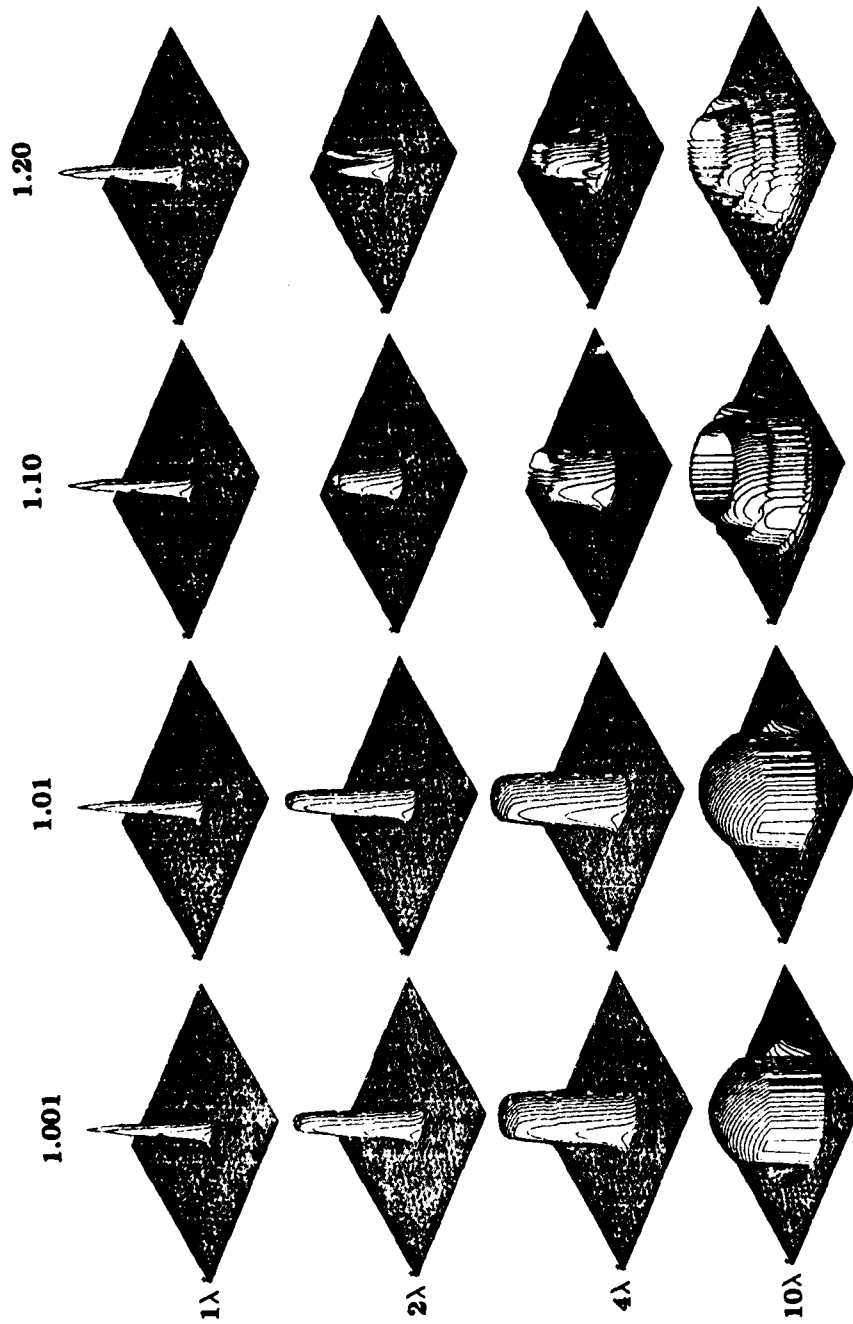


Figure 5.1
Simulated reconstructions using the Born approximation for
16 objects with four refractive indices between 1.001 and 1.20
and four radii between 1 and 10λ .

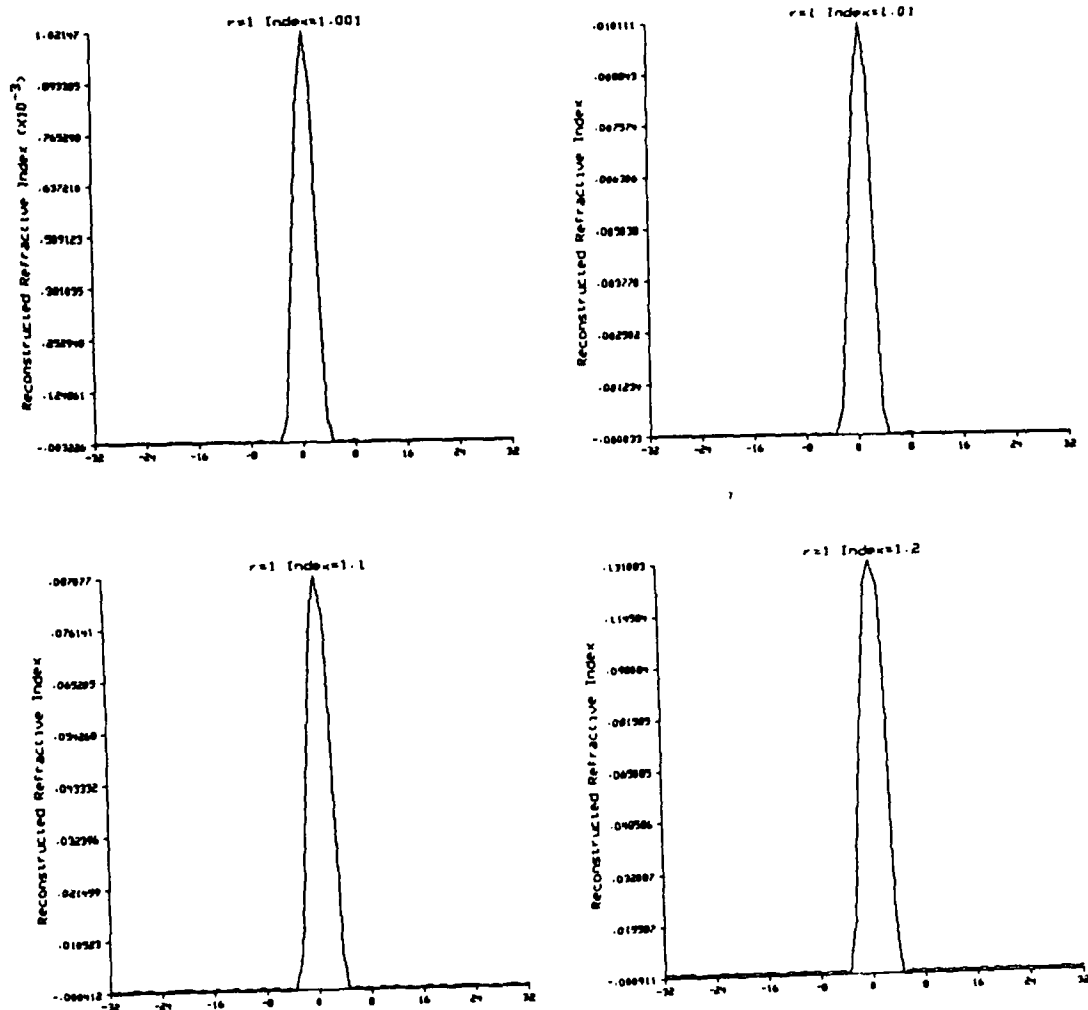


Figure 5.2 The center line for the reconstructions shown in Figure 5.1.

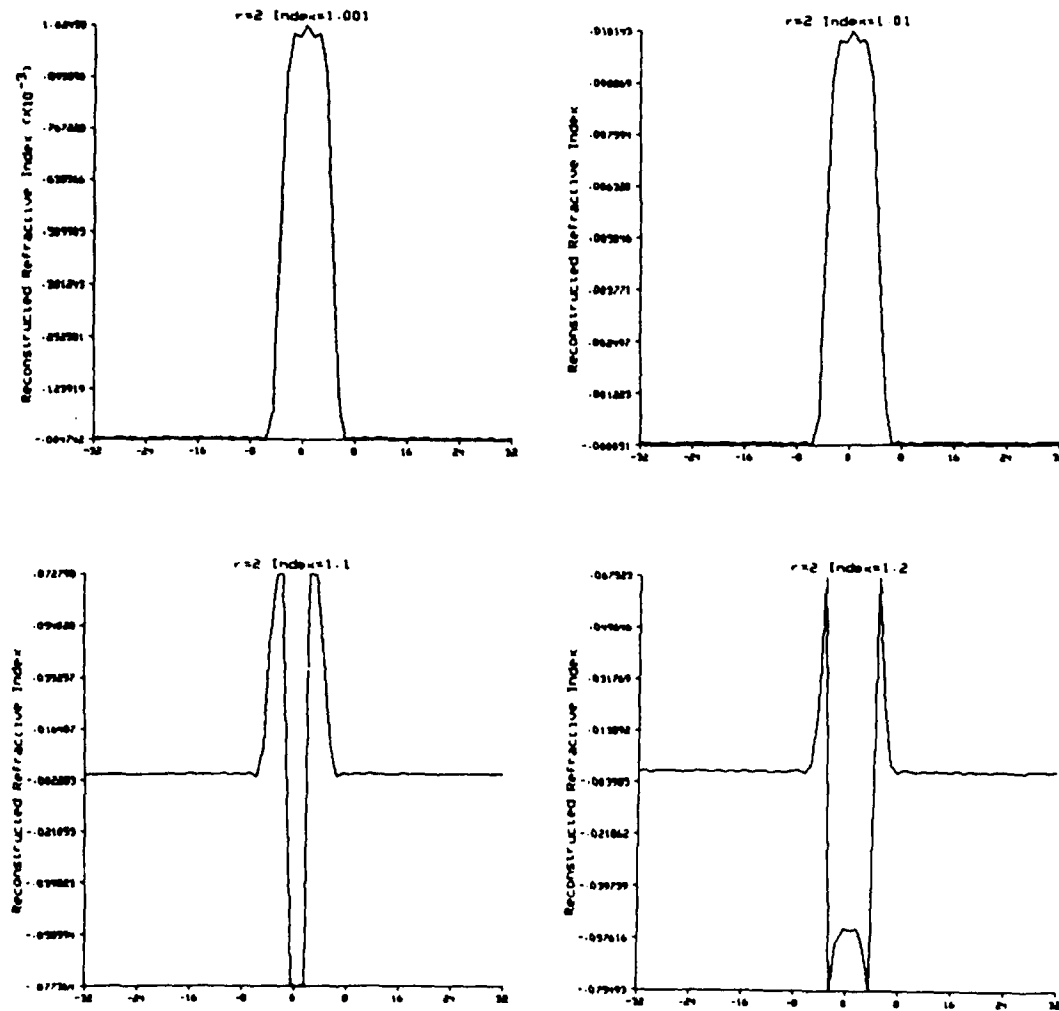


Figure 5.2 Continued.

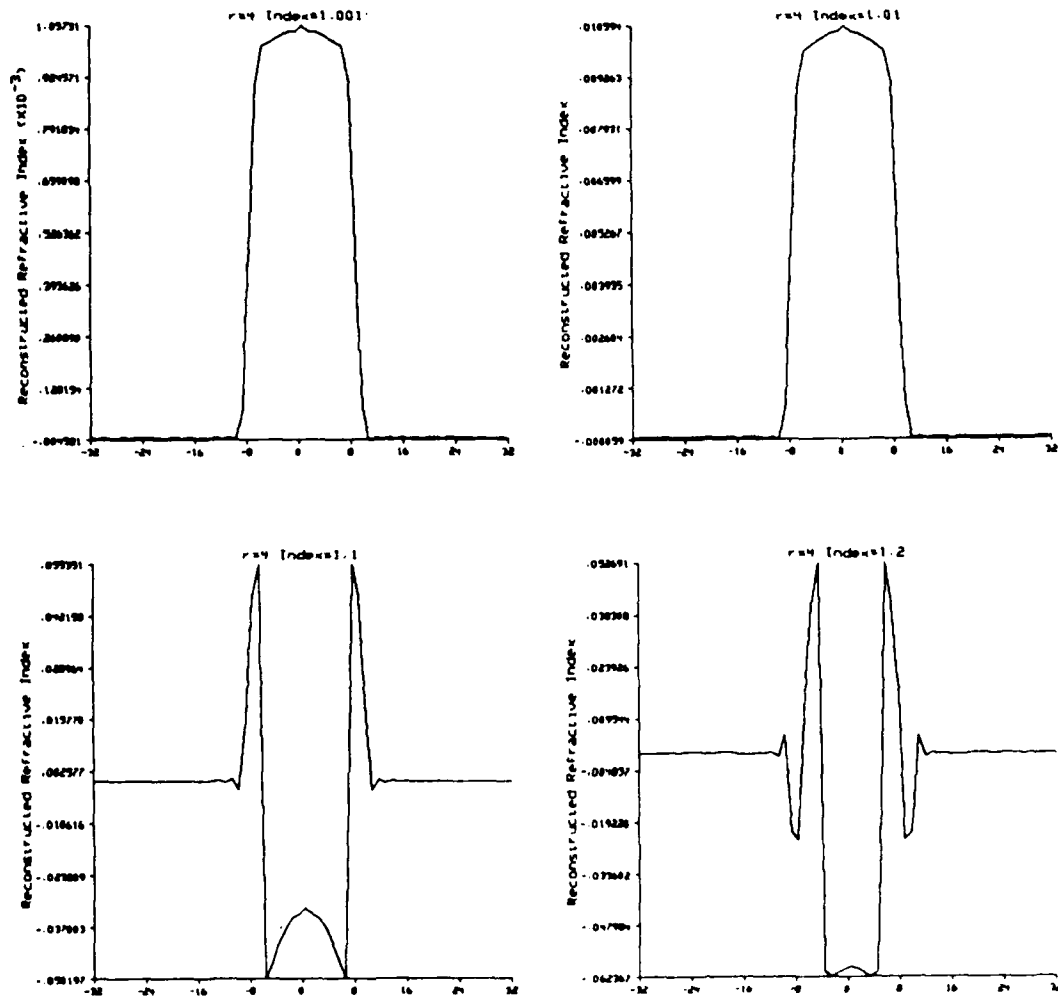


Figure 5.2 Continued.

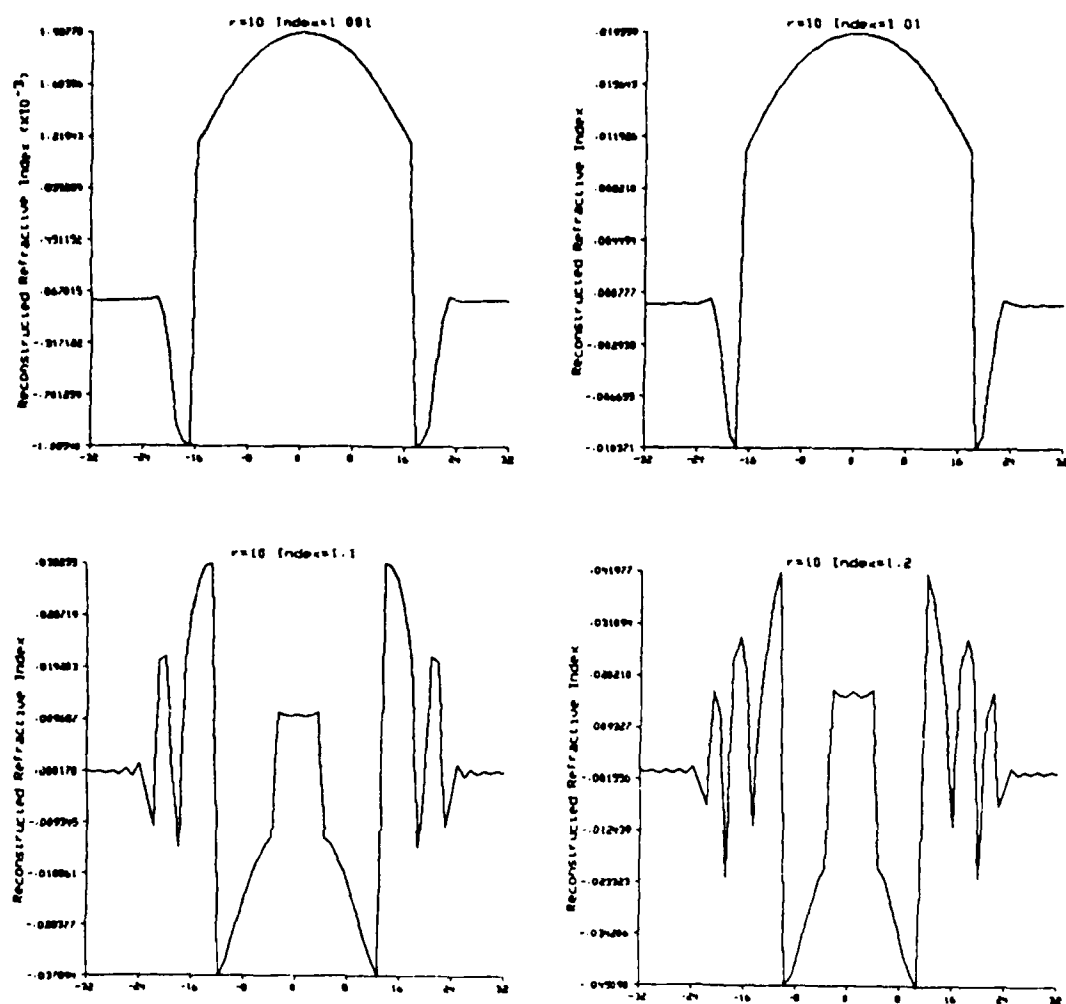


Figure 5.2 Continued.

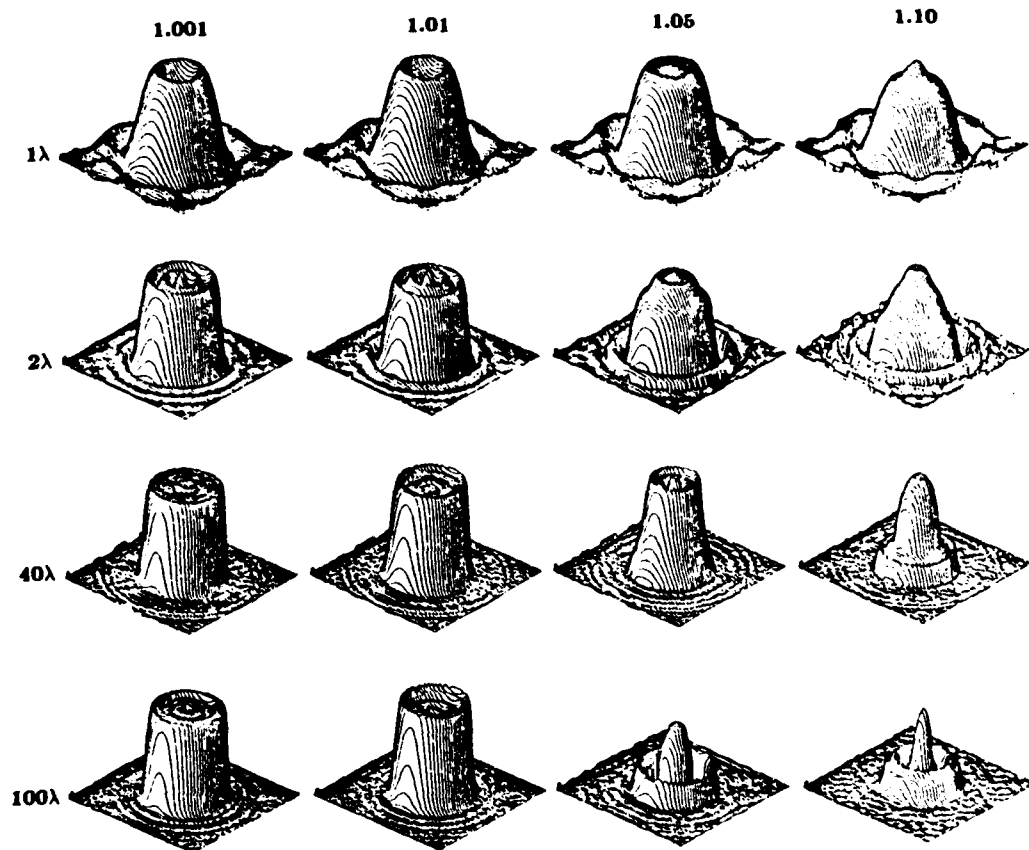


Figure 5.3

Simulated reconstructions using the Born approximation for 16 objects with four refractive indices between 1.001 and 1.10 and four radii between 1 and 100λ .

5.2.3 Comparison of the Born and Rytov Approximation

Reconstructions using exact scattered data show the similarity of the Born and the Rytov approximation. Within the limits of the Fourier Diffraction Theorem the reconstructions in Figure 5.1 and 5.3 of a 1λ object with a small refractive index are similar. In both cases the reconstructed change in refractive index is close to that of the simulated object.

The two approximations differ for objects that have a large refractive index change or have a large radius. The Born reconstructions are good at a large refractive index as long as the phase shift of the incident field as predicted by equation (5.1) is less than π .

On the other hand the Rytov approximation is very sensitive to the refractive index but produce excellent reconstructions for objects as large as 100λ . Unfortunately for object with a refractive index larger than 1% the Rytov approximation quickly deteriorates.

In addition to the qualitative studies a quantitative study of the error in the Born and Rytov reconstructions is also possible. As a measure of error the relative mean squared error in the reconstruction of the object function is integrated over the entire plane. If the actual object function is $o(r)$ and the reconstructed object function is $o'(r)$ then the relative Mean Squared Error (MSE) is given by

$$\frac{\iint [o(r) - o'(r)]^2 dr}{\iint [o(r)]^2} \quad (5.2)$$

This study presents the Mean Squared Error for 120 reconstructions based on the exact scattered fields from a cylinder. In each case a 512 point receiver line is at a distance of 10λ from the center of the cylinder. Both the receiver line and the object reconstruction are sampled at $1/4\lambda$ intervals.

The plots of Figure 5.4 present a summary of the mean squared error for cylinders of 1, 2 and 3λ in radius and for twenty refractive indices between 1.01 and 1.20. In each case the error for the Born approximation is shown as a solid line while the Rytov reconstruction is shown as a dashed line. The data used for these simulations was the exact scattered fields from a cylinder measured at 512 receiver points along a receiver line 10λ from the center of the cylinder.

Many researchers [Kav82, Kel69, Sou83] have postulated that the Rytov approximation is clearly superior to the Born but as the actual reconstructions represented by Figure 5.4 show for a 1λ cylinder this is not necessarily true. It

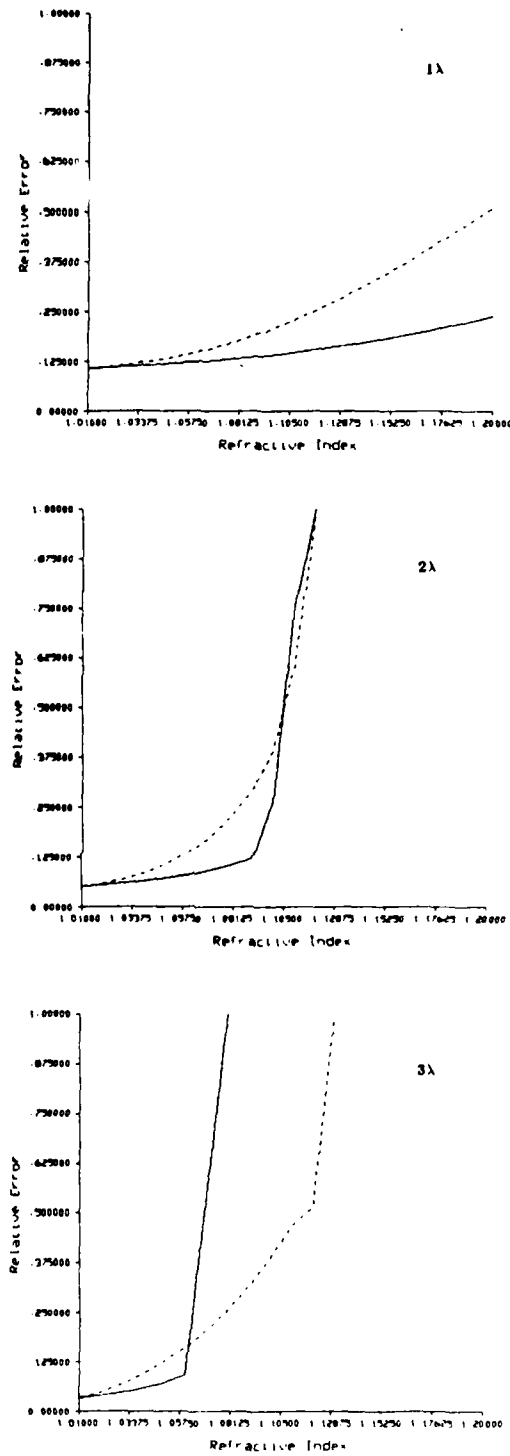


Figure 5.4

The relative mean squared error for reconstructions using the Born (solid line) and Rytov (dashed line) approximations. The error for a total of 60 objects with a radius of 1, 2 and 3 wavelengths are shown.

is interesting to note that, while the Rytov approximation shows a steadily increasing error with higher refractive indices, the error in the Born reconstruction is relatively constant until a threshold is reached. For the 2λ and 3λ cylinders, this breakpoint occurs at a phase shift across the cylinder of 0.6 and 0.7π . Thus, a criteria for the validity of the Born approximation is that the product of the radius of the cylinder in wavelengths and the change in refractive index must be less than .175.

Figure 5.5 presents a summary of the relative mean squared errors for cylinders with refractive indices of 1.01, 1.02 and 1.03 for forty radii between 1 and 40λ . Because the size of the cylinders varied by a factor of forty, the simulations parameters were adjusted accordingly. For a cylinder of radius R , the scattered field was calculated for 512 receivers along a line $2R$ from the center of the cylinder and spaced at $1/16R$ intervals.

In each of the simulations, the Born approximation is only slightly better than the Rytov approximation until the Born approximation crosses its threshold with a phase shift of 0.7π . Because the error in the Rytov approximation is relatively flat, it is clearly superior for large objects with small refractive indices. Using simulated data and the Rytov approximation objects as large as 2000λ in radius have been reconstructed.

5.3 Evaluation of Reconstruction Algorithms

To study the approximations involved in the reconstruction process it is necessary to calculate scattered data assuming the forward approximations are valid. This can be done in one of two different ways. As already discussed the Born and Rytov approximations are valid for small objects and small changes in refractive index. Thus, if the exact scattered field for a small and weakly scattering object is calculated then it can be assumed that either the Born or the Rytov approximations is exact.

A better approach is to recall the Fourier Diffraction Theorem, which says that the Fourier transform of the scattered field is proportional to the Fourier transform of the object along a circular arc. Since this theorem is the basis for the first order inversion algorithms if it is assumed correct the approximations involved in the reconstruction process can be studied.

If the Fourier Diffraction Theorem holds, the exact scattered field can be calculated exactly for objects that can be modeled as ellipses. The analytic expression for the Fourier transform of the object along an arc is then proportional to the scattered fields. This procedure is fast and allows the

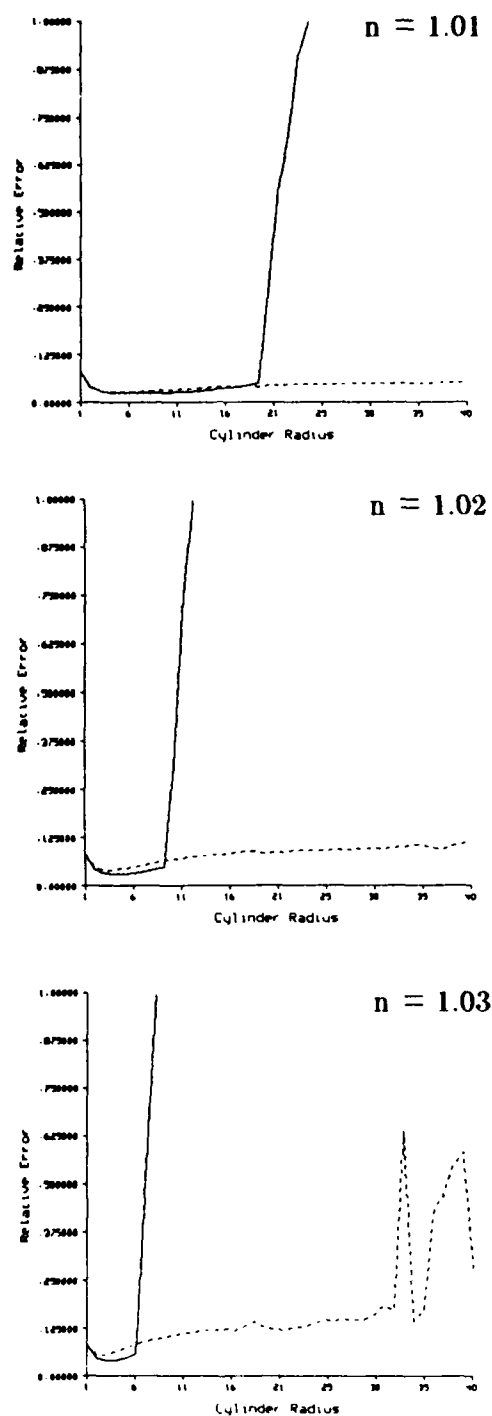


Figure 5.5

The relative mean squared error for reconstructions using the Born (solid line) and Rytov (dashed line) approximations. The error for a total of 120 objects with a refractive index of 1.01, 1.02 and 1.03 are shown.

scattered fields to be calculated for testing reconstruction algorithms and experimental parameters.

To illustrate the accuracy of the interpolation based algorithms, the image in Figure 5.6a will be used as a test "object" for showing computer simulation results. Figure 5.6a, with its gray levels as shown in Figure 5.6b, is a modification of the Shepp and Logan "phantom" described in [She74] to the case of diffraction imaging [Dev83, Pan83]. The gray levels shown in Figure 5.6 represent the refractive index values. This test image is a superposition of ellipses, with each ellipse being assigned a refractive index value as shown in Table 5.1.

Table 5.1. Summary of parameters for diffraction tomography simulations

Center Coordinate	Major Axis	Minor Axis	Rotation Angle	Refractive Index
(0,0)	0.92	0.69	90	1.0
(0,-0.0184)	0.874	0.6624	90	-0.5
(0.22,0)	0.31	0.11	72	-0.2
(-0.22,0)	0.41	0.16	108	-0.2
(0,0.35)	0.25	0.21	90	0.1
(0,0.1)	0.046	0.046	0	0.15
(0,-0.1)	0.046	0.046	0	0.15
(-0.08,-0.605)	0.046	0.023	0	0.15
(0,-0.605)	0.023	0.023	0	0.15
(0.06,-0.605)	0.046	0.023	90	0.15

A major advantage of using an image like Figure 5.6a for computer simulation is that the analytical expressions for the transforms of the diffracted projections can be written. The Fourier transform of an ellipse of semi-major and semi-minor axes A and B, respectively, is given by

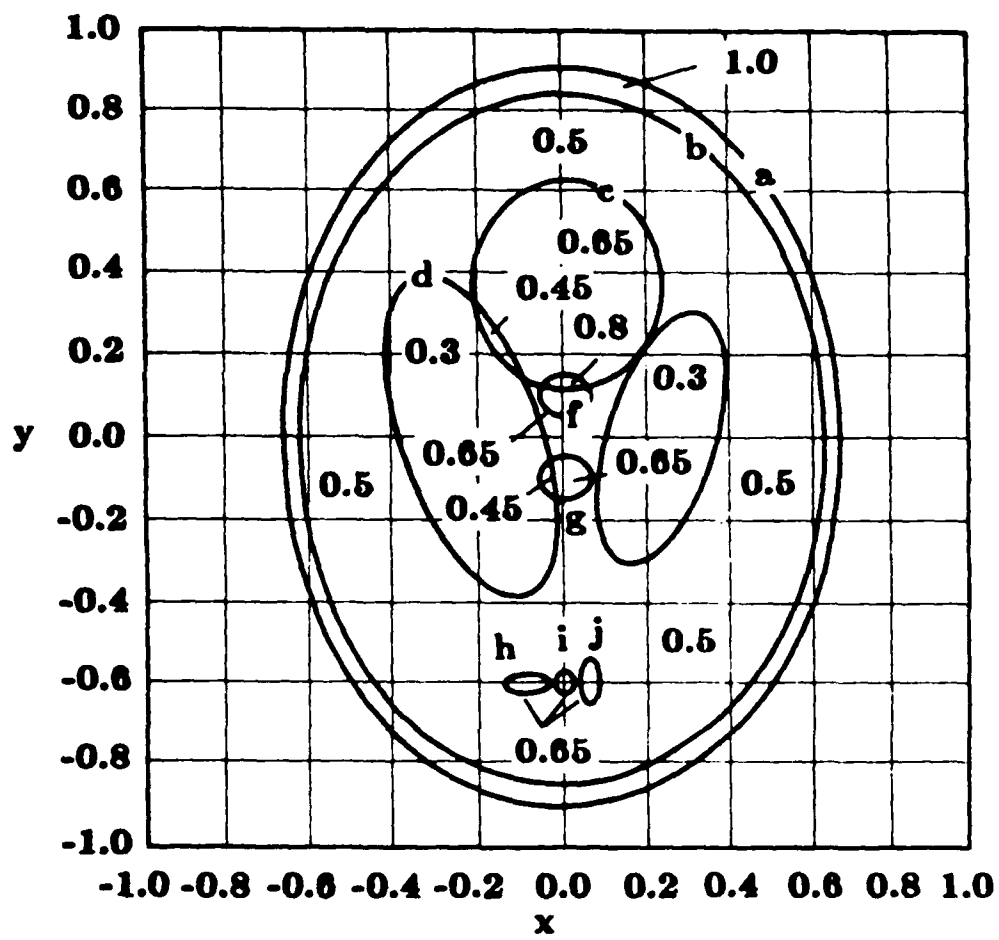


Figure 5.6

A modified version of the Shepp and Logan head phantom is used to test reconstruction algorithms. The numbers represent the relative change in refractive index from the background value of 1.0.

$$O_{\text{ellipse}}(u,v) = \frac{2\pi A J_1 \left[B \sqrt{(uA/B)^2 + v^2} \right]}{\sqrt{(uA/B)^2 + v^2}} \quad (5.3)$$

where u and v are spatial angular frequencies in the x - and y -directions, respectively; and J_1 is a Bessel function of the first kind and order 1. When the center of this ellipse is shifted to the point (x_1, y_1) , and the angle of the major axis tilted by α , as shown in Figure 5.7b, its Fourier transform becomes

$$e^{-j(ux_1 + vy_1)} \cdot \frac{2\pi A J_1 \left\{ B \left[((u')A/B)^2 + (v')^2 \right]^{1/2} \right\}}{\left[((u')A/B)^2 + (v')^2 \right]^{1/2}} \quad (5.4)$$

where

$$u' = u \cos \alpha + v \sin \alpha \quad (5.5)$$

and

$$v' = -u \sin \alpha + v \cos \alpha. \quad (5.6)$$

Now consider the situation where the ellipse is illuminated by a plane. By the Fourier Diffraction Theorem the Fourier transform of the transmitted wave fields measured on the receiver line is given by the values of the above function on a circular arc. For the test object of Figure 5.7b, if weak scattering is assumed and therefore there is no interaction among the ellipses, the Fourier transform of the total forward scattered field measured on a line, is the sum of the values of functions like (5.4) over the circular arc. This procedure is used to generate the diffracted projection data for the test image.

It should be mentioned that by using this procedure to calculate the diffracted projection data only the accuracy of the reconstruction algorithm is tested, without checking whether or not the "test object" satisfies the underlying assumption of weak scattering. In order to test this crucial assumption, it is necessary to generate the forward scattered data of the object. For multi-component objects, such as the one shown in Figure 5.6a, it is very difficult to do so due to the interactions between the components.

Pan and Kak [Pan83] presented the simulations shown in Figure 5.8. Using a combination of increasing the sampling density by zero padding the signal and bilinear interpolation, results are obtained in 2 minutes of CPU time on a VAX 11/780 minicomputer with a floating point accelerator (FPA). The reconstruction is shown over a 128 by 128 grid using 64 views and 128 receiver positions. The number of operations required to carry out the interpolation

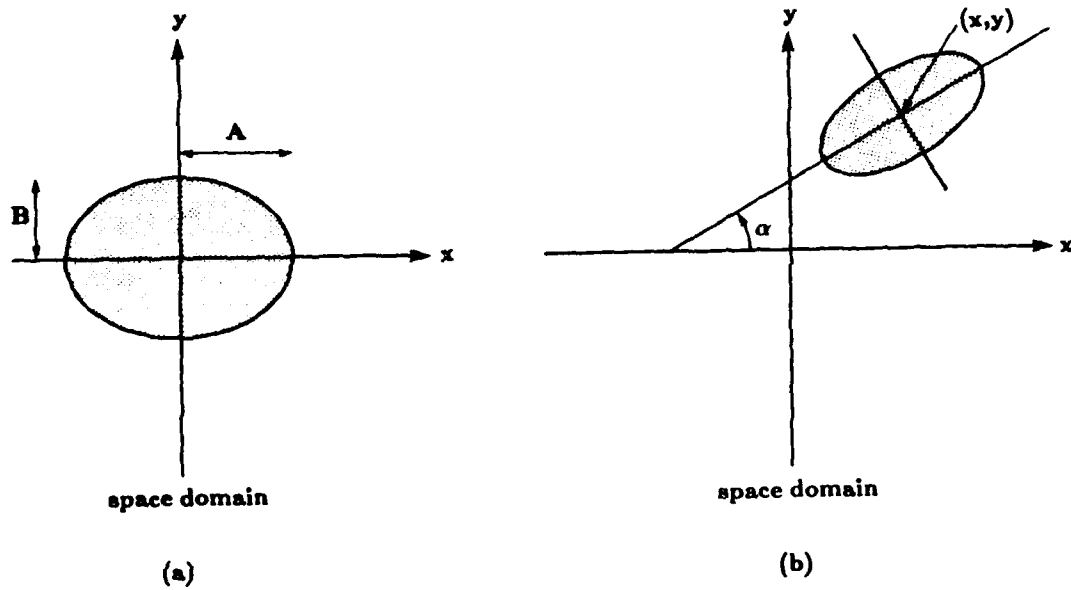


Figure 5.7

Assuming the Fourier Slice Theorem is valid the scattered field can easily be computed as the values of the Fourier transform of the rotated and translated ellipse.

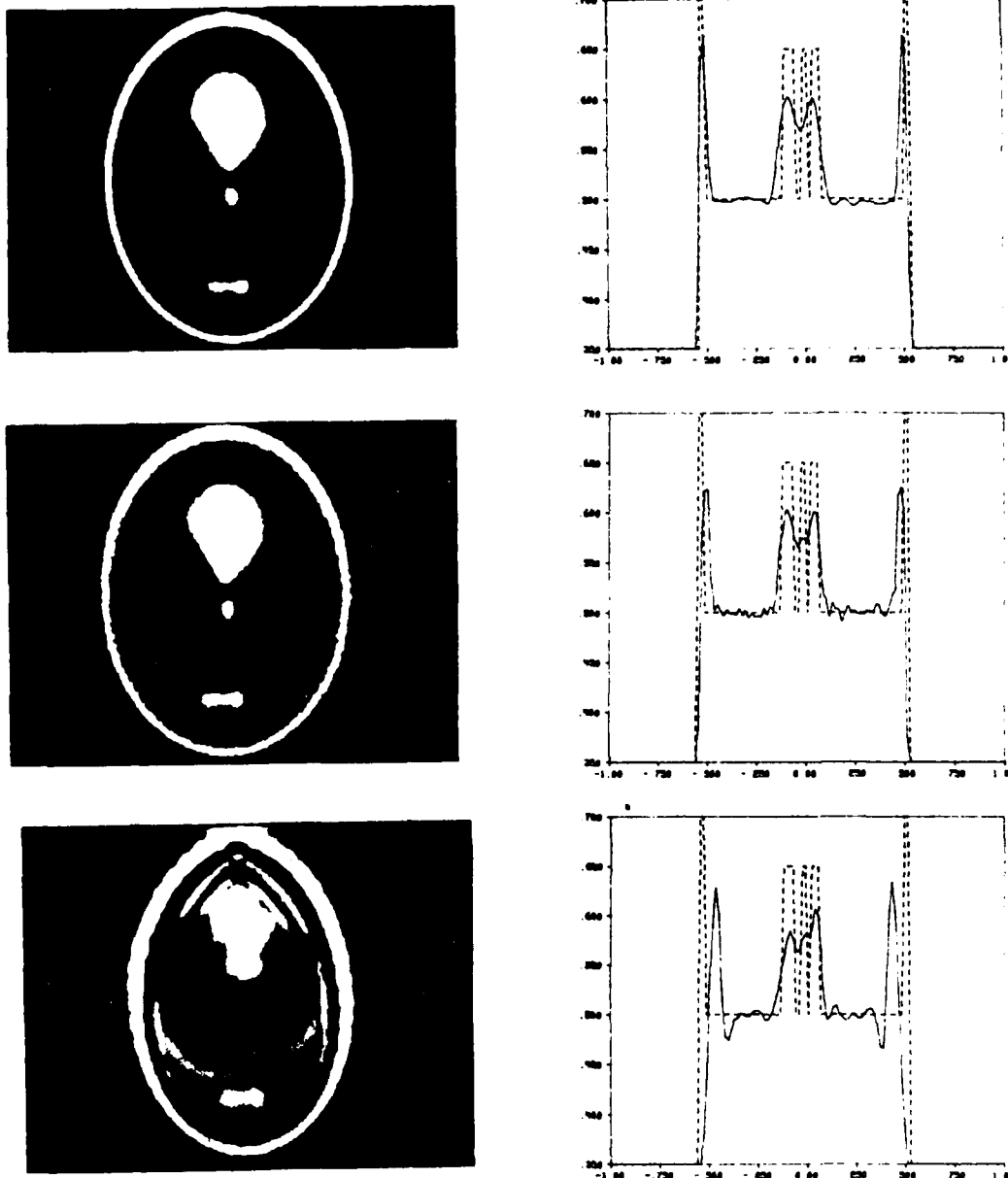


Figure 5.8

The above images show the results of using the (a) interpolation, (b) backpropagation and (c) modified backpropagation algorithms on reconstruction quality. The solid lines in the graphs represent the reconstructed value along a line through the center of the three ellipses at the bottom of the phantom.

and invert the object function is on the order of $N^2 \log N$. The resulting reconstruction is shown in Figure 5.8a.

Figure 5.8b represents the result of back propagating the data to 128 depths for each view while Figure 5.8c is the result of back propagation to only a single depth centered near the three small ellipses at the bottom of the picture. The results were calculated on a VAX 11/780 minicomputer with a Floating Point Accelerator (FPA) and the resulting reconstructions were done over a 128 by 128 grid. Like the previous image the input data consists of 64 projections of 128 points each.

There is a significant difference in not only the reconstruction time but also the resulting quality. While the modified back propagation only took 1.25 minutes the resulting reconstruction is much poorer than the full back propagation which took 30 minutes of CPU time. A comparison of the various algorithms is shown in Table 5.2.

Table 5.2. Comparison of Algorithms

Algorithm	Complexity	CPU Time
Interpolation	$N^2 \log N$	2 Minutes
Back Propagation	$N_d N_\phi N \log N$	30 Minutes
Modified Back Propagation	$N_\phi N \log N$	1.25 Minutes

5.4 Experimental Limitations

In addition to the limits on the reconstructions imposed by the Born and the Rytov approximations there are also experimental limitations. These additional factors are caused by

- Wave propagation in free space
- Sampling the data along the receiver line
- Finite receiver length
- Limited views of the object

In inverse scattering theory the measured complex amplitude of a received wave is sampled, filtered and then interpolated to estimate the Fourier transform of the object function. The reconstruction process is linear because

it consists only of filtering the data and then calculating its inverse Fourier transform.

The first three factors each can be modeled as a simple constant low-pass filtering of the scattered field. Because the entire process is linear the net effect is a single low filter at the lowest of the three frequencies. The experiment can be optimized by adjusting the parameters of the experiment so that each low pass filter cuts off at the same frequency.

A limited number of views also can be modeled as a low pass filter. In this case, though, the cutoff frequency varies with the radial direction.

5.4.1 Evanescent Waves

The most fundamental limitation is that evanescent waves are ignored. Since these waves have a complex wavenumber they are severely attenuated over a distance as small as several wavelengths. This limits the highest received wavenumber to

$$k_{\max} = \frac{2\pi}{\lambda}. \quad (5.7)$$

This is a fundamental limit of the propagation process and the resolution of the reconstruction can only be improved by moving the experiment to a higher frequency (or shorter wavelength.)

5.4.2 Sampling the Received Wave

After the wave has been scattered by the object and propagated to the receiver line it must be measured. This is usually done with the a point receiver. Unfortunately it is not possible to sample at every point, so a non zero sampling interval must be chosen. This introduces a measurement error into the process. By the Nyquist theorem this can be modeled as a low pass filtering operation, where the highest measured frequency is given by

$$k_{\text{meas}} = \frac{\pi}{T} \quad (5.8)$$

and T is the sampling interval. Of course this analysis has ignored the non-linear effects of aliasing and the resulting frequency shifts that occur.

5.4.3 The Effects of a Finite Receiver Length

Not only are there physical limitations on the finest sampling interval but usually there is a limitation on the amount of data that can be collected. This generally means that samples of the received waveform will be collected at only a finite number of points along the receiver line. This is usually justified by taking data along a line long enough so that the unmeasured data can be safely ignored. Because of the wave propagation process this also introduces a low pass filtering of the received data.

Consider for a moment a single scatterer at some distance, l_0 , from the receiver line. The wave propagating from this single scatterer is a cylindrical wave in two dimensions or a spherical wave in three dimensions. This effect is diagrammed in Figure 5.9. It is easy to see that the spatial frequencies vary with the position along the receiver line.

An optician studying this problem would be interested in knowing the resolving power of the system as a function of the size of the aperture [Goo68]. The analysis would normally be carried out assuming that the object is far enough from the aperture so that it can be assumed it is in the aperture's far field. But in this work the frequency content of the measured field is a limiting factor in the reconstruction quality so the effect of a limited aperture will be analyzed with an emphasis on the spatial frequency content of the received field. The two approaches to be considered here use a point source and analyze the frequency content at the aperture. Since all points in space are in the far field of a point source this analysis gives identical results to classical optics theory.

It is easier to analyze the effect by considering the expanding wave to be locally planar at any point distant from the scatterer. At the point on the receiver line closest to the scatterer there is no spatial variation [Goo68]. This corresponds to receiving a plane wave or a received spatial frequency of zero.

Higher spatial frequencies are received at points along the receiver line that are farther from the origin. The received frequency is a function of the sine of the angle between the direction of propagation and a perpendicular to the receiver line. This function is given by

$$k(y) = k_{\max} \sin \theta \quad (5.9)$$

where θ is the angle and k_{\max} is the wavenumber of the incident wave. Thus at the origin, the angle, θ , is zero and the received frequency is zero. Only at infinity does the angle become equal to ninety degrees and the received spatial frequency approach the theoretical maximum.

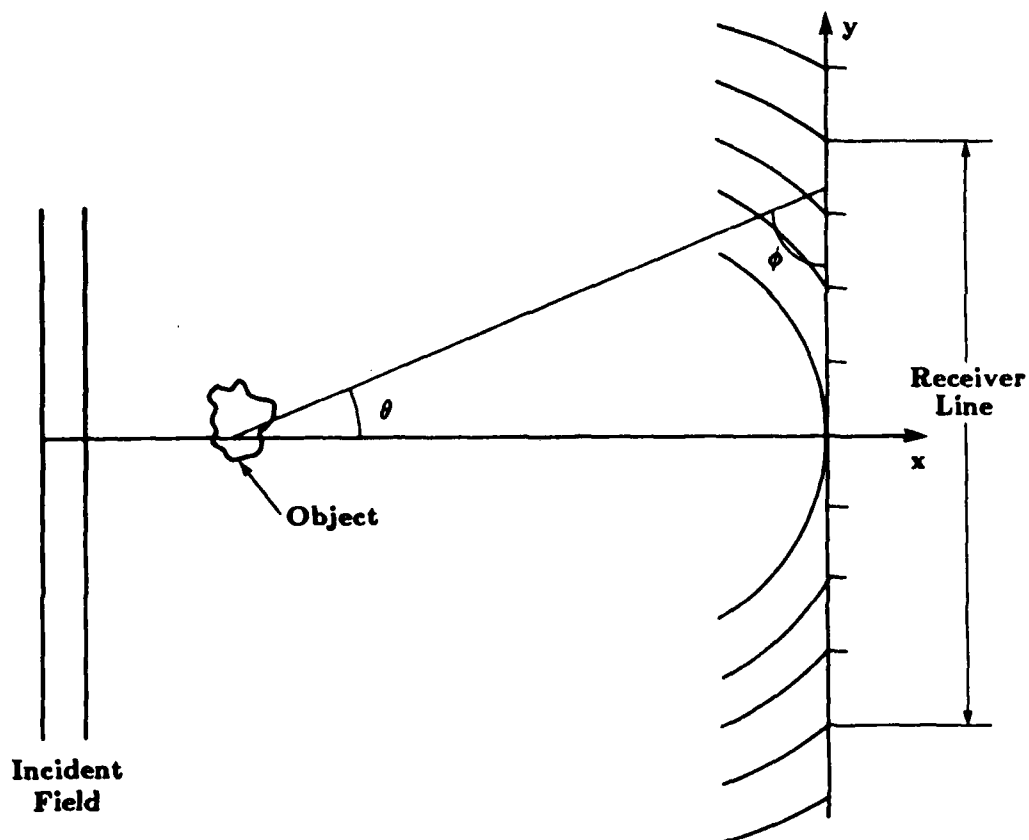


Figure 5.9

The field scattered by an object is measured along a receiver line with finite length.

This reasoning can be justified on a more theoretical basis by considering the phase of the propagating wave. The received wave at a point $(x=l_0, y)$ due to a scatterer at the origin is given by

$$u(x=l_0, y) = \frac{e^{jk_0\sqrt{x^2+y^2}}}{\sqrt{x^2+y^2}}. \quad (5.10)$$

The instantaneous spatial frequency along the receiver line (y varies) of this wave can be found by taking the partial derivative of the phase with respect to y [Gag78]

$$\text{phase} = k_0\sqrt{y^2+x^2} \quad (5.11)$$

$$k_{\text{recv}} = \frac{k_0 y}{\sqrt{x^2+y^2}} \quad (5.12)$$

where k_{recv} is the spatial frequency received at the point $(x=l_0, y)$. From Figure 5.9 it is easy to see that

$$\sin\theta = \frac{y}{\sqrt{x^2+y^2}} \quad (5.13)$$

and therefore equation (5.9) and (5.12) are equivalent.

This relation, (5.12), can be inverted to give the length of the receiver line for a given maximum received frequency, k_{max} . This becomes

$$y = \pm \frac{k_{\text{max}} x}{\sqrt{k_0^2 - k_{\text{max}}^2}}. \quad (5.14)$$

Since the highest received frequency is a monotonically increasing function of the length of the receiver line it is easy to see that by limiting the sampling of the received wave to a finite portion of the entire line that a low passed version of the entire scattered wave is measured. The highest measured frequency is a simple function of the distance of the receiver line from the scatterer and the length of measured data. This limitation can be better understood if the maximum received frequency is written as a function of the angle of view of the receiver line. Thus substituting

$$\tan(\theta) = \frac{y}{x} \quad (5.15)$$

it is easy to see that

$$k_{\text{recv}} = \frac{k_0 \frac{y}{x}}{\sqrt{\left(\frac{y}{x}\right)^2 + 1^2}} \quad (5.16)$$

and

$$k_{\text{recv}} = \frac{k_0 \tan \theta}{\sqrt{\tan^2 \theta + 1}} \quad (5.17)$$

Thus k_{recv} is a monotonically increasing function of the angle of view, θ . It is easy to see that the maximum received spatial frequency can be increased by either moving the receiver line closer to the object or by increasing the length of the receiver line.

5.4.4 Evaluation of the Experimental Effects

Exact scattered data is used to verify the optimum experimental values and the effect of a finite receiver length is shown in Figure 5.10. The spatial frequency content of a wave is found by taking the FFT of the sampled points along the receiver line and is compared to the theoretical result as predicted by the Fourier Transform of the object. The theory predicts that more of the high frequency components will be present as the length of the receiver line increases and this is confirmed by simulation.

While the above derivation only considered a single scatterer it is also approximately true for many scatterers collected at the origin. This is possible because the inverse reconstruction process is linear and each point in the object scatterers an independent cylindrical wave.

5.4.5 Optimization

Since each of these three factors is independent, their effect in the frequency domain can be found by simply multiplying each of their frequency responses together. As has been described above each of these effects can be modeled as a simple low-pass filter of the theoretical data so the combined effect is also a low pass filter but at the lowest frequency of the cut-off of the three effects.

First consider the effect of ignoring the evanescent waves. Since the maximum frequency of the received wave is limited by the propagation filter to

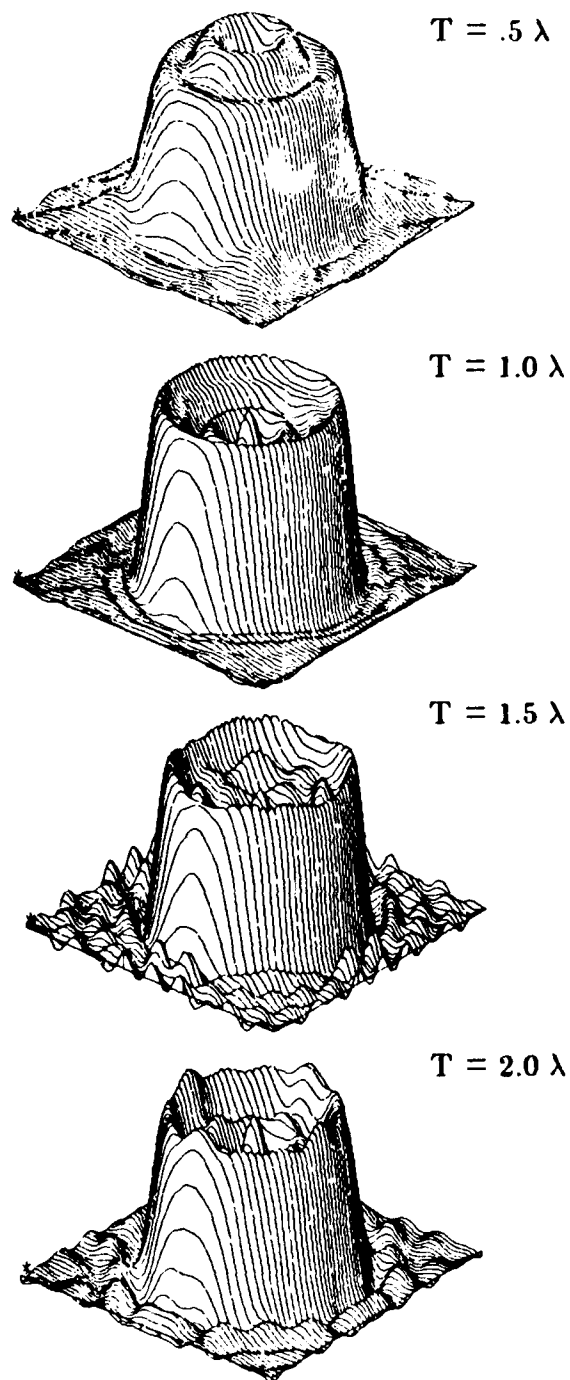


Figure 5.10 Reconstructions of an object using a detector spacing of (a) $.5\lambda$, (b) 1.0λ , (c) 1.5λ and (d) 2.0λ are shown here.

$$k_{\max} = \frac{2\pi}{\lambda} \quad (5.18)$$

it is easy to combine this expression with the expression for the Nyquist frequency into a single expression for the smallest "interesting" sampling interval. This is given by

$$k_{\max} = k_{\text{meas}} \quad (5.19)$$

or

$$\frac{2\pi}{\lambda} = \frac{\pi}{T} \quad (5.20)$$

and rearranging

$$T \geq 1/2\lambda. \quad (5.21)$$

Thus if the received waveform is sampled with a sampling interval of more than $1/2$ wavelength the measured data might not be a good estimate of the received waveform because of aliasing. On the other hand it is not necessary to sample the received waveform any finer than $1/2$ wavelength since this provides no additional information. Doing this it is possible to conclude that the sampling interval should be greater than $1/2$ wavelength.

In general the experiment will also be constrained by the number of data points (M) that can be measured along the receiver line. The distance from the object to the receiver line will be considered a constant in the derivation that follows. If the received waveform is sampled uniformly, the range of the receiver line is given uniquely by

$$y_{\max} = \pm \frac{MT}{2}. \quad (5.22)$$

This is also shown in Figure 5.9.

For a receiver line at a fixed distance from the object and a fixed number of receiver points this is a classical optimization problem. As the sampling interval is increased the length of the receiver line increases and more of the received wave's high frequencies are measured. On the other hand increasing the sampling interval lowers the maximum frequency that can be measured before aliasing occurs.

The optimum value of T can be found by setting the cutoff frequencies for the Nyquist frequency equal to the highest received frequency due to the finite receiver length and then solving for the sampling interval. If this constraint is not met then some of the information that is passed by one process will be attenuated by the others. This results in

$$\frac{\pi}{T} = \frac{k_0 y}{\sqrt{y^2 + x^2}} \quad (5.23)$$

evaluated at

$$k_0 = \frac{2\pi}{\lambda} \quad (5.24)$$

and

$$y = \frac{MT}{2}. \quad (5.25)$$

Solving for T^2 the optimum value for T is given by

$$\left(\frac{T}{\lambda}\right)^2 = \frac{\sqrt{64\left(\frac{x}{\lambda}\right)^2 + M^2} + M}{8M}. \quad (5.26)$$

Making the substitution

$$\alpha = \frac{x}{\lambda M} \quad (5.27)$$

the optimum sampling interval is given by

$$\left(\frac{T}{\lambda}\right)^2 = \frac{\sqrt{64\alpha^2 + 1} + 1}{8}. \quad (5.28)$$

This substitution is similar to the $\tan\theta$ substitution that is made in the heuristic approach above. Also notice that the smallest positive value that the sampling interval can become is $1/2$ wavelength. This corresponds to the Nyquist frequency for a propagating wave.

The optimum sampling interval is confirmed by simulations. Again, using the method described above for calculating the exact scattered fields, four simulations are shown of an object of radius 10 wavelengths using a receiver that is 100 wavelengths from the object. In each case the number of receiver positions is fixed at 64. The resulting reconstructions for a sampling interval of .5, 1, 1.5 and 2 wavelengths are shown in Figure 5.10. Equation (5.28) predicts an optimum sampling interval of 1.3 wavelengths and this is confirmed by the simulations. The best reconstruction occurs with a sampling interval between 1 and 1.5 wavelengths.

5.4.6 Limited Views

In many applications it is not possible to generate or receive plane waves from all directions. The effect of this is to leave holes where there is no estimate of the Fourier transform of the object.

Since the ideal reconstruction algorithm produces an estimate of the Fourier transform of the object for all frequencies within a disk a limited number of views introduces a selective filter for areas where there is no data. As shown by Devaney [Dev84] for the VSP case a limited number of views degrades the reconstruction by low pass filtering the image in certain directions. Devaney's results are reproduced in Figures 5.11 and 5.12.

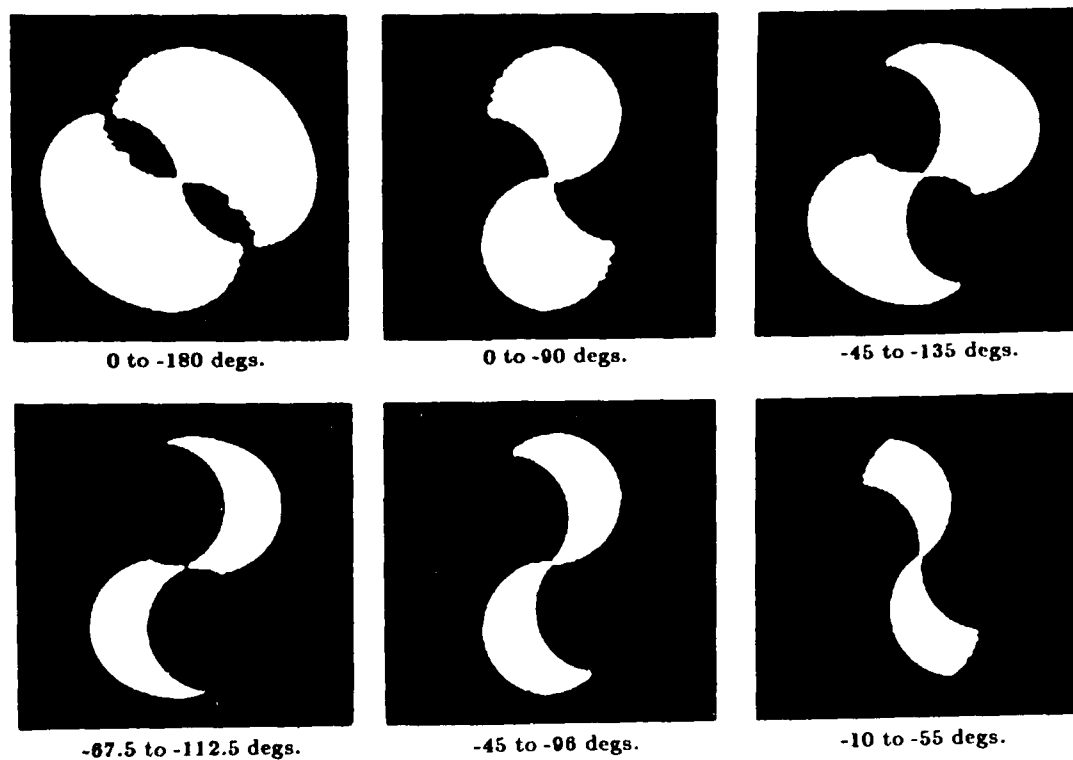


Figure 5.11

These figures show the coverage in the frequency domain for six different receiver limitations (from [Dev84]).

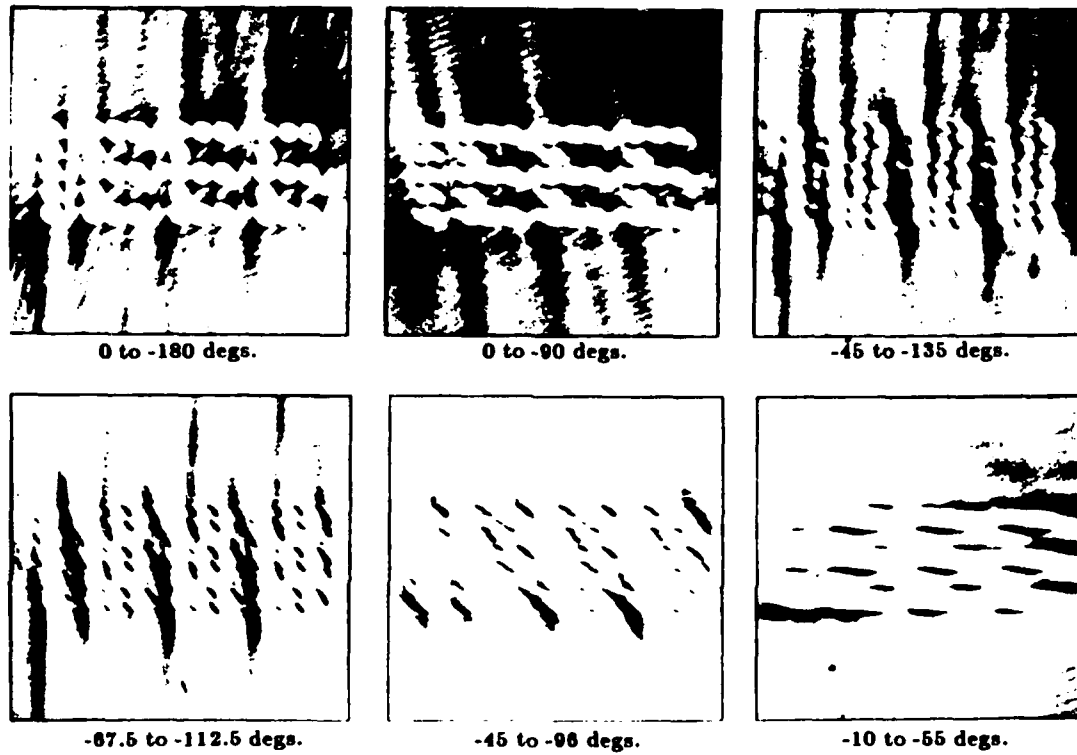


Figure 5.12 Images due to the limited field of views as shown in Figure 5.11 from [Dev84].

References

- [Dev83] A. J. Devaney, "A computer simulation study of diffraction tomography," *IEEE Transactions on Biomedical Engineering*, Vol. BME-30, July 1983, pp. 377-386.
- [Dev84] A. J. Devaney, "Geophysical diffraction tomography," *IEEE Transaction Geological Science, Special Issue on Remote Sensing*, Vol. GE-22, January 1984, pp. 3-13.
- [Gag78] R. Gagliardi, *Introduction to Communications Engineering*, John Wiley and Sons, 1978.
- [Goo68] J. W. Goodman, *Introduction to Fourier Optics*, McGraw Hill Book Company, San Francisco, 1968.
- [Kav82] M. Kaveh, M. Soumekh, and R. K. Mueller, "Tomographic imaging via wave equation inversion," *ICASSP 82*, May 1982, pp. 1553-1556.
- [Kel69] J. B. Keller, "Accuracy and validity of the Born and Rytov approximations," *Journal of the Optical Society of America*, Vol. 59, 1969, pp. 1003-1004.
- [Mor68] P. M. Morse and K. U. Ingard, *Theoretical Acoustics*, McGraw Hill Book Company, New York, 1968.
- [Pan83] S. X. Pan and A. C. Kak, "A computational study of reconstruction algorithms for diffraction tomography: Interpolation vs. filtered-backpropagation," *IEEE Transactions on Acoustics, Speech and Signal Processing*, October 1983, pp. 1262-1275.
- [She74] L. A. Shepp and B. F. Logan, "The Fourier reconstruction of a head section," *IEEE Trans. Nucl. Sci.*, Vol. NS-21, 1974, pp. 21-43.
- [Sou83] M. Soumekh, M. Kaveh, and R. K. Mueller, "Algorithms and experimental results in acoustic tomography using Rytov's approximation," *ICASSP 83 Proceedings*, April 1983, pp. 135-138.
- [Wee64] W. L. Weeks, *Electromagnetic Theory for Engineering Applications*, John Wiley and Sons, Inc., New York, 1964.

CHAPTER 6

HIGHER ORDER APPROXIMATIONS TO THE SCATTERED FIELD

6.1 Introduction

Reconstruction algorithms based on the theory presented in Chapter 2 generate severe artifacts for objects larger than a few wavelengths or a change in refractive index greater than a few percent. These reconstruction algorithms are limited by the first Born or the first Rytov approximations and thus any improvement in the reconstructions will be accomplished by modeling the scattered fields more accurately. With this more accurate model it will again be necessary to invert the equation to arrive at an estimate of the object.

This section will describe iterative techniques that more accurately model the scattered fields. In addition to the theoretical derivations a number of simulations will be presented and the convergence of each series will be discussed.

Two approaches to more accurately compute the scattered field will be discussed here. Both approaches are iterative but they differ widely in their philosophy. The first approach, known as a fixed point method, assumes an initial guess that is a small perturbation from the correct solution. If the scattering integral is a "contracting" operator then this procedure converges to the correct answer. The second approach, based on a matrix formulation of the discrete wave equation, refines an initial guess by projecting it onto hyperplanes. Since each projection reduces the error this method always converges. Unfortunately the matrix formulation is more expensive (requires more calculations) than the fixed point method by a factor of several hundred.

6.2 The Singularity of the Green's Function

In each of the procedures to be discussed in this chapter it is necessary to evaluate an integral of the form

$$\int f(\vec{r}') g(\vec{r}-\vec{r}') d\vec{r}' \quad (6.1)$$

where $g(\vec{r}-\vec{r}')$ is the Green's function described in Chapter 2 or

$$g(\vec{r}-\vec{r}') = \frac{-N_0(R) + jJ_0(R)}{4} \quad (6.2)$$

and $R = |\vec{r}-\vec{r}'|$. This integral in equation (6.1) would be straightforward except for the fact that $N_0(R)$ tends to ∞ as R goes to zero.

The effect of this singularity is further complicated since for computer simulation it is necessary to sample the function at discrete positions. If straightforward sampling is performed on such a function any small change in the location of the sampling grid would cause a large change in the sampled value at the origin.

Fortunately it is possible to derive an approximate value for the sample at the origin. The actual value at the origin is not so important but when the Green's function is multiplied by the sampled kernel and integrated the result should be identical to a sampled version of the continuous integral.

Since all functions have been sampled they can be assumed to be reasonably smooth and the integral approximated

$$\sum_{r_i} f(\vec{r}_i) g(\vec{r}_j, \vec{r}_i). \quad (6.3)$$

When \vec{r}_i is equal to \vec{r}_j the area around the singularity is evaluated and the contribution of the \vec{r}_j term of the summation should be equal to the original integral in a square region around the origin.

All functions are sampled with interval T , in both the x and the y directions, so the following equality is necessary

$$f(\vec{r}_j) g(\vec{r}_j, \vec{r}_i) = \int_{-\frac{T}{2}}^{\frac{T}{2}} \int_{-\frac{T}{2}}^{\frac{T}{2}} f(\vec{r}') g(\vec{r}, \vec{r}') d\vec{r}'. \quad (6.4)$$

If $f(\vec{r}_i)$ is smooth enough then it can be considered a constant within the small region of the integral and brought out of the integral. The sample of the Green's function is now written

$$g(\vec{r}_j, \vec{r}_i) = \int_{-\frac{T}{2}}^{\frac{T}{2}} \int_{-\frac{T}{2}}^{\frac{T}{2}} g(\vec{r}, \vec{r}') d\vec{r}' . \quad (6.5)$$

While it is possible to evaluate this integral using approximations to the Bessel functions, a better solution is to evaluate the integral numerically. The approximate expansions for the Bessel functions are only valid for small values of R and are no longer accurate as the sampling interval, T , approaches a quarter of a wavelength.

A better solution is to numerically integrate this function by dividing the original $T \times T$ region into a $N \times N$ grid of points and summing up each of the samples. The samples of the real part of $g(\vec{r} - \vec{r}')$ are shown in Figure 6.1 for a grid size of 4×4 and 16×16 . As shown in this figure the point exactly at the origin can be ignored by offsetting the grid so that the singularity at the origin is never sampled. The effect of ignoring this undefined location can then be seen by examining the progression of average values as the number of samples in the T^2 region near the origin is increased. These values are shown in Table 6.1 for a sampling interval of $\frac{1}{4}$ wavelengths. Notice that this is a Cauchy sequence and converges to an average value for the Green's function over the $T \times T$ region. It is this value that will be used as the value of the Green's function at the origin in each of the computational procedures to be discussed in the remainder of this chapter.

6.3 Fixed Point Methods

The fixed point method is the most straightforward computational approach to solve an equation. In the remainder of this section it will be used to find a solution of both the Born integral and the Ricatti equation.

Consider a fixed point solution to the equation $x = f(x)$ defined over the region $x \in [a, b]$. Given an initial guess, x_0 a better estimate of the solution, ξ , can be found by [Sto80]

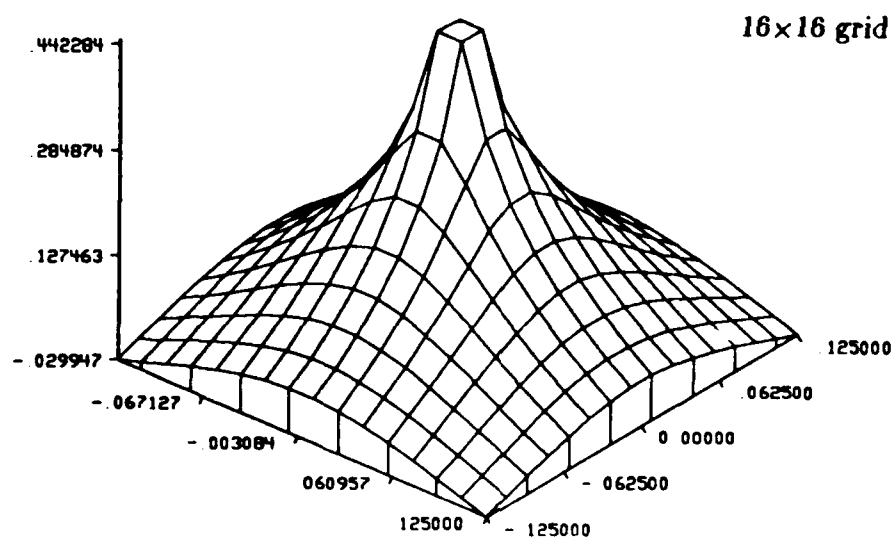
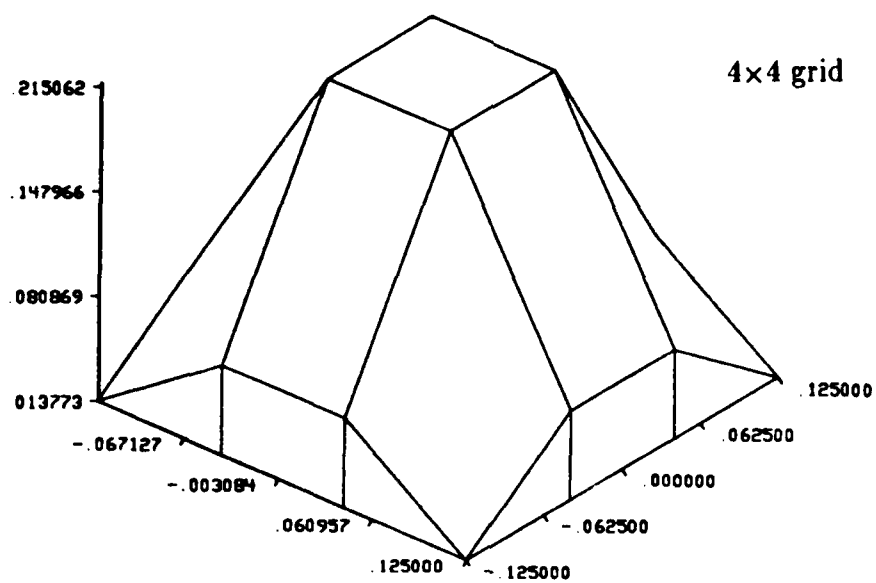


Figure 6.1

The real part of the function $g(\vec{r}-\vec{r}')$ is shown here sampled on a 4x4 grid (top) and a 16x16 grid (bottom).

Table 6.1. Average value of the Green's function over a $\frac{1}{4}\lambda$ region sampled on an NxN grid.

N	G(0)
4	0.0925259 + j0.226659
8	0.0927197 + j0.225568
16	0.0927666 + j0.225296
32	0.0927782 + j0.225228
64	0.0927811 + j0.225211
128	0.0927818 + j0.225207
256	0.092782 + j0.225206
512	0.092782 + j0.225206
1024	0.092782 + j0.225206

$$x_1 = f(x_0) \quad (6.6)$$

or more generally

$$x_{i+1} = f(x_i). \quad (6.7)$$

This is illustrated in Figure 6.2.

While this method doesn't always converge, it is possible to show that it will converge to a unique solution if the absolute value of the function's first derivative is always less than one. Mathematically this condition can be written

$$|f'(x)| < 1 \quad x \in [a, b]. \quad (6.8)$$

If this condition is true then it is also possible to show that $f()$ is a contraction operator or

$$|f(x_1) - f(x_2)| \leq K |x_1 - x_2| \quad x \in [a, b] \quad (6.9)$$

where $K < 1$.

That these two conditions are equivalent is easy to show by considering two cases. First, assume that $f()$ is a contracting operator. From the definition of the derivative

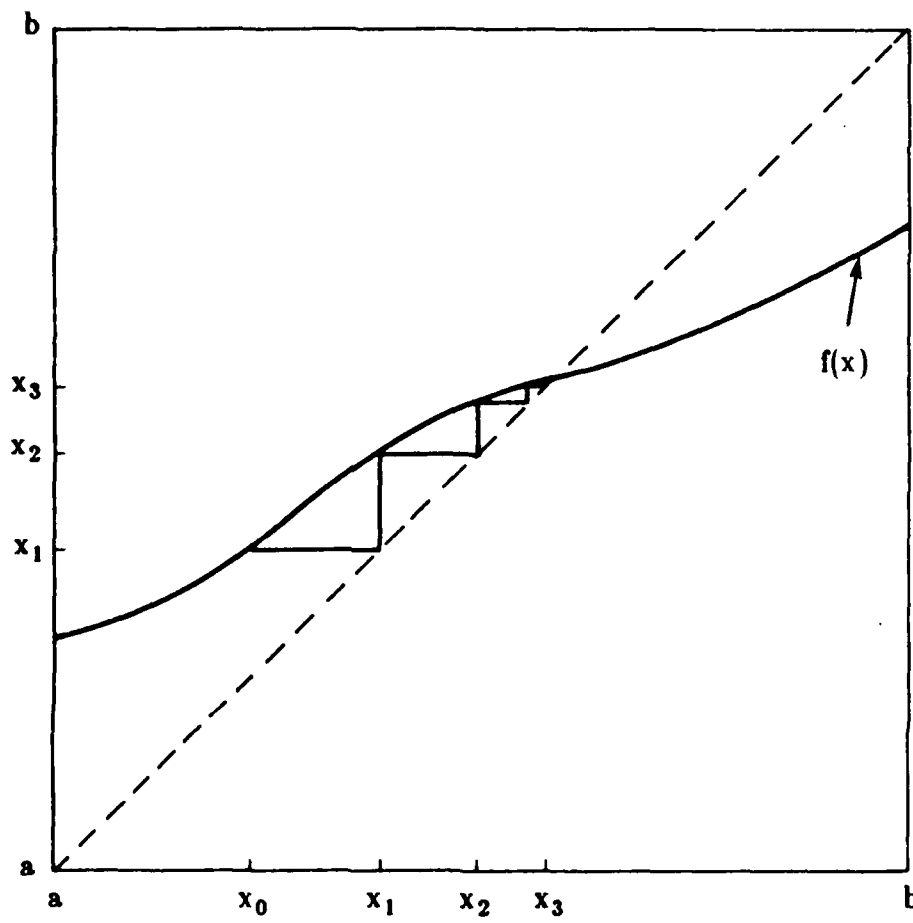


Figure 6.2

An initial estimate for the solution of the equation $f(x) = 0$ is refined using the iteration $x_i = f(x_{i-1})$.

$$|f'(x)| = \lim_{h \rightarrow 0} \left| \frac{f(x+h)-f(x)}{(x+h)-x} \right|. \quad (6.10)$$

But from equation (6.9) this ratio and the derivative are less than K .

To show the converse or that

$$|f'(x)| < 1 \quad x \in [a, b] \quad (6.11)$$

implies a contracting operator first assume the opposite case $|f(x_2)-f(x_1)| > |x_2-x_1|$. Without loss of generality assume x_2 is greater than x_1 and write the following integral

$$|f(x_2)-f(x_1)| = \int_{x_1}^{x_2} f'(x) dx. \quad (6.12)$$

There are two cases to consider. First assume that $f(x_2)-f(x_1) > 0$ and write

$$0 \leq f(x_2)-f(x_1) = \int_{x_1}^{x_2} f'(x) dx. \quad (6.13)$$

But if $f'(x) < K$ then this integral can be bounded from above by

$$0 \leq |f(x_2)-f(x_1)| = \int_{x_1}^{x_2} f'(x) dx < (x_2-x_1)K. \quad (6.14)$$

This contradicts the original assumption.

For the opposite case, $f(x_2)-f(x_1) < 0$,

$$|f(x_2)-f(x_1)| = f(x_1)-f(x_2) = -\int_{x_1}^{x_2} f'(x) dx. \quad (6.15)$$

But if $f'(x) > -K$ then

$$0 > f(x_2)-f(x_1) = \int_{x_1}^{x_2} f'(x) dx > -(x_2-x_1)K. \quad (6.16)$$

For both cases, $f(x_1) > f(x_2)$ and $f(x_2) > f(x_1)$, the original assumption is contradicted therefore proving that if $|f'(x)| < K$ then the function is a contracting operator.

To study the convergence of the fixed point method to the correct solution, ξ , assume a value for x_i . Then the error after the $i+1$ iteration is given by

$$\text{Error} = |x_{i+1} - \xi| = |f(x_i) - \xi|. \quad (6.17)$$

But since ξ is a fixed point solution of the function f this expression for the error can be written

$$\text{Error} = |x_{i+1} - \xi| = |f(x_i) - f(\xi)|. \quad (6.18)$$

By the contraction property of Equation (6.9) this last term is bounded from above by

$$|x_{i+1} - \xi| = |f(x_i) - f(\xi)| < K |x_i - \xi|. \quad (6.19)$$

Thus the error after the $i+1$ th iteration will always be less than the error after i iterations. In addition since K is less than one the sequence $|x_i - \xi|$ is bounded from above by the converging geometric series $x_0 K^i$ therefore the fixed point method converges to a correct answer.

That this solution is unique can be seen by assuming two solutions, ξ_1 and ξ_2 , to the equation $x=f(x)$. But these two solutions violate the contraction property since

$$|\xi_1 - \xi_2| = |f(\xi_1) - f(\xi_2)| > K |\xi_1 - \xi_2|. \quad (6.20)$$

Thus if $f()$ is a contracting operator then the fixed point solution will converge to the correct answer.

6.3.1 The Born Series

Recall from Chapter 2 the scattered field can be written

$$u_s(\vec{r}) = \int g(\vec{r} - \vec{r}') o(\vec{r}') u_0(\vec{r}') d\vec{r}' + \int g(\vec{r} - \vec{r}') o(\vec{r}') u_s(\vec{r}') d\vec{r}'. \quad (6.21)$$

The first Born approximation, as already described, simply represents the first iteration of the fixed point method with the initial guess $u_s^{(0)} = 0$. Thus the first iteration is written

$$u_s(\vec{r}) \simeq u_B(\vec{r}) = \int g(\vec{r} - \vec{r}') o(\vec{r}') u_0(\vec{r}') d\vec{r}'. \quad (6.22)$$

If the kernel, $g(\vec{r} - \vec{r}') o(\vec{r}')$, is a contracting operator an even better estimate can be found by substituting $u_0(\vec{r}) + u_B(\vec{r})$ for $u_0(\vec{r})$ in equation (6.22) to find

$$u_B^{(2)}(\vec{r}) = \int g(\vec{r} - \vec{r}') o(\vec{r}') [u_0(\vec{r}') + u_B(\vec{r}')] d\vec{r}'. \quad (6.23)$$

In general the i -th order Born field can be written

$$u_B^{(i+1)}(\vec{r}) = \int g(\vec{r} - \vec{r}') o(\vec{r}') [u_0(\vec{r}') + u_B^{(i)}(\vec{r}')] d\vec{r}'. \quad (6.24)$$

An alternate representation is possible if the total field is written

$$u(\vec{r}) = u_0(\vec{r}) + u_1(\vec{r}) + u_2(\vec{r}) + \dots \quad (6.25)$$

where

$$u_{(i+1)}(\vec{r}) = \int u_i(\vec{r}') o(\vec{r}') g(\vec{r} - \vec{r}') d\vec{r}' \quad (6.26)$$

By expanding equation (6.24) it is possible to see that the fixed point approximation for the scattered field, $u_B^{(i)}$, is

$$u_B^{(i)}(\vec{r}) = \sum_{j=0}^i u_j(\vec{r}) \quad (6.27)$$

and in the limit

$$u(\vec{r}) = u_0(\vec{r}) + u_1(\vec{r}) + u_2(\vec{r}) + u_3(\vec{r}) + \dots \quad (6.28)$$

This representation (6.28) has a more intuitive interpretation analogous to the Huygens principle. The Green's function gives the scattered field due to a point scatterer and thus the integral of equation (6.24) can be interpreted as calculating the first order scattered field due to the field u_i . For this reason the first order Born approximation represents the first order scattered field and u_i represents the i 'th order scattered field.

A variation of the integral Born series presented here was first described and implemented by Azimi and Kak [Azi83]. In [Azi83] the scattered fields are calculated for an object that consists of multiple cylinders by considering the interactions of the scattered field with the other objects. Using the equations presented in Chapter 5 and [Wee64] and [Mor68] it is possible to calculate the exact scattered field from a cylindrical object illuminated with a plane wave. Unfortunately it is not possible to calculate the exact fields scattered by a pair of cylinders using this approach because the field from one object interferes with the other.

Instead Azimi and Kak propose a multiple scattering approach where the incident field is first scattered against each cylinder and then the scattered fields from each cylinder are propagated to the other cylinder(s) where they are scattered again. This is illustrated in Figure 6.3 where the incident field is denoted by u_0 and the field u_{ijk} denotes the field that has scattered off of object i , then object j and finally object k .

Since the field scattered by a cylinder is not a plane wave the key to this procedure is to calculate the scattered fields along lines between the cylinders. The field along this line can then be decomposed into plane waves [Goo68] and each plane wave scattered separately by the cylinder.

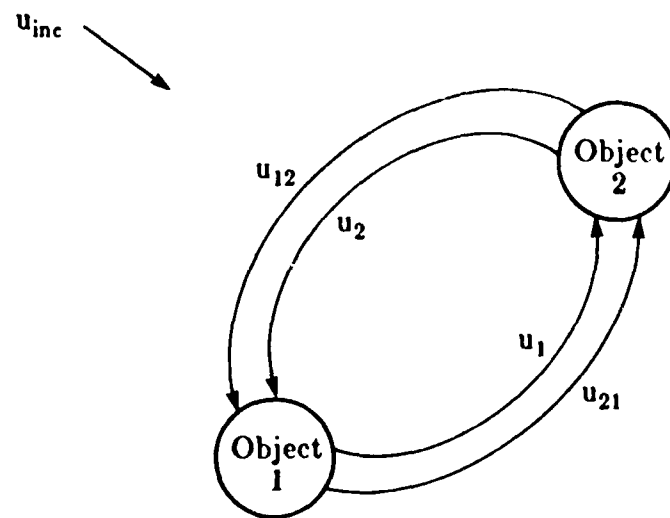


Figure 6.3

The incident field is scattered against each cylinder and the resulting fields are propagated to other cylinder for additional scattering.

While nothing is known about the convergence of this series its use in diffraction tomography is limited because it is only practical when the field scattered from each object can be computed exactly. Thus it has been used as a method to generate data for testing diffraction tomography algorithms.

Under both the Born and Rytov approximations an integral of the form

$$u_{i+1}(\vec{r}) = \int u_i(\vec{r}') o(\vec{r}') g(\vec{r}-\vec{r}') d\vec{r}' \quad (6.25)$$

is to be evaluated. A naive approach to this integral would be to evaluate it numerically but doing this requires on the order of N^4 operations. Performing the integration over a 128×128 grid, for example, would require over 270 million operations per iteration. This is clearly unreasonable.

The computational requirements can be greatly reduced by noting that the Green's function, $g(\vec{r}-\vec{r}')$, is only a function of the difference between the two points and that the integral can also be interpreted as a convolution. Thus representing the convolution in the frequency domain allows for an efficient implementation requiring only $6N^2 \log N$ operations to do the integration. For a 128×128 grid this is only 700 thousand operations or a reduction in the computational complexity by almost 400. This approach is efficient using an array processor and for an object sampled over a 64×64 grid this integral can be computed in under 2 seconds using a Floating Point Systems AP120B array processor.

To evaluate the Born integral on a digital computer it is necessary to use a truncated and sampled version of the object function and the field. Truncating the two functions is error free because the object function is assumed to have finite support. In addition since only a finite number of receivers are present this further limits the number of data points that need to be calculated. On the other hand, since any function with finite support has infinite bandwidth it is not possible to sample the data without introducing errors. For smoothly varying data it is possible to approximate the data with discrete samples. In the work to follow the samples are taken over a rectangular grid using different sampling intervals, all less than a wavelength.

If the series u_i decays to zero then the total field is given by a summation of each scattered field, or

$$u_s(\vec{r}) = \sum_{i=1}^{\infty} u_i(\vec{r}) \quad (6.29)$$

Two different studies were performed to verify this approach to solving the wave equation. Most importantly it was necessary to verify that the total scattered field converged to the same answer as predicted by an exact solution to the wave equation. In addition it was necessary to determine the region of convergence of the Born series. These issues will be discussed later in this chapter.

As mentioned before, the integral equation in (6.25) is efficiently evaluated by implementing the convolution in frequency domain. Recapitulating this discussion, the frequency domain implementation can be summarized as follows.

First for all x_j and y_k , the scattering potential, S , is calculated from the product of the "incident" field and the object,

$$S(x_j, y_k) = U_i(x_j, y_k) O(x_j, y_k). \quad (6.30)$$

Then by using two-dimensional FFT's, determine the following two transforms

$$S(u_j, w_k) = T^2 \text{FFT} \left\{ S(x_j, y_k) \right\} \quad (6.31)$$

$$G_i(u_j, w_k) = T^2 \text{FFT} \left\{ G(x_j, y_k) \right\}. \quad (6.32)$$

To find the Fourier transform of the scattered field form the following product in the frequency domain for all u_j and w_k

$$U_{i+1}(u_j, w_k) = S(u_j, w_k) G(u_j, w_k). \quad (6.33)$$

The $i+1$ 'th scattered field is then found by inverting the above expression to find

$$u_{i+1}(x_j, y_k) = \frac{1}{T^2} \text{IFFT} \left\{ U_{i+1}(u_j, w_k) \right\}. \quad (6.34)$$

To properly calculate the integral using the FFT approach it is necessary to remember that the discrete multiplication implements a circular convolution. A circular convolution can be turned into an aperiodic convolution by zero padding the data [Opp75]. For example a Floating Point Systems (FPS) AP120B Array Processor with 65,536 words of main data memory can only deal with arrays up to 128×128 elements. This memory limitation and the need to implement an aperiodic convolution limits the evaluation of the field to a 64×64 grid.

The exact scattered field from a dielectric cylinder with plane wave illumination is well known in the literature. This exact solution to the wave equation can be used to check the results of the Born iteration. Figure 6.4 shows a simulated experiment. In this experiment a plane wave is incident on a cylinder of radius 2λ and a refractive index of 1.1. The scattered field was calculated at 64 receiver positions along a line 7.75λ from the center of the object.

Figure 6.5 show the exact scattered field along the receiver line. In each of the plots that follow the real components of the field will be shown with a solid line, while the dotted lines represent the imaginary part of the field.

Figure 6.6 shows the result of iterating the Born integral. The first Born approximation (Figure 6.6a) gives a very poor estimate of the exact field since this estimate is based only on first order scattering.

In order to accurately calculate the scattered fields it is necessary to include the higher order scattered fields. This is shown in figure 6.6. Clearly in this case even the 30'th to 100'th order scattered fields are significant to the total field.

By comparing figures 6.6 and 6.5 it can be seen that in this case the Born series converges to the exact scattered fields. This simple example shows the correctness of the Born iteration code.

The Born integral defines an infinite series of partial scattered fields that are summed to find the total scattered field. An important measure of any infinite series is its region of convergence. The region of convergence defines a class of objects where the Born iteration converges to the exact scattered field. For an arbitrarily complex object the region of convergence is defined over an infinite dimensional space since an infinite number of parameters are needed to describe the object.

There are two trivial objects that can be analyzed analytically. First consider a pair of point scatterers separated by a distance of R located at \vec{r}_1 and \vec{r}_2 . If each scatter has an area (or volume) of σ and the object function for each of these scatterers is equal to O then an approximation to the first order Born field at \vec{r}_2 due to the scatterer at \vec{r}_1 is

$$u_1^1(\vec{r}_2) \simeq \sigma G(R)O \quad (6.35)$$

Clearly there exists a value of O such that u_1^1 will have a magnitude greater than the incident field. This field, u_1^1 , can then be scattered with the point scatterer at \vec{r}_2 and measure the field at \vec{r}_1 to find

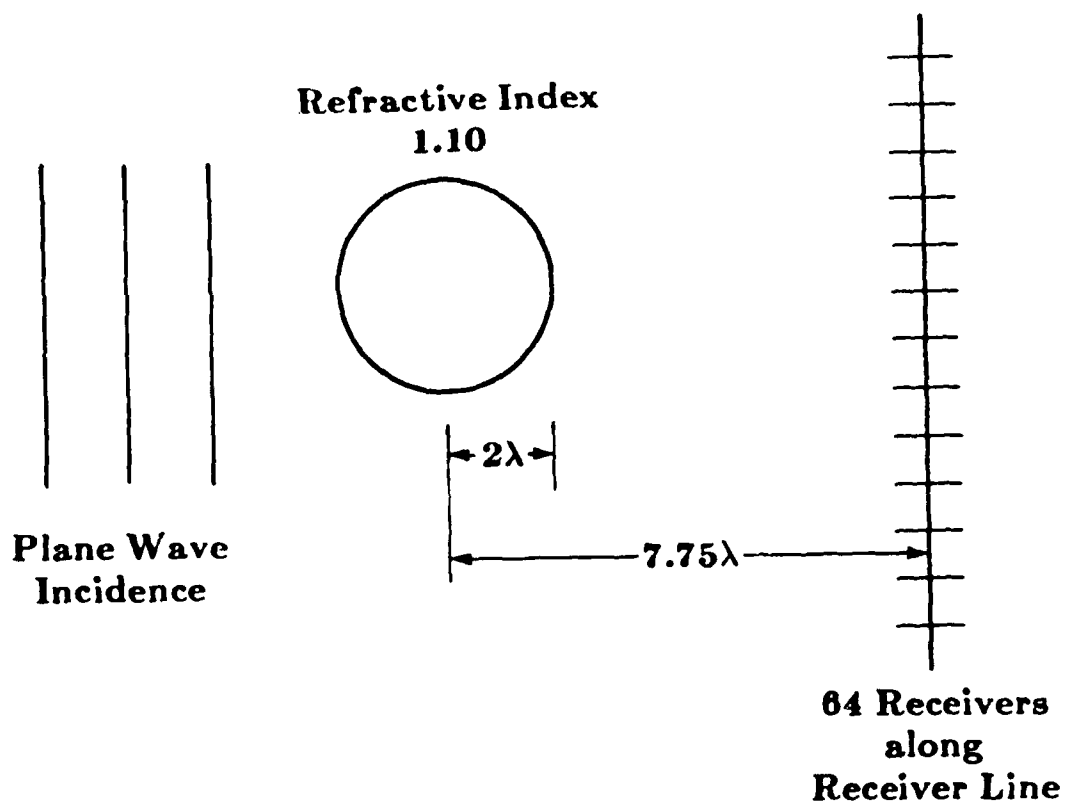


Figure 6.4

An experiment used to illustrate the higher order Born series.

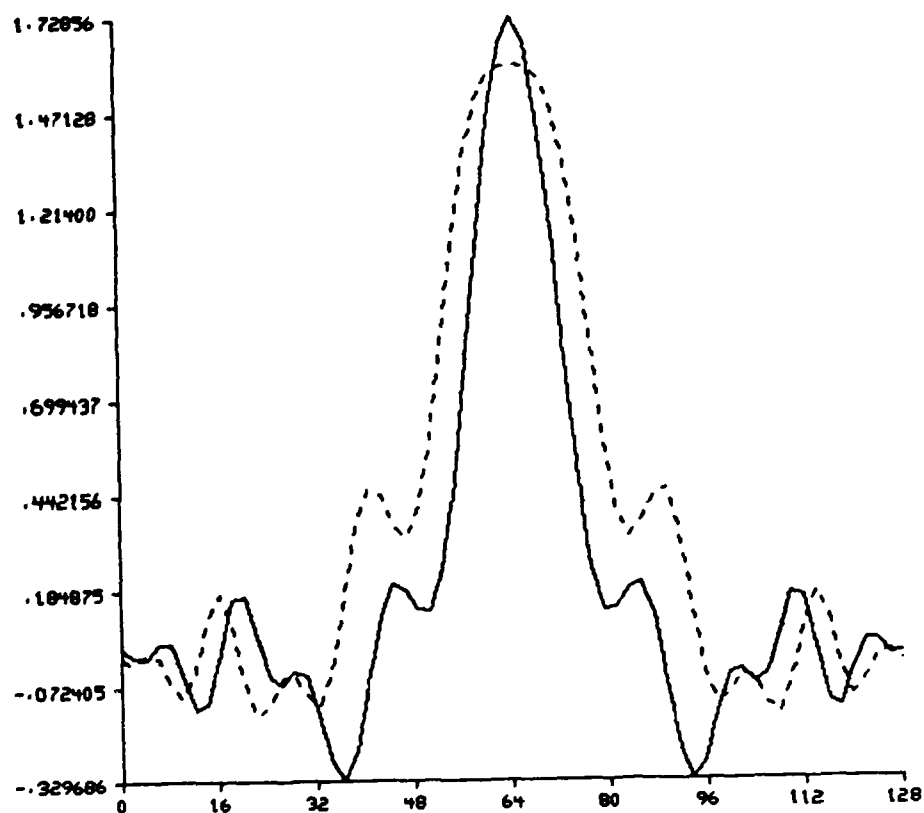


Figure 6.5

Exact scattered field for the object shown in Figure 6.4. The real component of the field is shown as a solid line while the imaginary component is dashed.

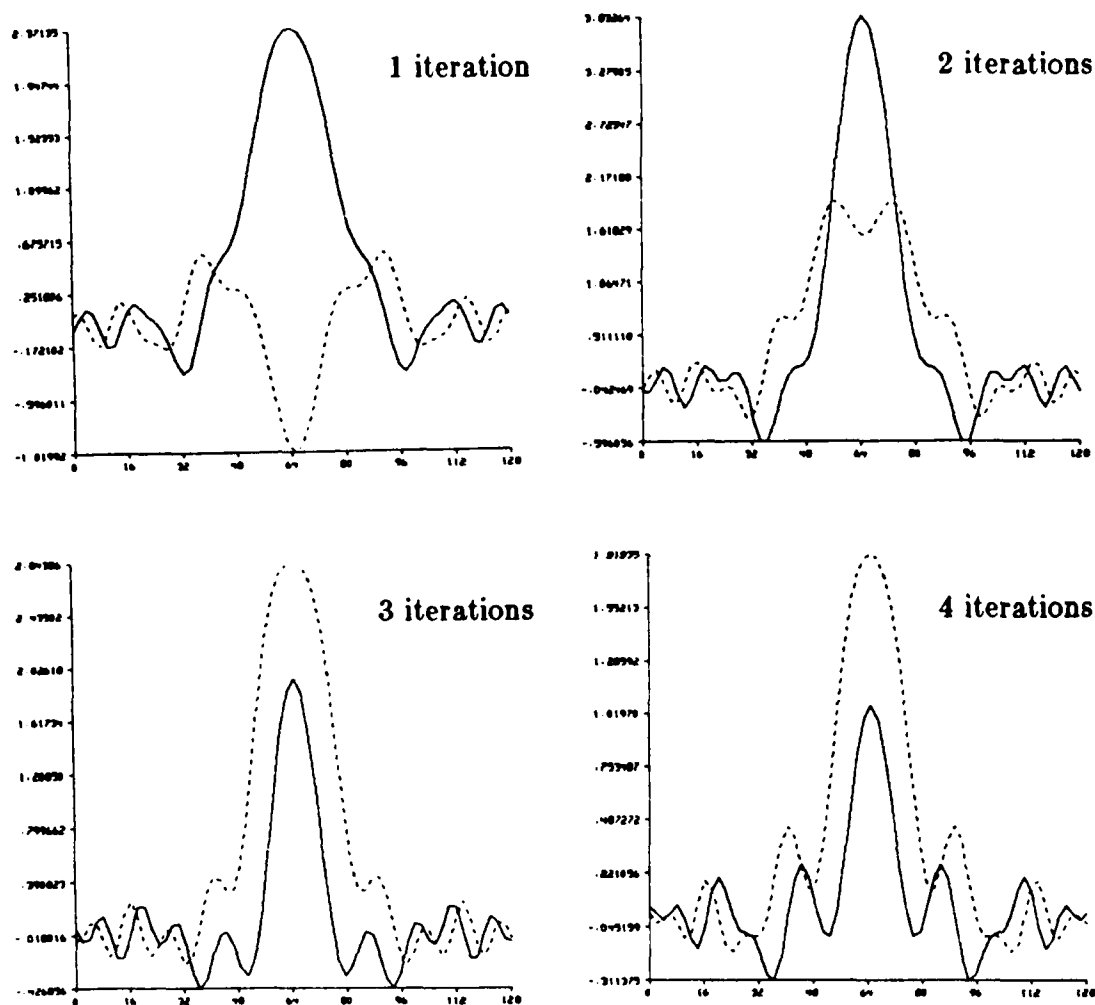


Figure 6.6

The scattered field as calculated from the Born series using terms numbered from 1 to 100.

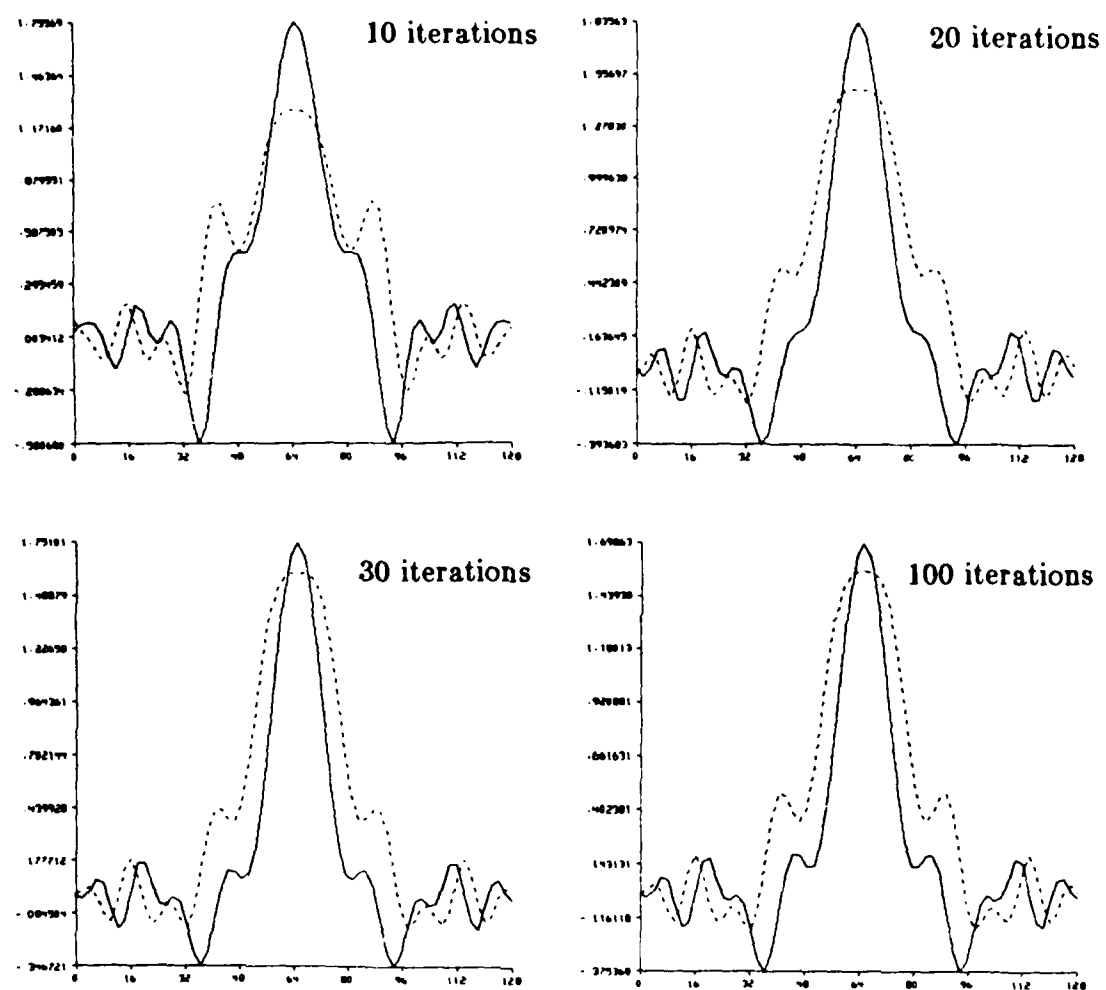


Figure 6.6

Continued.

$$u_2^{12}(\vec{r}_1) \simeq \sigma G(R) O[u_1^1(\vec{r}_2)] \quad (6.36)$$

If the term $\sigma G(R)O$ is greater than one then each succeeding term of the series u_i will diverge. This analysis has ignored the effect of the other scatterer and the field at \vec{r}_1 caused by the scatterer at \vec{r}_1 but this doesn't change the basic conclusion, that the Born series can converge or diverge depending on the object.

This effect can also be analyzed in the frequency domain. By taking the Fourier transform of equation (6.25) the convolution with the Green's function can be expressed as a multiplication in the spatial frequency domain. Equation (6.25) becomes [Sla83, Sla84]

$$U_{i+1}(\vec{K}) = G(\vec{K}) \left\{ \hat{O}(\vec{K}) * U_i(K) \right\} \quad (6.37)$$

where '*' represents convolution in the frequency domain.

If the object function is assumed to be constant for all space then $O(\vec{K})$ becomes an impulse and equation (6.37) above becomes

$$U_{i+1}(\vec{K}) = OG(\vec{K})U_i(K). \quad (6.38)$$

This is a simple result and it is easy to see that the series, u_i , will diverge if there is any frequency where

$$G(\vec{K})O > 1. \quad (6.39)$$

In this simulation study the region of convergence for a single homogeneous cylindrical object was examined. Since any cylinder can be completely described by its size and refractive index the region of convergence is defined over a two dimensional space. More complicated objects could be studied but the results would not be as graphical.

It has already been shown that for either small cylinders or small changes in the refractive index the first Born approximation provides a good estimate to the exact scattered field. This is equivalent to saying that the higher order scattered fields decay quickly towards zero. It is easy to see that under these two conditions the Born integral series will quickly converge to the exact solution.

The total energy in the two dimensional field is used as a simple measure of convergence. Obviously if the total energy in the i 'th scattered field is decaying towards zero as the Born integral is iterated then the series is

converging. On the other hand if the total energy is increasing then the Born integral can not possibly converge.

For a given object radius the region of convergence is determined by conducting a binary search for the largest refractive index where the Born series converges. For each combination of object size and refractive index it is necessary to make a decision of convergence or divergence and adjust the refractive index accordingly.

The decision of convergence or divergence is made by studying the total energy in the partial scattered field as the iterations are performed. For this purpose a series is defined to be convergent if during each of four iterations the total energy in the partial scattered fields is monotonically decreasing. While if the energy is monotonically increasing then it is decided that the series diverges. As long as the last four terms are not monotonic than the iterations continue. The energy versus iteration number for the experiment of figure 6.4 is shown in figure 6.7.

Figure 6.8 displays the region of convergence for sampling intervals of 0.125λ , 0.25λ and 0.5λ . Each plot shows the maximum refractive index as a function of cylinder radius. For all experiments with a refractive index below the line the Born series converges, while for all experiments above the line the series diverges.

In each case the shape of the curve agrees with the original observation; the Born series converges for either small objects or small changes in the refractive index. The dependence of the region of convergence on the sampling interval is still under study. One possible explanation is that the numerical errors are larger for the larger sampling intervals.

While more complicated objects can be simulated it is more difficult to present the region of convergence in a simple fashion. In general the region of convergence will be described over a multidimensional space but can be reduced to two dimensions by keeping some of the parameters fixed. Two simple families of object that can be reduced to a two dimensional space will be described next. In each case the results will be compared to the results for a cylindrical object.

A simple extension of the previous work for a single cylinder is to consider two cylinders separated by a small distance. Figure 6.9 shows the region of convergence for two orientations of the cylinders with respect to the incident field. In both cases two identical cylinders are separated by a distance of 1λ . Thus the region of convergence is reduced to two dimensions, the radius of the

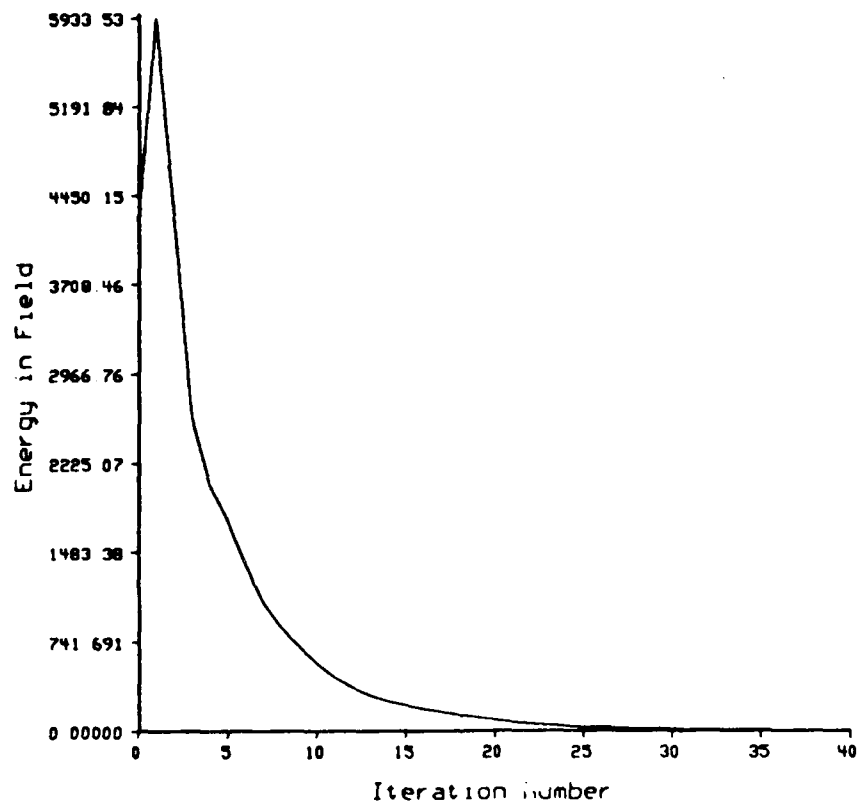


Figure 6.7 Total energy in the higher order scattered field versus iteration number.

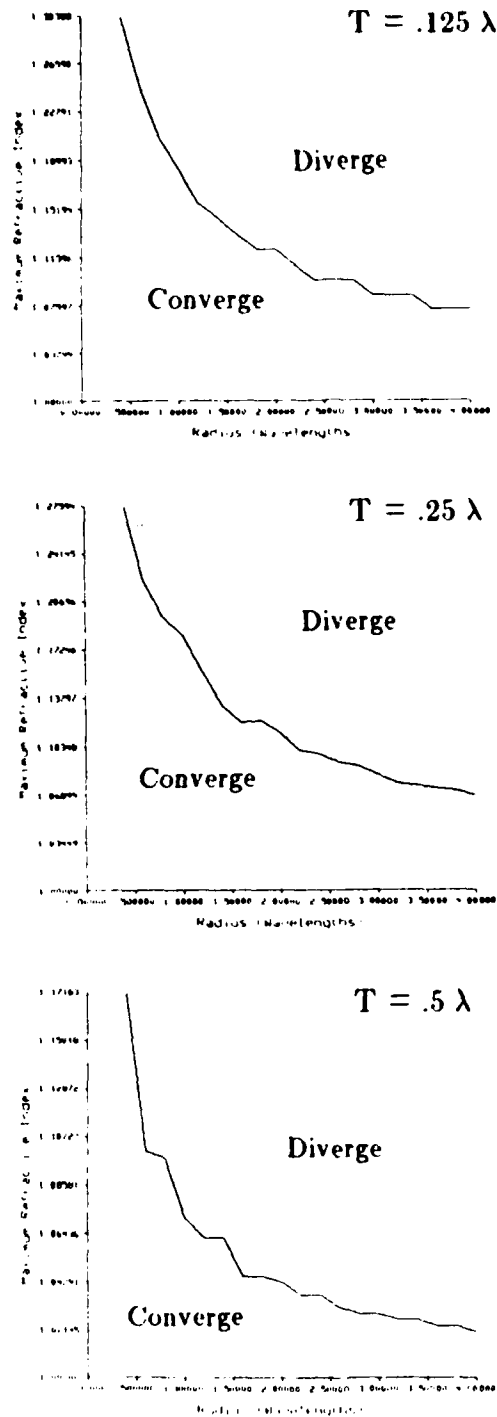


Figure 6.8

Region of convergence for the Born series using sampling intervals of $.125\lambda$, $.25\lambda$ and $.5\lambda$.

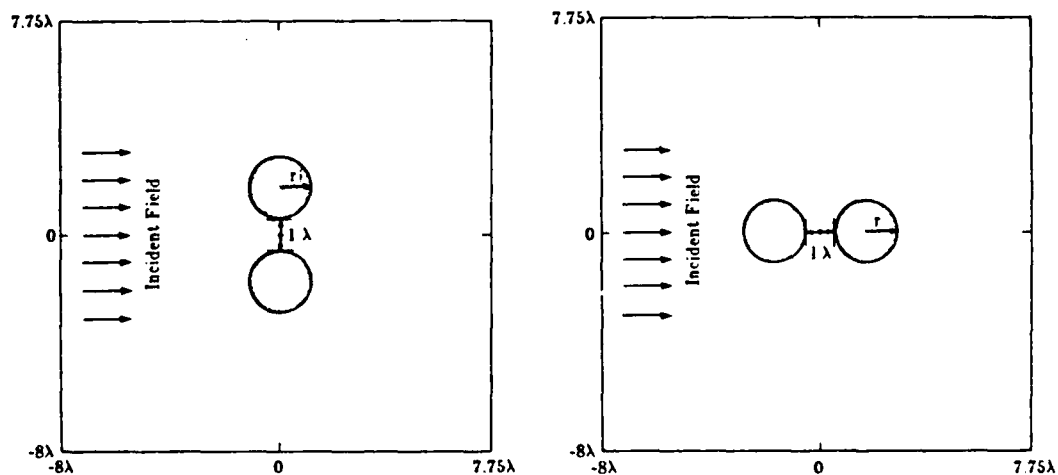
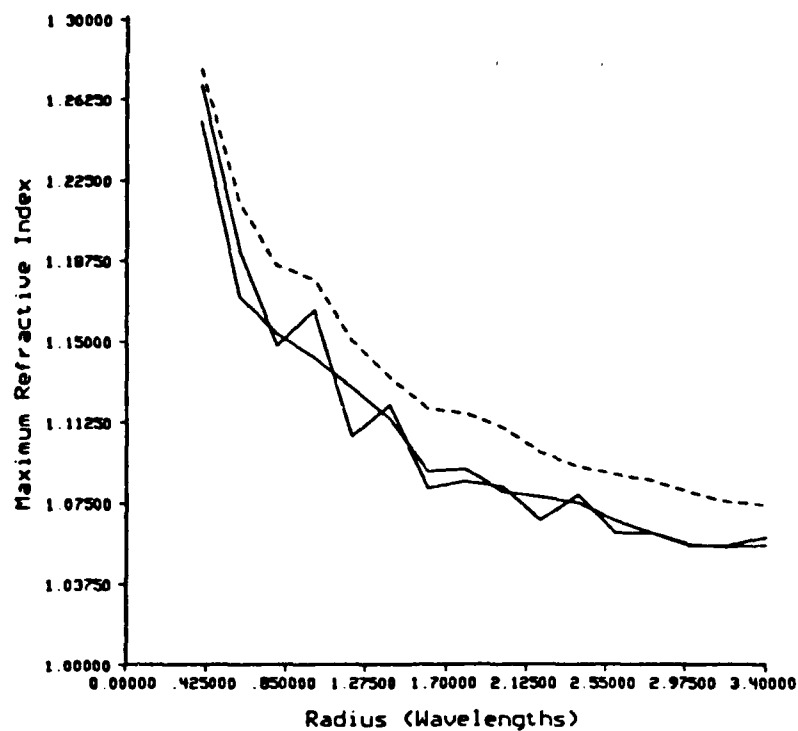


Figure 6.9

Born series region of convergence for two cylinders of radius r separated by 1λ . The solid lines show the convergence for two orientations. The dashed line shows the convergence for a single cylinder of radius r .

two cylinders and their refractive index. The solid lines in Figure 6.9 show the region of convergence for the two cylinders compared to that for a single cylinder (shown as a dashed line).

As would be expected the region of convergence for two cylinders is always smaller than that for a single cylinder. This is true since the convergence is plotted as a function of the radius of one of the cylinders and adding another cylinder increases the scattered field. As already described increasing the scattered field can only cause the Born series to converge more slowly.

Figures 6.10 and 6.11 show the region of convergence for a single ellipse with an eccentricity of 2 (length of major axis over minor axis is 2.) Since an ellipse can not be described by its radius the region of convergence is plotted as a function of the length of both the major and minor axis of the ellipse. The two figures differ only in the orientation of the ellipse with the incident field and in both cases the convergence for a single cylinder as a function of its radius is plotted as a dashed line.

The convergence of the Born series for an ellipse (solid lines) compared to a cylinder (dashed lines) is consistent with the idea that more scattering leads to the divergence of the Born series. The upper solid lines show the convergence plotted as a function of the ellipse's major axis and is above the dashed lines for all lengths. This is because an ellipse with major axis of length $2r$ has less area than a circle of radius r . Conversely the lowest line (solid) plots the convergence as a function of the ellipse's minor axis and is always below the dashed lines. (Note that the two solid lines represent the same ellipse. The only difference is that region of convergence is plotted with respect to different parameters.)

Figure 6.12 shows the same data as the previous two figures but now the two orientations are superimposed. From this figure it is easy to see that the convergence of the Born series is sensitive to the orientation of the ellipse. When the major axis of the ellipse is parallel to the direction of the incident field the region of convergence is reduced. This is consistent with the limitation described in Chapter 2 that the phase change in the field as it travels through the object is a good indication of the validity of the Born approximation. When the major axis is aligned with the incident field the phase change is larger than when it is perpendicular to the field and thus the Born series is more likely to diverge.

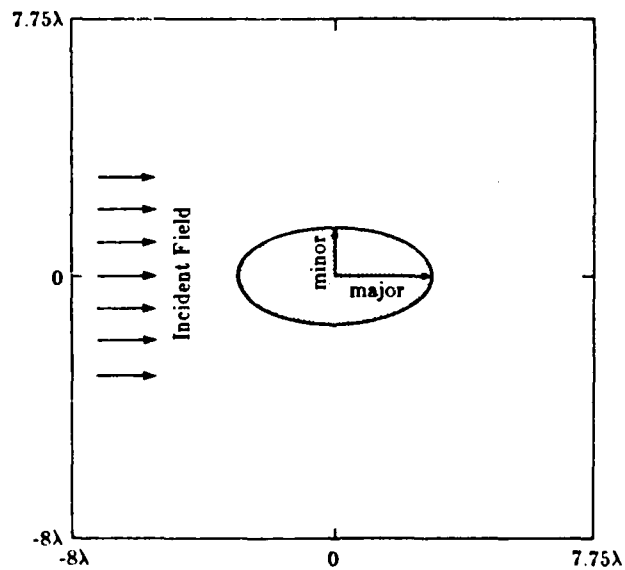
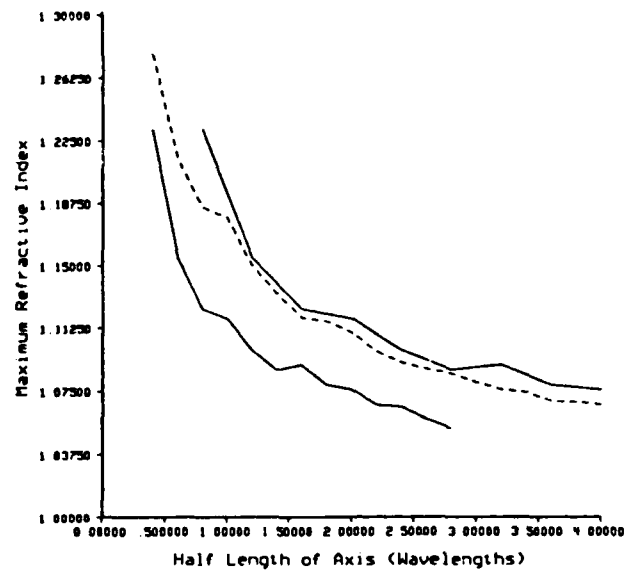


Figure 6.10

Born series region of convergence for an ellipse. The solid lines show the convergence for the ellipse as a function of its major axis (upper line) and minor axis (lower line). The dashed line shows the convergence for a single cylinder.

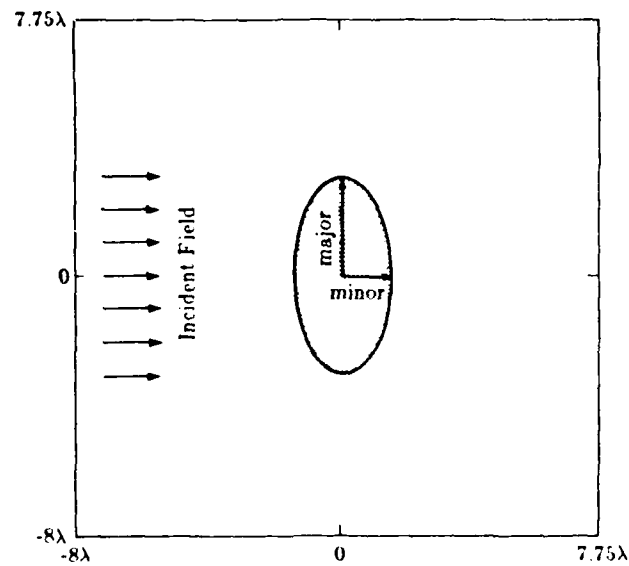
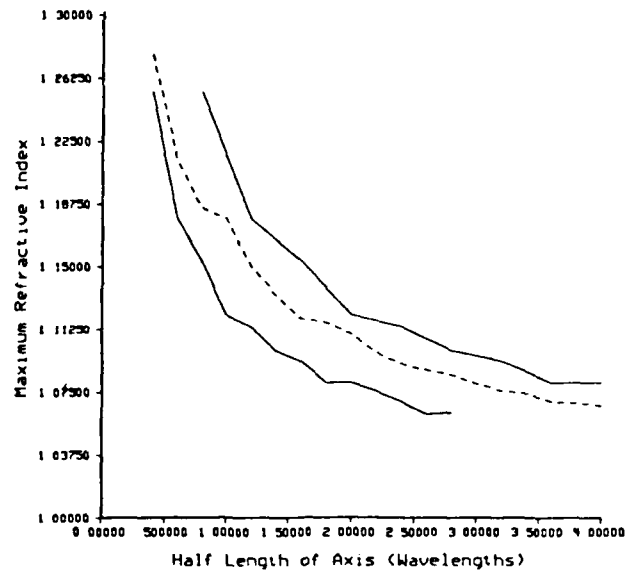


Figure 6.11

Born series region of convergence for the object shown in Figure 6.10 but rotated 90 degrees.

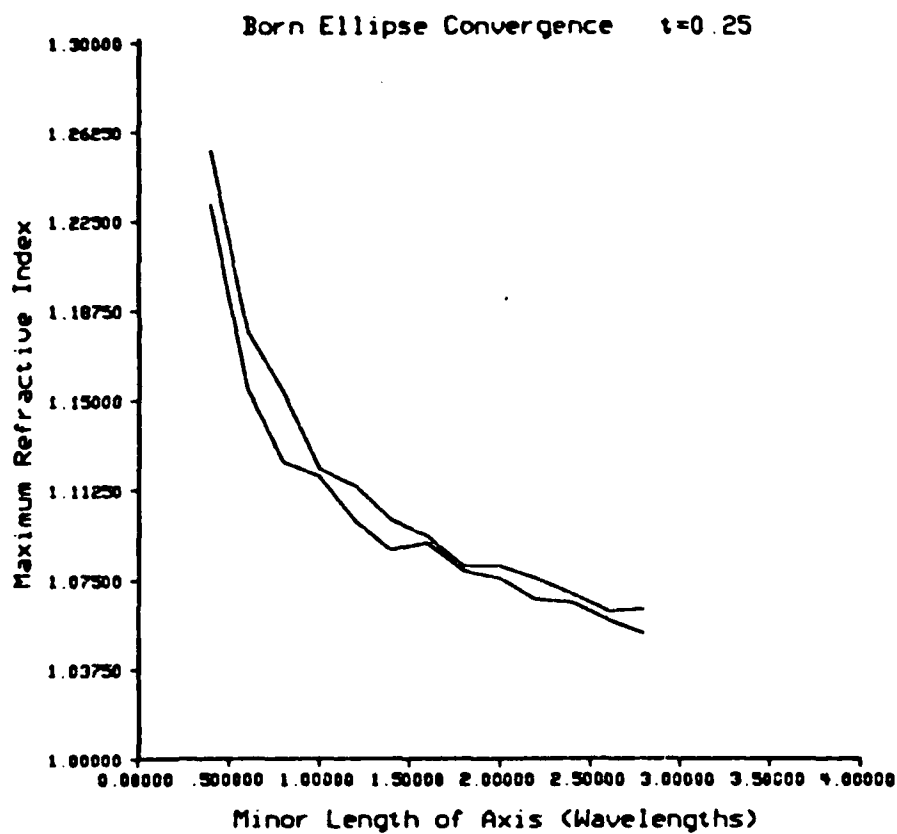


Figure 6.12

The region of convergence for two orientations of an ellipse are compared. The upper curve represents the convergence for the ellipse shown in Figure 6.11 while the lower curve represents the convergence shown in Figure 6.10.

6.3.2 Born Series with Attenuation

While to this point only fields in non-attenuating media have been discussed it is easy to also talk about the Born series when attenuation is present. Now the refractive index and the wavenumber are no longer just real valued and include an imaginary component to represent the attenuation.

The relationship between the real and imaginary components of the wavenumber are easily seen by examining one solution to the homogeneous wave equation

$$u_0(\vec{r}) = e^{jk_0x} \quad (6.40)$$

where $\vec{r} = (x,y)$. If k_0 is complex and equal to

$$k_0 = k_r + jk_i \quad (6.41)$$

then the real component will continue to represent the periodic component of the field. The imaginary component, k_i , contributes a multiplicative term, $e^{-k_i x}$, that causes attenuation of the plane wave with increasing distance.

There are two approaches that can be used to deal with attenuation. In the simpler approach the average wavenumber, k_0 , is real and all of the attenuation is a perturbation from the average wavenumber. Thus the object function is complex and as will be shown shortly the region of convergence is reduced for large attenuations. In the second approach the attenuation is included in the average wavenumber thus reducing the magnitude of the object function. The only difference in the formulation is that the Green's function changes but now increasing attenuation leads to a larger region of convergence.

When the attenuation of the object is treated as just a perturbation of the object function from the real valued wavenumber then the effect is to reduce the region of convergence. This is shown in Figure 6.13 where it can be seen that the magnitude of the object function, not just the refractive index, determines the convergence of the Born.

The work first done with the Born approximation assumed that the average refractive index was real valued only. Since the real part of the wavenumber represents the speed of the wave and the imaginary part its attenuation, any attenuation in the object is included in the unknown perturbation. The magnitude of the perturbation determines the applicability of the Born and Rytov series therefore a more accurate estimate of the average refractive index will lead to smaller perturbations and better results with first order diffraction tomography algorithms.

Born Convergence

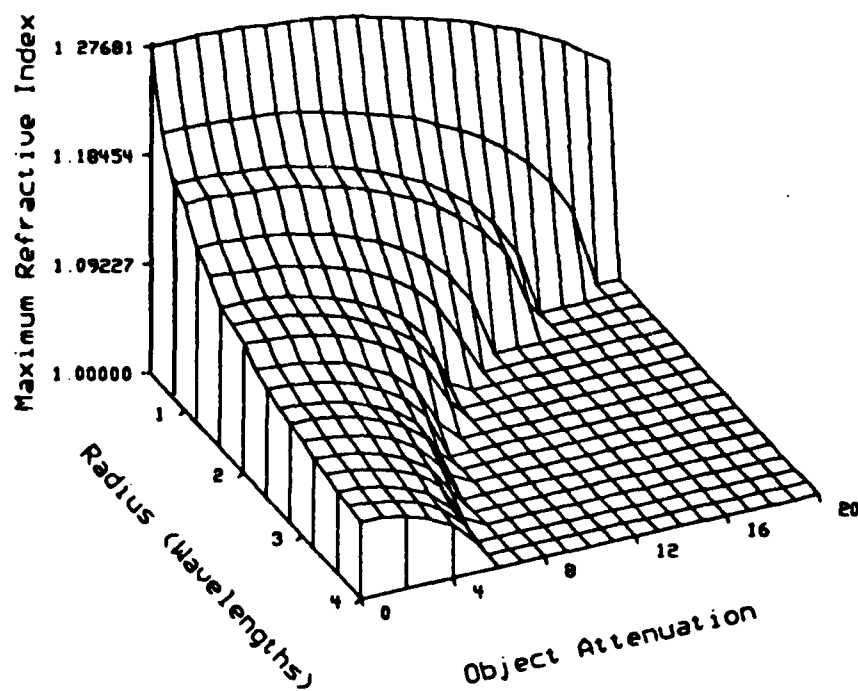


Figure 6.13

The region of convergence for the Born series as a function of cylinder radius and attenuation. The attenuation is plotted in units of nepers (1 neper represents an attenuation of the fields amplitude by 63% per wavelength.).

Consider an experiment where an object and the surrounding media are both highly attenuating. This might be typical of a microwave tomography experiment where the attenuation of microwaves is predominately due to the water molecule.

In this case a small perturbation model would be more accurate if the average value of the wavenumber, k_0 , is assumed to include an imaginary component. Thus the real part continues to represent the spatial frequency of the wave while the imaginary part indicates the bulk attenuation of the wave as it travels through the media.

An important part of this derivation is to remember that a field can be described in two different manners; if you like, there are two sets of basis functions that can be used. A field that satisfies the Helmholtz equation is usually described in terms of plane waves. A plane wave is an exponential solution to the Helmholtz equation and for a plane field described by

$$u(\vec{r}) = e^{j\vec{k}\cdot\vec{r}} \quad (6.42)$$

where

$$\vec{k} = (k_x, k_y) \quad (6.43)$$

then valid plane waves satisfy

$$k_x^2 + k_y^2 = k_0^2. \quad (6.44)$$

k_0 in this equation represents the wavenumber of the media.

A problem with this approach is that both k_x and k_y can be complex. The complex valued wavevectors lead to evanescent waves which attenuate with distance. While for most applications the evanescent fields can be ignored (they tend to be small compared to the non attenuating components) the same assumption can not be made when calculating the field inside the object or when the object is in an attenuating media.

Consider an attenuating plane wave propagating in the x direction

$$u(\vec{r}) = e^{j\vec{k}\cdot\vec{r}} = e^{jkx} = e^{j(\alpha + j\beta)x} \quad \beta \geq 0 \quad (6.45)$$

In this case α represents the phase term, while β represents the attenuation. For positive x this is an attenuating plane wave, but for negative x the wave grows exponentially. Thus it is normally necessary to specify that the wave is zero for $x < 0$.

Due to the non symmetry of attenuating plane waves and the efficiency of Fast Fourier Transform algorithm a much more natural set of basis functions is provided by the Fourier domain. In this approach the field is represented as a

sum of Fourier components. If the field does not have any evanescent components the Fourier and the plane wave representations are identical.

The distinction becomes important when attenuating fields are considered. Mathematically the two approaches are equally valid but while an attenuating plane wave has a single component in the plane wave representation it has an infinite number of Fourier components. The difference is further illuminated if an attenuating plane wave is propagating through a homogeneous media. This field is represented as a single plane wave that satisfies the wave equation but its Fourier representation has an infinite number of components. While each of its Fourier components do not satisfy the wave equation they do represent a set of basis functions for describing linear operators. For this reason the Fourier approach is optimum for propagation problems [Goo68] and convolution integrals.

Again, like was done for the non attenuating Born, Figure 6.14 shows the components of the Born integral for a complex wavenumber. The major differences are that the incident field becomes an attenuating plane wave and the attenuating Green's function is more straightforward to calculate since it no longer has a singularity in the frequency domain.

The incident field

$$u(\vec{r}) = e^{j(\alpha + j\beta)x} \quad x > 0 \quad (6.46)$$

is a complex (2 dimensional) function and its Fourier transform can be found by considering it as a multiplication of a complex sinusoid by a one sided exponential. The following one dimensional Fourier pairs are used:

$$e^{j\omega_0 t} \leftrightarrow 2\pi\delta(\omega - \omega_0) \quad (6.47)$$

and

$$e^{-\alpha t} \quad t \geq 0 \leftrightarrow \frac{1}{j\omega + \alpha} \quad (6.48)$$

Multiplication in the space domain corresponds to convolution in the frequency domain so the Fourier transform of an attenuating sinusoid is written

$$\frac{2\pi}{j(\omega - \omega_0) + \alpha} \quad (6.49)$$

In two dimensions the Fourier transform of the incident field is written

$$U_0(\vec{K}) = \frac{\delta(k_y)2\pi}{j(k_x - \alpha) + \alpha} \quad (6.50)$$

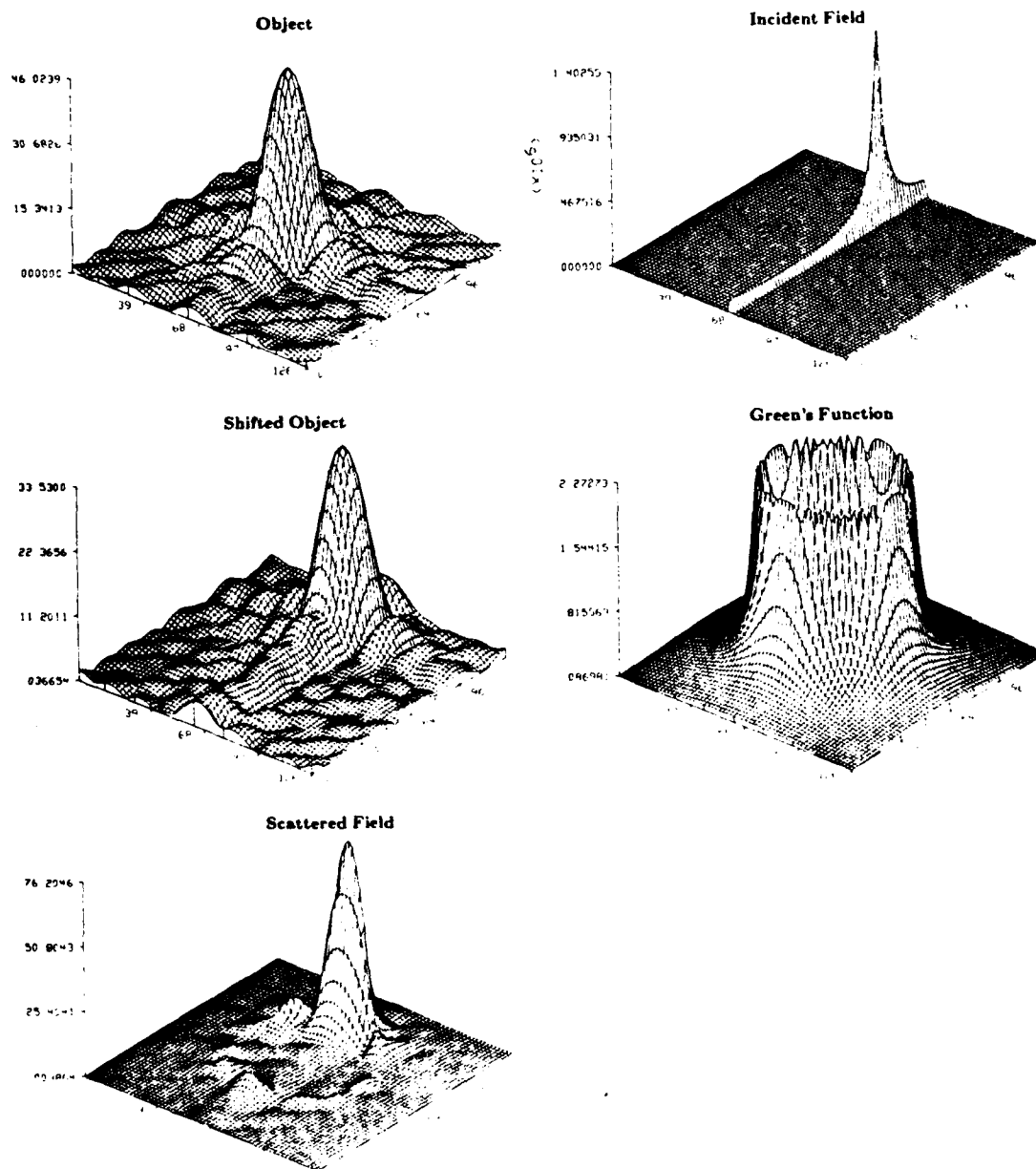


Figure 6.14

The Fourier transform of several steps in the derivation of the scattered field in an attenuating media.

where the wavevector of the incident field is given by $\vec{\Lambda} = (\alpha, \beta)$. This is shown in Figure 6.14(Incident Field).

The Green's function for complex values of k_0 is even simpler than the non-attenuating case. By taking the Fourier transform of the wave equation with a delta forcing function it is easy to see that

$$G(\vec{\Lambda}) = \frac{1}{|\vec{\Lambda}|^2 - k_0^2}. \quad (6.51)$$

Since $|\vec{\Lambda}|^2$ is real and k_0^2 is complex there are no singularities in this function. The Fourier transform of the Green's function is still circularly symmetric and is shown in Figure 6.14(Green's Function).

The Fourier transform of the two dimensional scattered field can be written now as

$$U_s(\vec{K}) = G(\vec{K}) [U_0(\vec{K}) * O(\vec{K})]. \quad (6.52)$$

The convolution of the incident field and the object is a shifted and a smeared version of the Fourier transform of the object. The convolution can be considered in two parts. The smearing caused by the width of the incident field in the spatial frequency domain can be ignored since it just redistributes some of the energy of the object function's Fourier transform. The remaining component, the shift in the frequency domain, is identical to the non attenuating Born case.

As derived above, the Green's function for an attenuating media does not have a ring of singularities and therefore samples a semi-circular region of the modified object function. This is shown in Figure 6.14(Scattered Field).

This procedure naturally leads to the Born series for objects with bulk attenuation. Figure 6.15 shows a composite graph of the region of convergence for a number of different attenuating media between 0 and 1 nepers per wavelength. It is interesting to note that the region of convergence gets larger as the attenuation increases. This is due to the reduction in multiple scattering because to the attenuating term in each wave. Thus for an average attenuation of 1 neper per wavelength (the amplitude of the field drops by 3dB per wavelength) the Born series converges for all objects with a refractive index less than 20%. In addition the convergence of the Born is less sensitive to the size of the object since the waves are attenuated before they travel the complete distance of the object.

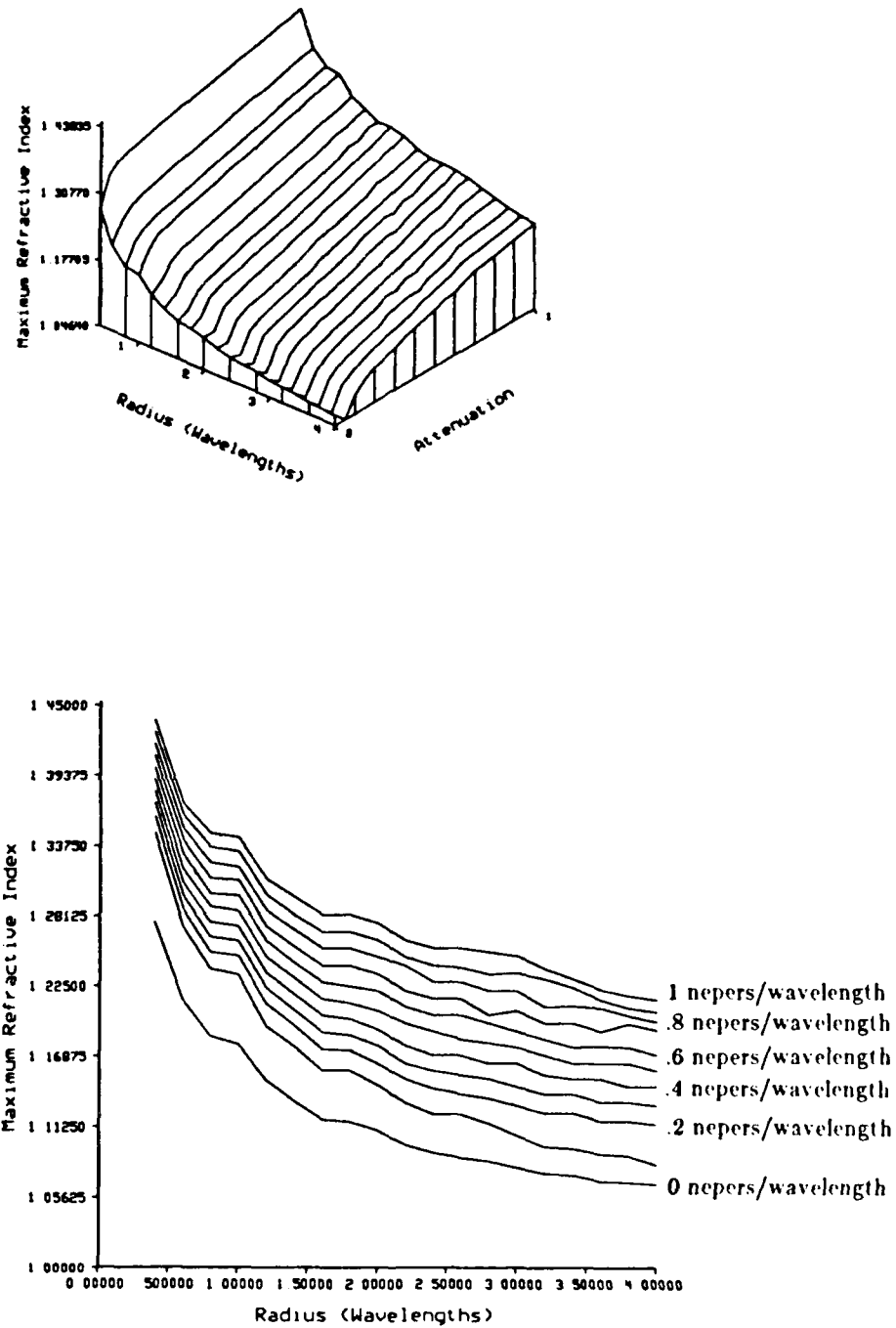


Figure 6.15

The region of convergence for the Born series as a function of cylinder radius and average attenuation of the media.

6.3.3 Rytov Series

The implementation of the Rytov series is much like that of the Born. Thus from Chapter 2 the Rytov integral for the scattering phase is written

$$\psi_1(\vec{r}) = \frac{1}{u_0(\vec{r})} \int_V g(\vec{r}-\vec{r}') [\nabla \psi_1(\vec{r}') \cdot \nabla \psi_1(\vec{r}') + o(\vec{r}')] u_0(\vec{r}') d\vec{r}'. \quad (6.53)$$

A fixed point solution to this equation is possible if a guess for $\psi_1^{(0)}$ is used in the right side of this equation and a new value for the scattered phase, $\psi_1^{(1)}$, is computed. If the kernel of equation (6.53) is a contracting operator then $\psi_1^{(1)}$ will be a better estimate of the scattered phase. This iteration step can be carried out as often as desired until the change in the scattered phase is small.

The computer implementation of the Rytov series is more difficult than the Born due to the derivatives inside the integral. In the Born approximation it is possible to decompose the series and think of the entire iteration as modeling higher order scattering. On the other hand in the Rytov integral the $[\nabla \psi_1(\vec{r}') \cdot \nabla \psi_1(\vec{r}')] u_0(\vec{r}')$ term is a non-linear function of the scattered phase and thus it is not possible to consider each term separately.

The computer implementation of the Rytov series is made especially difficult since the scattered potential does not have finite support as it does in the Born series. Recall, in the Born series the scattering potential is a function of the product of the scattered field and the object function and the convolution integral need be evaluated only where the object function is non-zero. Thus carrying out the Born integration over a finite region does not introduce any errors.

This is not the case with the Rytov integral since the scattering potential is now given by the expression

$$[\nabla \psi_1(\vec{r}') \cdot \nabla \psi_1(\vec{r}')] u_0(\vec{r}'). \quad (6.54)$$

In general, the scattered phase, ψ_1 , is not equal to zero so limiting the integration to a finite region will always introduce errors.

Since the derivative is a linear operator it can be implemented as a convolution integral. Unfortunately, as will be shown shortly, the structure of the problem is such that the most accurate method, based on FFT's, is not workable.

When using an FFT to implement a convolution integral it is necessary to zero pad the original data so that the FFT represents an aperiodic convolution. While this technique works very well for most signals it has disastrous consequences when calculating the derivative of the field. Since the field never

goes completely to zero there is always a sharp transition between the field and the start of the zero padding. This transition leads to a large value of the derivative at this point and eventually to large errors in the scattered field.

The standard procedure for dealing with this problem is to use a window to smooth out the transition. This solution is not viable here since the problem is to calculate the scattered phase at the outer edge of the grid, exactly where the effect of the window is greatest. Thus even though the kernel for the derivative operator is very compact the long tails lead to errors with an FFT based implementation.

A better solution is to approximate the derivative operator with a two point kernel and make appropriate adjustments at the edges of the grid. A third order polynomial is fit to the three points $(-t, y_{-1})$, $(0, y_0)$ and (t, y_1) with the function [Sto80]

$$f(x) = \frac{y_{-1}x(x-t)}{2t^2} + \frac{y_0(x-t)(x+t)}{-t^2} + \frac{y_1(x+t)x}{2t^2}. \quad (6.55)$$

The first derivative of this polynomial is found to be

$$f'(x) \Big|_{x=0} = \frac{y_1 - y_{-1}}{2t}. \quad (6.56)$$

At the edge of the grid all three values of the field are not available and so a second order polynomial is fit to the two points and the derivative becomes

$$f'(x) \Big|_{x=0} = \frac{y_0 - y_{-1}}{t} \quad (6.57)$$

or

$$f'(x) \Big|_{x=0} = \frac{y_1 - y_0}{t}. \quad (6.58)$$

These operators are straightforward and allow the ∇^2 operator to be computed quickly in the time domain.

The convergence of the Rytov series is much like that of the Born. That the Rytov series converges to the correct answer is shown in Figures 6.16 and 6.17. Figure 6.16 shows the exact scattered field from a 2λ cylinder with a refractive index of 1.13. The field was measured at a receiver line 7.75λ from the center of the cylinder and sampled every $1/4\lambda$. Finally Figure 6.17 shows

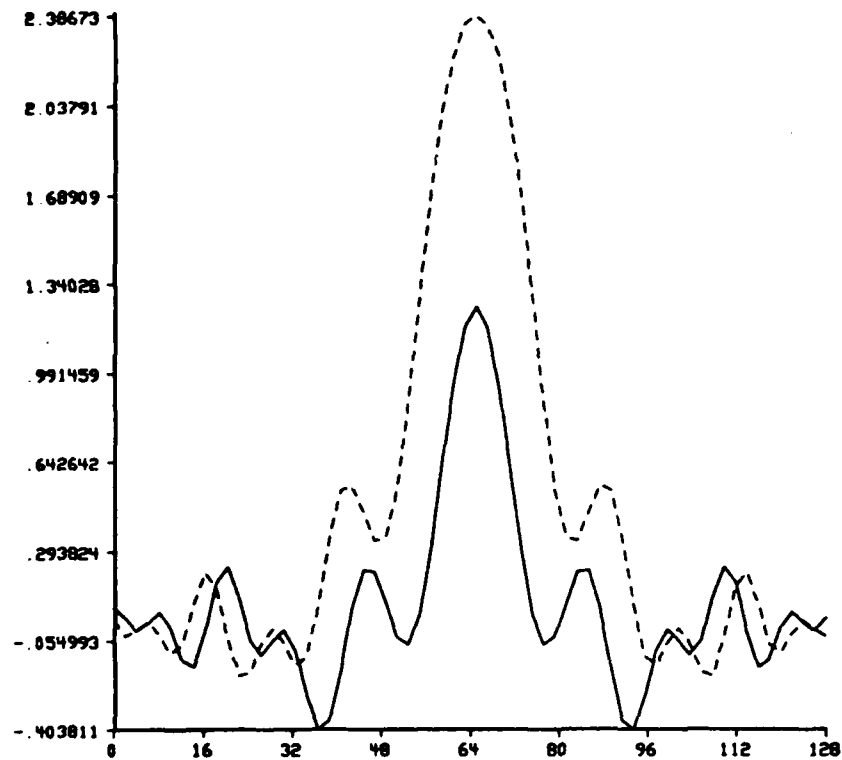


Figure 6.16

The exact scattered field from a 2λ cylinder with a refractive index of 1.13 is shown here. The real part of the field is shown as a solid line while the imaginary component is represented as a dashed line.

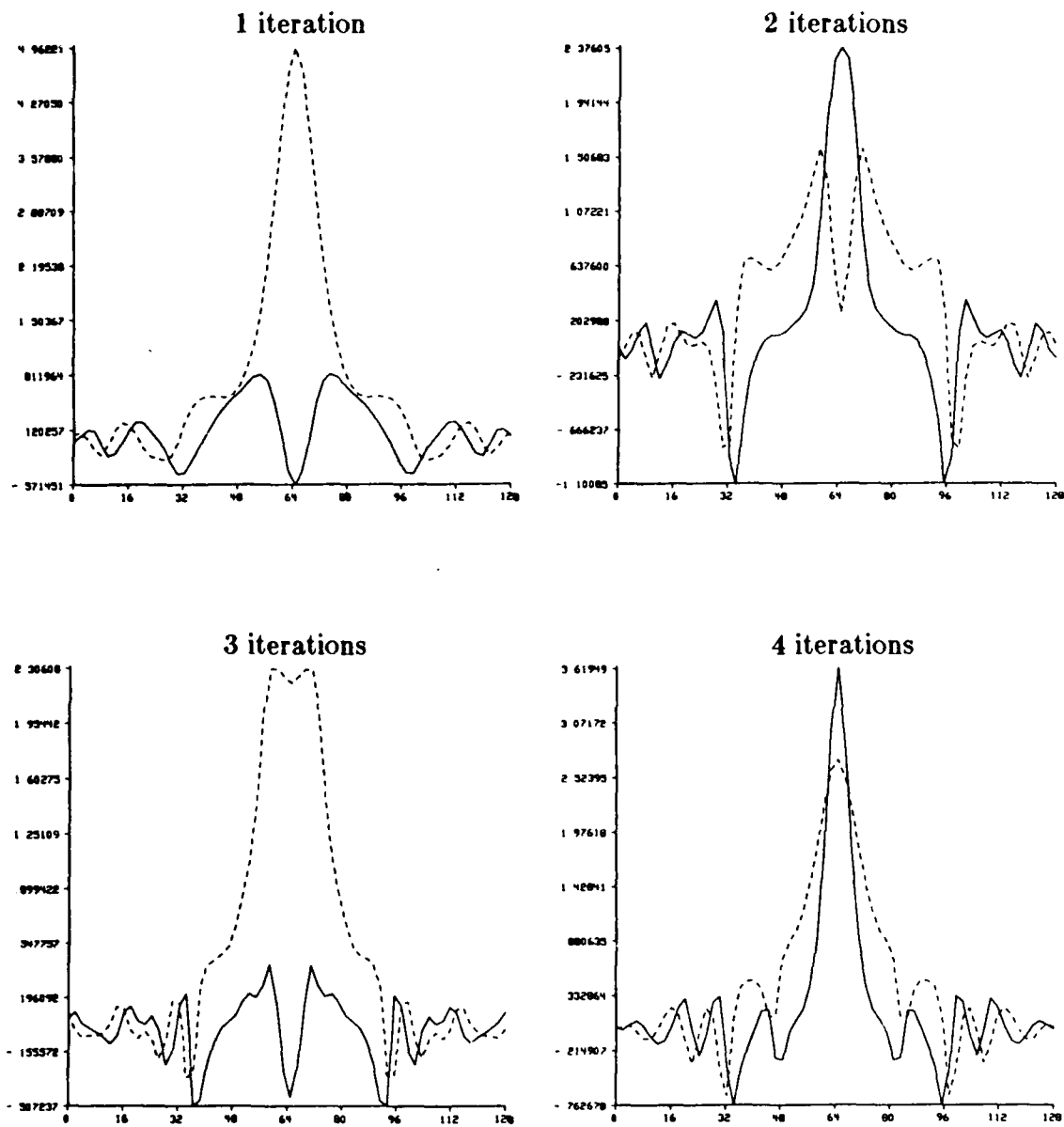


Figure 6.17 Twenty iterations of the Rytov series are shown demonstrating the convergence of the Rytov series to the field shown in Figure 6.16.

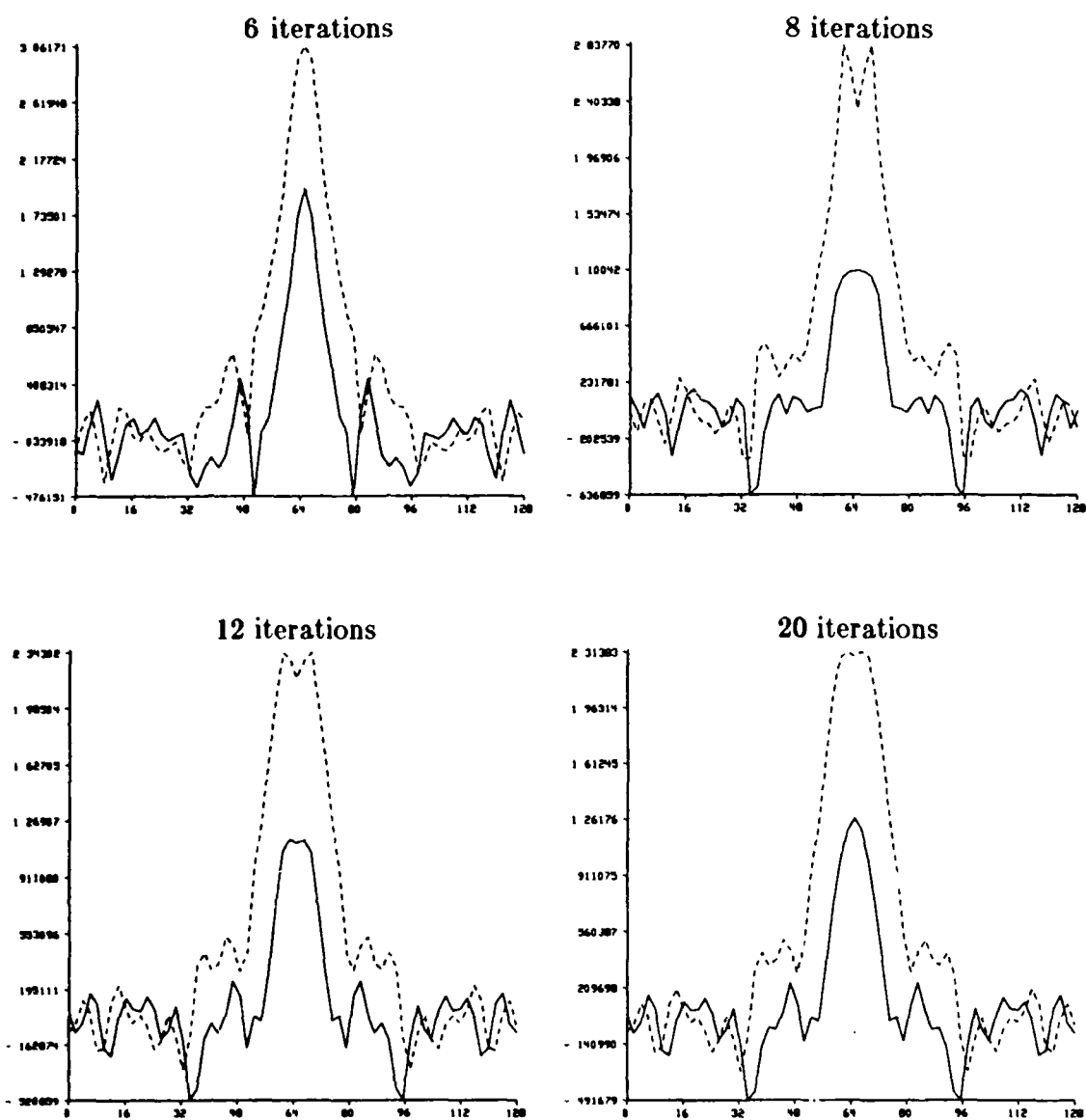


Figure 6.17

Continued.

that the Rytov series does converge to the exact solution for the scattered field.

The region of convergence of the Rytov series is compared to that of the Born in Figure 6.18. A number of works [Kel69, San70, Man70 and Wes84] have discussed this issue but it is not clear from the theoretical work which series is superior. These numerical implementations of the Born and Rytov series show the Rytov to converge for a large range of objects than the Born does. This is especially surprising considering the different domains of validity of the Born and Rytov approximations.

The difference between the Born and Rytov series is highlighted in Figures 6.19 and 6.20. These two figures show the convergence of the Rytov series for an object made up of two cylinders and an elliptical object. While in the Born approximation the orientation of the object changed the convergence of the series the same is not true for the Rytov series. The convergence results for the Rytov series are identical for either orientation (0 and 90 degrees).

The behavior of the Rytov series with an attenuating object is shown in Figure 6.21. Like the Born series the Rytov series is relatively insensitive to attenuation in the object until the attenuation becomes large enough. The attenuation at which the convergence of the Rytov series falls to zero is dependent on the radius of the cylinder.

If the object and the media have an average attenuation then the Rytov series will converge more easily. This is shown in Figure 6.22. Using an attenuating Green's function reduces the field at distances far from the object and thus makes it easier for the Rytov series to converge.

6.4 Matrix Formulation

An alternative to the fixed point methods like the Born and the Rytov was shown by Kaczmarz [Kac37], applied to the forward scattering problem by Richmond [Ric65] and extended to inverse scattering by Johnson [Joh83, Tra83 and Joh84]. The Kaczmarz algorithm has found widespread use in tomographic imaging based on ray tracing. Its use for this type of problem and a discussion of several possible optimizations and tricks is discussed in [Her73, Her76 and Her80]. While the Born and the Rytov series use discrete math to implement a continuous solution to the Helmholtz equation, a different approach is possible if the field and the object are first discretized. The Helmholtz equation now becomes a matrix equation and with appropriate manipulations can be put in the form

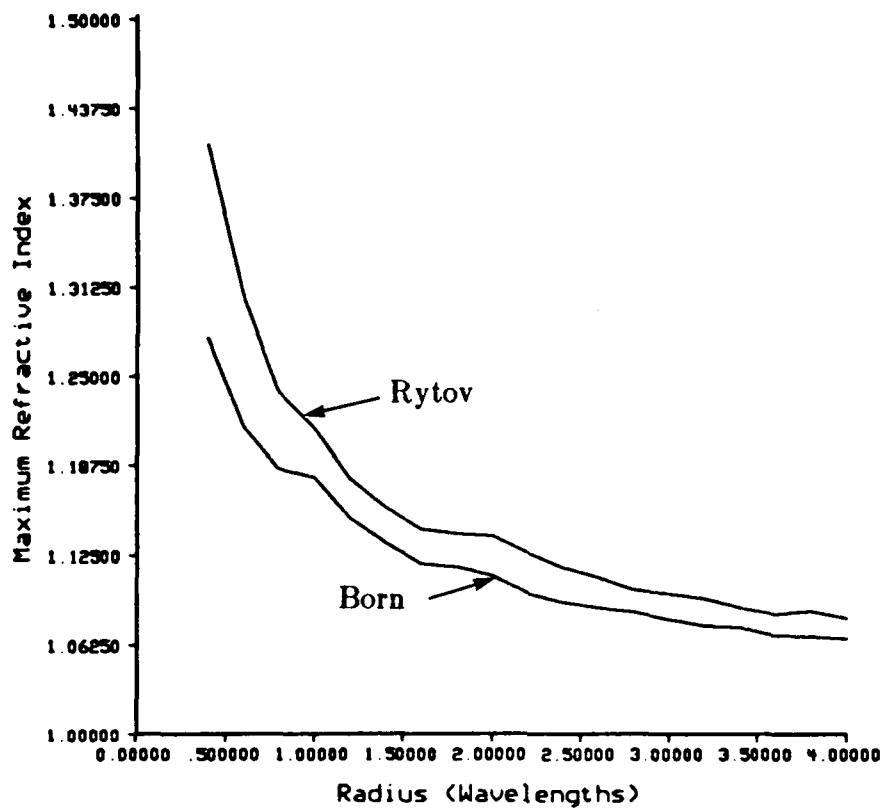


Figure 6.18

The convergence of the Born and the Rytov series are compared. The upper line represents the Rytov series.

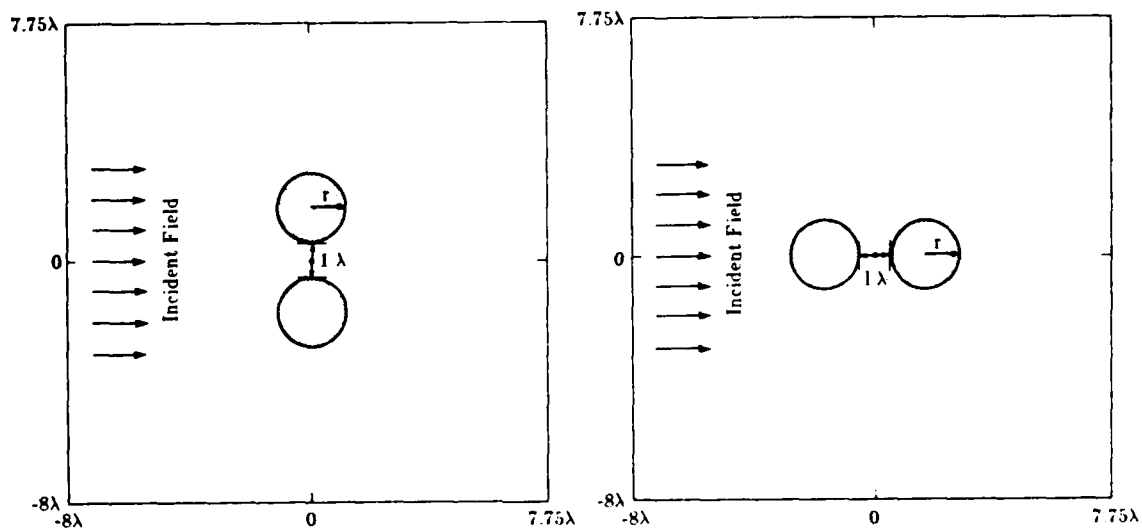
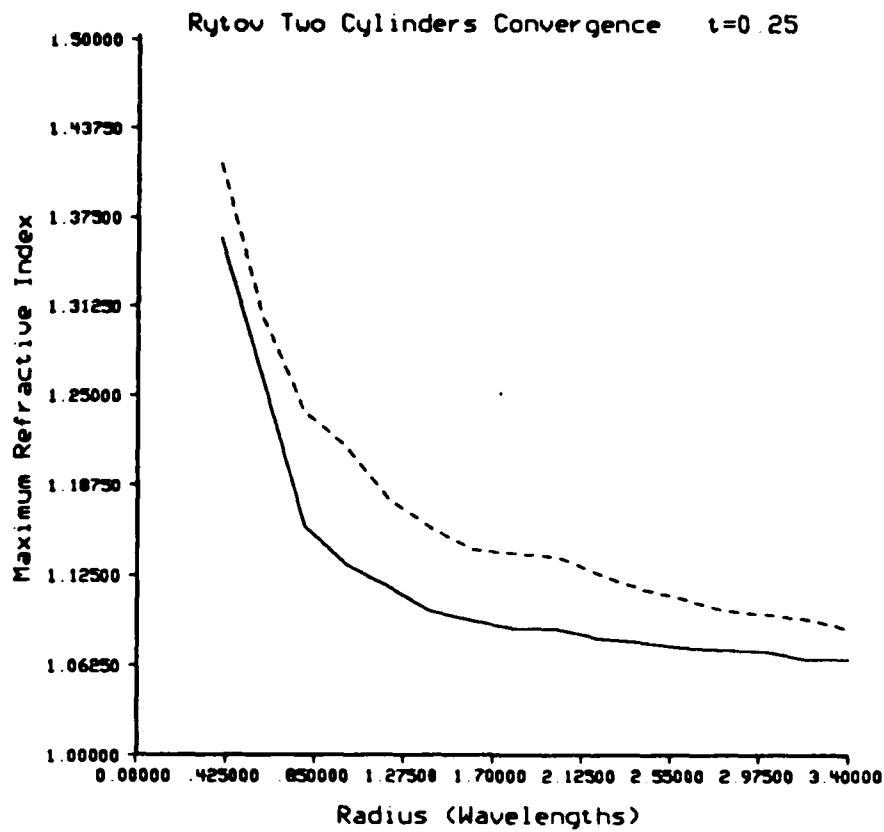


Figure 6.19

The region of convergence of the Rytov series for two cylinders. The experiment here is identical to that shown in Figure 6.9 but the results are independent of orientation.

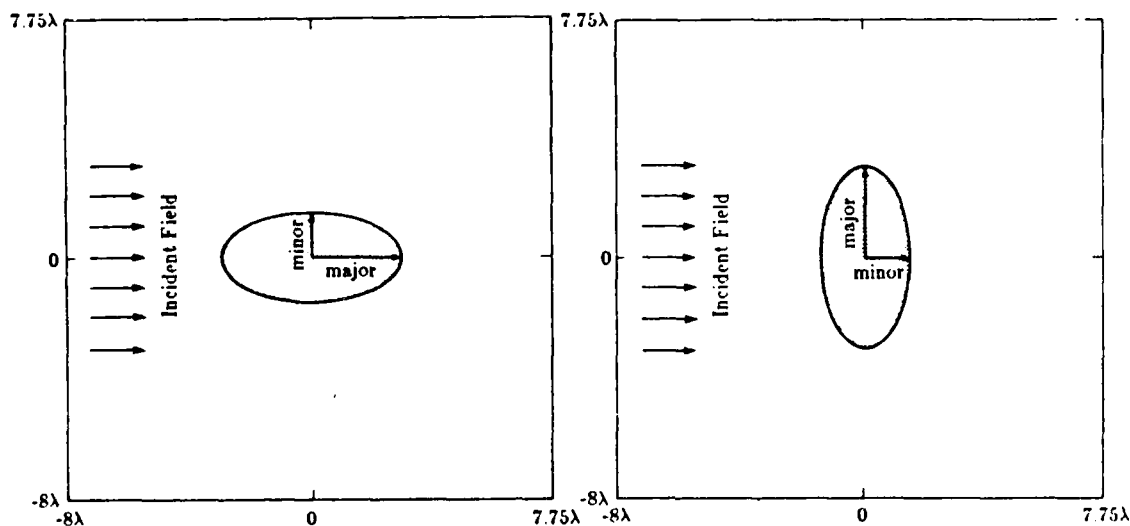
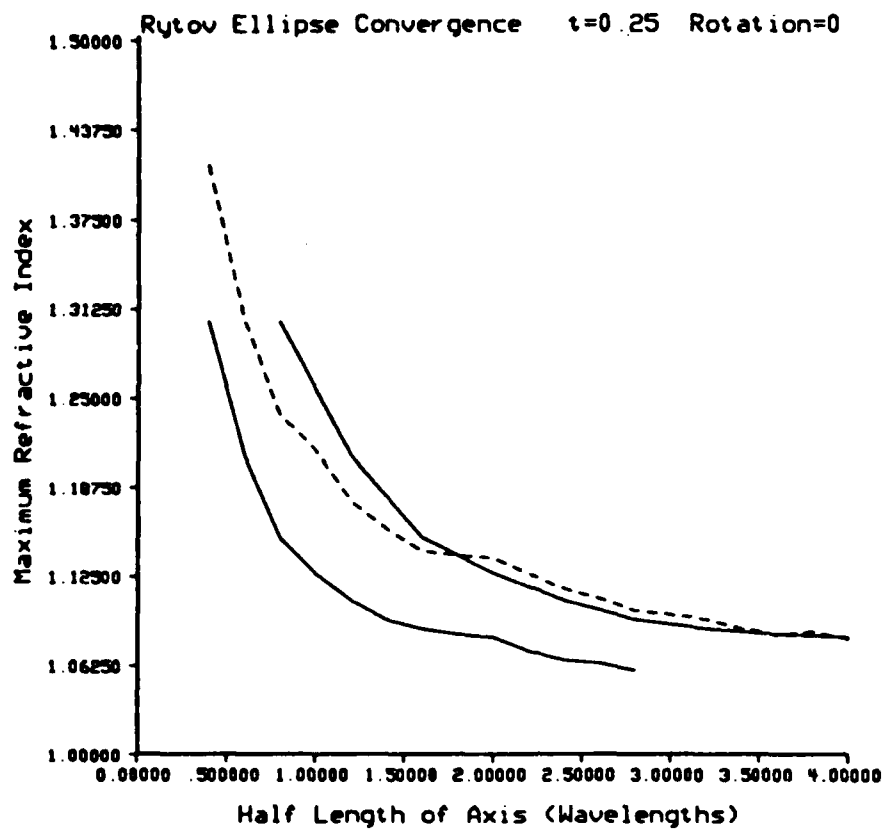


Figure 6.20

The region of convergence of the Rytov series for an ellipse. The upper solid line is plotted as a function of the major axis while the lower solid line is a function of the minor axis. The solid line represents the convergence for a single cylinder.

Rytov Convergence

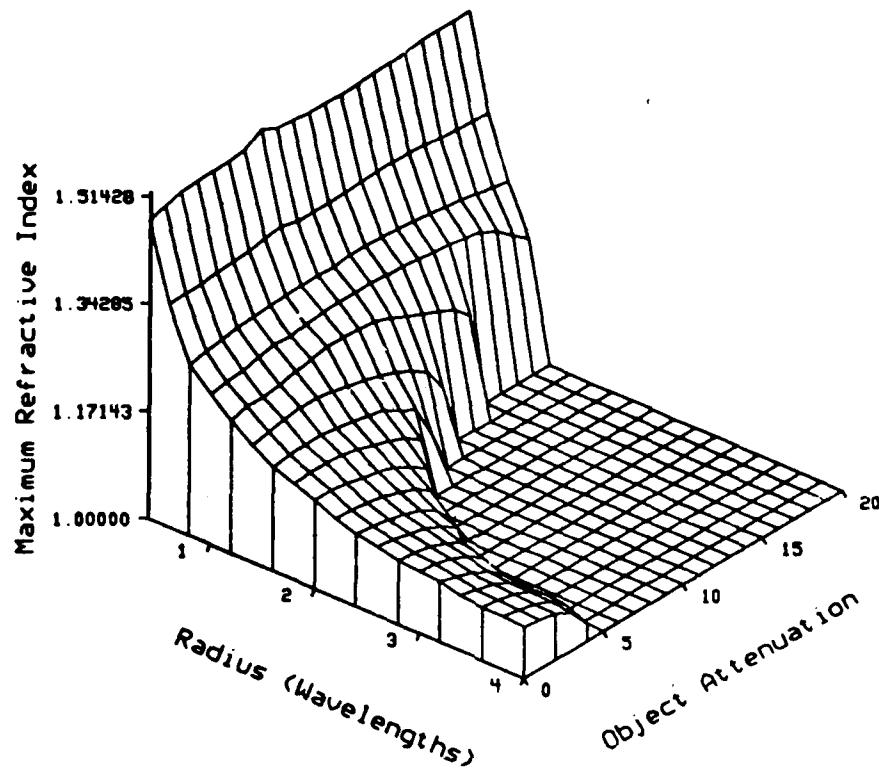


Figure 6.21

The convergence of the Rytov series is shown as a function of the cylinders radius and attenuation. The attenuation of the object is shown in nepers.

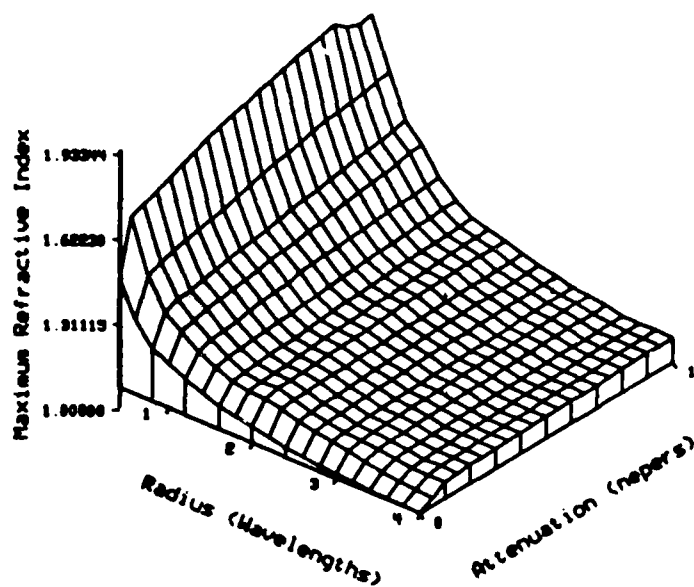


Figure 6.22

The convergence of the Rytov series is shown as a function of the cylinder radius and the average attenuation of the media. The attenuation is shown in nepers.

$$Ax = b \quad (6.59)$$

where x is the continuous field, A is a function of the object and the Green's function and b represents the effects of the incident field.

The Kaczmarz algorithm is used to solve this matrix equation because it operates on only one row of the matrix at a time. This property is important due to the large size of the matrix involved (as many as 4000 equations and unknowns.) The Kaczmarz algorithm belongs to a class of operators known as Row Action Methods and is described by Tanabe [Tan71] and by Censor [Cen81].

Most work with large matrices assumes that a significant fraction of the matrix is zero. Thus it is only necessary to store the location and the value of the non zero elements and then it is possible to use sparse matrix techniques to solve the equation (see, for example, Chapter 3 of [Hey85].) Since every element of the Green's matrix is non zero it is not possible to use these techniques and instead the Kaczmarz approach allows the calculation of a solution using modest amounts of computer memory.

As will be shown later the Kaczmarz algorithm always converges to a proper solution of the discrete equation $Ax = b$. If the discrete representation of the field, the object and the Green's function accurately model the true functions then the Kaczmarz solution will satisfy the Helmholtz equation.

An exact solution to the wave equation is given by the integral equation

$$u_s(\vec{r}) = \int o(\vec{r}') [u_0(\vec{r}') + u_s(\vec{r}')] g(\vec{r}-\vec{r}') d\vec{r}'. \quad (6.60)$$

By sampling faster than the Nyquist rate, each of the terms in the above equation can be discretized without errors as

$$u_s^{ij} = u_s(iT, jT) \quad (6.61)$$

$$u_0^{ij} = u_0(iT, jT) \quad (6.62)$$

$$o^{ij} = o(iT, jT) \quad (6.63)$$

$$g^{ij} = g(iT, jT). \quad (6.64)$$

The discrete version of the Helmholtz equation can now be written

$$u_s^{ij} = \sum_{k=-\infty}^{\infty} \sum_{l=-\infty}^{\infty} o^{kl} [u_0^{kl} + u_s^{kl}] g^{i-k, j-l} \quad (6.65)$$

Again, as in the implementation of the Born and Rytov series, assume that the object has finite support. Since the object multiplies each term in the

summation the summation need be carried out only for those values of k and l where $o^{k,l}$ is non-zero. Thus without loss of generality the object will be assumed to exist only for $1 \leq i \leq N$ and $1 \leq j \leq N$ and all summations will be assumed to go from 1 to N .

The forward process will be described first. To do this rearrange the discrete version of the wave equation to find

$$\sum_k \sum_l o^{k,l} u_0^{k,l} g^{i-k,j-l} = u_s^{i,j} - \sum_k \sum_l o^{k,l} u_s^{k,l} g^{i-k,j-l}. \quad (6.66)$$

The $u_s^{i,j}$ term can then be moved into the summation to find

$$\sum_k \sum_l o^{k,l} u_0^{k,l} g^{i-k,j-l} = \sum_k \sum_l [\delta_{i,j}^{k,l} - o^{k,l} g^{i-k,j-l}] u_s^{k,l} \quad (6.67)$$

where the Kroenker delta, $\delta_{i,j}^{k,l}$, is defined as

$$\delta_{i,j}^{k,l} = \begin{cases} 1 & \text{for } i=k \text{ and } j=l \\ 0 & \text{elsewhere} \end{cases} \quad (6.68)$$

To put this in standard matrix form represent each field as a one-dimensional vector as follows

$$x_0 = \left[x_0^{0,0}, x_0^{0,1}, \dots, x_0^{0,N-1}, x_0^{1,0}, x_0^{1,1}, \dots, x_0^{1,N-1}, \dots, \right. \\ \left. x_0^{N-1,0}, \dots, x_0^{N-1,N-1} \right]^T \quad (6.69)$$

and

$$x = \left[x^{0,0}, x^{0,1}, \dots, x^{0,N-1}, x^{1,0}, x^{1,1}, \dots, x^{1,N-1}, \dots, \right. \\ \left. x^{N-1,0}, \dots, x^{N-1,N-1} \right]^T \quad (6.70)$$

where $[]^T$ represents vector transpose. An $N^2 \times N^2$ matrix, A , can now be defined that represents the effects of all summations. Since the object and the Green's function are both known they can be combined into a single matrix and the discrete version of the wave equation can be written

$$Ax = b \quad (6.71)$$

where the terms of the A matrix are given by

$$A = \begin{bmatrix} 1 - o^{0,0} g^{0,0} & -o^{0,1} g^{0,-1} & \dots & -o^{N-1,N-1} g^{-N+1,-N+1} \\ -o^{0,0} g^{0,1} & 1 - o^{0,1} g^{0,0} & \dots & -o^{N-1,N-1} g^{-N+1,-N+2} \\ -o^{0,0} g^{0,2} & -o^{0,1} g^{0,1} & \dots & -o^{N-1,N-1} g^{-N+1,-N+3} \\ -o^{0,0} g^{0,3} & -o^{0,1} g^{0,2} & \dots & -o^{N-1,N-1} g^{-N+1,-N+4} \\ \dots & \dots & \dots & \dots \\ -o^{0,0} g^{N-1,N-2} & -o^{0,1} g^{N-1,N-3} & \dots & -o^{N-1,N-1} g^{0,-1} \\ -o^{0,0} g^{N-1,N-1} & -o^{0,1} g^{N-1,N-2} & \dots & 1 - o^{N-1,N-1} g^{0,0} \end{bmatrix} \quad (6.72)$$

The field, x , is a one dimensional matrix with N^2 elements and the constant vector b is given by

$$b = Ax_0 \quad (6.73)$$

At first glance this equation (6.71) represents an especially simple form for the scattered field; that is until the size of the vectors are considered. For a small 64x64 reconstruction the b and x vectors have 4096 complex elements and the A matrix is a square 4096x4096 matrix with more than 16 million complex elements. Inverting a matrix of this size would require over 32 Megawords of memory or more than that which exists on all but a handful of processors today.

There are two tricks to solving this problem. The first of which is to realize that it is not necessary to find the inverse of the A matrix but only to find a vector field, x , which satisfies the discrete wave equation. Secondly by using a row action method such as that proposed by Kaczmarz and Johnson et al, it is no longer necessary to store the entire A matrix in memory. Thus it is possible to solve the system of equations storing only $4N^2$ equations at a time. For a 64x64 field this represents only 16000 elements so the storage requirements are reduced by a factor of 1000.

As described in [Ros82], the Kaczmarz method finds a vector x that satisfies the equation $Ax=b$ by considering each row of the matrix A to represent a separate equation. Thus the matrix

$$A = \begin{bmatrix} a_{11} & a_{12} & a_{13} \\ a_{21} & a_{22} & a_{23} \\ a_{31} & a_{32} & a_{33} \end{bmatrix} \quad (6.74)$$

can be considered to be three equations of the form

$$\begin{aligned}
 b_1 &= a_{11}x_1 + a_{12}x_2 + a_{13}x_3 \\
 b_2 &= a_{21}x_1 + a_{22}x_2 + a_{23}x_3 \\
 b_3 &= a_{31}x_1 + a_{32}x_2 + a_{33}x_3
 \end{aligned}
 \tag{6.75}$$

In terms of an n -dimensional space each of these equations represents a single hyperplane and the intersection of all ' n ' planes describes a single solution point x .

The Kaczmarz algorithm iteratively refines an initial guess by projecting the point onto each hyper-plane in sequence. The process of computing the projection onto the hyperplane also represents finding the point on the hyperplane closest to the original guess. As will be shown later this new x will always lie closer to the new solution vector than the original guess.

If the i 'th row of the A -matrix is denoted as a_i and \langle , \rangle represents the dot product then a better solution to the equation $Ax^j=b$ is given by

$$x^{j+1} = x^j - \frac{\langle a_i, x^j \rangle - b_i}{\langle a_i, a_i \rangle} a_i. \tag{6.76}$$

This operation is illustrated in Figure 6.23.

Simple geometrical arguments should convince the reader that this equation, (6.75) will always produce a better estimate of the solution vector x . For a two dimensional case this situation is illustrated in Figure 6.24. In this example a point, x_1 , on the line CD will first be projected onto the line AB or a solution of the equation

$$a_{11}x_1 + a_{12}x_2 = b_1. \tag{6.77}$$

For any point on the line CD, the point x_2 on the line AB is always a better estimate of the solution than the original point. Thus the Kaczmarz algorithm always converges. The distance between two points x_j and x_{j+1} will be defined in the normal Euclidean sense or

$$\text{Distance}^2 = \langle x^j - x^{j+1}, x^j - x^{j+1} \rangle. \tag{6.78}$$

Since the solution vector, x , lies along the line AB an initial estimate x^j can always be improved by projecting the point onto the line. The point x^{j+1} is closer to the solution than all other points on the line CD so this always represents a better estimate. Since all points on the line CD project to the point x^{j+1} this procedure always reduces the error. Thus it is easy to see that the error is monotonically decreasing and in addition will always converge to zero. (For now the cases where the system is either over determined or underdetermined are ignored. Both of these cases represent systems of

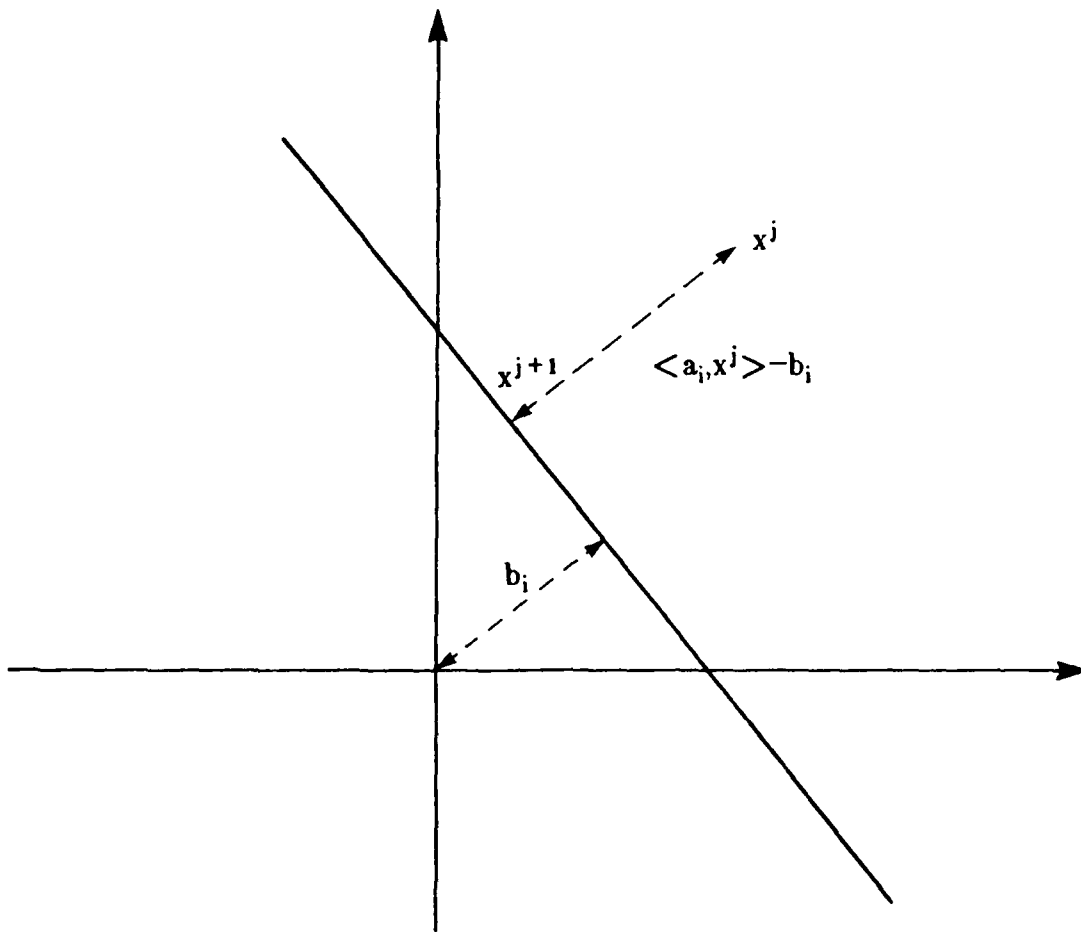


Figure 6.23 An initial estimate for the solution, x^j , is refined by finding the closest point on the line, x^{j+1} .

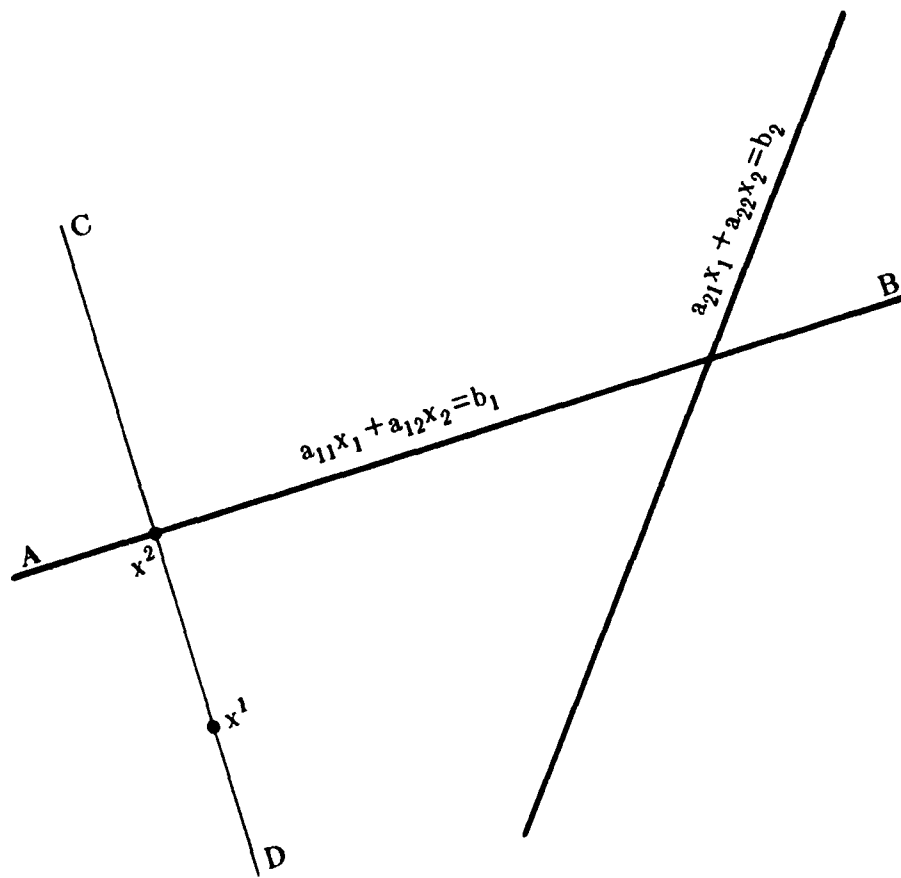


Figure 6.24

The point x^2 is a better estimate of the solution point than any other point on the line DC .

equations that don't necessarily have a unique solution.)

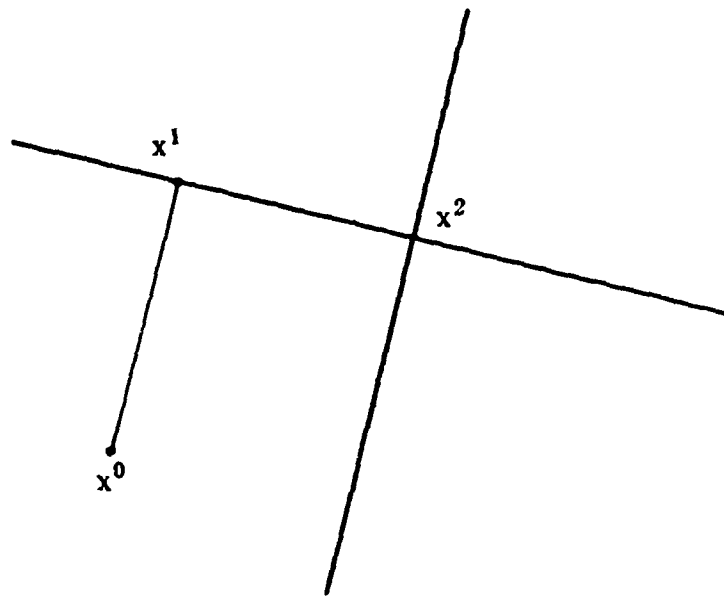
The speed of convergence is proportional to the independence of the rows of the A matrix. Figure 6.25 shows the convergence for two widely separated cases. In Figure 6.25a the two hyperplanes are perpendicular and the Kaczmarz algorithm converges to the solution in one iteration, no matter what the starting point is. (One iteration is defined as projecting the x vector onto each of the hyperplanes.) On the other hand in Figure 6.25b the hyperplanes are nearly parallel and it will take Kaczmarz algorithm many iterations to converge to the correct solution.

Since the Kaczmarz method only works with a single row of the A matrix at a time it is possible to make a space-time tradeoff. The form of the A matrix is simple enough that it is relatively inexpensive to recompute each row of the matrix as it is needed. While on many computer systems it is possible to precompute the A matrix and store it on disk, getting the data back off can be time consuming. For the computers accessible at Purdue (Floating Point Systems AP120B and Control Data Corporation Cyber 205) it is more cost effective to recompute the A matrix as needed. This approach has made the problem solvable for more than trivial sized matrices.

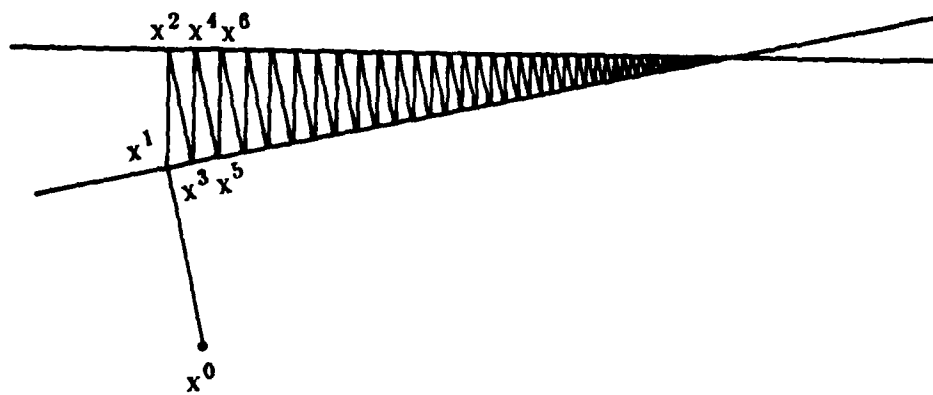
For an implementation of the forward scattering problem on a CDC Cyber 205 super computer calculating one row of the A matrix requires 98,000 floating point operations (64x64 grid). Since calculating the projection requires 57,000 floating point operations this implementation takes 2.7 times longer than the ideal (all values of the A matrix available immediately.) On the other hand retrieving the data off disk, either explicitly or using virtual memory, could take 100 times longer than the ideal situation*. Thus for this system of equations the tradeoff is easy to make. With a Cyber 205 one iteration of the Kaczmarz algorithm takes 233 million floating point operations and can be computed in 1 second of CPU time. This represents a real cost of 21¢ per iteration as charged at the standard rate by the Purdue University Computer Center.

To make the implementation of the Kaczmarz algorithm as fast as possible several quantities are precomputed and stored for quick access. The x and y coordinates of each grid point do not change during the course of the problem

* Theoretically it should be possible to organize the data on the disk in a sequential fashion and overlap execution time with IO time. With high enough bandwidth the total execution time should be nearly equal to the ideal situation. Unfortunately, most operating systems are not this cooperative.



(a)



(b)

Figure 6.25

The orthogonality of the hyperplanes determines the rate of convergence. If the hyperplanes are perpendicular then the solution will be reached in only one iteration (a) while it will take much longer if the hyperplanes are nearly parallel (b).

and thus it is possible to store these in main memory and not recalculate them. In addition the Green's function is circularly symmetric and thus a function of only the radial distance. By precomputing the values of the Green's function along a single radial it is possible to use bilinear interpolation to quickly compute the Green's function for each grid point given the radial distance and the values along the radial.

The algorithm for one iteration of the Kaczmarz algorithm can be written as

For each equation (representing the scattered field at a single point)

 Compute the Green's Function

- Subtract a vector representing the x position of each grid point from the current equation.
- Subtract a vector representing the y position of each grid point from the current equation.
- Square each distance and add
- Find square root and multiply by scaling factor to find the argument of the Green's function.
- Use bilinear interpolation to find the Green's function at every point.

 Find the A matrix

- Multiply the Green's function and the object
- Subtract from the identity matrix (δ_{ij})

 Project x^j onto the hyperplane.

An additional complication in this approach is caused by the use of complex numbers. While the dot product operation is defined for complex vectors better results are obtained if each complex equation is considered to be two real valued equations. This simple change reduces the error by a factor of 100 or more but does increase the number of equations for a 64x64 image from 4096 to 8192. While the number of unknowns remains the same (4096 complex values or 8192 real values) there are now two projections that are needed for each row. Fortunately the number of operations remains the same.

The implementation of this algorithm was tested by comparing the results of the exact solution for a small cylinder. Using the incident field as the first "guess" for the solution several iterations were calculated and the real part of the solution is shown in Figure 6.26. This compares favorably with the exact

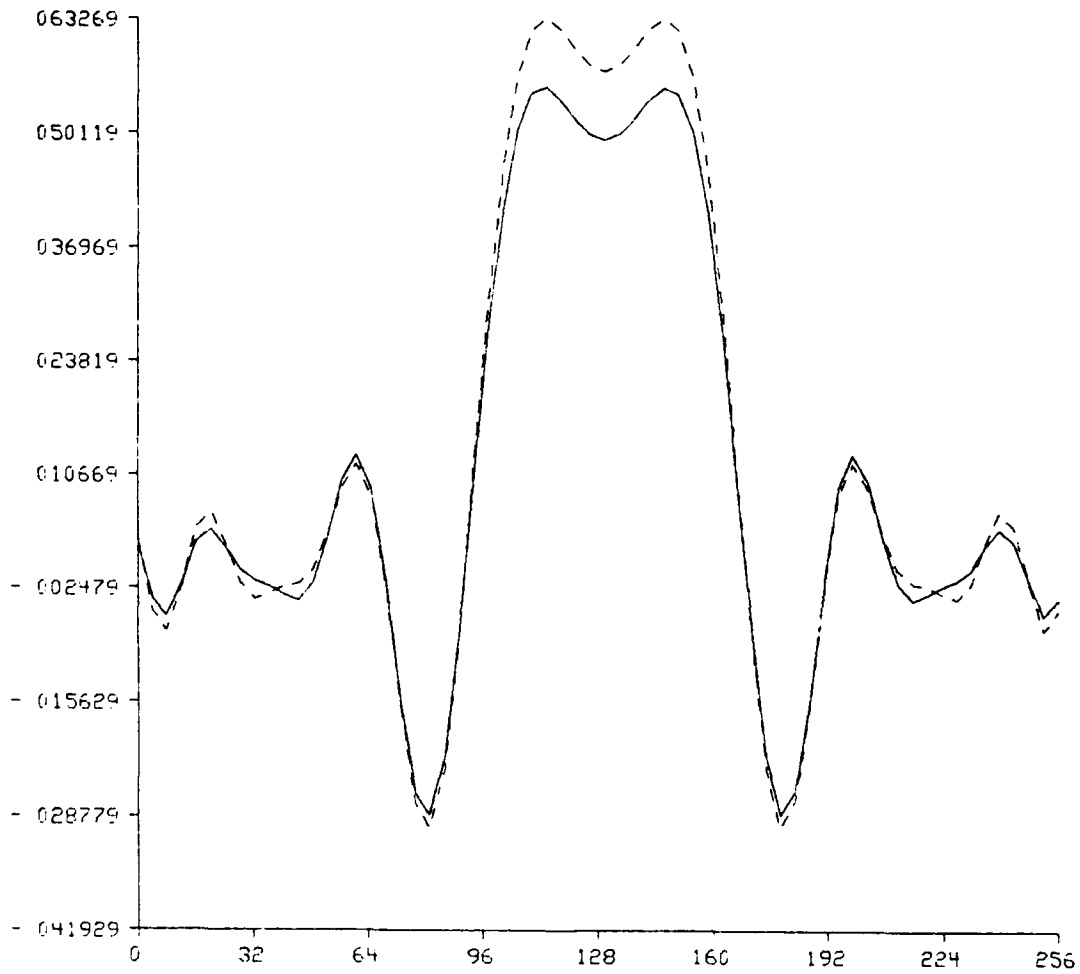


Figure 6.26

The real parts of the scattered field are compared as computed by the Kaczmarz approach (solid line) and the exact solution to the boundary conditions (dashed line).

solution shown as a dashed line. In this example and the work to follow one iteration is defined as projecting a vector, x^0 , onto each of the N^2 hyperplanes.

The speed at which this algorithm converges to the correct answer is shown in Figure 6.27. Here the real part of the field for a section of space near the origin is shown before iterating (the incident field is the initial guess) and then after one, two and three iterations. This result is especially encouraging because the first iteration has changed so rapidly towards the correct answer.

Ramakrishnam [Ram79] proposed that faster convergence of a projection algorithm could be obtained by using pair wise orthogonalization. As already described, the Kaczmarz approach will converge in one step when all the equations are orthogonal and as the hyperplanes become more parallel it will take longer for the method to converge.

Certainly the best way to speed up convergence is to first orthogonalize the system of equations. Then it would be possible to solve the system of equations in a single iteration. Unfortunately the work required to orthogonalize the system is identical to that needed to find the inverse of the matrix. In addition it then would be necessary to compute and store all the elements of the matrix. Due to the large size of the matrix this is not practical.

Ramakrishnam proposed that pair wise orthogonalization be used to make each hyperplane perpendicular to the previous hyperplane. With this approach the equation for the field at each point is made orthogonal to the preceding one using the relation

$$\tilde{A}_i = A_i - \tilde{A}_{i-1} \left(\frac{\langle \tilde{A}_i, \tilde{A}_{i-1} \rangle}{\langle \tilde{A}_{i-1}, \tilde{A}_{i-1} \rangle} \right) \quad (6.79)$$

and

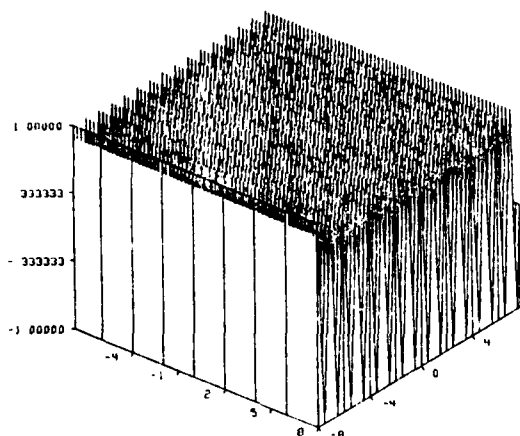
$$\tilde{b}_i = b_i - \tilde{b}_{i-1} \left(\frac{\langle \tilde{A}_i, \tilde{A}_{i-1} \rangle}{\langle \tilde{A}_{i-1}, \tilde{A}_{i-1} \rangle} \right) \quad (6.80)$$

Here the new orthogonalized system of equations are denoted with the matrix \tilde{A} and the vector \tilde{b} , A_i is one row of the A matrix and b_i is the corresponding element of the b vector.

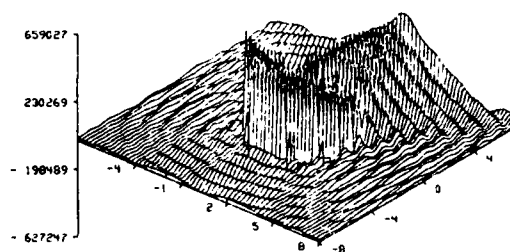
While this approach is not optimum it does have the advantage that at each step storage for only one extra row of the A matrix is needed. Ramakrishnam showed for a simple restoration problem that pair wise orthogonalization reduced the number of iteration needed to obtain a given

Real Part of Scattered Field
 Radius = 3λ , Refractive Index = 1.01

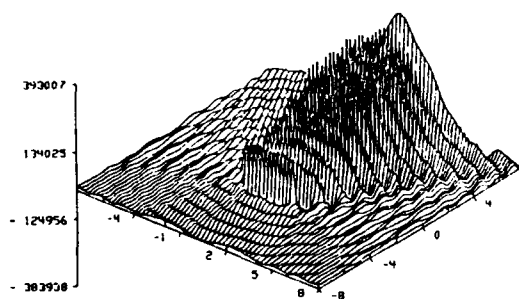
Incident Field



1 Iteration



2 Iterations



3 Iterations

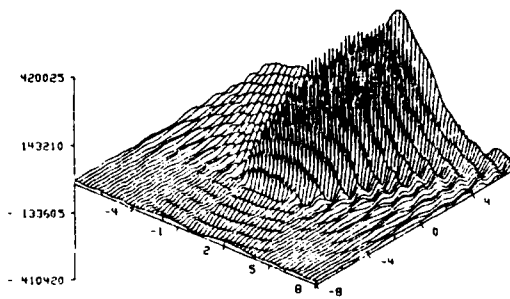


Figure 6.27

Three iterations of the Kaczmarz algorithm are shown to demonstrate the convergence of the approach to a single answer.

mean squared error by a factor of two. Since the orthogonalization is done with several dot products the reduction in iterations more than balances the extra work.

An alternative approach is rearrange the order of the equations to reduce their interdependency. This idea was first published by Hounsfield in the original patent for CT imaging [Hou72]. It seems reasonable that the hyperplanes describing the field at adjacent points (less than a quarter wavelength apart) would be nearly parallel. When the solution vector is first projected onto one plane then projecting onto a second parallel hyperplane will not significantly improve the answer. Thus convergence will be faster if the parallel hyperplane is saved till later in the iteration sequence.

This idea is illustrated in Figure 6.28 for a two dimensional case with four hyperplanes. In each case the order projections are considered is indicated as the hyperplane number at the end of the line. First in Figure 6.28a the two sets of parallel planes are considered separately while in Figure 6.28b the two sets are interleaved. It is easy to see that the first ordering will take twice as many iterations as the second.

To calculate the scattered field using the Kaczmarz algorithm a system of equations is set up that represents the field at each point as a function of the refractive index distribution. For ease of programming the x vector, the field at each point in the grid, is organized so that adjacent elements in the vector represent the field at adjacent points in the grid. Thus if the hyperplanes are considered in order there will be a high degree of correlation between the equations and convergence will be slow.

The degree of independence of two equations can be found by finding the angle between the two hyperplanes. If two equations contain nearly the same information then the angle between their respective hyperplanes will be zero while if the two equations are independent there will be an angle of 90 degrees. From standard vector theory the angle between two hyperplanes is defined as

$$\cos\theta = \frac{\langle A_i, A_j \rangle}{\sqrt{(\langle A_i, A_i \rangle \langle A_j, A_j \rangle)}} \quad (6.81)$$

where A_i and A_j represent the rows of the A matrix or the normal vector to the two hyperplanes.

The order equations are considered is a function of a parameter called δ_E that represents the change in equation number. For each iteration of a $N \times N$ grid the parameter i steps from 0 to N^2-1 and is mapped into an equation number, j , by the relation

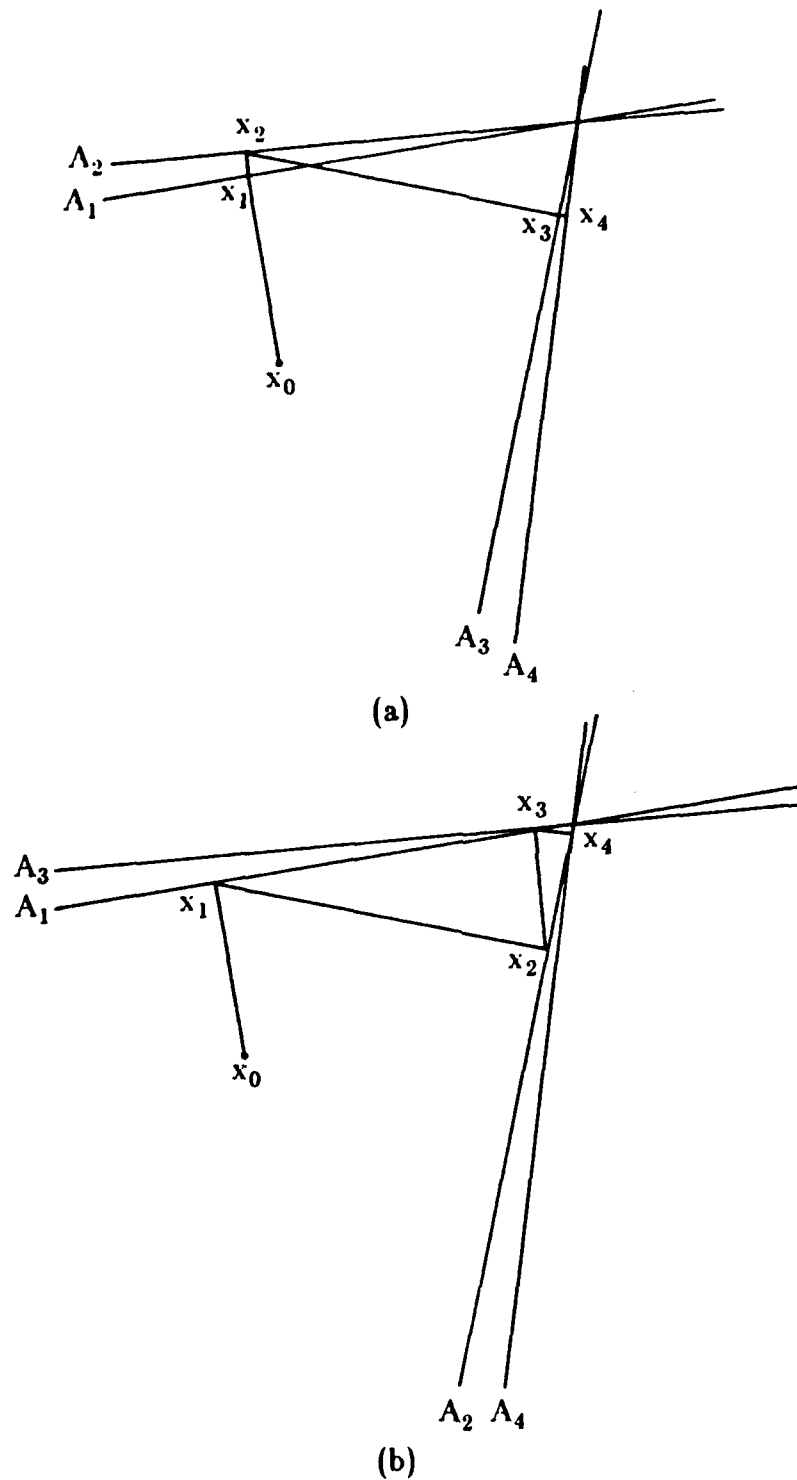


Figure 6.28

The order equations are considered can affect the rate of convergence. If the two sets of parallel lines are considered separately (a) then the convergence is twice as slow as it would be if they are interleaved (b).

$$j = (i * \delta_E) \bmod N^2. \quad (6.82)$$

With the proper choice of δ_E the equation number j will step through all N^2 equations.

The table below 6.2 shows the average and maximum cosine of the angle for a range of refractive indices between 1.01 and 1.5. A system of 1024 equations is used to define the scattered field over a 32 x 32 grid. Thus when the parameter δ_E is 1 adjacent equations are compared while the equations are as far apart as possible when δ_E is set to 513.

Table 6.2. The average and maximum cosine of the angle between hyperplanes is shown as a function of the refractive index and the number of equations skipped.

Refractive Index	δ_E	Average $\cos\theta$	Maximum $\cos\theta$
1.01	1	.000592	.010902
	513	.000125	.001338
1.1	1	.019414	.1682
	513	.001981	.013842
1.2	1	.064287	.377699
	513	.005448	.025288
1.5	1	.238268	.623253
	513	.022828	.06990

From the information in this table two points are apparent. First, as the refractive index is increased both the average and the maximum cosine of the angle increases. For small refractive indices the A matrix is dominated by the diagonal terms and thus each equation is nearly independent of the others. This also explains why the Kaczmarz algorithm converges much faster for small refractive indices.

Secondly, equations describing the field at widely spaced points have a large angle between their respective hyperplanes. As can be seen from the above table by comparing equations that are widely separated the average and the maximum cosine of the angle are reduced by a factor of 10. Thus even

with a refractive index as great as 1.5 the minimum angle between hyperplanes is increased to 86 degrees by skipping a large number of equations.

The advantages gained by considering non adjacent equations is confirmed by considering the convergence of the algorithm. For the system of equations defined by $Ax = b$ the residue is given by

$$\text{Residue} = \langle A_i, x \rangle - b. \quad (6.83)$$

The residue measures the distance between the solution vector x and the hyperplane described by A_i and the total residue is defined as the sum of the squares of the residues from each row of A . This figure can then be used as a measure of quality of the solution.

The total residue when calculating the scattered field from a cylinder of radius 1λ and refractive index 1.1 is shown in Figure 6.29. The study was done for 16 iterations and compares the total residue when the equations are considered in order (δ_E is 1) and when the equations are widely separated (δ_E is 513). To reach any given total residue, iterating the solution by considering adjacent equations takes twice as long to converge as when the equations are widely separated.

Considering widely separated points gives the same benefits as pair wise orthogonalization (convergence is twice as fast) but without the extra work. In addition when the equations are widely separated the planes are nearly perpendicular and thus there is little to be gained by pair wise orthogonalization.

It is also possible to study the effect of projecting the field in a non sequential fashion by considering the field after one iteration. Figure 6.30 shows the exact (dashed line) and the Kaczmarz field (solid line) from a cylinder of radius 1λ . The cylinder has a refractive index of 1.01 and the Kaczmarz iteration is carried out over a 32×32 grid. In addition, to emphasize the difference made by changes in δ_E , the initial guess, x_0 , for the field was the incident field.

While at first glance all of the Kaczmarz fields are very poor approximations to the exact field it is important to note that after one more iteration all of them have converged to the correct answer. Thus the only effect of altering the order of the equations is to change the rate of convergence.

The reason for the difference in one iteration of the Kaczmarz is best seen by comparing the field when δ_E is one and 1023. Recall that skipping 1023 equations in a system of 1024 equations projects adjacent equations, like the

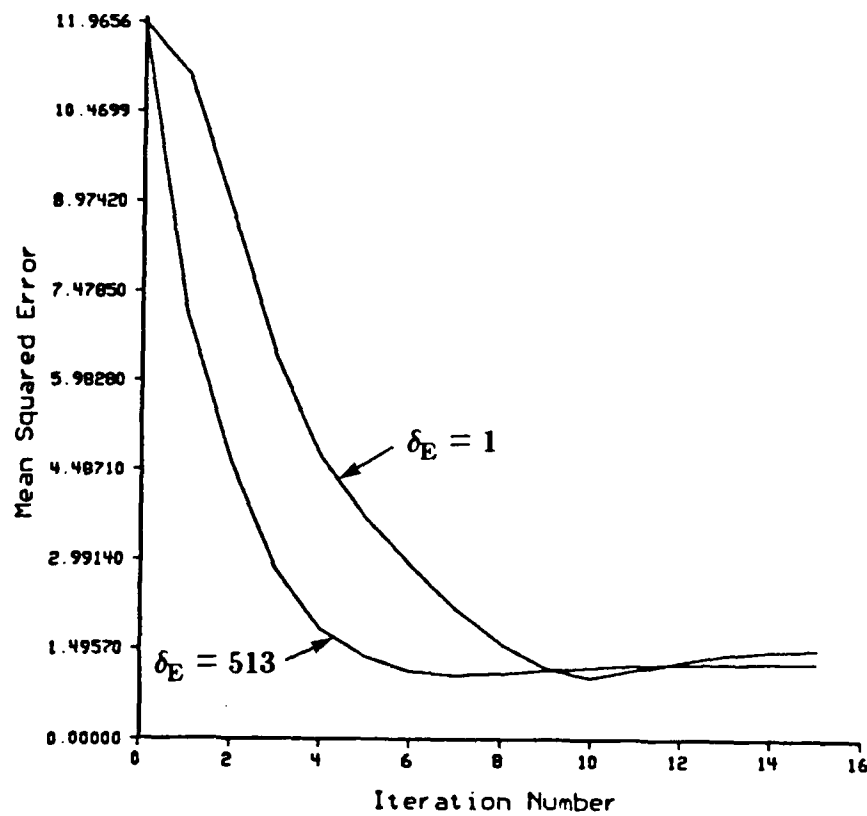


Figure 6.29

The residue remaining after the first 16 iterations of the Kaczmarz algorithm are shown as a function of the number of equations skipped (δ_E).

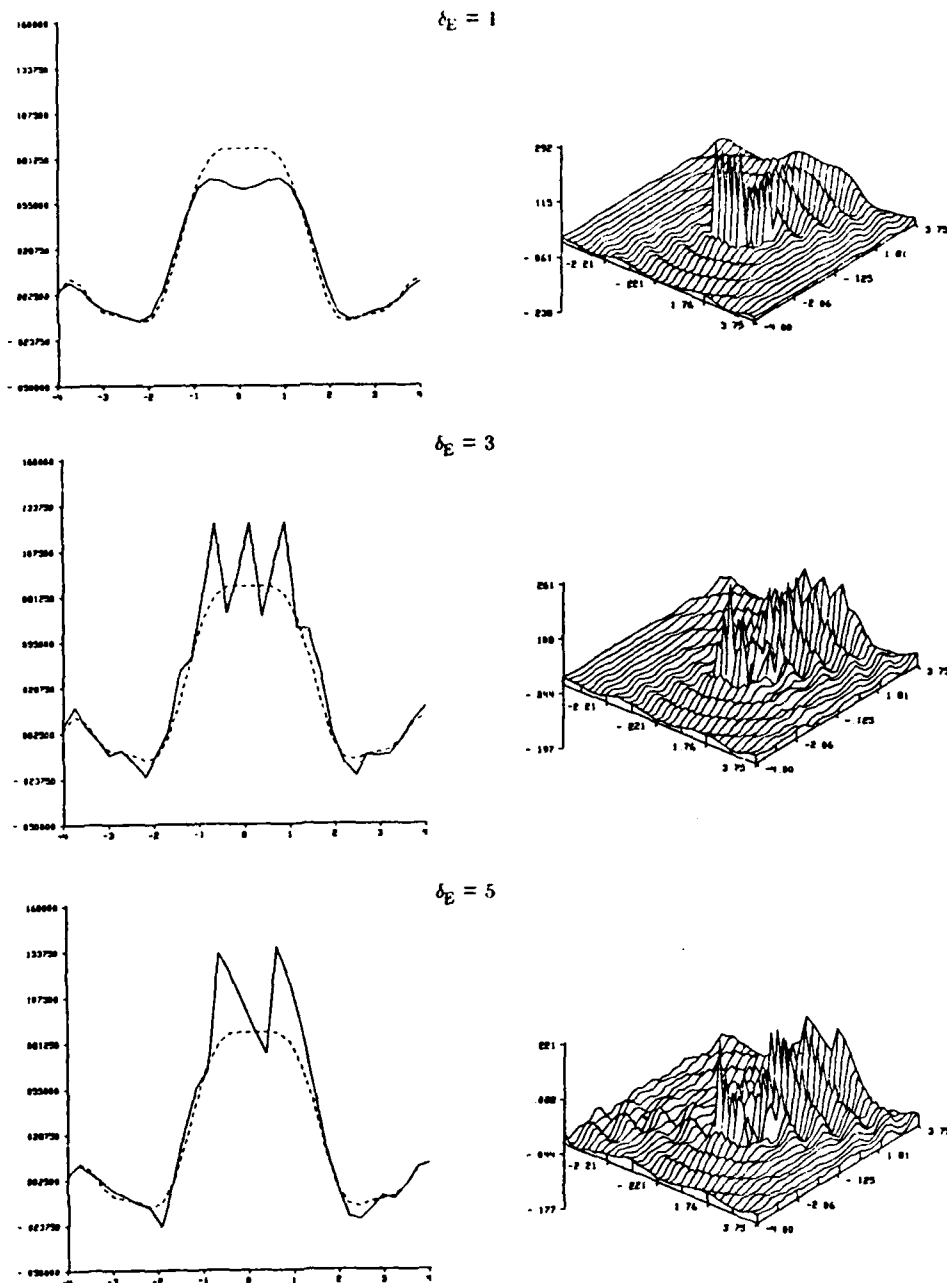


Figure 6.30

The field after one iteration is shown as a function of the number of equations skipped.

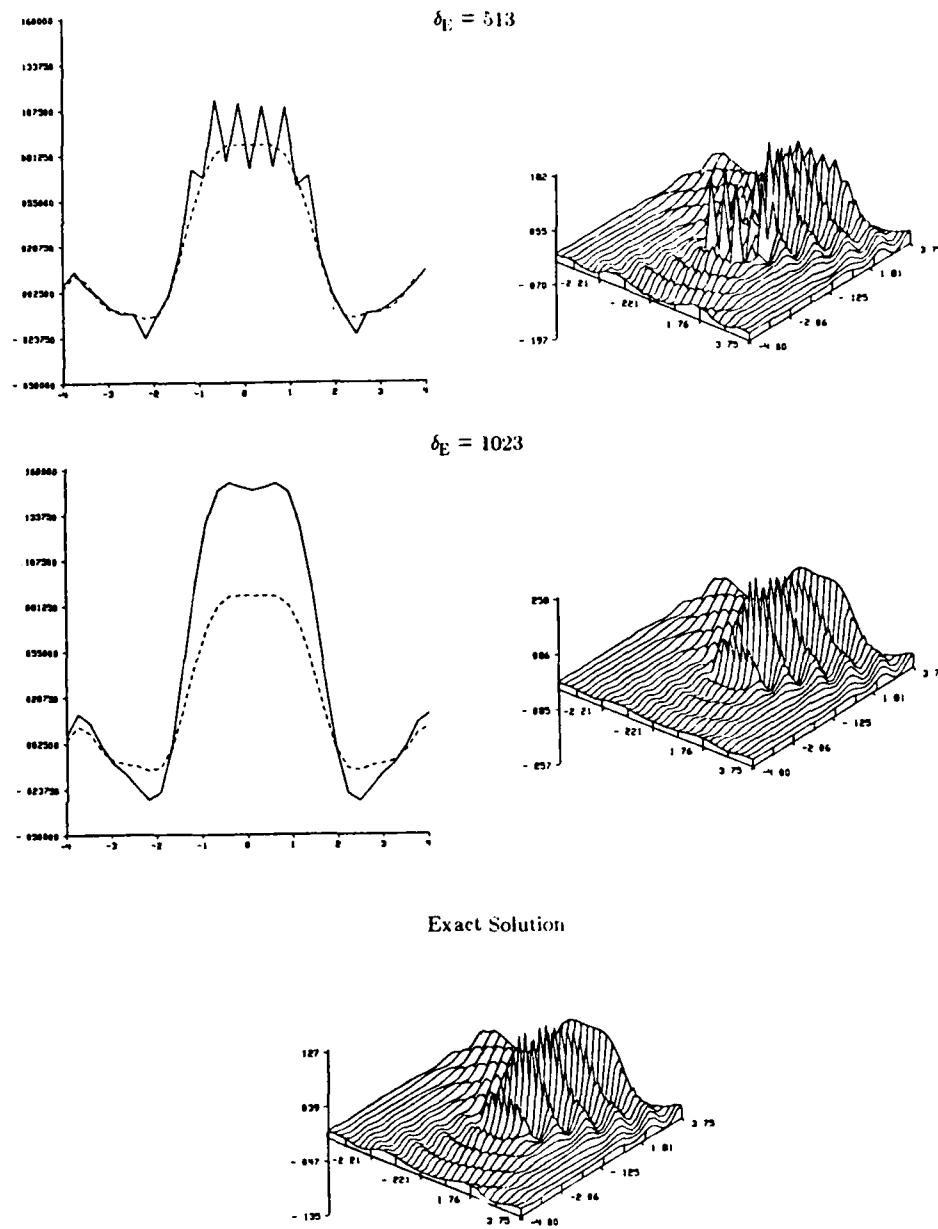


Figure 6.30 Continued.

original case with $\delta_E=1$, but instead the equations are treated in reverse order.

Since the diagonal elements of the A matrix dominate the matrix with a refractive index of 1.01 each projection only modifies the field at one point in the grid. Thus with $\delta_E = 1$ the field is calculated in the same direction as the incident field travels, from negative to positive y. This means that the field inside the cylinder has been calculated before the field is calculated at the receiver line. On the other hand when the equations are projected with $\delta_E = 1023$ the field at the receiver line is calculated before the field has been adjusted for the scattering inside the cylinder.

Unlike the fixed point algorithms (Born and Rytov series) the Kaczmarz algorithm should always converge to the correct scattered field. The speed the series converges is related to the average orthogonality of the defining equations and as shown in Table 6.2 the equations become more dependent as the object's refractive index increases. Thus the Kaczmarz algorithm converges more slowly for objects with large refractive index.

Two other factors determine the rate of convergence of the Kaczmarz series. As shown in Figure 6.29 the order the equations are considered changes the rate of convergence of the series. For this reason most of the simulations shown in this work were done using a δ_E equal to $N^2/2 + 1$ where the size of the grid is $N \times N$. While it hasn't been investigated, even better performance could possibly be obtained by alternating different values for δ_E .

Finally quantization and sampling errors slow the rate of convergence. This is shown in Figure 6.31 for a sampling interval of $.1\lambda$ and $.25\lambda$. In both cases the radius of the cylinder is equal to eight times the sampling interval and the calculations were performed over a 32×32 grid. The plots show the real (solid line) and imaginary (dashed line) components of the scattered field as calculated by the Kaczmarz algorithm and an exact algorithm based on the Bessel function expansions described in [Wee64 and Mor68].

Each of the plots in Figure 6.31 shows the scattered field after 32 iterations. While the exact limits of the Kaczmarz algorithm are difficult to define it is possible to say that the Kaczmarz algorithm has converged for refractive indices up to 1.4 with a sampling interval of $.1\lambda$ and up to 1.2 with a sampling interval of $.25\lambda$. Calculating the scattered field from objects with larger refractive indices might be possible but will need more accurate implementations.

All the results shown here were sampled using rectangular basis functions. While according to the sampling theorem a rectangular set of basis functions

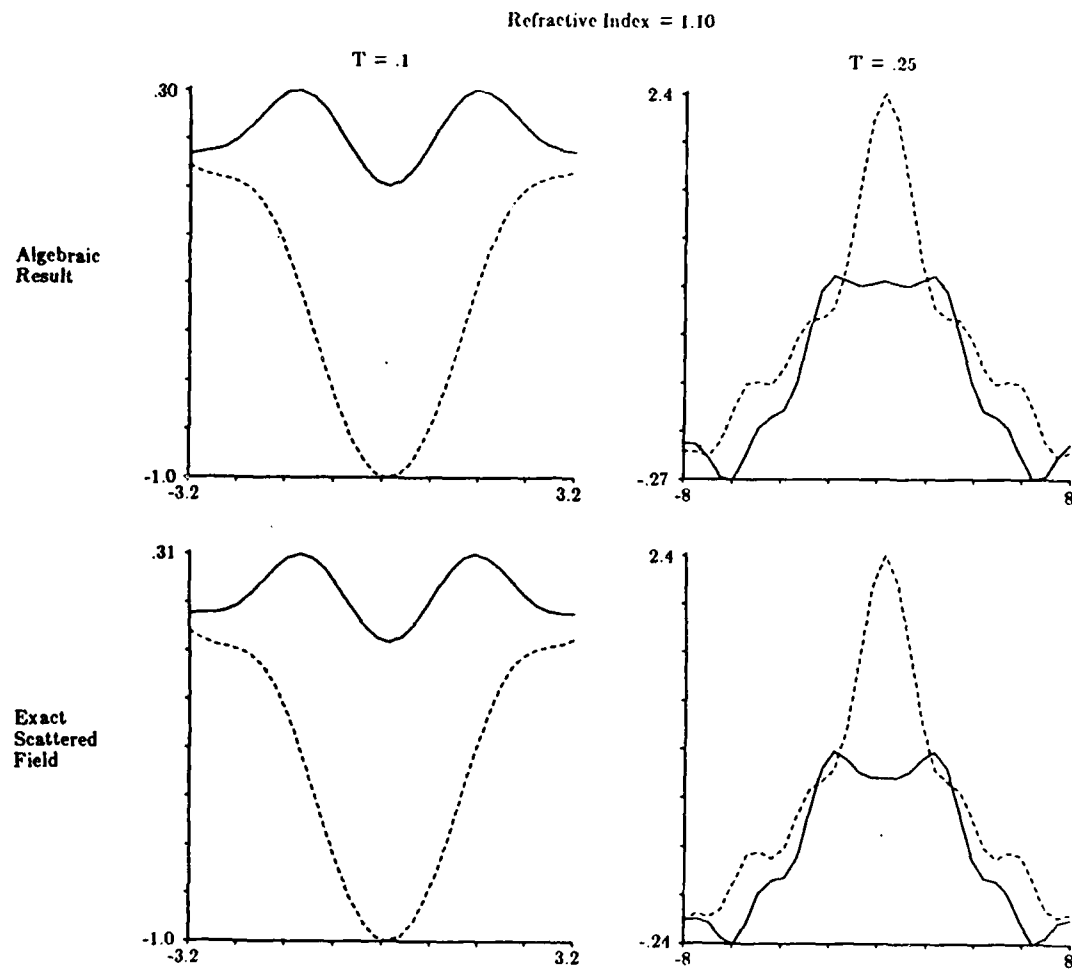


Figure 6.31

The exact scattered field and the result of 32 iterations of the Kaczmarz algorithm are compared here. In each case the real component of the field is shown as a solid line while the imaginary component is shown as a dashed line.

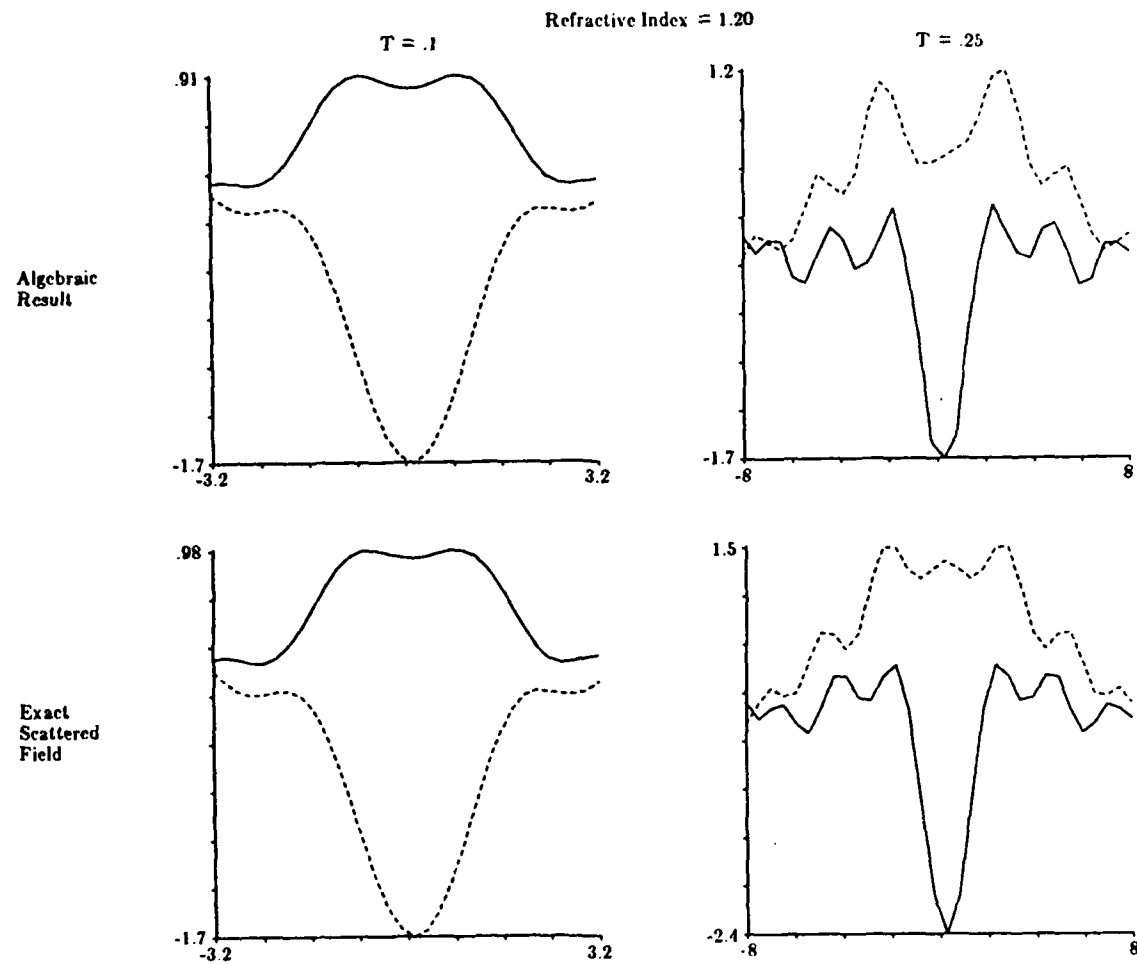


Figure 6.31

Continued.

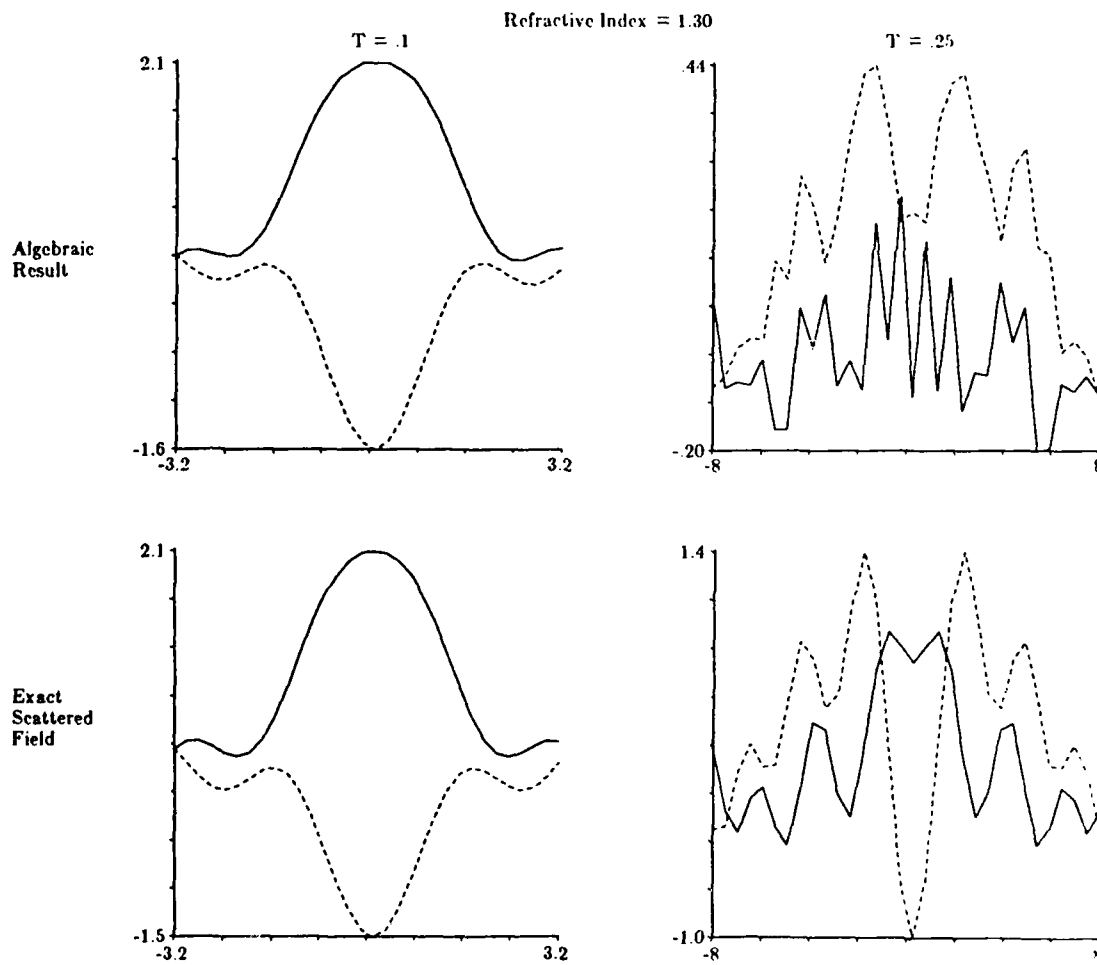


Figure 6.31

Continued.

AD-A184 923

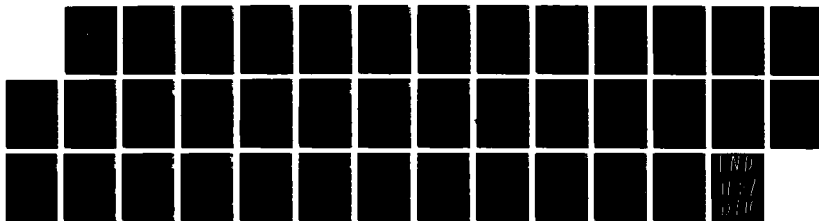
METHODS FOR CORRECTION OF REFRACTIVE ERRORS(U) PURDUE
UNIV LAFAYETTE IN SCHOOL OF ELECTRICAL ENGINEERING
A C KAK 31 DEC 85 DAHD17-82-C-2819

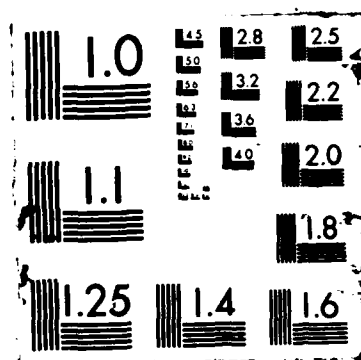
3/3

UNCLASSIFIED

F/O 28/6

NL





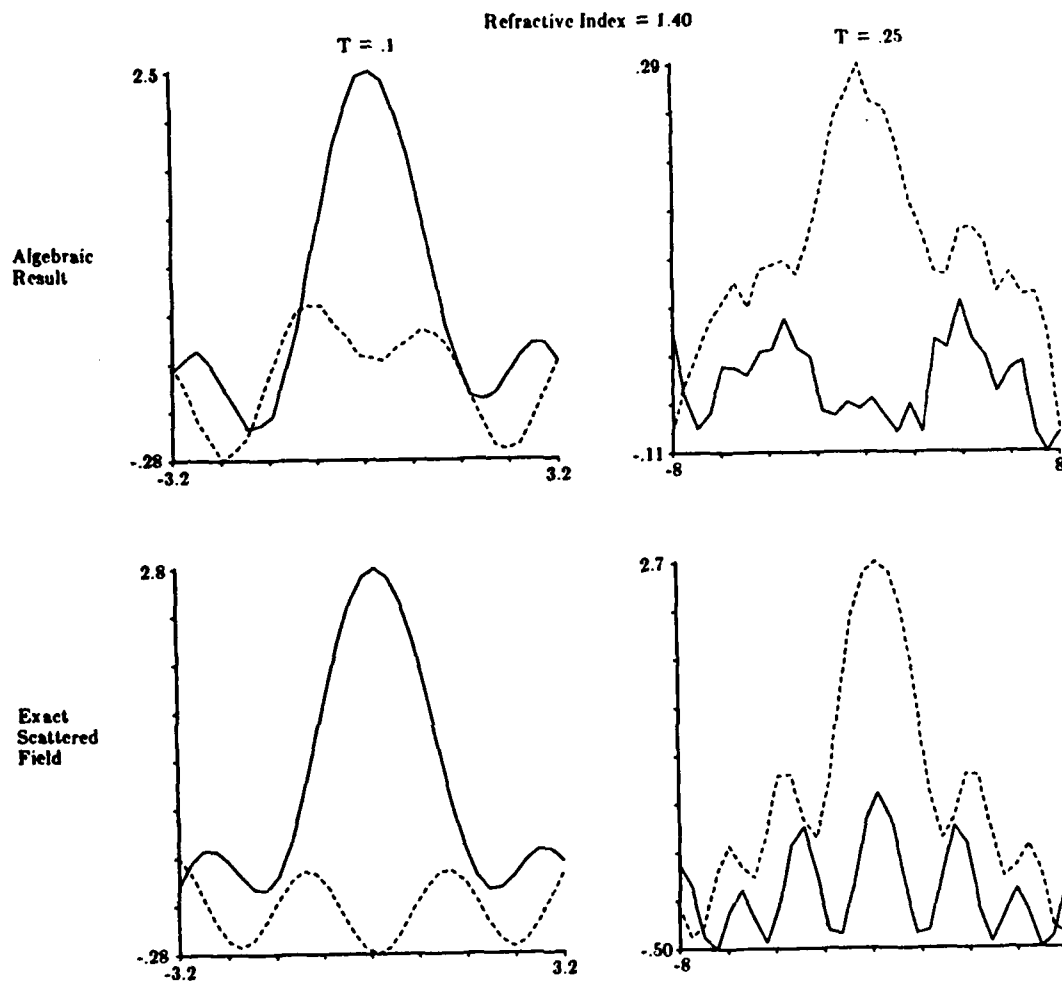


Figure 6.31

Continued.

can represent the original continuous function without errors more accurate integrations might be possible using sinc functions [Joh83, Ste81]. This idea has not been explored here.

References

- [Azi83] M. Azimi and A. C. Kak, "Distortion in diffraction imaging caused by multiple scattering," *IEEE Transactions on Medical Imaging*, Vol. MI-2, December 1983, pp. 176-195.
- [Cen81] Y. Censor, "Row-actions methods for huge and sparse systems and their applications," *SIAM Review*, Vol. 23, October 1981, pp. 444-466.
- [Goo68] J. W. Goodman, *Introduction to Fourier Optics*, McGraw Hill Book Company, San Francisco, 1968.
- [Her73] G. T. Herman, A. Lent, and S. Rowland, "ART: Mathematics and applications: A report on the mathematical foundations and on applicability to real data of the algebraic reconstruction techniques," *J. Theor. Biol.*, Vol. 43, 1973, pp. 1-32.
- [Her76] G. T. Herman, A. V. Lakshminarayanan, A. Naparstek, E. L. Ritman, R. A. Robb, and E. H. Wood, "Rapid computerized tomography," *Med. Data Process.*, 1976, pp. 582-598.
- [Hey85] G. T. Heydt, *Computer Analysis Methods for Power Systems*, MacMillan, New York, 1985.
- [Hou72] G. N. Hounsfield, *A method of apparatus for examination of a body by radiation such as x-ray or gamma radiation*, Patent Specification 1283915, The Patent Office, 1972.
- [Joh83] S. A. Johnson and M. L. Tracy, "Inverse scattering solutions by a sinc basis, multiple source, moment method -- Part I: Theory," *Ultrasonic Imaging*, Vol. 5, 1983, pp. 361-375.
- [Kac37] S. Kaczmarz, "Angenaherte auflosung von systemen linearer gleichungen," *Bull. Acad. Polon. Sciences et Lettres A*, 1937, pp. 355-357.
- [Kel69] J. B. Keller, "Accuracy and validity of the Born and Rytov approximations," *Journal of the Optical Society of America*, Vol. 59, 1969, pp. 1003-1004.

- [Man70] K. Mano, "Interrelationship between terms of the Born and Rytov expansions," *Proceedings of the IEEE*, Vol. 58, July 1970, pp. 1168-1169.
- [Mor68] P. M. Morse and K. U. Ingard, *Theoretical Acoustics*, McGraw Hill Book Company, New York, 1968.
- [Opp75] A. V. Oppenheim and R. W. Schaffer, *Digital Signal Processing*, Prentice-Hall, Englewood Cliffs, NJ, 1975.
- [Ram79] R. S. Ramakrishnan, S. K. Mullick, R. K. S. Rathore, and R. Subramanian, "Orthogonalization, Bernstein polynomials, and image restoration," *Appl. Opt.*, Vol. 18, 1979, pp. 464-468.
- [Ric65] J. Richmond, "Scattering by a dielectric cylinder of arbitrary cross section shape," *IEEE Transactions on Antennas and Propagation*, Vol. AP-13, 1965, pp. 334-341.
- [Ros82] A. Rosenfeld and A. C. Kak, *Digital Picture Processing*, Academic Press, Second Edition, 1982.
- [San70] M. I. Sancer and A. D. Varvatsis, "A comparison of the Born and Rytov methods," *Proceedings of the IEEE*, Vol. 58, January 1970, pp. 140-141.
- [Sla83] Malcolm Slaney and A. C. Kak, "Diffraction tomography," *Proceedings of the SPIE*, Vol. 413, April 1983, pp. 2-19.
- [Sla84] Malcolm Slaney, A. C. Kak, and L. E. Larsen, "Limitations of imaging with first order diffraction tomography," *IEEE Transactions on Microwave Theory and Techniques*, August 1984, pp. 860-873.
- [Ste81] F. Stenger, "Numerical methods based on Whittaker cardinal, or sinc functions," *SIAM Review*, Vol. 23, April 1981, pp. 165-224.
- [Sto80] Josef Stoer and Roland Bulirsch, *Introduction to Numerical Analysis*, Springer-Verlag, New York, 1980.
- [Tan71] K. Tanabe, "Projection method for solving a singular system," *Numer. Math.*, Vol. 17, 1971, pp. 203-214.
- [Tra83] M. L. Tracy and S. A. Johnson, "Inverse scattering solutions by a sinc basis, multiple source, moment method -- Part II: Numerical evaluations," *Ultrasonic Imaging*, Vol. 5, 1983, pp. 376-392.

- [Wee64] W. L. Weeks, *Electromagnetic Theory for Engineering Applications*, John Wiley and Sons, Inc., New York, 1964.

CHAPTER 7

HIGHER ORDER RECONSTRUCTION ALGORITHMS

7.1 Introduction

Reconstructions based on the theory in the first five chapters of this work are based on first order approximations to the scattered field. In other words for both the Born and the Rytov approximations it is necessary to assume that the field inside the object is equal to the incident field and then it is possible to derive a simple (linear) expression for the scattered field as a function of the object. Finding a better estimate for the field inside the object is the central problem in improving diffraction reconstructions.

The reconstruction problem is more difficult than the forward problem discussed in Chapter 6 because now both the object and the field inside the object are unknown. This means that it is necessary to design a procedure that simultaneously estimates both the object and the field inside the object. This procedure is made more difficult because the reconstruction is formed by illuminating the object by a number of different fields and the exact field inside the object must be calculated for each view.

Three approaches to the inverse problem will be described here. Most general and therefore computationally most expensive is to write a system of equations that describes both the field and the object and then find the solution vector that gives the smallest error. Unfortunately the system of equations is non-linear and some sort of search procedure must be used to find the best solution. This approach to the problem was first discussed by Johnson et al [Joh83].

Computationally less demanding solutions to the problem are based on iterative algorithms. A perturbational approach much like that used to generate the Born or the Rytov series was first proposed by Jost and Kahn [Jos52] and later extended by Moses [Mos56] and Prosser [Pro69, Pro76]. This approach was first developed for quantum scattering problems but is equally valid for the electromagnetic and acoustic wave equations.

A hybrid approach to the problem was first proposed by Johnson [Joh83] and is a two step iteration procedure. It is based on the idea that it is only necessary to calculate the object since for any given object and incident field it is possible to calculate the exact field inside the object. Thus the reconstruction procedure first estimates the object's refractive index distribution and then an estimate of the field inside the object can be calculated using any one of the procedures described in Chapter 6. The key to this procedure is then to calculate a better estimate of the object given a better estimate of the actual field inside the object. This approach will be described in section 7.4 as an example of a fixed point iteration.

7.2 Non Linear Approach

The most general approach to estimate the object given the scattered field is to define a solution space that includes both the refractive index of the object and the exact field inside the object for each of the views. Both the non-linear equations and the number of unknowns combine to make this a difficult problem. The non-linear nature of the problem means that a search procedure must be used to find the best solution and unlike fixed point or perturbation methods it is not possible to say a priori how fast the search will reduce the error or whether it will ever converge.

The unknowns in this problem are defined over an $N \times N$ grid and consist of the object and the exact scattered field from N_ϕ views. If the number of views, N_ϕ , is on the same order as N then there are a total of N^3 unknowns and thus at least N^3 defining equations are needed for a well behaved solution [Sar81].

For each view N_M measurements of the scattered field are taken and this defines $N_\phi N_M$ equations of the form

$$u_{M,\phi}(\vec{r}) = \int u_{t,\phi}(\vec{r}') o(\vec{r}') g(\vec{r}-\vec{r}') d\vec{r}' \quad (7.1)$$

where $u_{M,\phi}$ is the measured scattered field for a view at angle ϕ and position \vec{r} . Both $u_{t,\phi}(\vec{r})$, the total field inside the object for the view at angle ϕ , and $o(\vec{r})$, the object's refractive index, are unknown. Since the unknowns are calculated over a discrete $N \times N$ grid the integral above becomes a summation or

$$u_{M,\phi}(\vec{r}_j) = T^2 \sum_i u_{t,\phi}(\vec{r}'_i) o(\vec{r}'_i) g(\vec{r}-\vec{r}'_i). \quad (7.2)$$

Unfortunately the measured points only contribute $N_\phi N_M$ equations therefore there are more unknowns than equations by a factor of approximately N (again assuming that N_ϕ and N_M are on the same order as N). The

additional equations are defined by noting that the field inside the object must also satisfy the Helmholtz equation. There are $N_\phi N^2$ equations of the form

$$u_{t,\phi}(\vec{r}) = u_{0,\phi}(\vec{r}) + \int u_{t,\phi}(\vec{r}') o(\vec{r}') g(\vec{r}-\vec{r}') d\vec{r}' \quad (7.3)$$

or in discrete form

$$u_{t,\phi}(\vec{r}_i) = u_{0,\phi}(\vec{r}_i) + T^2 \sum u_{t,\phi}(\vec{r}'_j) o(\vec{r}'_j) g(\vec{r}_i - \vec{r}'_j). \quad (7.4)$$

Thus the combination of equations (7.2) and (7.4) define a total of $N_\phi N_M + N_\phi N^2$ equations which must be solved for both $u_{t,\phi}(\vec{r})$ and $o(\vec{r})$.

The difficulty caused by the large number of unknowns is compounded by the non linearity in the equations. In both equations (7.2) and (7.4) the product of the two unknowns, the field and the object, is convolved with the Green's function and this product means that the Kaczmarz algorithm as used in Chapter 6 is no longer applicable.

The usual approach to solve a system of non-linear equations is to define the error as a function of the difference between the left and right side of the equations. An optimum solution is then formed by a search procedure that looks for a minimum in the error function. One implementation of this algorithm reported by Tracy et al [Tra83] took 7 hours of computer time on a small minicomputer to find the object over an 11x11 grid. Calculating the object over a larger grid (at least 128x128 is probably needed for medical imaging) would be prohibitively expensive.

7.3 Perturbation Algorithms

As already described in Chapter 6 perturbation algorithms are an important technique for solving the scattering problem. This technique was first used to solve the inverse scattering equation by Jost and Kahn and the general techniques are described in more detail in the books by Nayfeh [Nay73, Nay81]. A discrete version of the work by Jost and Kahn was first reported by Devaney in [Dev82].

A perturbational expansion of the forward scattering problem is found by letting the object function be written in terms of a small perturbation parameter ϵ or

$$o(\vec{r}) = \epsilon \chi(\vec{r}) \quad (7.5)$$

and the total field written as a polynomial in terms of the same perturbation parameter or

$$u(\vec{r}) = \sum_{i=0}^{\infty} \epsilon^i u_i(\vec{r}). \quad (7.6)$$

Now both the object and the field are expressed as a function of the free variable ϵ . At first glance the problem is made more difficult by the addition of the extra perturbation parameter but by gathering together the powers of ϵ the problem can be easily solved.

The equation for the total field

$$u(\vec{r}) = u_{inc}(\vec{r}) + \int u(\vec{r}') o(\vec{r}') g(\vec{r}-\vec{r}') d\vec{r}' \quad (7.7)$$

is now written as a function of ϵ or

$$\sum_{i=0}^{\infty} \epsilon^i u_i(\vec{r}) = u_{inc} + \int \sum_{i=0}^{\infty} \epsilon^i u_i(\vec{r}') \epsilon \chi(\vec{r}') g(\vec{r}-\vec{r}') d\vec{r}'. \quad (7.8)$$

Rearranging this equation as a polynomial function of ϵ both the scattered field and the object satisfy an equation of the form

$$0 = [u_0(\vec{r}) - u_{inc}] + \quad (7.9)$$

$$\epsilon [u_1(\vec{r}) - \int u_0(\vec{r}') \chi(\vec{r}') g(\vec{r}-\vec{r}') d\vec{r}'] +$$

$$\epsilon^2 [u_2(\vec{r}) - \int u_1(\vec{r}') \chi(\vec{r}') g(\vec{r}-\vec{r}') d\vec{r}'] +$$

$$\epsilon^3 [u_3(\vec{r}) - \int u_2(\vec{r}') \chi(\vec{r}') g(\vec{r}-\vec{r}') d\vec{r}'] + \dots$$

In order for this equation to be valid each coefficient of ϵ in the series expansion must be identically equal to zero. This requirement is all that is necessary to solve the more general problem for u_i as a function of the perturbation parameter ϵ , but in the scattering problem only the solution for $\epsilon=1$ is interesting. Therefore by setting the coefficient of each power of ϵ equal to zero and then setting the value of ϵ equal to one the following equations result

$$u_0 = u_{inc} \quad (7.10)$$

$$u_1(\vec{r}) = \int u_0(\vec{r}') \chi(\vec{r}') g(\vec{r}-\vec{r}') d\vec{r}' \quad (7.11)$$

and in general

$$u_i(\vec{r}) = \int u_{i-1}(\vec{r}') \chi(\vec{r}') g(\vec{r}-\vec{r}') d\vec{r}' \quad i \geq 1. \quad (7.12)$$

This is the same system of equations defined as the Born series in Chapter 6 therefore the same conditions define the region of convergence for this

perturbation solution. This method of analysis was also applied to the scattering problem by Keller [Kel69] and by Oristaglio [Ori85].

The forward scattering problem represents a relatively simple example of the perturbation method. The inverse problem is solved by assuming that the Born series converges and writing the total scattered field as

$$u_s(\vec{r}) = \int u_0(\vec{r}') o(\vec{r}') g(\vec{r}-\vec{r}') d\vec{r}' + \quad (7.13)$$

$$\begin{aligned} & \int \int u_0(\vec{r}') o(\vec{r}') g(\vec{r}''-\vec{r}') d\vec{r}' o(\vec{r}'') g(\vec{r}-\vec{r}'') d\vec{r}'' + \\ & \int \int \int u_0(\vec{r}') o(\vec{r}') g(\vec{r}''-\vec{r}') d\vec{r}' o(\vec{r}'') g(\vec{r}'''-\vec{r}'') d\vec{r}'' \\ & o(\vec{r}''') g(\vec{r}-\vec{r}''') d\vec{r}''' + \dots \end{aligned}$$

Now replace the scattered field by

$$u_s(\vec{r}) = \epsilon \psi(\vec{r}) \quad (7.14)$$

and express the object as a polynomial in ϵ or

$$o(\vec{r}) = \sum_{i=0}^{\infty} \epsilon^i o_i(\vec{r}). \quad (7.15)$$

The scattered field is now written

$$\epsilon \psi = \int u_0(\vec{r}') \sum_i \epsilon^i o_i(\vec{r}') g(\vec{r}-\vec{r}') d\vec{r}' + \quad (7.16)$$

$$\begin{aligned} & \int \int u_0(\vec{r}') \sum_i \epsilon^i o_i(\vec{r}') g(\vec{r}''-\vec{r}') d\vec{r}' \sum_j \epsilon^j o_j(\vec{r}'') g(\vec{r}-\vec{r}'') d\vec{r}'' + \\ & \int \int \int u_0(\vec{r}') \sum_i \epsilon^i o_i(\vec{r}') g(\vec{r}''-\vec{r}') d\vec{r}' \sum_j \epsilon^j o_j(\vec{r}'') g(\vec{r}'''-\vec{r}'') d\vec{r}'' \\ & \sum_k \epsilon^k o_k(\vec{r}''') g(\vec{r}-\vec{r}''') d\vec{r}''' + \dots \end{aligned}$$

where S_i is used to denote scattering by object u_i .

This expression can be simplified by defining an integral operator S that maps an incident field into the field scattered by the object. If an incident field, $u_0(\vec{r})$, is scattered by an object, $o(\vec{r})$, then the scattering operator is defined by the following integral

$$u_s(\vec{r}) = S(u_0) \leftrightarrow \int u_0(\vec{r}') o(\vec{r}') g(\vec{r}-\vec{r}') d\vec{r}'. \quad (7.17)$$

Now the Born series in equation (7.13) can be written

$$u_s(\vec{r}) = S(u_0) + S^2(u_0) + S^3(u_0) + \dots \quad (7.18)$$

where

$$S^i(u_0) = S[S^{i-1}(u_0)]. \quad (7.19)$$

Using this notation (7.16) can be written

$$\begin{aligned} \epsilon\psi = & \sum_i \epsilon^i S_i(u_0) + \\ & \sum_i \sum_j \epsilon^i \epsilon^j S_j(S_i(u_0)) + \\ & \sum_i \sum_j \sum_k \epsilon^i \epsilon^j \epsilon^k S_k(S_j(S_i(u_0))) + \dots \end{aligned} \quad (7.20)$$

This expression can be simplified even further by denoting the iterated kernel $S_j(S_i(u_0))$ by the expression $S_{ji}(u_0)$. Now the Born series is written

$$\begin{aligned} \epsilon\psi = & \sum_i \epsilon^i S_i(u_0) + \\ & \sum_i \sum_j \epsilon^i \epsilon^j S_{ji}(u_0) + \\ & \sum_i \sum_j \sum_k \epsilon^i \epsilon^j \epsilon^k S_{kji}(u_0) + \dots \end{aligned} \quad (7.21)$$

Notice that the first summation above represents first order scattering from a number of different objects while the second set of summations represents all possible second order scatterings from the same ensemble of objects.

A series solution for the object function is found by gathering together the coefficients of like powers of ϵ . This gives the following polynomial in ϵ

$$\begin{aligned} \epsilon\psi(\vec{r}) = & \epsilon S_1(u_0) + \epsilon^2 [S_2(u_0) + S_{11}(u_0)] + \\ & \epsilon^3 [S_3(u_0) + S_{21}(u_0) + S_{12}(u_0) + S_{111}(u_0)] + \dots \end{aligned} \quad (7.22)$$

Just as was done in deriving the Born series each power of ϵ is independent and therefore the following equalities can be written

$$\psi = S_1(u_0) \quad (7.23)$$

$$S_2(u_0) = -S_{11}(u_0) \quad (7.24)$$

$$S_3(u_0) = -S_{21}(u_0) - S_{12}(u_0) - S_{111}(u_0) \quad (7.25)$$

and in general

$$S_i(u_0) = - \sum_{i_1+i_2+\dots+i_n=i} S_{i_1 i_2 \dots i_n}(u_0) \quad n \geq 2. \quad (7.26)$$

Consider first the equation for ψ . The solution for the object functions is only interesting when $\epsilon=1$ therefore $\psi=u_s$ and the first equality above can be written

$$u_s(\vec{r}) = \int u_0(\vec{r}') o_1(\vec{r}') g(\vec{r}-\vec{r}') d\vec{r}'. \quad (7.27)$$

This equation represents the measured scattered field as the first order scattered field from the object o_1 and by the Fourier Diffraction Theorem this equation can be solved exactly for o_1 . Because the object is illuminated with the incident field this is true for all experiments, regardless of the size of the object and its refractive index. This contrasts with first order diffraction tomography where the object is modulated by the total field and thus the Fourier Diffraction Tomography is only valid when the total field can be approximated by the incident field.

While equation (7.23) only expresses the scattered field from one view of the object it is possible to combine the scattered field from a number of different views and then use the first order reconstruction algorithm described in Chapter 4. Thus the result of the first order reconstruction algorithms described in Chapter 4 and 5 is exactly equal to o_1 .

The second order object is slightly more difficult to compute. From equation (7.23) the first order scattering from the second order object is given by

$$S_2(u_0) = -S_{11}(u_0). \quad (7.28)$$

The expression $S_{11}(u_0)$ represents the second order scattering from the first order object and is easily calculated because o_1 has already been computed. The higher order terms follow in a similar fashion except a number of partial scattered fields are summed to find the first order scattered field from o_1 .

The procedure used to calculate the higher order object is slightly different from that of the first order object because of the location of the receiver line. The first order object is a function of the scattered field and the placement of the receiver line is limited by experimental constraints. On the other hand the higher order fields are defined on a rectangular grid since an FFT based implementation of the Born integral is the most efficient procedure. Thus for

the higher order terms the field are calculated over the entire grid and then only the field along one side of the grid is used as input to the reconstruction procedure.

In summary the algorithm for reconstructing the object using the higher order Born series is

- Use the measured fields and the first order Born reconstruction algorithm to compute o_1 .
- For each $i > 1$ do the following.
 - Calculate the higher order scattered field from each of the already computed objects (See equation (7.26)).
 - Use the first order inversion algorithm to invert S_i and find o_i .
- Sum up each of the o_i to get the object reconstruction.

Notice that this algorithm is "exact." Except for the numerical approximations needed for the reconstruction procedure there are no mathematical approximations to limit the quality of the reconstruction.

The most expensive part of this algorithm is not doing the reconstructions but instead in computing the higher order scattered field, S_i . While it is easy to implement a fast algorithm to compute each partial field in S_i the total number of integrals increases rapidly with each succeeding iteration. Table 7.1 shows the number of partial fields and the total number of integrals needed for each of the first twenty iterations. Since each integral takes a constant amount of CPU time, no matter how it is implemented, the practical limit of this algorithm with today's computers is certainly under ten iterations.

The convergence of this series is dependent on the convergence of both the forward Born series shown in equation (7.13) and the object series shown in equation (7.15). Thus if either series is divergent then this reconstruction procedure will also diverge and produce an undefined answer.

The convergence of the forward series was discussed in Chapter 6. This, for example, showed that for an object of radius 2λ the scattered fields could be calculated using the Born series only for objects with a refractive index of less than about 11%. This puts a severe limitation on the type of objects that can be reconstructed with the higher order Born series. For objects that do fall within the allowable range the reconstruction with the higher order Born series should be quantitatively more accurate than that done with a first order algorithm.

Table 7.1. The number of partial field terms and integrals needed to calculate each iteration of the inverse higher order Born series.

Iteration	Terms	Integrals
1	0	0
2	1	2
3	3	7
4	7	19
5	15	47
6	31	111
7	63	255
8	127	575
9	255	1279
10	511	2815
11	1023	6143
12	2047	13311
13	4095	28671
14	8191	61439
15	16383	131071
16	32767	278527
17	65535	589823
18	131071	1245183
19	262143	2621439

The seriousness of this limitation is further seen by recalling that the higher order Born series only converges when the first order field closely approximates the total scattered field. This is the same condition that determines the accuracy of the first order reconstruction algorithms so the ultimate improvement is limited by the quality of first order reconstructions. Thus it will not be possible to image any object with a larger refractive index or radius than those in Figure 7.1 using an algorithm based on the Born series.

The convergence of the object series has yet to be determined. Jost and Kahn in [Jos52] report the convergence of the higher order Born inversion procedure for two quantum mechanical scattering experiments.

While the above derivation of the perturbation approach has expanded the object as a perturbation about zero it is also possible to consider the object to be a small perturbation of a known object. This generalization is known as the Distorted Wave Born Approximation (DWBA) and is described in [Tay83, New66, Dev83 and Bey85]. This procedure is made more difficult because the Green's function used in the integral now represents the scattered field from a point source with the effect of the known object included. The convergence of this procedure is not known.

7.4 Fixed Point Algorithms

A third untested approach to solve the inverse diffraction problem is to use a fixed point algorithm. While the overall algorithm is relatively straightforward it is necessary to perform a first order reconstruction of the object when illuminated by an arbitrary field. This is much more difficult than the first order reconstruction algorithms based on plane wave illumination described in Chapter 4. (The synthetic aperture approach does use point sources, but since a different phase is added to the scattered field for each transmitter position a plane wave is synthesized.)

A fixed point algorithm for calculating the object that scattered a measured field is based on the equation

$$o = f(o) \quad (7.29)$$

where o is the desired object function. Within the limits of convergence of the series, an initial guess o_{i-1} can be improved upon by iterating the equation

$$o_i = f(o_{i-1}). \quad (7.30)$$

The exact form of the iteration function, f , can take a number of different forms. Given only the scattered fields then either the Born or the Rytov

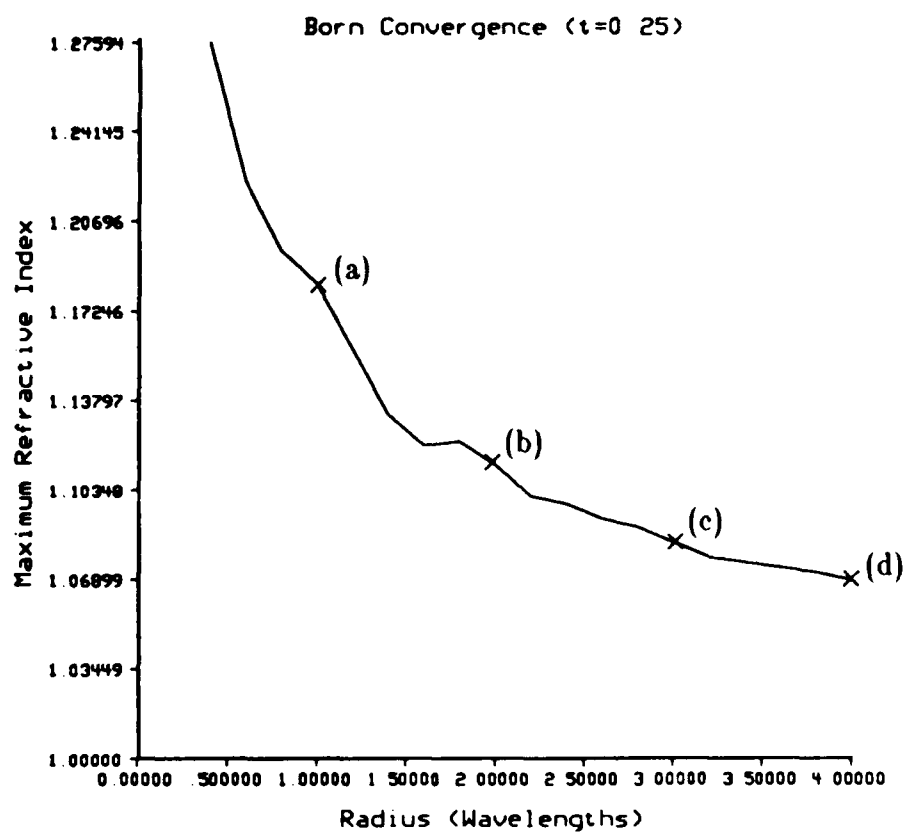
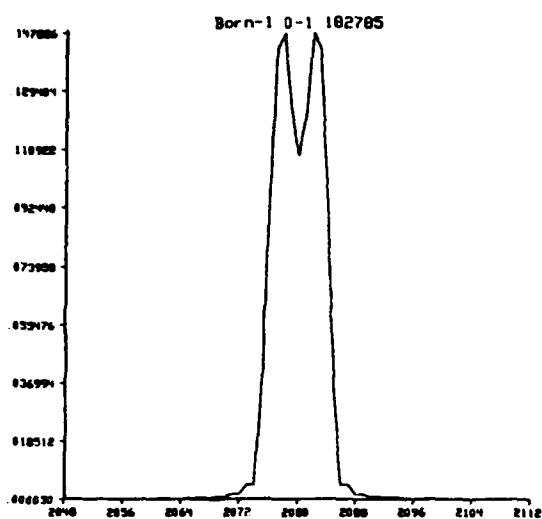
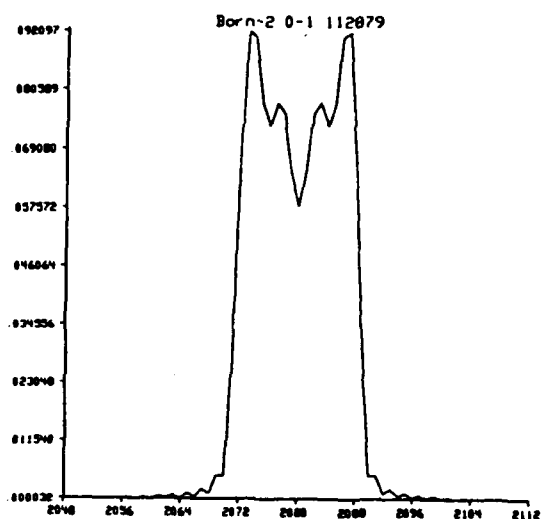


Figure 7.1

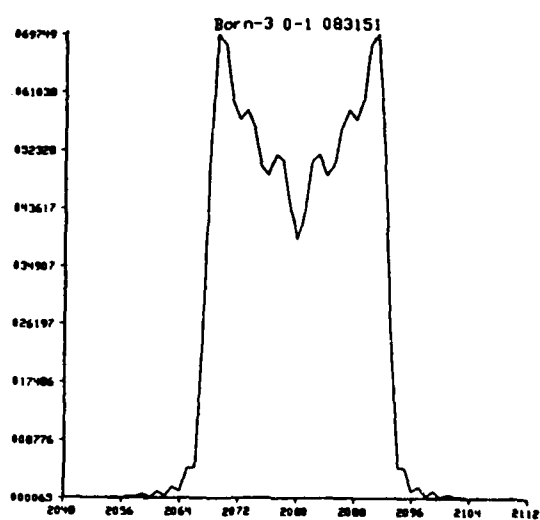
First order reconstructions of four objects at the limit of the Born series are shown here. Objects with a reconstruction worse than these can not be improved by an inversion procedure based on the Born series because the Born series will not converge.



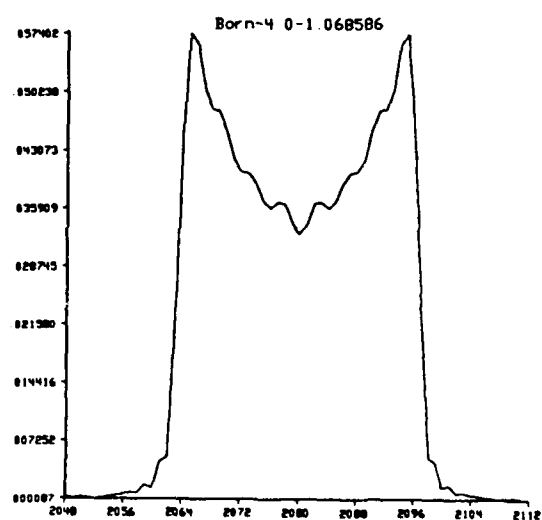
(a)



(b)



(c)



(d)

Figure 7.1

Continued.

approximation can be used to make an initial guess for the object. Both of these approximations assume that the field inside the object can be approximated by the incident field and this is the major source of error in the first order reconstruction procedures.

It seems reasonable that a better estimate of the object function could be found if the field inside the object is known. While it is not possible to know this without knowing the object first, a good estimate of the field should be possible given an estimate of the object. If the initial estimate of the object is "good enough" then a calculation of the scattered field given this estimate of the object should be more accurate than just using the incident field.

Using this new estimate for the field inside the object a better estimate of the object function should be possible. The general iteration formula can now be written

$$o_i = \text{Reconstruct}(\text{Estimate Field}(o_{i-1})) \quad (7.31)$$

Here the function labeled "Estimate Field" consists of estimating the total fields inside the object o_{i-1} and the function labeled "Reconstruct" consists of estimating the object given the total field in the object. The first iteration is the simplest since the estimate of the total field in the object is simply the incident field. Higher order iterations are made even more difficult since it is necessary to estimate the fields inside the object for each of the N_ϕ views.

Any number of means can be used to implement the two different steps in the algorithm. Estimating the field inside the object can be done with any of the procedures described in Chapter 6, including the Born and Rytov series or the algebraic approach. The procedure to use would depend on whether the object falls in the algorithm's region of convergence and on the efficiency of the algorithm with the available hardware.

Inverting the total fields to get an estimate for the object is the most difficult part of the algorithm. The Fourier Diffraction Theorem only applies to objects illuminated with a plane wave so a more general approach is needed. One solution to this problem was proposed by Vezzetti and Aks [Vez79]. Their work still assumes plane waves inside the object but now the field inside the object is modified by the average refractive index. With this approach they do show an improvement in the quality of the reconstruction but it is doubtful whether this approach would be accurate enough for a fixed point algorithm.

A complete solution for the object given an arbitrary set of illuminating fields would undoubtedly be based on a least squared approach. While there are enough equations, given the field everywhere, to determine the object the

system of equations would be very unstable because the Green's function only samples one arc of the scattering potential's Fourier transform. This means that if the field is known over an $N \times N$ grid and it is desired to calculate the object over the same grid then there would be a total of $N^2 N_\phi$ equations defining the N^2 unknowns. Thus the system of equations to determine the object is overdetermined and any error in the field estimates will lead to an inconsistent set of equations. A least squared approach could then be used to find the solution vector that best satisfies the defining equations.

The convergence of this method is unknown. Like the fixed point methods discussed in Chapter 6 it is necessary for the "derivative" of the function be less than one in some region for the algorithm to converge. It probably isn't unreasonable to assume that this method will only converge when the first order estimate of the object is "good."

References

- [Dev82] A. J. Devaney and E. Wolf, "A new perturbation expansion for inverse scattering from three-dimensional finite-range potentials," *Physics Letters*, Vol. 89a, May 24, 1982, pp. 269-272.
- [Dev83] A. J. Devaney and M. L. Oristaglio, "Inverse procedure for inverse scattering within the distorted wave Born approximation," *Physical Review Letters*, Vol. 51, July 25, 1983, pp. 237-240.
- [Joh83] S. A. Johnson and M. L. Tracy, "Inverse scattering solutions by a sinc basis, multiple source, moment method -- Part I: Theory," *Ultrasonic Imaging*, Vol. 5, 1983, pp. 361-375.
- [Jos52] R. Jost and W. Kohn, "Construction of a potential from a phase shift," *Physical Review*, Vol. 87, September 15, 1952, pp. 977-992.
- [Kel69] J. B. Keller, "Accuracy and validity of the Born and Rytov approximations," *Journal of the Optical Society of America*, Vol. 59, 1969, pp. 1003-1004.
- [Mos56] H. E. Moses, "Calculation of the scattering potential from reflection coefficients," *Physical Review*, Vol. 102, April 15, 1956, pp. 559-567.
- [Nay73] A. H. Nayfeh, *Perturbation Methods*, John Wiley and Sons, New York, 1973.
- [Nay81] A. H. Nayfeh, *Introduction to Perturbation Methods*, John Wiley and Sons, New York, 1981.
- [New66] R. G. Newton, *Scattering Theory of Waves and Particles*, McGraw-Hill Book Company, New York, 1966.
- [Ori85] M. L. Oristaglio, "Accuracy of the Born and Rytov approximations for the laws of refraction and reflection at a plane surface," *Journal of the Optical Society of America*, Submitted for Publication.
- [Pro69] R. T. Prosser, "Formal solutions of inverse scattering problems," *Journal of Mathematical Physics*, Vol. 10, October 1969, pp. 1819-1822.

- [Pro76] R. T. Prosser, "Formal solutions of inverse scattering problems, II," *Journal of Mathematical Physics*, Vol. 10, October 1976, pp. 1775-1779.
- [Sar81] T. K. Sarkar, D. D. Weiner, and V. K. Jain, "Some mathematical considerations in dealing with the inverse problem," *IEEE Transactions on Antenna and Propagation*, Vol. AP-29, 1981, pp. 373-379.
- [Tay83] J. R. Taylor, *Scattering Theory: The Quantum Theory of Nonrelativistic Collisions*, Robert E. Krieger Publishing Company, Malabar, FL, 1983.
- [Tra83] M. L. Tracy and S. A. Johnson, "Inverse scattering solutions by a sinc basis, multiple source, moment method -- Part II: Numerical evaluations," *Ultrasonic Imaging*, Vol. 5, 1983, pp. 376-392.
- [Vez79] D. J. Vezzeetti and S. O. Aks, "Reconstructions from scattering data: Analysis and improvements of the inverse Born approximation," *Ultrasonic Imaging*, Vol. 1, 1979, pp. 333-345.

CHAPTER 8 CONCLUSIONS

A number of ideas are new to this work. While they have served to answer a number of questions about diffraction tomography there remains much work to be done. This chapter, therefore, reviews the state of the art of diffraction tomography as presented by this work and indicates directions for future research.

Chapter 2 reviewed the wave equation and its integral solution. While this material is well known among people doing research in diffraction tomography and inverse scattering its presentation here emphasized the common mathematical problems in acoustic and electromagnetic scattering. For this reason all distances were expressed in wavelengths and the object function represented the (complex) refractive index variation of an inhomogeneity for either acoustic or electromagnetic waves. Researchers more concerned with experimental work will want to use the relationships presented in Chapter 2 to convert the results presented in the remainder of this work to more physical quantities.

Finally Chapter 2 also presented two approximations, the Born and the Rytov, which allow linearized versions of the wave equation to be written. These two first order perturbational approximations are important because they allow simple inversion algorithms to be derived. Since these approximations are so critical to first order diffraction tomography the mathematical limitations of each approximation are also discussed.

The Fourier Diffraction Theorem relates the scattered field measured on a line to the Fourier transform of the object and is presented in Chapter 3. This theorem is only true when either the Born or the Rytov approximation is valid but it has generated much excitement in the research community.

The Fourier Diffraction Theorem was derived by two different methods in this work. Both approaches to the Fourier Diffraction Theorem lead to the same relationship between the scattered field and the object's Fourier transform. The conventional approach is to decompose the Green's function,

the field scattered by a point scatterer, into plane waves and simply substitute this result into the integral solution to the wave equation. A second, new approach, is to consider the Fourier Diffraction Theorem entirely in the Fourier domain. This method points toward a more natural computer implementation and was exploited in Chapter 6 for computing better approximations to the scattered field.

The remainder of Chapter 3 discussed experimental methods for collecting enough scattered data so that a unique estimate for the object can be formed. The potential methods described include using a plane wave to illuminate the object, synthesizing plane waves much like what is done in phase array antenna design and broadband (in time) incident fields.

Chapter 4 discussed two mathematical algorithms for inverting the scattered data to estimate the object's (complex) refractive index. Much like conventional (straight ray) tomography there are two approaches that can be used to invert the scattered data. These two algorithms, often described as interpolation in the space domain and frequency domain, were presented here and their algorithmic complexity was discussed.

In addition several signal processing concerns were examined in Chapter 4. By calculating the Mean Squared Error between the object and the reconstruction it was concluded that zero padding each projection is a good way to reduce the interpolation error in the frequency domain. On the other hand, using a Hamming window to shape the projection and reduce the effect of the finite aperture severely attenuates the high frequency information in the projection and increases the error.

The limitations of first order diffraction tomography were discussed in Chapter 5. Two types of errors limit the quality of the reconstruction: mathematical limitations caused by the approximations used to derive the Fourier Diffraction Theorem and experimental limitations caused by the ability to only collect a finite amount of data. The mathematical limitations are the most severe. In deriving the Born and the Rytov approximations it was necessary to assume that the scattered fields were small compared to incident fields. This is equivalent to saying that the object must be weakly scattering for the first order diffraction tomography algorithms to hold and if this condition isn't met then the reconstruction will have serious artifacts.

The limits of first order diffraction tomography are easily described in terms of the magnitudes of the scattered fields but a more meaningful measure is to study the range of objects where the approximations are valid. This was done in Chapter 5 by calculating the exact scattered fields from a large number

of cylinders and then making an estimate of the object assuming that the first order diffraction tomography algorithms are valid. Thus it was concluded that the Born approximation is valid when the product of the diameter of the cylinder (in wavelengths) and the absolute value of the refractive index change is less than 0.5. On the other hand the size of the object is not as critical to the Rytov approximation. Instead the refractive index change is the limiting factor and reconstructions based on the Rytov approximation are good as long as the refractive index of the object is less than a few percent.

The experimental limitations, on the other hand, can always be minimized by collecting more data. Thus it is clear that interpolation error can always be reduced by increasing the number of projections or the number of samples per projection. Another, less obvious, limitation is the finite aperture of the projection. Unlike conventional (straight ray) tomography where the projection of a finite sized object has a finite length, the same is not true for scattered fields. With diffraction tomography the scattered field never goes to zero and the sampling interval for the projection must be carefully balanced to prevent aliasing but yet large enough to measure the high frequency information far from the center of the projection. An expression for this relationship was derived in Chapter 5 and several reconstructions were presented with different sampling intervals to confirm the optimum sampling interval.

The limitations of first order reconstruction algorithms were addressed in Chapters 6 and 7. The most severe limitation is caused by the first order perturbation models assumed in deriving the Fourier Diffraction Theorem. Thus Chapter 6 discussed several approaches to more accurately model the scattered fields. With one of these more accurate models it should then be possible to invert the relationship and derive a better reconstruction algorithm. A survey of several possible approaches to inverting the scattered data is presented in Chapter 7.

Since better reconstructions will be based on more accurate models of the field inside the object two approaches to more accurately model the scattered field were presented in Chapter 6. The most severe limitation of first order algorithms is the assumption that the field inside the object is approximately equal to the incident field. Thus when this condition is not valid the Born and the Rytov approximations are no longer valid.

The simplest technique is to assume that the perturbational model used to derive the Fourier Diffraction Theorem is approximately correct and simply include more of the higher order terms. The result is a series of terms much

like a Taylor series. This is an iterative procedure and was applied to both the Born and the Rytov approximations.

An important measure of any series is a description of its region of convergence. In this case the region of convergence is a function of the entire object and the results presented in Chapter 6 were simplified by considering the convergence as a function of size and refractive index of simple objects. Thus the region of convergence can be described by two parameters and all objects outside this region (because they are larger or have a greater refractive index change) will cause the series to diverge.

The series described in Chapter 6 were calculated by sampling the object and the fields and then using an efficient algorithm based on Fourier transforms. In each case the scattered field was calculated by multiplying a function of the object by a field and then convolving this "scattering potential" with the Green's function. The convolution represents the most expensive part of the algorithm and can be efficiently calculated using FFT's.

The convergence properties of the Born and the Rytov series were determined by a binary search procedure. Thus for a given size the refractive index of the object was varied till a point was found where the series converged for all refractive indices that were smaller and diverged if the refractive index was larger than this point. By varying the size of the object it was possible to show a region of convergence as a function of both object size and refractive index.

The simulations of the Born series showed it to converge only when the first iteration is an accurate estimate of the field inside the object. Thus the phase change of the field as it travels through the object is a good indication of not only the quality of a first order Born reconstruction but also describes the region of convergence of the Born series.

The convergence of the Rytov series is more surprising. For all cases studied the Rytov series' region of convergence includes the region of convergence for the Born. This is especially surprising since the first order Born and Rytov approximations have different regions of validity.

In addition Chapter 6 also presented a study of the effects of attenuation on both the Born and the Rytov series. A key part of this work is the idea that attenuating plane waves can be described either in terms of a solution to the wave equation or in the Fourier domain. In a non-attenuating media the two approaches are identical since plane wave solutions to the wave equation are also Fourier waves.

Considering an attenuating plane wave in the Fourier domain makes it possible to calculate the higher order Born and Rytov series for attenuating media. While the algorithms remain the same there is a significant difference in its convergence properties. Since the energy in the field is attenuated as it travels away from the scattering site the region of convergence for both the Born and the Rytov series is increased as the attenuation of the media is increased. Thus the attenuation of the media balances the extra field caused by a larger scattering potential.

A second approach to calculating the scattered fields from a known object was also discussed in Chapter 6. By sampling the object and the fields a set of discrete equations can be written that relate the field and the object. Without using any approximations it is then possible to express the field as the solution of a linear matrix equation.

While the form of the matrix equation is simple, the large amount of data makes this problem difficult to compute directly with today's computers. Instead it was necessary to use an iterative technique known as the Kaczmarz approach to solve the matrix. While the iterative technique used can be shown theoretically to always converge, numerical errors limit the range of objects to those that have a refractive index change of less than 20-40%.

The rate of convergence of this method is only a function of the orthogonality of the defining equations. Thus when the object has a small refractive index the defining equations are nearly orthogonal and the Kaczmarz approach quickly converges to the correct field. On the other hand as the refractive index is increased the hyperplanes defined by the equations become nearly parallel and convergence is much slower. Since the Kaczmarz approach treats each equation for the field separately faster convergence is often possible by sequencing the equations so that each equation is nearly parallel to the one before it.

Finally Chapter 7 presented a survey of several techniques for reconstructing an object without using first order approximations. The most difficult part of this problem is that it is now necessary to actually compute the field inside the object. In first order diffraction tomography the field inside the object is assumed to be a plane wave but this can't be true with higher order approximations. Since it is necessary to illuminate the object from a number of different directions to perform the reconstruction a calculation of the field is necessary for each view. The large number of equations makes this a difficult and expensive process.

A straightforward approach is to write a system of equations that describes both the field inside the object and the refractive index of the object. It should then be possible to solve this system of equations for both the field and the object. Unfortunately it is a non-linear system of equations because the defining equations are a function of the product of the two unknowns. For this reason it is necessary to use some type of search procedure to solve for both the fields and the object.

A second approach, first used in high energy physics and described in Chapter 7, is to do a perturbation expansion for the object. This is similar to the Born and the Rytov series described in Chapter 6 but now the object is assumed to consist of a series of components.

The convergence of this approach is a function of two series. Since this approach is based on a Born series expansion for the scattered field it is only valid when the field inside the object can be described as a converging Born series. As seen in Chapter 6 this is a rather severe limitation. In addition the object is expressed as a separate series expansion and for this approach to converge it is necessary for both the Born series and the object series to converge.

Finally a third approach, described in Chapter 7, is to make a first order estimate for the object and then use this object to calculate a better estimate for the field inside the object. Like the Born and the Rytov series described in Chapter 6 this is a fixed point algorithm. This approach is made even more difficult than first order reconstruction algorithms since it is necessary to calculate an estimate of the object given an arbitrary illuminating field. Since each projection is no longer independent the Fourier Diffraction Theorem is not valid and a reconstruction procedure will need to look at all the scattered data simultaneously. This can be easily done using a matrix formulation but there is a severe performance penalty.

The convergence properties of this particular series is not known although it is probably reasonable to assume that the region of convergence will be a function of the quality of the first order estimate of the field. If using the first order estimate of the field is not better than the original assumption to use the incident field then certainly the series will diverge. This condition represents a severe limitation for the technique.

Future work on this problem could continue in several areas. The perturbational approach has a limited range of convergence but for objects that fall within this range a better quantitative estimate of the object should be possible than that which is possible using first order algorithms. The same is

also true for the fixed point approach but more work is needed to determine the range of convergence.

Certainly the only guaranteed approach to solve the inverse scattering problem is to find a solution to a non-linear set of equations. There are a number of algorithms that can be used but the large number of equations (a 128x128 reconstruction has over 2 million unknowns and equations) makes this a very difficult problem.

BIBLIOGRAPHY

BIBLIOGRAPHY

- F. S. Acton, *Numerical Methods that Work*, Harper & Row, New York, 1970.
- A. H. Andersen and A. C. Kak, "Digital ray tracing in two-dimensional refractive fields," *The Journal of the Acoustical Society of America*, Vol. 72, November 1982, pp. 1593-1606.
- A. H. Anderson and A. C. Kak, *The application of ray tracing towards a correction for refracting effects in computed tomography with diffracting sources*, TR-EE 84-14, School of Electrical Engineering, Purdue University, 1984.
- M. Azimi and A. C. Kak, "Distortion in diffraction imaging caused by multiple scattering," *IEEE Transactions on Medical Imaging*, Vol. MI-2, December 1983, pp. 176-195.
- H. P. Baltes (editor), *Inverse Source Problems in Optics*, Springer-Verlag, 1978.
- H. H. Barrett and W. Swindell, *Radiological Imaging: The Theory of Image Formation, Detection and Processing*, Academic Press, New York, 1981.
- William H. Carter, "Computational reconstruction of scattering objects from holograms," *Journal of the Optical Society of America*, Vol. 60, March 1970, pp. 306-314.
- W. H. Carter and P. C. Ho, "Reconstruction of inhomogeneous scattering objects from holograms," *Applied Optics*, Vol. 13, January 1974, pp. 162-172.
- P. L. Carson, T. V. Oughton, and W. R. Hendee, "Ultrasound transaxial tomography by reconstruction," in *Ultrasound in Medicine II*, D. N. White and R. W. Barnes, eds., Plenum Press, 1976, pp. 391-400.
- Y. Censor, "Row-actions methods for huge and sparse systems and their applications," *SIAM Review*, Vol. 23, October 1981, pp. 444-466.
- L. A. Chernov, *Wave Propagation in a Random Medium*, McGraw Hill Book Company, New York, 1960.

David Colton and Rainer Kress, *Integral Equation Methods in Scattering Theory*, John Wiley and Sons, New York, NY, 1983.

S. D. Conte and C. deBoor, *Elementary Numerical Analysis*, McGraw-Hill, New York, 1980.

C. R. Crawford and A. C. Kak, "Aliasing artifacts in computerized tomography," *Appl. Opt.*, Vol. 18, 1979, pp. 3704-3711.

A. J. Devaney, "A filtered backpropagation algorithm for diffraction tomography," *Ultrasonic Imaging*, Vol. 4, 1982, pp. 336-350.

A. J. Devaney and E. Wolf, "A new perturbation expansion for inverse scattering from three-dimensional finite-range potentials," *Physics Letters*, Vol. 89a, May 24, 1982, pp. 269-272.

A. J. Devaney, "A computer simulation study of diffraction tomography," *IEEE Transactions on Biomedical Engineering*, Vol. BME-30, July 1983, pp. 377-386.

A. J. Devaney and M. L. Oristaglio, "Inverse procedure for inverse scattering within the distorted wave Born approximation," *Physical Review Letters*, Vol. 51, July 25, 1983, pp. 237-240.

A. J. Devaney, "Geophysical diffraction tomography," *IEEE Transaction Geological Science, Special Issue on Remote Sensing*, Vol. GE-22, January 1984, pp. 3-13.

R. Gagliardi, *Introduction to Communications Engineering*, John Wiley and Sons, 1978.

G. H. Glover and J. L. Sharp, "Reconstruction of ultrasound propagation speed distribution in soft tissue: Time-of-flight tomography," *IEEE Trans. Sonics and Ultrasonics*, Vol. SU-24, July 1977, pp. 229-234.

J. W. Goodman, *Introduction to Fourier Optics*, McGraw Hill Book Company, San Francisco, 1968.

J. F. Greenleaf, S. A. Johnson, S. L. Lee, G. T. Herman, and E. H. Wood, "Algebraic reconstruction of spatial distributions of acoustic absorption within tissue from their two dimensional acoustic projections," in *Acoustical Holography*, Plenum Press, 1974, pp. 591-603.

J. F. Greenleaf, S. A. Johnson, W. F. Wamoya, and F. A. Duck, "Algebraic reconstruction of spatial distributions of acoustic velocities in tissue from their time-of-flight profiles," in *Acoustical Holography*, Plenum Press, 1975, pp. 71-90.

J. F. Greenleaf, S. K. Kenue, B. Rajagopalan, R. C. Bahn, and S. A. Johnson, "Breast imaging by ultrasonic computer-assisted tomography," in *Acoustical Imaging*, A. Methereil, ed., Plenum Press, 1978.

G. T. Herman, A. Lent, and S. Rowland, "ART: Mathematics and applications: A report on the mathematical foundations and on applicability to real data of the algebraic reconstruction techniques," *J. Theor. Biol.*, Vol. 43, 1973, pp. 1-32.

G. T. Herman, A. V. Lakshminarayanan, A. Naparstek, E. L. Ritman, R. A. Robb, and E. H. Wood, "Rapid computerized tomography," *Med. Data Process.*, 1976, pp. 582-598.

G. T. Herman, *Image Reconstructions from Projections*, Academic Press, New York, 1980.

G. T. Heydt, *Computer Analysis Methods for Power Systems*, MacMillan, New York, 1985.

Harry Hochstadt, *Integral Equations*, John Wiley and Sons, New York, NY, 1973.

G. N. Hounsfield, *A method of apparatus for examination of a body by radiation such as x-ray or gamma radiation*, Patent Specification 1283915, The Patent Office, 1972.

A. Ishimaru, *Wave Propagation and Scattering in Random Media*, Academic Press, New York, 1978.

K. Iwata and R. Nagata, "Calculation of refractive index distribution from interferograms using the Born and Rytov's approximations," *Jap. J. Appl. Phys.*, Vol. 14, 1975, pp. 1921-1927.

C. V. Jakowatz Jr. and A. C. Kak, *Computerized tomography using x-rays and ultrasound*, Research Report TR-EE 76-26, School of Electrical Engineering, Purdue University, 1976.

S. A. Johnson and M. L. Tracy, "Inverse scattering solutions by a sinc basis, multiple source, moment method -- Part I: Theory," *Ultrasonic Imaging*, Vol. 5, 1983, pp. 361-375.

R. Jost and W. Kohn, "Construction of a potential from a phase shift," *Physical Review*, Vol. 87, September 15, 1952, pp. 977-992.

S. Kaczmarz, "Angenaherte auflosung von systemen linearer gleichungen," *Bull. Acad. Polon. Sciences et Lettres A*, 1937, pp. 355-357.

A. C. Kak, "Tomographic imaging with diffracting and non-diffracting sources," in *Array Signal Processing*, Simon Haykin, ed., Prentice Hall, 1984.

A. C. Kak and B. Roberts, "Image reconstruction from projections," in *Handbook of Image Processing*, T. Y. Young and K. S. Fu, eds., Academic Press, 1985.

M. Kaveh, M. Soumekh, and R. K. Mueller, "Tomographic imaging via wave equation inversion," *ICASSP 82*, May 1982, pp. 1553-1556.

M. Kaveh, M. Soumekh, and J. F. Greenleaf, "Signal processing for diffraction tomography," *IEEE Transactions on Sonics and Ultrasonics*, Vol. SU-31, July 1984, pp. 230-239.

J. B. Keller, "Accuracy and validity of the Born and Rytov approximations," *Journal of the Optical Society of America*, Vol. 59, 1969, pp. 1003-1004.

S. K. Kenue and J. F. Greenleaf, "Limited angle multifrequency diffraction tomography," *IEEE Transactions on Sonics and Ultrasonics*, Vol. SU-29, July 1982, pp. 213-217.

Z. Q. Lu, M. Kaveh, and R. K. Mueller, "Diffraction tomography using beam waves: Z-average reconstruction," *Ultrasonic Imaging*, Vol. 6, January 1984, pp. 95-102.

Albert Macovski, *Medical Imaging Systems*, Prentice Hall, Englewood Cliffs, NJ, 1983.

K. Mano, "Interrelationship between terms of the Born and Rytov expansions," *Proceedings of the IEEE*, Vol. 58, July 1970, pp. 1168-1169.

R. McGowan and R. Kuc, "A direct relation between a signal time series and its unwrapped phase," *IEEE Transactions on Acoustics, Speech and Signal Processing*, Vol. ASSP-30, October 1982, pp. 719-726.

Philip M. Morse and Herman Feshbach, *Methods of Theoretical Physics*, McGraw Hill Book Company, New York, 1953.

P. M. Morse and K. U. Ingard, *Theoretical Acoustics*, McGraw Hill Book Company, New York, 1968.

H. E. Moses, "Calculation of the scattering potential from reflection coefficients," *Physical Review*, Vol. 102, April 15, 1956, pp. 559-567.

R. K. Mueller, M. Kaveh, and G. Wade, "Reconstructive tomography and applications to ultrasonics," *Proceedings of the IEEE*, Vol. 67, 1979, pp. 567-587.

D. Nahamoo and A. C. Kak, *Ultrasonic diffraction imaging*, TR-EE 82-20, School of Electrical Engineering, Purdue University, 1982.

D. Nahamoo, S. X. Pan, and A. C. Kak, "Synthetic aperture diffraction tomography and its interpolation-free computer implementation," *IEEE Transactions on Sonics and Ultrasonics*, Vol. SU-31, July 1984, pp. 218-229.

A. H. Nayfeh, *Perturbation Methods*, John Wiley and Sons, New York, 1973.

A. H. Nayfeh, *Introduction to Perturbation Methods*, John Wiley and Sons, New York, 1981.

R. G. Newton, *Scattering Theory of Waves and Particles*, McGraw-Hill Book Company, New York, 1966.

B. T. O'Connor and T. S. Huang, *Techniques for determining the stability of two-dimensional recursive filters and their application to image restoration*, TR-EE 78-18, School of Electrical Engineering, Purdue University, pp 6-24.

A. V. Oppenheim and R. W. Schaffer, *Digital Signal Processing*, Prentice-Hall, Englewood Cliffs, NJ, 1975.

M. L. Oristaglio, "Accuracy of the Born and Rytov approximations for the laws of refraction and reflection at a plane surface," *Journal of the Optical Society of America*, Submitted for Publication.

S. X. Pan and A. C. Kak, "A computational study of reconstruction algorithms for diffraction tomography: Interpolation vs. filtered-backpropagation," *IEEE Transactions on Acoustics, Speech and Signal Processing*, October 1983, pp. 1262-1275.

R. T. Prosser, "Formal solutions of inverse scattering problems," *Journal of Mathematical Physics*, Vol. 10, October 1969, pp. 1819-1822.

R. T. Prosser, "Formal solutions of inverse scattering problems, II," *Journal of Mathematical Physics*, Vol. 10, October 1976, pp. 1775-1779.

R. S. Ramakrishnan, S. K. Mullick, R. K. S. Rathore, and R. Subramanian, "Orthogonalization, Bernstein polynomials, and image restoration," *Appl. Opt.*, Vol. 18, 1979, pp. 464-468.

J. Richmond, "Scattering by a dielectric cylinder of arbitrary cross section shape," *IEEE Transactions on Antennas and Propagation*, Vol. AP-13, 1965, pp. 334-341.

A. Rosenfeld and A. C. Kak, *Digital Picture Processing*, Academic Press, Second Edition, 1982.

M. I. Sancer and A. D. Varvatsis, "A comparison of the Born and Rytov methods," *Proceedings of the IEEE*, Vol. 58, January 1970, pp. 140-141.

T. K. Sarkar, D. D. Weiner, and V. K. Jain, "Some mathematical considerations in dealing with the inverse problem," *IEEE Transactions on Antenna and Propagation*, Vol. AP-29, 1981, pp. 373-379.

L. A. Shepp and B. F. Logan, "The Fourier reconstruction of a head section," *IEEE Trans. Nucl. Sci.*, Vol. NS-21, 1974, pp. 21-43.

Malcolm Slaney and A. C. Kak, "Diffraction tomography," *Proceedings of the SPIE*, Vol. 413, April 1983, pp. 2-19.

Malcolm Slaney, A. C. Kak, and L. E. Larsen, "Limitations of imaging with first order diffraction tomography," *IEEE Transactions on Microwave Theory and Techniques*, August 1984, pp. 860-873.

M. Soumekh, M. Kaveh, and R. K. Mueller, "Algorithms and experimental results in acoustic tomography using Rytov's approximation," *ICASSP 89 Proceedings*, April 1983, pp. 135-138.

M. Soumekh, M. Kaveh, and R. K. Mueller, "Fourier domain reconstruction methods with application to diffraction tomography," *Acoustical Imaging*, Vol. 13, 1984, pp. 17-30.

M. Soumekh and M. Kaveh, "Image reconstruction from frequency domain data on arbitrary contours," *International Conference on Acoustics, Speech and Signal Processing*, 1984, pp. 12A.2.1 - 12A.2.4.

F. Stenger, "Numerical methods based on Whittaker cardinal, or sinc functions," *SIAM Review*, Vol. 23, April 1981, pp. 165-224.

Josef Stoer and Roland Bulirsch, *Introduction to Numerical Analysis*, Springer-Verlag, New York, 1980.

K. Tanabe, "Projection method for solving a singular system," *Numer. Math.*, Vol. 17, 1971, pp. 203-214.

J. R. Taylor, *Scattering Theory: The Quantum Theory of Nonrelativistic Collisions*, Robert E. Krieger Publishing Company, Malabar, FL, 1983.

M. L. Tracy and S. A. Johnson, "Inverse scattering solutions by a sinc basis, multiple source, moment method -- Part II: Numerical evaluations," *Ultrasonic Imaging*, Vol. 5, 1983, pp. 376-392.

J. M. Tribolet, "A new phase unwrapping algorithm," *IEEE Transactions on Acoustics, Speech and Signal Processing*, Vol. ASSP-25, April 1977, pp. 170-177.

D. J. Vezzeetti and S. O. Aks, "Reconstructions from scattering data: Analysis and improvements of the inverse Born approximation," *Ultrasonic Imaging*, Vol. 1, 1979, pp. 333-345.

W. L. Weeks, *Electromagnetic Theory for Engineering Applications*, John Wiley and Sons, Inc., New York, 1964.

E. Wolf, "Three-dimensional structure determination of semi-transparent objects from holographic data," *Optics Communications*, Vol. 1, 1969, pp. 153-156.

VITA

VITA

Malcolm Graham Slaney was born on August 6, 1959 in Harvey, IL. He entered Purdue University during the Fall of 1977 and was admitted to the Graduate School in December 1978.

He received his Bachelor of Science in Electrical Engineering with Honors in May 1981 and the Master of Science in Electrical Engineering in August 1981.

Since May 1981 he has been employed as a Research Associate in the Ultrasonic Imaging Laboratory of the School of Electrical Engineering at Purdue University. He is a member of Eta Kappa Nu, Tau Beta Pi, IEEE and ACM.

END

11-87

DTIC